Title
Development of Organic-Inorganic Hybrid Thermoelectrics

Author
Yee, Shannon Koa

Publication Date
2013

Development of Organic-Inorganic Hybrid Thermoelectrics

By

Shannon Koa Yee

A dissertation submitted in partial satisfaction of the

requirements for the degree of

Doctor of Philosophy

In

Mechanical Engineering

in the

Graduate Division

of the

University of California, Berkeley

Committee in charge:

Professor Rachel A. Segalman, Co-Chair
Professor Chris Dames, Co-Chair
Professor Arun Majumdar
Professor Van Carey
Professor Peidong Yang

Fall 2013

Development of Organic-Inorganic Hybrid Thermoelectrics

By Shannon K. Yee

Abstract

Development of Organic-Inorganic Hybrid Thermoelectrics

by

Shannon Koa Yee

Doctor of Philosophy in Mechanical Engineering

University of California, Berkeley

Professor Rachel A. Segalman, Co-Chair
Professor Chris Dames, Co-Chair

While greater than 80% of all electricity continues to be generated by heat engines, methods of directly converting heat into electricity will remain appealing. Thermoelectric generators are one technology that is capable of doing this but the low efficiency and high cost has limited their terrestrial deployment. Thermoelectrics are compact, solid state devices, without moving parts that directly convert a temperature difference into a voltage. Developing better thermoelectric materials is challenging and requires that materials be engineered with new transport physics. The interface between organic and inorganic materials is one example where new transport physics manifests. Therefore, it is possible that improvements in thermoelectrics can be made by engineering organic-inorganic hybrid thermoelectric materials.

Composite materials exhibit characteristics of their constituents where hybrid materials possess new properties that are distinctly different from their constituents. At the interface between organic and inorganic materials, hybrid properties manifest. One ideal system to understand this interface is in a metal-molecule-metal junction commonly referred to as a molecular junction. This is often a result of the discrete electronic energy levels of the organic hybridizing with the continuum of electronic states in the inorganic.

Herein, new transport phenomenon is observed in molecular junctions, which have great promise for thermoelectrics. It is observed that the transport property are positively correlated breaking the historic trends to improving thermoelectric efficiency. Towards the goal of higher efficiency thermoelectrics, the fundamental science of interfaces is first investigated in molecular junctions. Guiding principles from these fundamental studies are then applied to engineer a bulk, polymer-based, thermoelectric materials with high efficiency. These improvements are encouraging and motivated a cost analysis to evaluate their current market potential against competing thermoelectric materials. In all, this dissertation marks the progress in developing a new class of hybrid organic-inorganic materials for thermoelectric applications.

Dedicated

to

My parents, brothers, and family for allowing me to walk this path

and

To the numerous advisors, mentors, and friends who have guided me along the way

Table of Contents

List of Figures

List of Tables

Acknowledgements

I am most thankful to my family for the freedom to pursue my dreams for the last five years. Along the way, many sacrifices were made but without their emotional support I never would have been able to accomplish this dream. I would like to thank my father Don who was always willing to listen and offer his words of wisdoms. His consultation and encouragement kept me motivated and my heart always in the right place. I would like to thank my mother Sandy whose independence and strength I have always admired and tried to emulate. Since I was a young child, she has always been there to help pick me up, dust off my injuries, and send me back out to play. I would like to thank my older brother Sean whose led the way and blocked me from blows. Through shared experiences he understood the challenges along this road and always made me laugh. Finally, I would like to thank my brother Ed who was my closest confidant in the trenches and will be sorely missed.

Next, I would like to thank my advisor Arun Majumdar who first found me as an undergraduate student at OSU. Through the first year at Berkeley he led by example and showed me how to be a researcher. After a year and half at Berkeley, Arun was asked by President Obama to be the first Director of the Advanced Research Project Agency for Energy (ARPA-E). To my delight Arun invited me to join him at ARPA-E as the first ARPA-E Fellow. This experience has profoundly changed my life. It has given me a perspective unlike any other, and provided me with lifelong friends – a Band of Brothers. I learned more during my year in DC form Arun than I could have hoped for in 20 years of graduate school. From the late night conversations over beer, through the Snowmageddon and the first Summit, to canoeing on the Chesapeake, to connecting with student energy leaders, and to being claimed in front of President Clinton as "my graduate student" – it certainly has been a unforgettable and life changing experience. Thank you Arun!

I would like to thank my advisor Rachel Segalman who stood by me through every unconventional twist and turn of my graduate school experience. When I left for ARPA-E, she encouraged me to take research equipment with me so I would continue working on my PhD. Upon leaving she offered me some sage advice: "Remember if you ever get into trouble just remember you have a "get out of jail free card." Just shrug your shoulders and say 'that's why I'm still a graduate student.'" Rachel has always looked out for me even though I am not an easy student to teach and mentor. Rachel has shown tremendous patience with me and has taught me much about the finer points of academia. I am easily distracted and enjoy having multiple side projects, many unrelated to my PhD. Rachel served as an anchor and gently reminded me to remain focus on my PhD without which I know I would have been lost. Her steadfast encouragement and direction has seen me through this process. I am eternally grateful for her counsel and advice and know her words of wisdom will serve me well in my career.

I would also like to thank my advisor Chris Dames who pushed me to a higher academic standard. The long hours working together in his office have helped me become a more solid researcher and have provided the final polish to my PhD. Chris is a great role model and showed me another aspect of academia. Chris sincerely cares about mentoring each of his students extremely well. Through his example I have witness how he actively shapes his student's minds. It is a long process and requires steadfast determination. Through his example, I have learned what type of individual mentor I would like to be to my students. I truly hope I am able to follow his example with my own students.

Next, I would also like to especially thank Jonathan Malen who served as a mentor and role model for me. Upon his departure to CMU, Jon offered me one piece of advice and that is to "trust in myself." This has been my guiding principle through graduate school. I would also like to thank Joseph Feser who has been a close friend and mentor throughout my PhD; I thoroughly enjoyed our scientific conversations on the trail.

I would also like to especially thank some of my graduate school colleagues in the Majumdar Lab: Kedar Hippalgaonkar, Chuanhua Duan, Jayakanth Ravichandran, Kanhayalal (Kaal) Baheti, Renkun Chen, Jae Hun Seol, Cheng (Andy) Zheng, Karma Sawyer, Ming-Chang Lu, Vinod Srinivasan, Baoling Huang, Dongyan Xu, Robert Wang, Justyn Jaworski, Suzanne Singer, Marta Cerruti, Keisuke Yokoyama, Anders Greve, Yang Zhao, Renea Chu, Yusra Satoglu, and Pramod Reddy. I would also like to thank my graduate school colleagues in the Segalman Lab: Nelson Coates, Boris Russ, Bryan McCulloch, Miguel Modestino, Victor Ho, Bryan W. Boudouris, Megan Hoarfrost, Hannah Murnen, Adrianne Rosales, Kevin See, Wendy van Zoelen, Barbara Ekerdt, Eddie Buehler, Hilda Buss, William Chang, Cynthia Chen, Emily Davidson, Gabriel Sanoja, Kasper Moth-Poulsen, Saar Kirmayer, Jibin Sun, Young Rae Hong, and Lisa Strover. Finally, I'd like to thank my graduate school colleagues in the Dames Lab: Zhen Chen, Fan (Peter) Yang, Sean Lubner, Vivek Mishra, Imran Khan, and Jeffrey Crosby. I would also like to acknowledge my Mechanical Engineering colleagues: Matt Lucas, Matt Beres, Lindsay Miller, Jessy Rivest, Andrew North, and Rich Wilson who have helped me from time to time.

In addition, I would like to thank a number of Berkeley faculty members who have supported and encouraged me. Most notably: Ramamoorthy Ramesh, Joel Moore, Van Carey, Costas Grigoropoulos, and Samuel Mao. I'd also like to acknowledge collaborators in Chemistry, Don Tilley and Jibin Sun. I'd also like to thank collaborators at Stanford, Saniya Leblanc and Ken Goodson, and Matt Scullin of Alphabet Energy as we tackled the difficult and less celebrated question of thermoelectric costs. I would also like to thank Gang Chen, Ali Shakouri, and Ravi Prasher for encouragement and conversation through the years. I would also like to acknowledge collaborators at the Lawrence Berkeley National Laboratory, Jeffrey Neaton, Pierre Daracet, Jeffrey Urban, Kevin See, and Nelson Coates. I would also like to thank my previous advisors Vish Subramaniam, Xiaodong Sun, Steve Piet, and Jake Jacobson for continuing to provide advice.

I would also like to thank some close friends who have stood with me through this journey, most notably Matt Lucas and Noah Bronstein who have gone through the high and low times in energy with me. I'd like to thank some of my BERC colleagues for supporting my ambitions: Sebastien Lounis, Asher Burns-burg, Alex Luce, Adam Boscoe, Maria Schriver, and everyone else who helped make this a successful organization. I'd also like to thank my business partners Sarah Wood, Matthew Smith, Kevin Huang, and Rahul Malik who gave me the necessary distraction and extension of experiences that I needed to be well rounded. I would also like to thank the numerous student energy leaders around the country who have given me their support and aid when I asked: Brentan Alexander, Amit Desai, Teryn Norris, Adela Bardos, Caleb Wraugh, David Cohen-Tanugi, Addison Stark, and David Sanchez. I would also like to thank Matthew Trevithick, Matthew Nordan, Ray Rothrock, Will Coleman, KT Moortgat, Steve Vassalo, and Gabriel Kra in Venture Capitalism for always being willing to support my endeavors, encourage my learning, and tolerate my failures.

I am also grateful to the ARPA-E family: Dave Danielson, Eric Toone, Mark Hartney, Sanjay Wagle, Ravi Prasher, Rajeev Ram, Mark Johnson, Jonathan Burbaum, Tony DiGiovanni, Matthew Dunne, Ilan Gur, Dane Boysen, and the ARPA-E Fellows – Nick Cizek, Phil Larochelle, Karma Sawyer, Asegun Henry, Robert Conrado, Amul Tevar, Tim Heidel, Brad Zampf, Liz Santori, and Will Regan. I hope this friendship extends for a lifetime.

Finally I would like to gratefully acknowledge and thank the Fannie & John Hertz Foundation for my graduate school support as a Hertz Fellow and as a Big George Fellow. This fellowship gave me the freedom to innovate. Each day it augmented my graduate experience providing me the freedom to take non-linear paths and detours to follow my passions and make a lasting impact. I would especially like to thank Jay Davis, Lowell Wood, and Tom Weaver for overseeing my progress and offering support, guidance, advice, and encouragement. I'd also like to sincerely thank Ray Sidney for his unwavering assistance throughout my degree. Also, I am truly grateful to Louis Lerman for all his support and advice as a mentor. Finally, I'd like to thank Brian von Herzen for his encouragement to explore new topics in science.

Thank you to all those who have touched my life who I did not explicitly mention and thank you, the reader, for taking an interest in my dissertation and for reading this far…

Chapter 1 Fundamentals of Organic-Inorganic Thermoelectrics

Content adapted with permission from Elsevier: Jonathan A. Malen†, Shannon K. Yee, Arun Majumdar, and Rachel A. Segalman, "Fundamentals of energy transport, energy conversion, and thermal properties in organic–inorganic heterojunctions," *Chemical Physics Letter* **491**, 109-122, 2010.

Thermoelectrics are solid-state devices capable of converting heat directly into electricity. These devices can also be operated in reverse, where power is supplied to pump heat. To date, thermoelectrics have been constrained to applications that include vehicle waste-heat recovery prototypes, space vehicle power sources, seat coolers, solid-state refrigerators, and temperature control in laboratory equipment. Thermoelectrics have received renewed interest due to the development of better-performing materials and their potential to improve the efficiency of combustion systems through waste-heat recovery.[1-3] Most of these devices are planar where two semiconductors, an n-type leg and a p-type leg, are sandwiched between heat spreaders and connected electrically in series and thermally in parallel (Fig. 1.1). In the presence of a temperature difference, charge carriers thermally diffuse through the devices and establish an electric potential that can then power a load. Typically the performance of these generators at temperature T is quantified by the dimensionless figure of merit $ZT=S^2\sigma T/k$, which is a function of three material properties: Seebeck coefficient S [μV/K] (also commonly referred to as the thermopower), the electrical conductivity σ [S/cm], and the thermal conductivity k [W/m-K]. The numerator in this expression is the power factor ($S^2\sigma$) and describes the electrical nature of the device. The focus of this dissertation is the power factor.

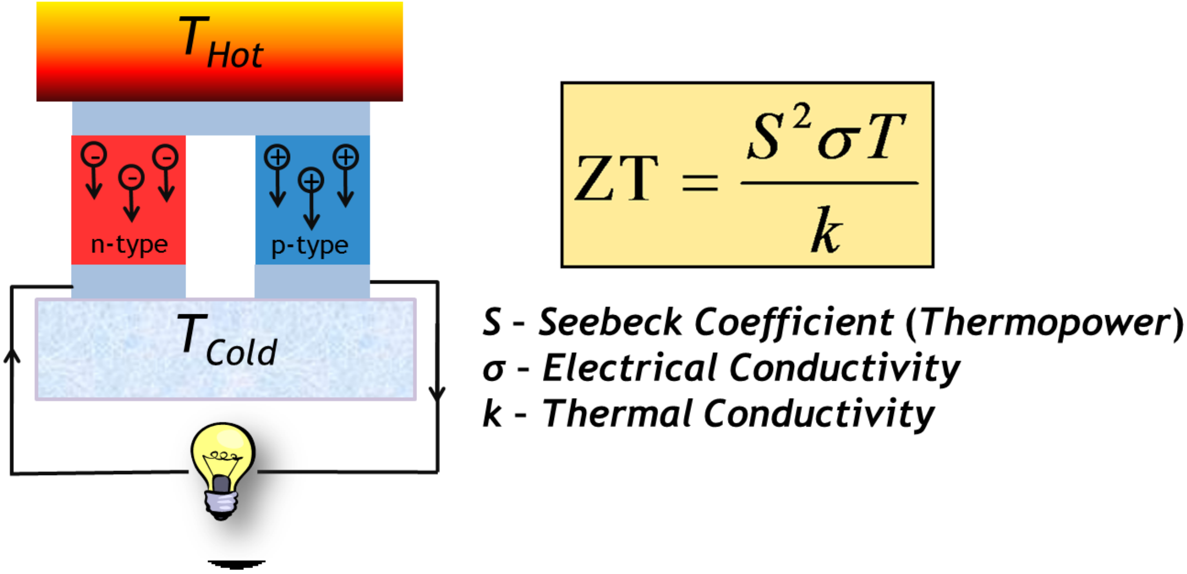

Figure 1.1 Conventional planar thermoelectric device. In the presence of a temperature difference charge carreirs thermally diffuse across the device which can power a load. The performance of the thermoelectric devices is quantified by the dimensionless figure-of-merit ZT which is a function of three material properties.

Improvements in material performance are on-going[4-6] since conversion efficiencies of typical thermoelectrics remain low.[3,7] The most common commercially available thermoelectric material is doped Bi_2Te_3, which has a power factor of ~4500 μW/m-K^2 and a thermal conductivity of ~1.4 W/m-K yielding a ZT of ~1.1 at room temperature and a resulting efficiency of <13% for a ΔT=250 K and T_C=300 K. The low efficiency and high cost of this material limits

its widespread adoption, but developing a material with better thermoelectric properties has proven difficult since S and σ are anti-correlated in most materials (both organic and inorganic).

One method, to improve the performance of thermoelectric materials has been through the use of nanoengineering where introducing nanostructures can effectively scatter phonons thus reducing the thermal conductivity without reducing the electrical conductivity.[8-10] This reduction in thermal conductivity is because the thermal conductivity is composed of two contributions, $k=k_{electron}+k_{phonon}$: a contribution from the electrons, $k_{electron}$, and a contribution from the phonons, k_{phonon}. $k_{electron}$ is a measure of the amount of heat carried by the electron and is often coupled to the electrical conductivity through the Wiedemann-Franz Law, (governing semi-classical transport) $k_{electron}/(\sigma T)=(\pi k_B/e)^2/3$. This simple relation demonstrates the correlation between $k_{electron}$ and σ that has limited improvements in ZT for many inorganic semiconductors. However, for most inorganic semiconductors, the phonon thermal conductivity couples weakly to the electrical conductivity (*i.e.*, electron-phonon coupling is small) and $k_{electron}$ and k_{phonon} are essentially independent. Therefore, if k_{phonon} can be reduced, the overall thermal conductivity can be reduced without sacrificing electrical performance.

This is most easily demonstrated by considering improving ZT of a semiconductor by (substituent/chemical) doping to increase the carrier concentration (Fig. 1.2). By increasing the carrier concentration, the electrical conductivity increases (*e.g.*, $\sigma=ne\mu$). However, as will be demonstrated later, this results in a decrease in the thermopower. Since the overall thermal conductivity is a function of the electronic component, as the electrical conductivity increases with increase carrier concentration, so does the electronic component of the thermal conductivity. However, since the phonon component is a weak function of the carrier concentration, it can be independently reduced without adversely affecting the electrical transport properties.

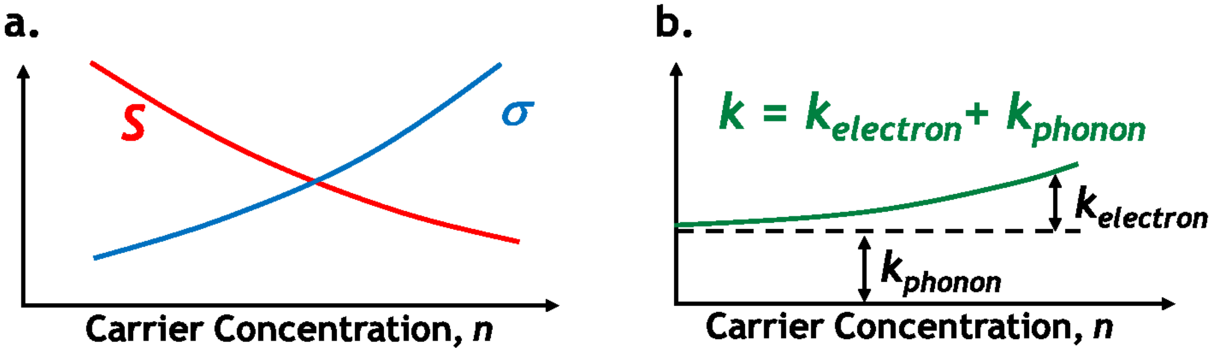

Figure 1.2 Competing thermoelectric trends typical of inorganic semiconductors. (a) Increasing the carrier concentration results in an increase in the electrical conductivity but a reduction in the thermopower. (b) Likewise, the electronic component of the thermal conductivity increases because electrons carry heat with increased electrical conductivity. The phonon component is largely independent of carrier concentration and therefore can be reduced by other mechanisms. Figure motivated and adapted from Ref. 11-13.

This mechanism to reduce k without reducing σ marked renewed interest into thermoelectrics where materials with ZT greater than bulk Bi_2Te_3 have been synthesized in the last decade and a half.[8,14] Shown in Fig. 1.3 is a time history of recent improvements primarily due to the renewed interest in nanostructuring thermoelectric materials. The nanostructures tend to have characteristic lengths that (potentially) match the mean free path that dominate the contribution to thermal conductivity; matching these length scales results in increased phonon scattering and a reduction in thermal conductivity. With this mechanism, one motivation is to start with a material that has a high power factor and, via nanostructuring, then reduce the thermal conductivity.

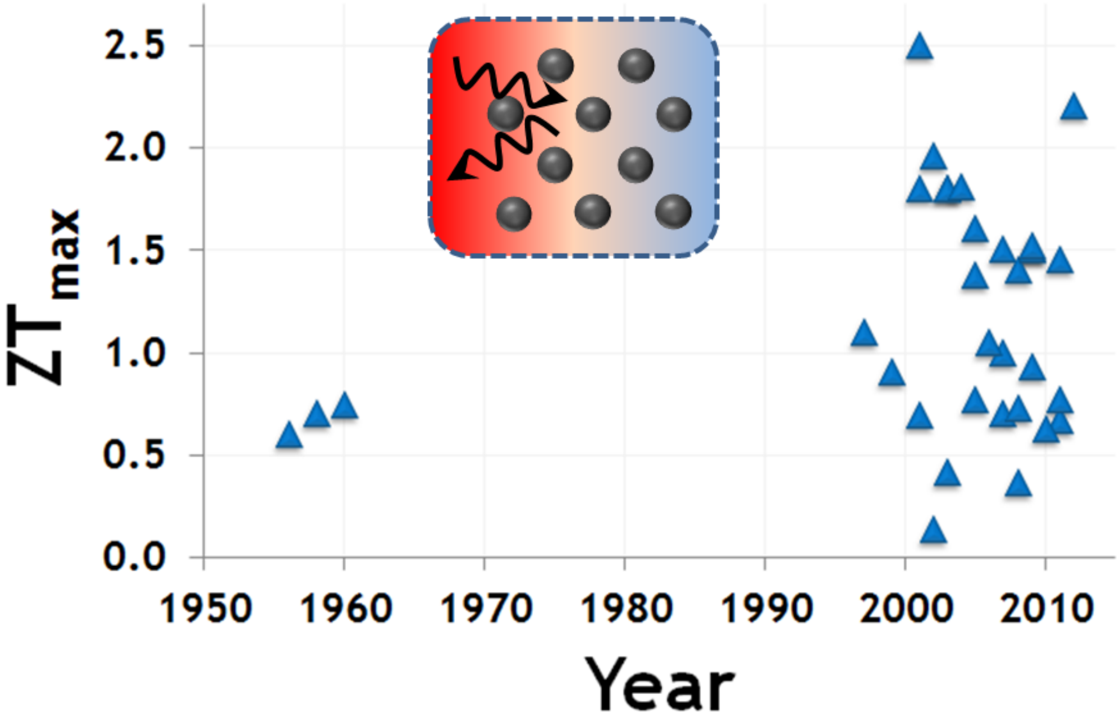

Figure 1.3 Historic improvements in *ZT*. There has been renewed interest in thermoelectric materials with high ZT since the advent of Bi_2Te_3 in the late 1950's. Many of these improvements have been due to introducing nanostructures which can scatter heat and reduce the thermal conductivity.

An alternative approach, which is explored in this dissertation, is to start with materials that have an inherently low thermal conductivity (*e.g.*, polymer-based materials) then find ways of breaking the anti-correlation between S and σ and optimizing S and σ. This motivation has led to the investigation of organic-inorganic thermoelectrics where the unique transport properties that occur at the interfaces between these two components can be leveraged for thermoelectric improvements.

1.1 Organization of this Dissertation

This dissertation is divided into *five chapters* which primarily focus on the thermopower and electrical conductivity contributions to the power factor. In large, the systems under consideration in this dissertation are determined to have inherently low thermal conductivity.

- This *first chapter* is intended to provide the theoretical background necessary to understand transport in organic-inorganic thermoelectric materials. It will also provide a summary of previously conducted single-molecule investigations into organic-inorganic interfaces which have demonstrated the validity of the theoretical background for p-type single-molecule thermopower measurements.

- The *second chapter* is devoted to extending this investigation to the first strongly n-type single-molecule thermopower measurements. The observations from this investigation suggested how the molecular binding strongly influences the electronic conductance.

- This naturally leads to the *third chapter* that investigates p-n single-diode-molecules which demonstrates the effect of molecular binding on the electronic conductance. This work demonstrates that, in organic-inorganic interface materials, opposite behavior to the bulk analog can be realized by controlling how the molecule binds (hybridizes) to the electrodes.

- This trend-breaking at the nanoscale is then extended to a bulk material in the *fourth chapter* where a new polymer-based hybrid organic-inorganic material is synthesized and characterized. This bulk material retrains the interface dominated transport characteristics and allows for record breaking thermoelectric performance. This demonstration opens a new field of hybrid organic-inorganic thermoelectric materials which maintain the low thermal conductivity and processability of the polymer.

- The low cost nature and the large areal manufacturing prospects of the polymer motivate the *final chapter*. In this last chapter, engineering cost considerations for fabricating thermoelectric devices are investigated. This investigation leads to the first design framework for engineering thermoelectric devices based upon minimizing the \$/W cost for power generation and the \$/kWh cost for thermoelectric cooling. This framework is applied to the suite of existing thermoelectric materials (in Fig. 1.3) and a novel polymer in the first system level cost comparison of thermoelectric materials.

Ultimately this dissertation begins with the unique transport phenomenon that occurs at the nanoscale and develops bulk thermoelectrics materials that result in the cost minimization of new thermoelectric devices. It is an ambitious adventure that is summarized in Fig. 1.4. This figure shows a map of the improvements in *ZT* that I have made during my PhD in developing this new class of thermoelectric materials enroute to realizing low cost thermoelectrics. From an engineering perspective, in the end, it is not all about *ZT*; cost maters. For this reason, I claim that organic-inorganic thermoelectrics have the potential to be a superior thermoelectric option in the future.

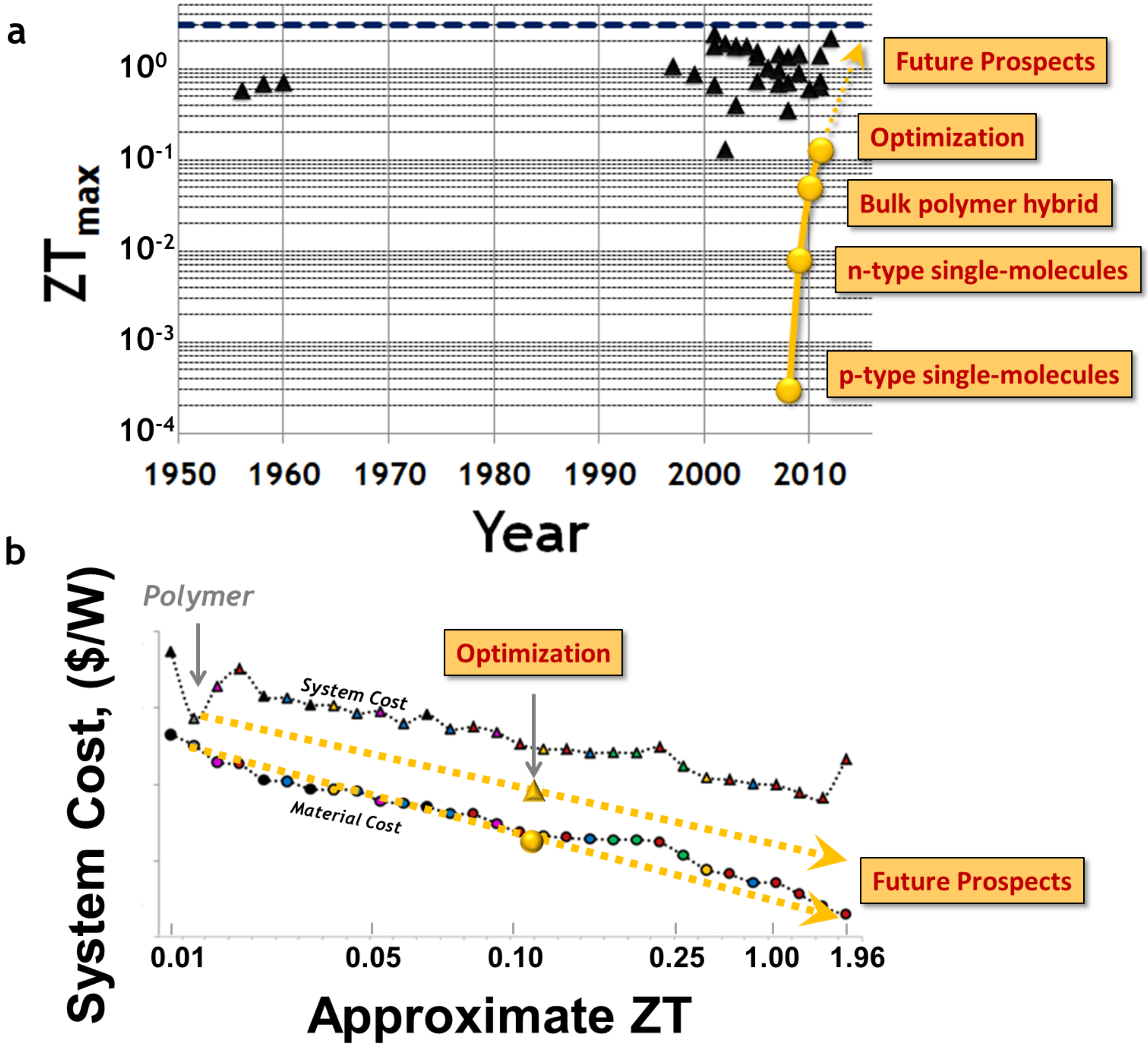

Figure 1.4 Dissertation Progress Summary. (a) Progress of increasing ZT for organic-inorganic thermoelectric materials compared against the other materials of Fig. 1.3. The dashed horizontal line corresponds to a goal of ZT=3. (b) Progress using polymer-based materials to reduce the cost of thermoelectric generators.

1.2 Fundamentals of Bulk Thermoelectric Transport

Most bulk thermoelectric materials are inorganic semiconductors whose transport is often described by the semi-classical theory of conduction governing band-like transport.[15] Some bulk organic materials (*e.g.*, conducting or semiconducting polymers) can also be described well by this theory,[16] however, many organic materials exhibit hopping like transports.[17,18] The bulk transport properties in both these materials are heavily dependent on "scattering," which is influenced by many geometric, temperature, and energetic factors.

1.2.1 Thermoelectric Transport in Bulk Metals and Semiconductors

In most bulk, inorganic materials, S and σ are in competition with one another. To demonstrate this, consider the semi-classical theory of conduction governing band-like transport[15] where the electrical conductivity is expressed as

$$\sigma_B = -\frac{e^2}{3}\int v^2 t_s g \frac{\partial f_0}{\partial E} dE = -\frac{e^2}{3}\int \sigma(E) dE \; . \tag{1.1}$$

Here e is the charge of the carrier (*i.e.*, electron), v is the velocity of the charge carrier, t_s is the scattering time, g is the electronic density of states, and f_0 is the equilibrium Fermi-Dirac distribution. The integrand in this expression is referred to as the differential electrical conductivity, $\sigma(E)$, which also appears in the expression for thermopower. The thermopower is

$$S_B = \frac{-1}{eT}\frac{\int (E-\mu)\sigma(E) dE}{\int \sigma(E) dE}, \tag{1.2}$$

where μ is the chemical potential. The denominator in this expression is proportional to the electrical conductivity, and therefore it is clear that S_B and σ_B are inversely related. For most inorganic materials, this anti-correlation limits the degree to which improvements in the power factor can be made and thus poses a fundamental challenge to improving ZT.

The numerator in this expression, demonstrates that S_B is a measure of asymmetry in the distribution of hot (electrons with energy greater than μ) and cold (electrons with energy less than μ) in the material. The symmetry of E-μ can be broken by the energy dependence of $v^2 t_s g$. While the velocity and the scattering time of the charge carrier are functions of energy, as an example, consider only the energy dependence of g. For most band-like material, the density of states is parabolic in energy (*i.e.*, $g \propto E^{1/2}$ for 3D) and therefore introduces a degree of asymmetry.

This is relationship is expressed graphically in Fig. 1.5. The differential conductivity is primarily a function of the product of g and $-\partial f_0/\partial E$ (Fig. 1.5a, left), which integrated over E yields the electrical conductivity. The peak in this distribution is offset from the chemical potential due to the curvature in g. The thermopower probes this curvature by measuring the difference in energy from the chemical potential (*i.e.*, E-μ), which splits the differential conductivity distribution into two (typically) unequal areas corresponding to hot and cold electrons (Fig 1.5a, right). The sum of these two areas (above and below μ) represents the thermopower which can be both positive and negative. The inequality of these areas can be enhanced by positioning the edge of the conduction band further away from μ. However, this results in a decrease in the area under the differential conductivity and a lower electrical conductivity (Fig. 1.5b). Thus metals have a low thermopower and a high electrical conductivity and insulators have a high thermopower and a low electrical conductivity demonstrating the anti-correlation in bulk inorganic thermoelectric materials.

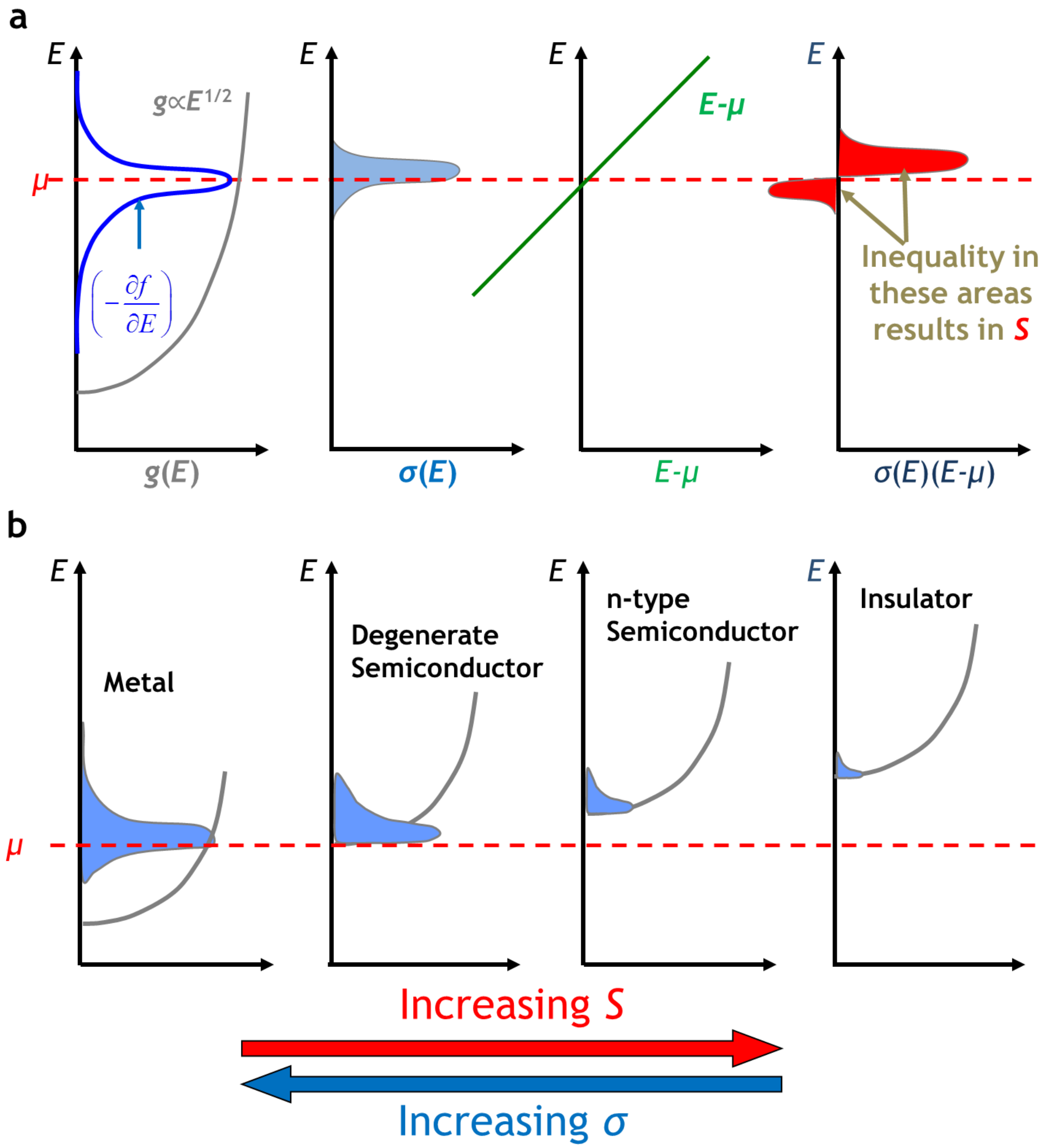

Figure 1.5 Graphical origin of thermoelectric properties in bulk inorganic materials. (a) The electrical conductivity is proportional to the area under the differential conductivity which is skewed by the curvature of the density of states. This skewing is quantified by the thermopower which results from the asymmetry of hot and cold carriers. (b) The asymmetry is enhanced by the position of the conduction band relative to the chemical potential. For this reason, insulators have a higher thermopower but a lower electrical conductivity than metals. Figure motivated and adapted from Ref. 11-13.

1.2.2 Thermoelectric Transport in Bulk Polymers

Organic materials face a similar challenge in optimization of the power factor. In some polymers, band-like transport has been observed,[16] and the preceding theory can be applied, but many semiconducting polymers are governed by hopping transport.[17,18] For hopping transport, the electrical conductivity and thermopower can be expressed as:[19]

$$\sigma_H = \sigma_0\, exp\left(-\left(\frac{T_0}{T}\right)^{\gamma}\right) \tag{1.3}$$

$$S_H = \frac{k_B^{\,2}}{2e}\left(T_0 T\right)^{1/2} \left.\frac{\partial\, ln(g)}{dE}\right|_{E=\mu} \tag{1.4}$$

where k_B is Boltzmann's constant, σ_0 is the conductivity prefactor (which is dependent on scattering), T_0 is the characteristic temperature (which is inversely related to the cube of the hopping range), and γ is the hopping exponent (which is dependent on the dimensionality and nature of the hopping transport, $\gamma = \frac{1}{4}, \frac{1}{3}, \frac{1}{2}, \text{or } 1$). Given the algebraic relations in both Eqn. 1.3 and 1.4, it is clear that S_H and σ_H are also inversely related through T_0, demonstrating that polymers with hopping transport face a similar decoupling challenge in S and σ as encountered in band-like transport.

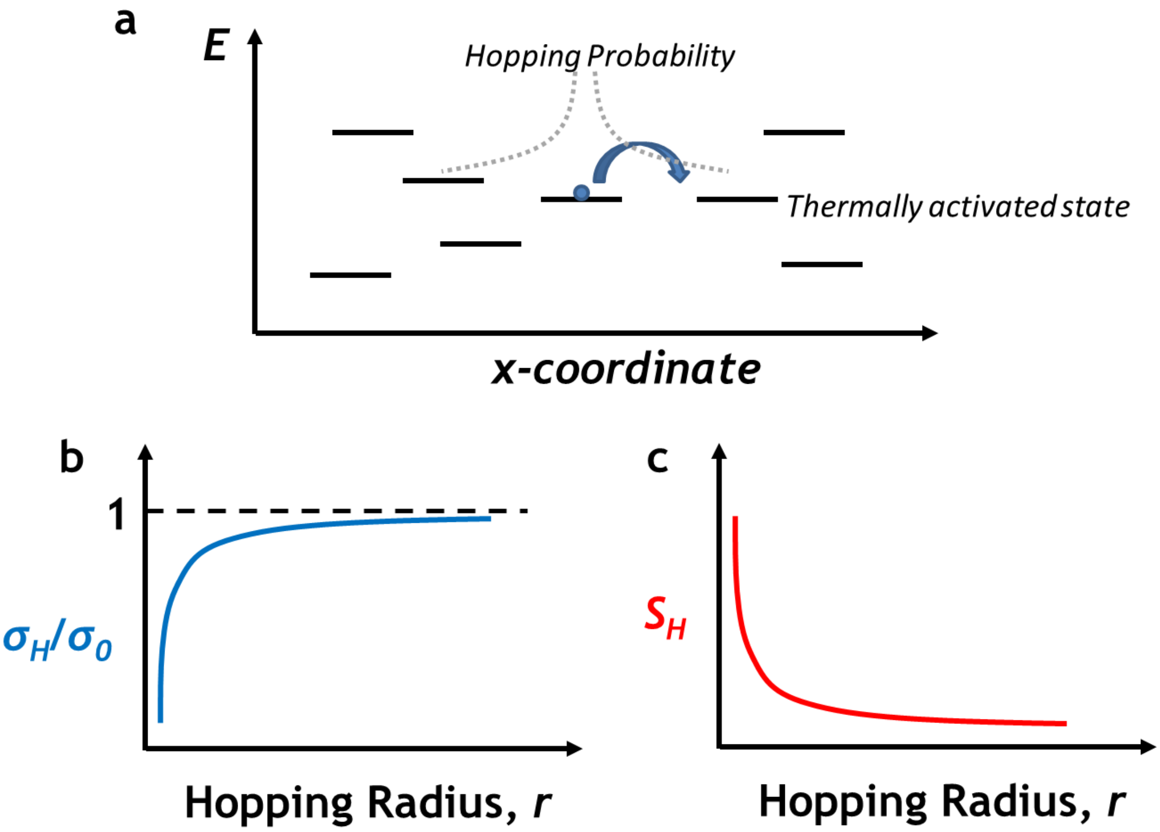

Figure 1.6 Graphical origin of thermoelectric properties in bulk organic materials. (a) Hopping transport is described by the probability for a carrier to "hop" from on site to another. Due to thermal fluctuations temporally, nearby unoccupied sites can become activated (*i.e.*, change energy to be commensurate with energy of the carrier) allowing the carrier to "hop;" there is a probability that a carrier can occupy the unoccupied site. (b) The hopping radius describes the distance a carrier is likely to "hop." The electrical conductivity increases with increasing hopping radius while the thermopower decreases with hopping radius.

1.2.3 Scattering Effects

Examples also exist where the anti-correlation between S and σ can be broken. One of those examples is by the use of energy filtering.[20-24] In energy filtering, energy dependent scattering (*i.e.,* $t_s = t_s(E)$) is employed, and charge carriers are selectively scattered at interfaces, modestly reducing the electrical conductivity but greatly improving the thermopower. This increase in thermopower is caused by an increase in asymmetry in the distribution of mobile charge carriers, which in turn results from the asymmetry of the energy dependent scattering time about the chemical potential (*i.e.,* $t_s(E)(E\text{-}\mu)$ is not symmetric about μ). Because the power factor scales as S^2, this trade-off results in a net increase in the power factor.

Beyond energy dependent scattering, weakly or non-energy dependent scattering mechanisms (*e.g.*, boundary, electron-phonon, and impurity scattering) still reduce the electrical conductivity, but they have little impact on the thermopower. To demonstrate this, the scattering mechanism can be separated into terms that are energy dependent, $t(E)$, and terms that are not energy dependent. These non-energy dependent scattering mechanisms may be functions of some characteristic scattering length, L (such as in boundary scattering), or they may be functions of temperature (such as in phonon-electron scattering), and are written as $t(L,T)$. If the scattering times of the energy dependent mechanisms are much longer than those of the non-energy dependent scattering then, by application of Matthiessen's rule, the following approximation can be made:

$$\frac{1}{t_s}=\frac{1}{t(E)}+\frac{1}{t(L,T)}\approx\frac{1}{t(L,T)} \tag{1.5}$$

Applying this approximation to the electrical conductivity and thermopower for band-like transport yields:

$$\sigma_{\mathrm{B}}=-\frac{e^2}{3}t(L,T)\int v^2\frac{\partial f_0}{\partial E}g\,dE \tag{1.6}$$

$$S_{\mathrm{B}}=\frac{-1}{eT}\frac{\int(E-\mu)v^2\frac{\partial f_0}{\partial E}g\,dE}{\int v^2\frac{\partial f_0}{\partial E}g\,dE} \tag{1.7}$$

where the scattering time only reduces the electrical conductivity and not the thermopower.

For hopping transport, a similar behavior is observed as the scattering effects are captured in the σ_0 prefactor appearing in Eqn. 1.3 but not in Eqn. 1.4. Therefore, when non-energy dependent scattering dominates in either transport regime, the electrical conductivity is reduced while the thermopower remains largely unaffected. Similarly, if non-energy dependent scattering is reduced, then the conductivity will increase while the thermopower remains largely unaffected, resulting in an increase in the power factor.

1.3 Transport in Single-Molecule Junctions

Transport at the interface between organic and inorganic materials can behave very differently than the bulk counterparts and understanding transport at these interfaces is an active area of research. At the organic-inorganic interface unique energy landscapes, non-existent in the separate components, manifest as the discrete orbitals in the organic hybridize with the continuum of states in the inorganic. These nanoscale interfaces are difficult to study experimentally. However, one method to repeatedly study the interface between organic and inorganic moieties is to consider transport through a single (or a few) organic molecule covalently bound to metal electrodes (Fig. 1.7). Aviram and Ratner[25] were one of the first to suggest that single-molecules would have unique transport properties. Since then, the field of molecular transport junctions[26] has grown and has been hailed as a scientific breakthrough[27]. This spurred investigators to find novel two-terminal techniques to observe these transport phenomena in single molecules using a variety of measurements including mechanical[28,29], electromigrated,[30,31] scanning tunneling microscope,[32,33] and conducting probe atomic force microscope[34-36] break junctions. All of these break junction techniques rely on molecules bridging a small (< 1 nm) gap between metal electrodes. In this manner, a unique electronic device is created where the electrodes act like electron reservoirs and the molecule acts like a transport channel. Under non-equilibrium conditions (*e.g.*, by the application of a potential differential), charge and energy can flow across the molecular junction with a signature that is unique to organic-inorganic interfaces referred to as molecular junctions.

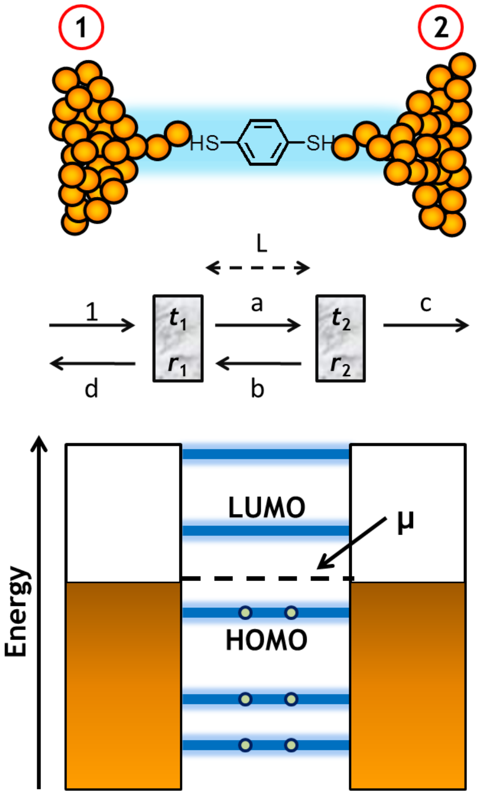

Figure 1.7 Single-molecule junction landscape. Organic-inorganic interfaces depicted in the form of a molecular junction (top) and the resulting double resonant tunneling model (bottom). The thiol binding groups of the benzenedithiol are depicted as tunneling barriers with complex transmission (t_1 and t_2) and reflection coefficients (r_1 and r_2). An impinging electron wave (1) has a probably of being reflected (d^2) and ultimately transmitted (c^2) as it tunnels through the barriers in series. The bound states (a and b) establish a resonant tunneling phenomenon where the discrete frontier molecular orbitals (*i.e.*, the HOMO and LUMO) assist in the transport of electrons. Figure motivated and adapted from Ref. 11-12.

1.3.1 Landauer Transport Formalism

To understand transport at these interfaces consider an ideal system consisting of a single-molecule bound to two metal electrodes (Fig. 1.7). If electrode 2 is held at a higher potential (voltage), V, than electrode 1, then electrons will flow from left to right. The current in that system can be described by Landaur's formalism of transport

$$I_{1-2} = -e\int_{0}^{\infty} \tau(E)\left(f_1 - f_2\right) vgdE\,, \qquad (1.8)$$

where the region between the electrodes (*i.e.*, channel) is treated as a black-box with an energy dependent transmission probability (or function) τ. Here f_1 and f_2 are the equilibrium occupation probabilities of electrons in electrodes 1 and 2 (for metallic electrodes these are Fermi distributions $f_i = \left(1+e^{(E-\mu_i)/k_B T_i}\right)^{-1}$).

1.3.2 Resonant Tunneling Transmission

In the case of the double resonant tunneling model, the molecular end group (*i.e.*, H-S thiols) act as tunneling barrier with complex transmission and reflection coefficient, t_i and r_i. These barriers are separated by a distance L corresponding to the length of the molecule. An electron wave of amplitude 1 is first impingent on the first tunneling barrier. That wave has a probability of being reflected and transmitted through the first barrier corresponding to the amplitude of the resulting waves. Similarly for those waves that transmit through the first barrier, when they encounter the second barrier, they have a probability of being reflected and transmitted. The transmission function is simply the probability of the final transmitted wave's amplitude squared (c^2) and is a complex function of the transmission and reflection coefficients of the barriers and of the phase φ of the wave in the bound state between the barriers.

$$\tau = \left|c^2\right| = \frac{|t_1|^2 |t_2|^2}{1+|r_1|^2 |r_2|^2 - 2|r_1||r_2| cos(\varphi)} \tag{1.9}$$

By preserving the phase of a wave (*i.e.*, resonance), and considering only elastic collisions, the transmission function can be recast in a Lorentzian form (Eqn. 1.10) that is peaked at energy levels E_n corresponding to the energies that preserve the phase. These energies are the resonant bound state energies between the barriers and in the case of a molecule are the discrete molecular orbitals.

$$\tau(E) = \sum_{n=1}^{\infty} \frac{4\Gamma_{n,1}\Gamma_{n,2}}{\left(\Gamma_{n,1}+\Gamma_{n,2}\right)^2 + 4\left(E-E_n\right)^2} \tag{1.10}$$

In a molecule (see Fig. 1.7), electrons are filled to the highest occupied molecular orbital (HOMO). The chemical potential of a molecular junction lies between the HOMO and the lowest unoccupied molecular orbital (LUMO). These two molecular orbitals constitute the frontier molecular orbitals and dominate transport. If transport is dominated by the HOMO then the molecule behaves like a p-type semiconductor and if the molecule is dominated by LUMO then the molecular behaves like an n-type semiconductor.

1.3.3 Quantum of Electronic Conductance

In an ideal situation, $\tau(E)$ is at most one and a fundamental limit to the electronic conductance applies even to ideal channels in the absence of elastic scattering mechanisms. This is best demonstrated by considering a one-dimensional transmission channel. For the zero temperature case, when a small positive voltage difference exists between electrode 1 and electrode 2, $\Delta V_{1\text{-}2}=V_1\text{-}V_2$, the difference between f_1 and f_2 is,

$$f_1 - f_2 = e\Delta V_{1-2}\left(-\frac{\partial f_0}{\partial E}\right)_{E=\mu} = e\Delta V_{1-2}\delta\left(E-\mu\right) \tag{1.11}$$

The above approximation makes use of the fact that $-df/dE$ demonstrates properties of a Dirac-delta function as the temperature tends towards 0 K. In a one dimensional, non-scattering wire, the density of states is inversely proportional to the group velocity of the electron, $g(E)=2/hv$. When this expression for $g(E)$ and Eqn. 1.11 are substituted into Eqn. 1.8, a statement of Ohm's law results,

$$I_{1-2} = \frac{2e}{h}\int_0^\infty \left(f_1 - f_2\right) = \frac{2e^2}{h}\Delta V_{1-2}\int_0^\infty \delta\left(E-\mu\right)dE = \frac{2e^2}{h}\Delta V_{1-2} = G_0\Delta V_{1-2} \quad (1.12)$$

where v has cancelled, resulting in a fundamental quantum of electronic conductance $G_0=2e^2/h$ that is independent of material properties.[37,38] This was experimentally verified when quantized conductance steps were observed for current flow across point electrodes made between continuum reservoirs.[38] Finite conductance, in the absence of scattering, results from resistances in the connections between the one-dimensional channel and each of the continuum reservoirs. Stronger coupling of the channel to the electrodes increase the velocity of electron propagation through the junction, but proportionally reduces the density of states.

1.3.4 Electronic Conductance of Molecular Junctions

If an obstacle is present in the channel (*e.g.*, a molecule) that transmits electrons with an energy dependent probability $\tau(E)$, ranging from zero to one, then Eqn. 1.8 is restated for a small voltage difference between the electrodes as,

$$I_{1-2} = \frac{2e}{h}\int_0^\infty \tau\left(E\right)\left(f_1 - f_2\right)dE = \frac{2e^2}{h}\left.\tau\left(E\right)\right|_{E=\mu}\Delta V_{1-2} \quad (1.13)$$

The ratio of the current to the voltage is the conductance and Eqn. 1.13 simplifies to define the electronic conductance of a molecular junction

$$G = G_0\left.\tau\left(E\right)\right|_{E=\mu}. \quad (1.14)$$

which is simply the value of the transmission function evaluated at the chemical potential and scales by the quantum of electronic conductance.

1.3.5 Thermopower of Molecular Junctions

Inspection of Eqn. 1.8 suggests that a current will be induced by different reservoir temperatures if the transmission function is not constant in the region of the chemical potential. The thermopower of the molecular junction is the property that quantifies the potential to drive that current. This relationship was first developed by Butcher[39] and is derived by setting Eqn. 1.8 equal to zero because S is defined at open circuit ($I_{1-2}=0$). Since electrodes 1 and 2 are held at different temperatures, their occupations are different. The occupation difference between the electrodes (f_1-f_2) is expanded, with reference to electrode 1, to account for differences in the chemical potentials $\Delta\mu_{1-2}$ and temperatures difference ΔT_{1-2}.

$$0 = \frac{2e}{h}\int_0^\infty \tau\left(E\right)\left[\left(\left.\frac{\partial f_0}{\partial \mu}\right|_{\mu=\mu_1}\right)_{T_1}\Delta\mu_{1-2} + \left(\left.\frac{\partial f_0}{\partial T}\right|_{T=T_1}\right)_{\mu_1}\Delta T_{1-2}\right]dE \quad (1.15)$$

The temperature derivative is then written in terms of energy, $\partial f_0/\partial T = -T^{-1}\left(E-\mu\right)\partial f_0/\partial E$, and the chemical potential derivative is then approximated as $\partial f_0/\partial\mu = -\partial f_0/\partial E \approx \delta\left(E-\mu\right)$. The following relationship is determined after substitution of these expressions into Eqn. 1.15,

$$\frac{\Delta\mu_{1-2}}{\Delta T_{1-2}} = \frac{1}{\left.\tau\left(E\right)\right|_{E=\mu_1}}\int_0^\infty \tau\left(E\right)\frac{\left(E-\mu_1\right)}{T_1}\frac{\partial f_1}{\partial E}dE. \quad (1.16)$$

The transmission function is then Taylor expanded $\tau(E) \approx \tau(E)\big|_{E=\mu_1} + (E-\mu_1)\partial\tau(E)/\partial E\big|_{E=\mu_1}$ which yields

$$\frac{\Delta\mu_{1-2}}{\Delta T_{1-2}} \approx \int_0^\infty \frac{(E-\mu_1)}{T_1}\frac{\partial f_1}{\partial E}dE + \left(\frac{1}{\tau(E)}\frac{\partial\tau(E)}{\partial E}\right)\Bigg|_{E=\mu_1} \int_0^\infty \frac{(E-\mu_1)^2}{T_1}\frac{\partial f_1}{\partial E}dE \quad (1.17)$$

where the first integral is zero because it is symmetric about the chemical potential, and the second integral requires use of the Somerfeld expansion. The change in chemical potential results in an observed voltage, $\Delta\mu_{1\text{-}2}= -eV_{1\text{-}2}$ which defines the thermopower of the molecular junction.

$$S = -\frac{\Delta V_{1-2}}{\Delta T_{1-2}} = -\frac{\pi^2 k_B{}^2 T}{3e}\left(\frac{1}{\tau(E)}\frac{\partial\tau(E)}{\partial E}\right)\Bigg|_{E=\mu} \quad (1.18)$$

and the subscript 1 has been dropped from μ and T. Hence, the thermopower is related to the derivative of the transmission function at the chemical potential of the electrodes.[39,40] Intuitively, this parallels the qualitative result for bulk materials, because the derivative is a quantitative measure of the asymmetry between hot and cold electrons. Stated more simply, the thermopower describes the slope of the transmission function evaluated at the chemical potential.

1.3.6 Summary of Transport Properties in Single-Molecular Junctions

Equations 1.14 and 1.18 are the two primary governing equations which describe thermoelectric transport in molecular junctions and serve as the center piece for understanding transport at organic-inorganic interfaces. The key result is summarized in Fig. 1.8. What is most unique about transport in molecular junctions is that the anti-correlation between S and σ is broken. In fact, S and σ can be positively correlated allowing for simultaneous enhancements which bode well for thermoelectrics. To obtain a high electrical conductivity (or conductance), the chemical potential must lie near resonance with one of the molecular orbitals thus maximizing the transmission function. The conductance would be high because the value of the transmission function is large (*i.e.*, nearly unity). Simultaneously, at this value the slope of the transmission function is large equating to a large thermopower. Thus in molecular junctions it is possible to obtain a large conductance and thermopower simultaneously! The challenge is then in selecting complimentary organic and inorganic components such that these interface properties can manifest.

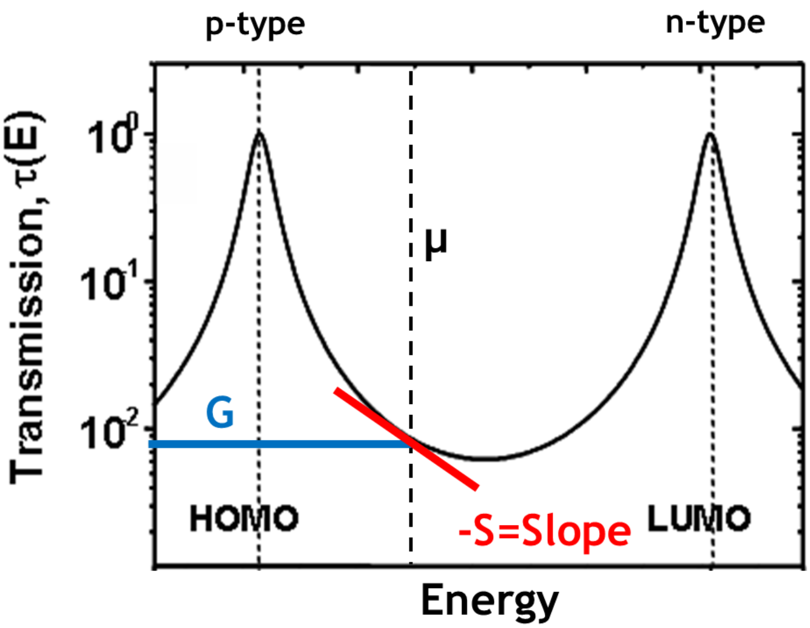

$$G = \frac{I_{1-2}}{\Delta V_{1-2}} = \frac{2e^2}{h}\tau(\mu)$$

$$S = -\frac{\Delta V_{1-2}}{\Delta T_{1-2}} = -\frac{\pi^2 k_B{}^2 T}{3e}\left(\frac{\partial \ln \tau(E)}{\partial E}\right)_{E=\mu}$$

Figure 1.8 Lorentzian transmission model for understanding transport in molecular junctions. The conductance is a measure of the transmission function. The thermopower is a measure of the slope of the transmission function. Both conductance and thermopower can be maximized by aligning the chemical potential to be on resonance with one of the molecular orbitals. Figure motivated and adapted from Ref. 11-12.

1.4 Previous Experimental Single-Molecule Work

While the conductance and thermopower theories of molecular junctions are well established, experimentally realizing this phenomenon is difficult. The conductance of a molecular junction is the ratio of the current flowing through the molecule to the applied voltage bias, $G=I/\Delta V$. Experimentally forming conductance junctions and accurately measuring the small current is challenging. The thermopower of a molecular junction is the ratio of the voltage induced across the junction in response to a thermal bias, $S=-\Delta V/\Delta T$. Experimentally measuring this voltage is challenging because thermopower voltages are small. To accomplish these measurements, a modified scanning tunneling microscope (STM) is typically used as previously reported.[41-45] This next section is devoted to summarizing the work that is most relevant to the following chapters.

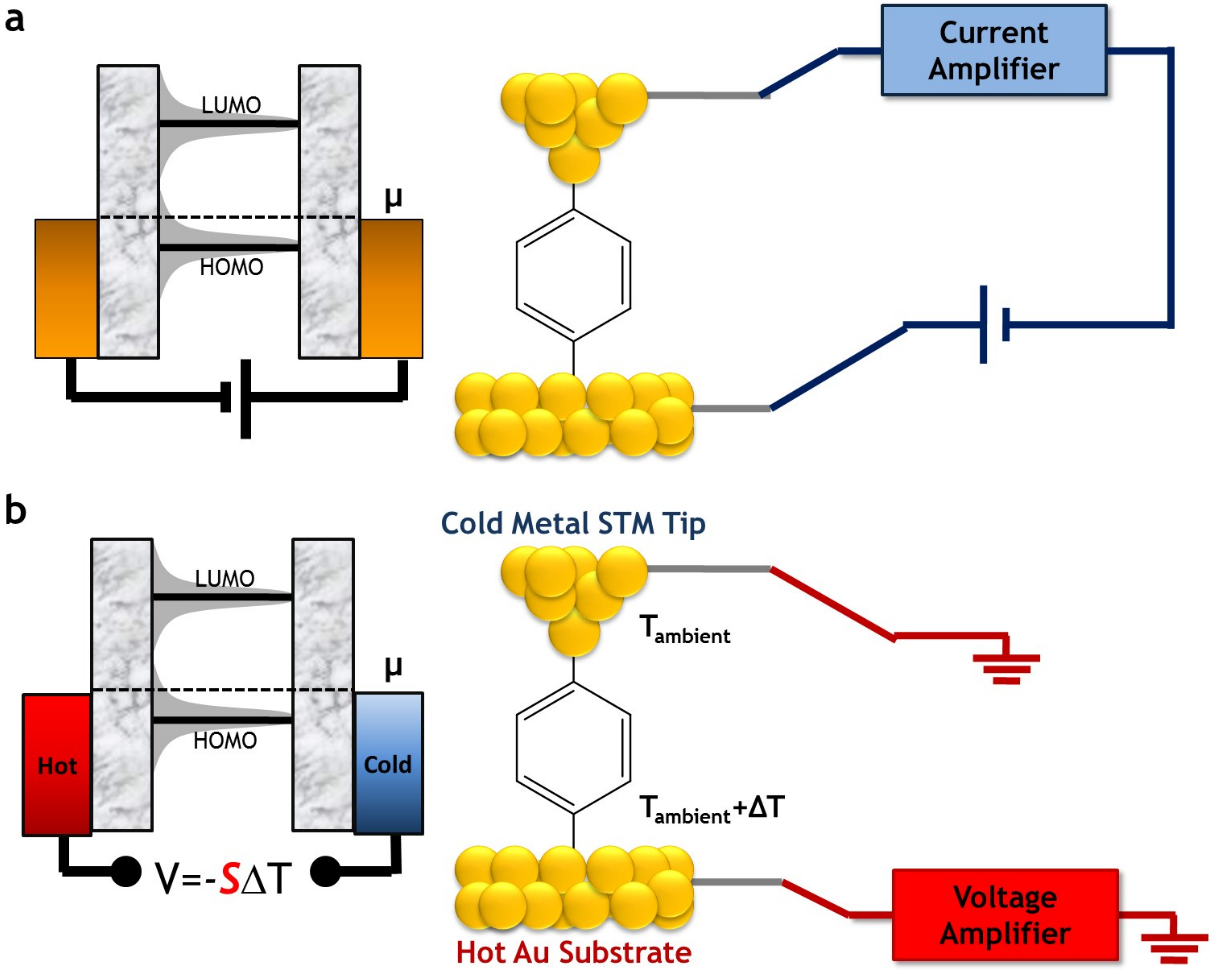

Figure 1.9 Schematic of an STM breakjunction setup for single-molecule conductance and thermopower. (a) For conductance measurements, a voltage bias is applied between the substrate and the STM tip and the current flowing through a molecule is monitored using a current amplifier. In this manner, the value of the transmission function at the chemical potential is evaluated. (b) For thermopower measurements, a temperature bias is a applied between the tip and the substrate and the resulting thermoelectric voltage is monitored using a voltage amplifier. In this manner, the value of the slope of the transmission function at the chemical potential is evaluated. Figure motivated and adapted from Ref. 11-12.

1.4.1 Summary of Electronic Conductance Methodology

The electronic conductance of a molecular junction can be measured by modifying an STM. The same electronics present in most STMs can be used and only a need to control the mechanical motion of the STM is necessary (Fig. 1.9a). In a standard measurement, a Au STM tip is maintained at a voltage (+100 mV) above a Au coated substrate. Smooth Au coated substrates are fabricated by freshly cleaving mica and evaporating Au (0.5 Å/s), to a thickness of 100 nm with a 5 nm Cr adhesion layer. The substrates are then cleaned using a hydrogen torch (1 Hz repetition) and allowed to cool before a dilute solution of molecules are drop cast onto the substrate and the solvent allowed to evaporate. STM tips are prepared by cutting Au wire at an acute angle; these tips are then subsequently cleaned in the hydrogen torch (also at a repetition of 1 Hz). The tip and substrate are then mounted into the STM.

The tip is then gently crashed into the surface and withdrawn. A current amplifier in-line with the voltage source is used to measure the current flowing between the tip and the substrate. The voltage across the tip and substrate is also monitored and the ratio of the current and voltage is the conductance between the tip and the substrate. As the tip is withdrawn steps in the conductance are visible at integer multiples of the quantum of conductance, G_0, as illustrated in Fig. 2.2. Eventually, the one-dimensional transmission channel corresponding to a conductance of 1 G_0 is broken. If no molecules are present then an exponential decay in the current is observed as the tip is withdrawn further corresponding to tunneling through a vacuum gap. If molecules are present, steps in conductance below 1 G_0 are observed corresponding to molecules bridging the gap. As the tip is withdrawn, molecular junctions break. The final step before tunneling is observed corresponds to the conductance of a single-molecule. This process is repeated hundreds (>500) of times to gather good statistics. These conductance traces are then histogrammed (on a log scale) and the peaks in these histograms correspond to the conductance of a single molecular junction.

1.4.2 Summary of Thermopower Methodology

A similar technique (Fig. 1.9b) is used to measure the thermopower of a molecular junction. In this technique, molecular junctions are repeatedly formed between the STM tip maintained at ambient temperature and the heated Au-coated mica substrate where molecules were previously deposited. During the approach sequence the current amplifier monitors the conductance of the junction as the STM tip approaches the molecule covered substrate. Once a threshold conductance corresponding to the previously measured conductance is observed, a switch disconnects the current amplifier and connects a voltage amplifier.[*] A thermoelectric voltage is then recorded while the tip is withdrawn. During the withdraw processes molecules continually detach until eventually only one molecule remains in the junction (which in turn eventually detaches as the tip continues to withdraw). Thermopower, unlike conductance, is insensitive to the number of molecules in the junction; the same thermopower voltage is observed for 1 molecule bridging the gap as 10 molecules in parallel bridging the gap. This is because the thermopower is proportional to $\partial \ln\tau/\partial E$. For N molecules in parallel this quantities is $\partial \ln(N\tau)/\partial E=\partial \ln\tau/\partial E$. As a result, steps in thermopower are never observed unlike conductance.

Several temperature differences ΔT are investigated ranging from 0 to 30 K. Consistent with the thermoelectric effect, as the temperature difference increases the voltage induced in the heterojunction also increases as seen in Fig. 1.10b. Hundreds (>500) of approach and withdraw sequences are then performed at each temperature difference to gather good statistics. Thermoelectric voltage histograms (Fig. 1.10c) at these temperature differences are obtained and a well-defined peak and width can be seen from each histogram. The thermoelectric voltage peak of each histogram with the full-width-half-max (FWHM) of the histogram (representing the

---

[*] Note that the switch used here is a transistor switch which is driven by a digital-to-analog converter (DAC). The power output of the DAC is not sufficient to fully drive the transistor switch to saturation so it is observed that a small leakage (~20 μV) bias is always applied across the tip and the substrate. Since a transistor's leakage current is temperature dependent (*i.e.,* function of k_BT), a small voltage offset is observed even at a tip-substrate temperature difference of ΔT=0 and varies from day-to-day with the temperature of the room. This variable offset does not affect the measurement as the thermopower is a measure of the slope not the offset.

error bars) is then plotted verses the temperature difference. A straight line is then fit to these points, and its slope ($V_{peak}/\Delta T$) is the thermopower of the molecular junction. The uncertainty in the thermopower power is then represented by the 95% confidence interval of the linear regression.

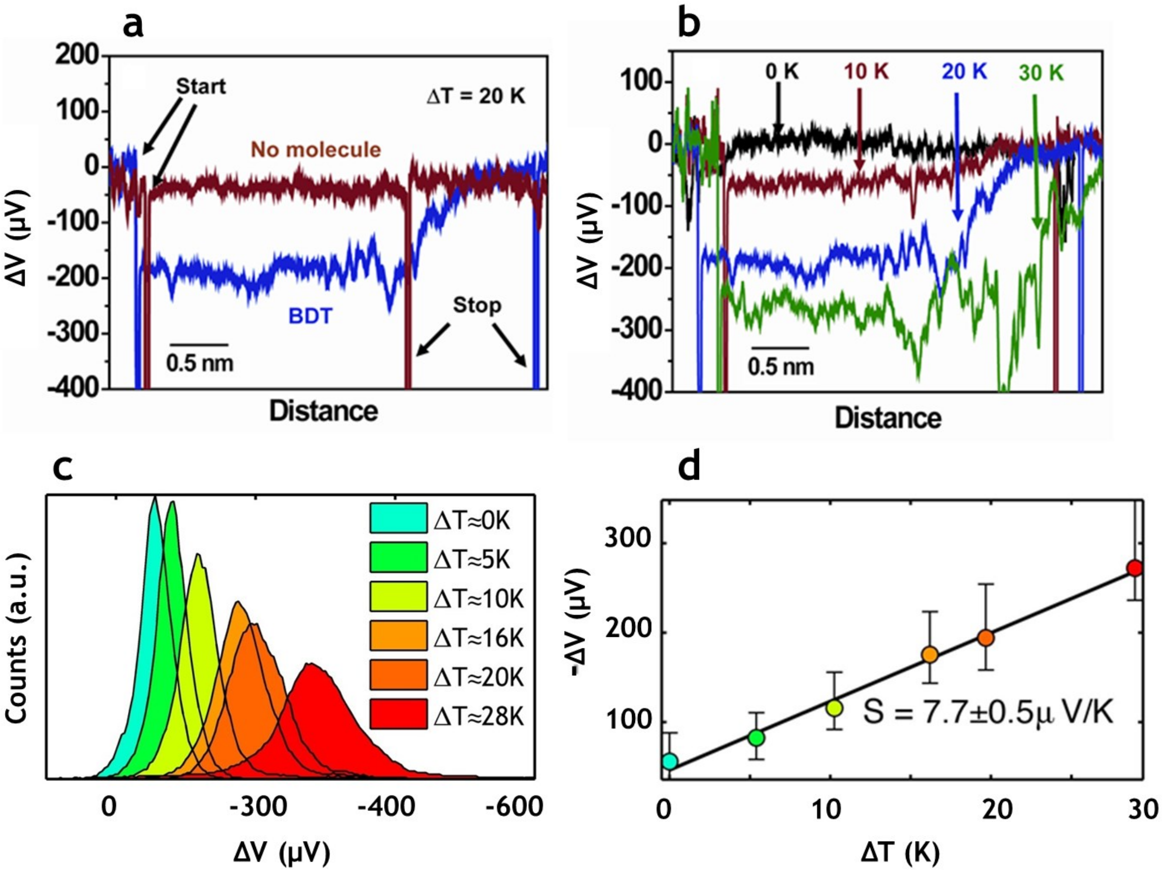

Figure 1.10 Example single-molecule thermopower measurements for benzenedithiol. (a) Typical thermopower voltage traces are observed at ΔT=20 K. A measureable thermoelectric voltage occurs when the benzenedithiol molecule is present. (b) As the temperature increases, the voltage increases consistent with the thermoelectric effect. (c) Histogramming these voltage traces yield peaks. (d) The (negative) peak voltages are plotted against the temperature difference where the error bars are the FWHM of the peak. The slope of the resulting straight line is the thermopower of the molecular junction with the error reported as the 95% confidence interval of the least squares fit. Figure 1.10ab from P. Reddy, S. Y. Jang, R. A. Segalman and A. Majumdar, *Science*, 2007, **315**, 1568-1571. Reprinted with permission from AAAS.

1.4.3 Previous Work from Our Group

Using this technique, Reddy *et al*. were the first to definitively show that thermopower in molecular junctions is an experimentally measurable quantity (Fig. 1.10ab).[43] Furthermore, this quantity is useful in determining the dominant transport orbital. For example, Reddy *et al*. demonstrated that 1,4-benzenedithiol molecular junctions had a positive thermopower showing that the HOMO dominates transport in that molecule. Prior to the realization of molecular thermopower, conductance experiments were inconclusive as to the dominant transport orbital and therefore the type (p- or n-type) of transport. Since thermopower is related to the slope of the transmission function, positive molecular thermopower corresponds to a molecule where the

HOMO dominates transport. This is analogous to p-type transport and transport through the LUMO is analogous to n-type transport. One advantage of molecular thermopower measurements as compared to conductance measurements is that it is independent of the number of molecules in the junction; thermopower is an intrinsic property. Since thermopower is proportional to the derivative of the logarithm of the transmission function, the measured thermopower is the same for a single molecule junction as it is for a junction with multiple trapped molecules. This is extremely powerful as it permits thermopower to be a more robust measurement technique than conductance for understanding transport.

Using this technique, Baheti *et al.* showed how chemistry can be used to predictably tune molecular thermopower for even greater enhancements in *ZT* (Fig. 1.11).[44] In this work, they investigated the effect of chemical substituents on molecular transport. Both electron-withdrawing (chlorine and fluorine substituents) were found to decrease the thermopower of 1,4-benzenedithiol while electron-donating groups (methyl substituents) increased the thermopower. This can be explained by how the HOMO shifts relative to the chemical potential of the electrode for these different substituent groups. This work was the first to show that small changes in chemistry (*i.e.*, chemical substituents) could have controllable effects for molecular thermopower.

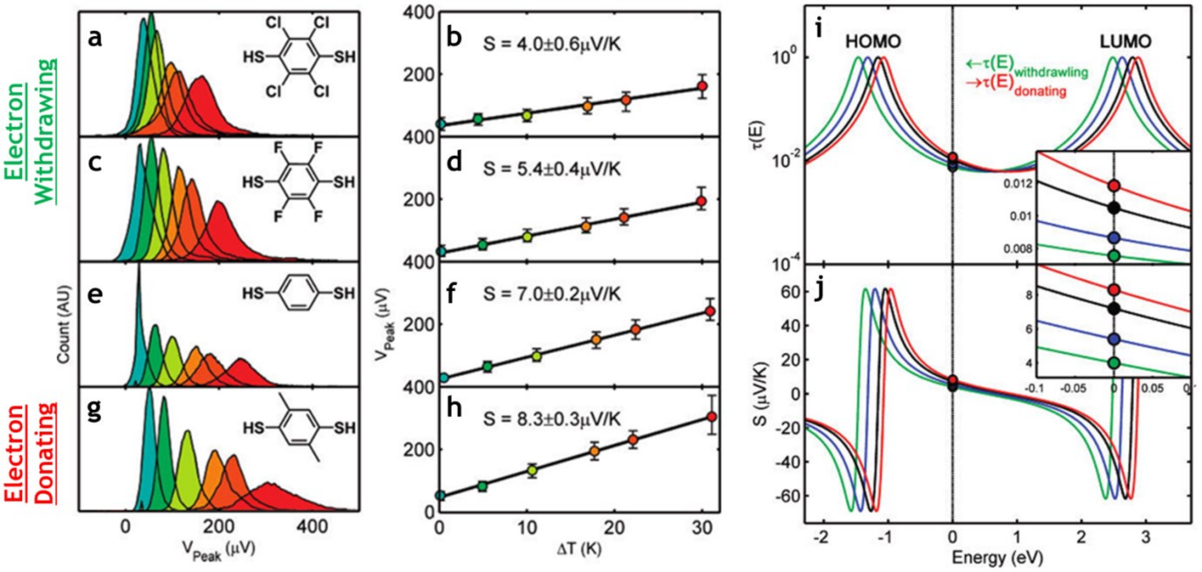

Figure 1.11 Thermopower measurements of benzenedithiol variations. Electron Withdrawing: (a-b) 2,3,5,6-tetrachloro-1,4-benzenedithiol, (c-d) 2,3,5,6-tetraflouro-1,4-benzenedithiol, Neutral: (e-f) 1,4-benzenedithiol, and Electron Donating: (g-h) 2,5-dimethyl-1,4-benzenedithiol. (i-j) As evident by the thermopower, using electron withdrawing substituent results in a shift in the transmission function to lower energies and electron donating substituents shift the transmission function to higher energies. Inset: transmission function and thermopower zoomed-in near the chemical potential. Adapted with permission from K. Baheti, J. A. Malen, P. Doak, P. Reddy, S. Y. Jang, T. D. Tilley, A. Majumdar and R. A. Segalman, *Nano Lett*, 2008, **8**, 715-719. Copyright 2008 American Chemical Society.

The dependence of thermopower on molecular length has also been investigated using phenylene and alkane chains.[42,43] Prior studies showed that electronic conductance varies exponentially with molecular length[46,47]

$$G = G_c e^{-\beta_G L}, \qquad (1.19)$$

where G_c is the extrapolated zero length contact conductance and β_G is the conductance decay constant. However, as theory predicts,[46] thermopower varies linearly with molecular length

$$S = S_c + \beta_S L, \tag{1.20}$$

where S_c is the extrapolated zero length contact thermopower and β_S is the thermopower decay constant that depends on the backbone of the molecule. Reddy *et al.* first noted this linear dependence using 1,4-benzenedithiol, 4,4-dibenzendithiol, and 4,4-tribenzenedithiol. Malen *et al.* later expanded upon this work to include different molecular backbones and end groups.[42,43] Here, they found that both thiols and amines have similar β_S values (*i.e.*, similar slope in Fig. 1.12) but very different S_c values (*i.e.*, y-intercept values in Fig. 1.12). Furthermore, alkanedithiols with N=2,3,4,5,6, and 8 CH_2 were investigated and unlike benzenedithiols the thermopower decreased with increasing length.

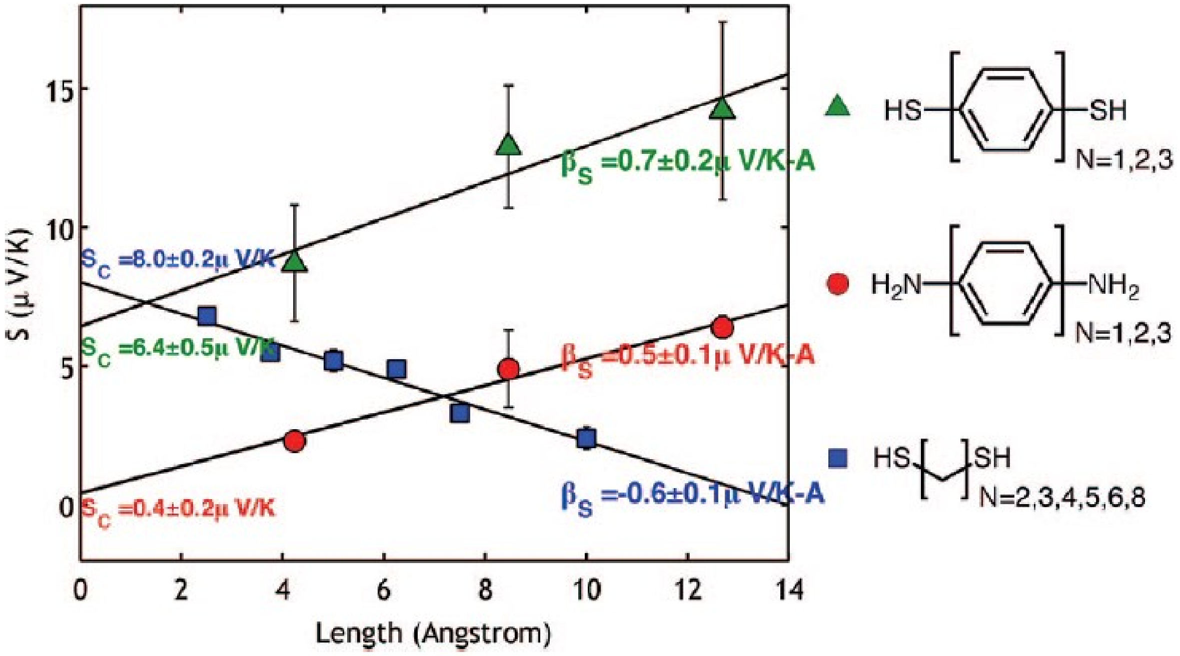

Figure 1.12 Thermopower *vs*. molecular length: (green triangles) benzenedithiols (N=1,2,3) , (red circles) Phyenyldiamines (N=1,2,3), (blue squares) alkanedithiols (N=2,3,4,5,6,8). The molecular length calculations exclude end groups with a single CH_2 having a length of 1.25 Å and a single phenyl ring having a length of 4.23 Å. Reprinted with permission from J. A. Malen, P. Doak, K. Baheti, T. D. Tilley, R. A. Segalman and A. Majumdar, *Nano Lett*, 2009, **9**, 1164-1169.. Copyright 2009 American Chemical Society.

For phenyls, the rational for this length dependence can be explained by analogy to the quantum mechanical "particle in a box;" as the length of the box increases the energy spacing between consecutive energy levels decreases. In this case, the energy spacing between the HOMO and LUMO will decrease. Using the Lorentzian picture of transport, the HOMO-LUMO peaks become closer together and the electrode-coupling orbital-broadening terms (*e.g.*, $\Gamma_{n,1}$, and $\Gamma_{n,2}$) decrease. This results in steeper Lorentzian peaks with deeper intermediate valleys. This suggests that for enhanced *ZT*, (similar to bulk materials) there is a maximum power factor for molecular length. Furthermore, the endgroups play a significant role and contribute to $\Gamma_{i,1}$, and $\Gamma_{i,2}$. However, by varying the endgroups, it was determined that the backbone is primarily responsible for the trend in length and orbital alignment while the endgroups are responsible for the extrapolated zero length thermopower. Specifically, dithiols have similar S_c values which differ significantly from diamines and S_c for thiols is appreciably larger than that for diamines. Qualitatively, this is correlated to the strength of the thiol-Au bond and suggests that thiol terminated molecules are good candidates for molecular thermoelectrics. However, amines are known to have well specified bonding site while thiols are much less specific.[48] This variation in bonding suggests that significant error and fluctuations are present in thiol terminated systems[49].

To further investigate this point of fluctuations, Malen *et al.* also investigated the nature of transport variation present in the thermopower of molecular junctions.[45] It was observed that the FWHM of each thermoelectric histogram also increased linearly with temperature (Fig. 1.10). The slope of this FWHM versus ΔT defines the fluctuations in thermopower, ΔS. To quantify the thermopower variation, the dimensionless parameter $\Delta S/S$ was introduced. It was argued that this parameter relates the observed variation in thermopower to variations in the energy levels of the molecule

$$\frac{\Delta S}{S} \approx \frac{\Delta E_{HOMO}}{\mu - E_{HOMO}} \tag{1.21}$$

where ΔE_{HOMO} is the fluctuation in the HOMO energy level, and $\mu\text{-}E_{HOMO}$ is the energy offset between the chemical potential and the HOMO.[45] The measurements indicate that $\Delta S/S$ varies between 0.3-0.8 depending on the length of the molecule—hence the HOMO's variation is similar in magnitude to its nominal offset from the chemical potential. In this previous work, two types of variations are suggested. The first type results from differences between consecutive junctions termed junction-to-junction variations and the second type accounts for the deviations within a junction termed junction-evolutions. The separate contributions are isolated by statistical analysis of the voltage traces. Junction-to-junction variations are quantified by the spread in the mean thermoelectric voltage among the approach and withdraw sequences and the junction evolutions are quantified by the spread within a given junction. They observed that the junction-to-junction variations dominate $\Delta S/S$. It was further hypothesized that the variations in transport could be caused by four mechanisms: (i) contact geometry and orbital hybridization as junctions are formed, (ii) intermolecular interactions (*e.g.*, aromatic coupling), (iii) intramolecular torsion (*e.g.*, ring-ring twists), and (iv) high frequency rotation and vibration of the molecule.

While these investigations into molecular thermopower explain many of the underlying physical principles of interfacial transport, they also provided insight into engineering systems with higher *ZT*. From this previous work, I learned how the thermoelectric properties can be modestly tuned by varying the chemistry. I also learned that large π-conjugated systems have larger thermopowers. Furthermore, I gained an appreciation for the importance of molecular end groups. This knowledge suggests to me that an ideal molecular junction is one where the molecule is (i) large such that the HOMO-LUMO gap is small, (ii) heavily conjugated leading to a high conductance, (iii) easily functionalize with chemical substituents for fine tuning, and (iv) paired well with the electrode for aligning the chemical potential with the frontier molecular orbitals. Furthermore, Bergfield and Stafford[50] provide further inspiration by showing that the thermoelectric effects can be enhanced if the flow of entropy is blocked by the quantum interference of the molecular junctions at transmission nodes. With this view, Bergfield and Stafford concluded that the temperature-independent maximum thermopower in a molecular junction is $\pm\pi k_B/(3^{1/2}e)\approx\pm156\ \mu\text{V/K}$. This value is approximately one order of magnitude larger than anything currently observed suggesting that vast improvements can still be made with molecular junctions.

All of the molecules described and measured so far have been dominated by transport through the HOMO. However, Baheti *et al.* found that for cyano terminated phenyl molecules the sign of the thermopower is weakly negative indicating that transport is weakly dominated by the LUMO. This could be advantageous, when it comes to choosing contacts, because improved alignment of the chemical potential with the LUMO can be achieved using common metals with lower work functions than Au, including Ag and Al. In contrast, there are limited electrode options for improved alignment of the chemical potential with the HOMO, since primarily precious metals like Pt and Pd have higher work functions than Au. Are there molecules that exhibit LUMO transport where metal electrodes with a lower work function can be selected? What is the maximum thermopower of a molecular junction? How can this be realized? These questions are just a few examples that spurred me to consider thermoelectric energy conversion in organic-inorganic hybrid materials.

Chapter 2 Thermoelectric Transport in Single Fullerene Molecules

Reproduced with permission from the American Chemical Society: Shannon K. Yee†, Jonathan A. Malen†, Arun Majumdar, and Rachel A. Segalman, *"Thermoelectricity in Fullerene – Metal Heterojunctions," Nano Letter* **11**, 4089-4094, 2011.

Thermoelectricity in molecular junctions, where a single-molecule is trapped between metal electrodes, has been used to understand transport properties at organic-inorganic interfaces.[43] The transport in these systems is highly dependent on the energy level alignment between the molecular orbitals (MOs) and the chemical potential (*i.e.*, Fermi level or work function) of the metal electrodes. To date, the majority of single-molecule measurements have focused on simple small molecules where transport is dominated through the highest occupied molecular orbital (HOMO).[51,52] In these systems, energy level alignment is limited by the absence of electrode materials with low Fermi levels (*i.e.*, large work functions). Alternatively, more controllable alignment between molecular orbitals and the Fermi level can be achieved with molecules (*i.e.,* fullerenes) whose transport is dominated by the lowest unoccupied molecular orbital (LUMO) because of readily available metals with lower work functions. Within this chapter, I report single-molecule thermoelectric transport measurements of fullerene molecules (*i.e.*, C_{60}, PCBM, and C_{70}) trapped between metal electrodes (*i.e.*, Pt, Au, Ag). Fullerene junctions demonstrate the first strongly n-type molecular thermopower corresponding to transport through the LUMO, and the highest measured magnitude of molecular thermopower to date. While the electronic conductance of fullerenes is highly variable, due to fullerene's variable bonding geometries with the electrodes, the thermopower shows predictable trends based on the alignment of the LUMO with the work function of the electrodes. Both the magnitude and trend of the thermopower suggest that at organic-inorganic interface, the thermoelectric performance can be enhanced, therein providing a new pathway for designing thermoelectric materials.

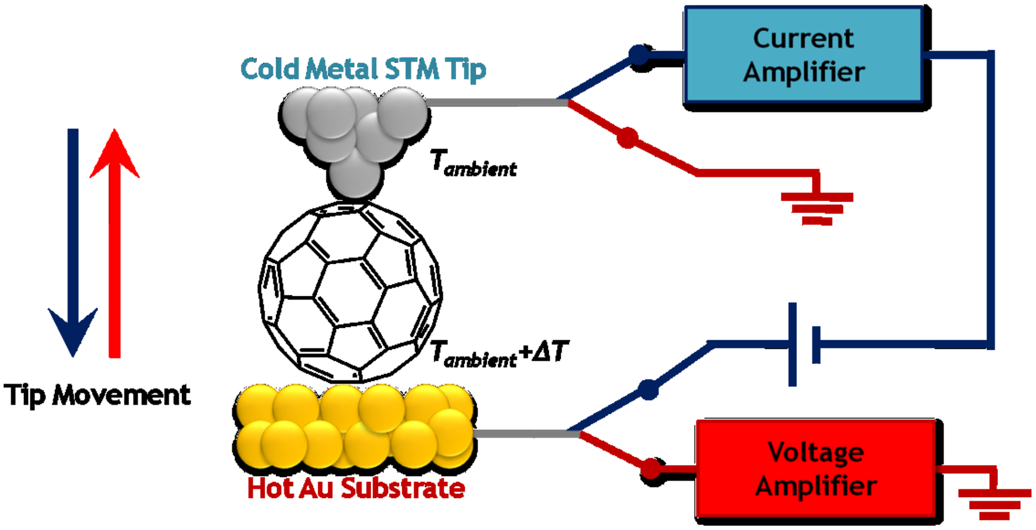

Figure 2.1 Measurement Setup. (a) Schematic of the experimental setup for measuring conductance and thermopower with a modified STM break junction. For conductance, a voltage bias is applied between the tip and substrate and the conductance is determined using a current amplifier. The STM tip contacts the substrate and traps fullerene molecules. For thermopower, fullerene molecules are trapped between the STM tip held at ambient temperature and a heated Au substrate held at ΔT above the ambient temperature. As the STM tip approaches a voltage bias is applied between the tip and substrate, and conductance is monitored. Once a threshold conductance of ~0.1 G_0 is reached, indicating formation of a molecular junction, the tip is withdrawn. During the withdrawal sequence, a switch disconnects the voltage bias and current amplifier in favor of a voltage amplifier. The induced thermoelectric voltage V is measured as the tip withdraws but before the junction breaks.

2.1 Single Fullerene Molecule Investigation Motivation

Alignment with MOs can be achieved in two ways: (i) by altering the MOs of the molecule by adding electron donating or withdrawing substituents or (ii) by varying the electrode material. Previous molecular junction measurements[51,52] have focused on molecules, such as benzenedithiol, whose transport is dominated through the HOMO. It has previously been demonstrated that for phenylene derivatives between Au electrodes, thermopower[44] and the conductance[53] can be predictably but modestly controlled using chemical substituents to shift the MOs. Similarly it has been shown that better alignment and thus higher conductance can be achieved by using Pt instead of Au where the higher work function places the Fermi level closer to the phenylene's HOMO[54,55] promising as much as an order of magnitude improvement in the conductance. However, for phenylene molecules, obtaining even better alignment is difficult because Pt's Fermi level is rivaled in magnitude only by rare elements such as osmium and selenium.

Previous thermopower and conductance measurements have focused primarily on relatively small alkane and phenyl derivatives.[32,33,42,44,48,53,56,57] Bergfield and Stafford[50] recently predicted that thermopowers exceeding 150 μV/K (on par with inorganic thermoelectric materials) are possible in more highly conjugated molecules. Fullerene molecules are highly conjugated and have additional characteristics necessary to realize high thermopower regimes[58,59] including: (i) small HOMO-LUMO gaps (*i.e.*, 2-3 eV *vs*. 5-10 eV for alkane or phenyl molecules) facilitating chemical potential alignment, (ii) degenerate orbitals attributed to the high symmetry, and (iii) LUMO dominated transport in the bulk, making them the common choice for acceptors in organic photovoltaics[60].

Single-fullerene conductance measurements (all under UHV) have yielded a wide range of values. Joachim *et al.*'s pioneering measurements of C_{60} between W and Au electrodes yielded a low conductance of $2.4\text{x}10^{-4} \pm 1.2\text{x}10^{-4}\ G_0$[61] (using an STM at 300 K), but more recent Au-C_{60}-Au[62] (using a mechanical breakjunction at 10 K), Pt-C_{60}-Pt[55] (using a mechanical breakjunction at 300 K), and W-C_{60}-Cu[63] (using an STM at 8 K) junctions have found conductances as high as 0.1, 0.2, and 0.25 G_0. The large spread in high and low conductance values is not surprising as it has been observed that the orientation of the molecules on surfaces strongly affects the alignment and coupling of frontier molecular orbitals with the electronic states of the metal. STM images, experiments, and measurements by Lu *et al.* on Ag[64,65], Néel *et al.* on Cu[66], and Rogero *et al.* on Au[67] substrates all support this claim. Specifically, Lu *et al.* show a distribution of conductance values due to the orientation and contact of the molecule at low temperatures and Rogero *et al.* show that no preferential orientation is present at 300 K. Some STM techniques, such as Joachim *et al.'s* and the work reported herein, sample a wide variety of molecular orientations and contact geometries by making multiple measurements at room temperature, where the thermal energy is sufficient for the molecule to transition between these orientations. This should result in a large spread of conductances extending as low as 10^{-4} G_0 as suggested by benzenedithiol experiments and theory.[45,68] This is different from the work of Bohler *et al.*[62] and Kiguchi *et al.*[55], which used a mechanical breakjunction to trap one molecule in a unique orientation preserved by low temperatures. Furthermore, this previous work has shown that the conductance of these junctions is dependent on the electrode material suggesting that alignment and coupling of the fullerene's LUMO and the work function of the metal is important.

Herein, I show how this alignment and coupling manifests itself in electronic transport by conducting a systematic study of thermopower and conductance of C_{60}, [6,6]-phenyl-C_{61}-butyric acid methyl ester (PCBM), and C_{70} heterojunctions trapped between Pt, Au, and Ag electrodes. I observe that the trend in thermopower versus metal work function agrees with MO alignment while no trend in conductance is observed which is expected based on the wide range of molecular orientations that are sampled. The weak dependence on orientation is one strength of using thermopower to probe electronic transport in molecular junctions. Finally, this work suggests a new pathway to improve thermoelectric performance by relying on interfacial transport phenomena.

2.2 Single Fullerene Molecule Methodology

Conductance and thermopower measurements were carried out as previously described in literature[42-44,51,56] and illustrated in Fig. 2.1. To summarize: a 1 mM dichlorobenzene solution containing a fullerene derivative (*i.e.*, either C_{60}, PCBM, or C_{70}) is first drop cast onto a freshly cleaned and annealed Au substrates and the solvent is permitted to evaporate. A modified STM is used to contact the molecules where the STM tip material varies between Pt, Au, and Ag. Au substrates were used for all measurements as I suspect that the malleability of Au is necessary to create junctions of acceptable duration for measurement. Special care was taken to prepare the tips and keep them free of contamination

2.2.1 Substrate and Tip Preparations

To prepare the substrates, 200 nm of Au is first sputtered onto freshly cleaved mica substrates, which are then flame annealed just before use using a hydrogen torch with a repetition rate of 1 Hz. Approximately 1 mM solutions of C_{60}, PCBM, and C_{70} in dichlorobenzene is prepared and sonicated to facilitate dissolving the fullerene molecules (>99% pure) before being drop cast (~10 µL) onto an annealed, Au-coated mica substrate where the solvent is allowed to evaporate under nitrogen. The STM tip is prepared from 250 µm diameter metal (>99.99% pure, Pt, Au, or Ag) wire. Just before use, the Pt and Au wire are cleaned by piranha and exposure to oxygen plasma then cut from the wire. Since Ag tarnishes and oxidizes, just before use, the Ag wire is flame annealed using a hydrogen torch to reduce the tarnish and oxide before being cut. The STM sample holder and electrical contacts are cleaned in a piranha bath, rinsed with deionized water and acetone, and dried under nitrogen to prevent contamination.

2.2.2 Conductance Measurements

Conductance measurements are performed using a modified STM setup that has been previously described in literature.[56] A +100 mV bias is applied between the initially separated tip and the substrate (ground referenced to the substrate) and a current amplifier monitors the conductance. The STM tip then approaches the molecule coated substrate until a conductance threshold of >6 G_0 is reached indicating contact with the surface. The STM tip is then retracted at a rate of ~1 nm/s eventually opening a 1D transmission channel corresponding to a conductance of G_0. The STM tip then continues to retract breaking that 1D channel, allowing for a molecule to bridge the gap. The tip continues to retract until a threshold conductance of $<10^{-5}$ G_0 is obtained suggesting only vacuum tunneling remains. Next the tip re-approaches the surface to form the next junction. >2000 junctions were gathered for each molecule and tip combination. Energy dispersive x-ray spectroscopy was acquired of new and used tips which showed no evidence of oxidation, tarnish, or contamination on any of the tips. Furthermore, no Au adhesion to the Pt or Ag tips was detected. This is because a withdraw conductance threshold of 6 G_0 does not produce sufficient pressure to cause the Au to plate the tip. Only data corresponding the withdraw sequence is analyzed; the $\log_{10}$ of this data normalized to G_0 is taken to represent the conductance trace. To help with data reduction, the second numerical derivative of each conductance trace is calculated after applying a Savitsky-Golay smoothing filter to reduce the increased variation associated with differentiation; this value corresponds to the curvature of the trace. Since sharp steps in conductance are expected, the base of each step should have a positive curvature and the tip of each step should have a negative curvature. Furthermore, exponential decay in current associated with tunneling should yield a straight line with a negative slope and thus zero curvature. Conductance data possessing a zero or positive curvature was excluded and only negative curvature data was placed in a histogram for further analysis Figure 2.2 shows verification for 1,4-benzenediamine which has been well documented in literature.[32]

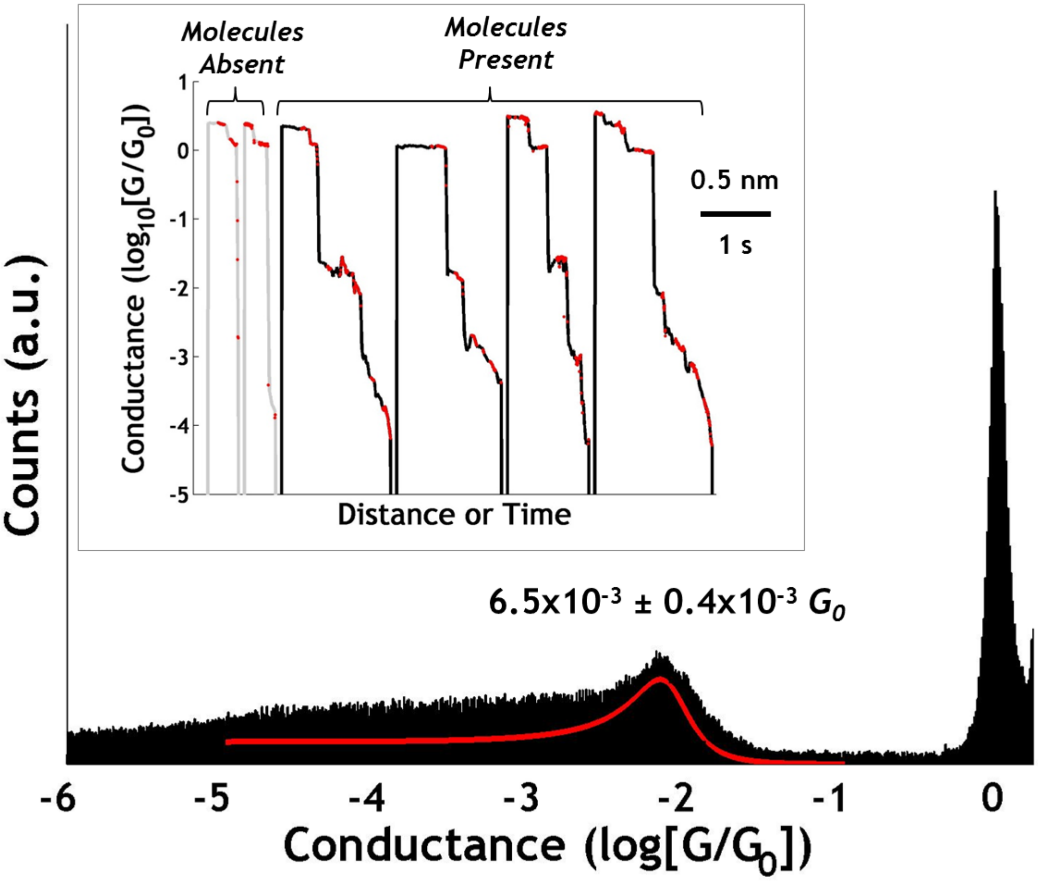

Figure 2.2 Benzenediamine Conductance Verification. Conductance histogram of 1,4-benzenediamine with a single conductance peak at $6.5x10^{-3} \pm 0.4x10^{-3}$ G_0. The uncertainty is a measure of the full-width-half-maximum of a Lorentzian least-squares non-linear regression (red). This is in good agreement with literature therefore validating the accuracy of the STM conductance breakjunction. (Inset) Example conductance traces for a bare Au surface with molecules absent (grey) and molecules present (black). Using a curvature data reduction, only points with a negative curvature (red) are selected for histograms.

For conductance measurements, a 100 mV bias is applied between the metal tip and the Au substrate. More than 2000 junctions are formed during repeated approach and withdraw sequences while continuously measuring the conductance. Lack of metal cross-contamination during these sequences likely results from our choice of a low threshold conductance (~6 G_0) which initiates the withdraw sequence. Steps in conductance are observed corresponding to 1-D metal-metal junctions at 1 G_0 and steps corresponding to molecules are observed below 1 G_0. Theory predicts that the value of 1 G_0 is independent of the material properties and hence should be consistent for all tips,[51,69,70] however, non-integer variations in this value have been experimentally observed.[71] To better distinguish between the steps in conductance and the exponential decay of tunneling currents, only data points possessing a negative curvature in conductance traces are selected for histograms.

2.2.3 Thermopower Measurements

Thermopower measurements were performed using a modified STM setup that has been previously described in literature.[43] Molecules are first captured between an STM tip held at ambient temperature and the Au substrate heated to ΔT above the ambient temperature. To capture molecules a voltage bias of +120 mV is applied between the initially separated STM tip and substrate (ground referenced to substrate). As the tip advances towards the surface, conductance is monitored with a current amplifier. Once the threshold conductance is exceeded, a junction has been formed, and a switch disconnects the current amplifier and voltage bias in favor of a voltage amplifier. Since thermopower is insensitive to the number of molecules (intrinsic property) in the junction, capturing one of a few molecules does not change the result. The thermoelectric voltage due to thermopower of the junction is measured between the tip and the substrate. Statistics are accumulated through >500 serial approach-withdrawal sequences at each ΔT (for $\Delta T \approx 0$, 5, 10, 15, 20, and 30 K). Voltage associated with incomplete isolation of the current amplifier resulting with a voltage offset at $\Delta T=0$ is rejected because thermopower reflects the slope of the voltage vs. ΔT not its absolute value. ΔT occurs across the junction, and not within the tip or substrate when a molecule is present;[43] when a molecule is not present, ΔT occurs across the STM tip. For further verification of this, thermopower was measured with the STM tip in contact with the substrate in the absence of molecules. Measured metal-metal thermopower voltages reproduce accepted thermopower values for Au, Ag, and Pt (Fig. 2.3). Furthermore, the temperature dependence of thermopower on the STM tip over the temperature range of interest is small compared to the thermopower of the heterojunction and within the error in thermopower.

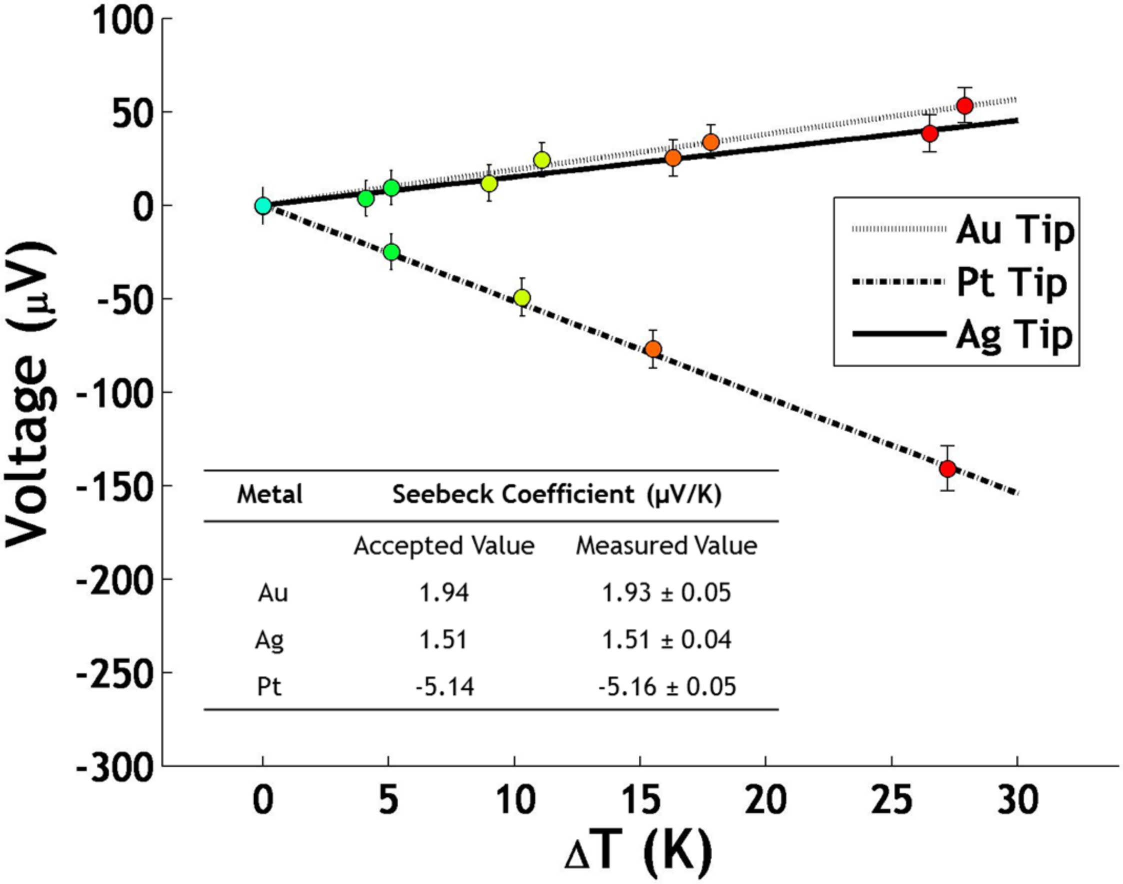

Metal	Seebeck Coefficient (μV/K)	
	Accepted Value	Measured Value
Au	1.94	1.93 ± 0.05
Ag	1.51	1.51 ± 0.04
Pt	-5.14	-5.16 ± 0.05

Figure 2.3 Metal-Metal Thermopower Measurements. Measured thermoelectric voltage of the measurement system for Au, Pt, and Ag STM tips in contact with the Au substrate. Lines represent the accepted thermopower values thus validating the accuracy of the measurement approach with different metal tips. This further suggests that the temperature drop in the system occurs primarily through the STM tip.

2.2.4 Contamination and Purity Considerations

In these experiments the tips and substrates were prepared as described above. To summarize, the Au and Pt tips were cleaned in a bath of piranha and then cleaned in an oxygen plasma. Since Ag oxidizes, it cannot be cleaned by piranha or in an oxygen plasma. For that reason, Ag is cleaned in a hydrogen flame where any Ag_2O or Ag_2S is reduced to Ag metal and any contaminants are incinerated. Tips were fabricated from metals wires that are >99.99% pure. Energy dispersive x-ray spectroscopy (EDS) in an SEM were performed for elemental analysis of the tips to verify that trace metals, oxides, and sulfur tarnish were not present. Three tips (one of each metal) were used as a control and designated as "new tips". The remaining three tips were used in the STM. Conductance experiments on a bare Au substrate were performed and designated as "used tips." A drop of dichlorobenzene was placed on the surface and allowed to evaporate to test for contamination in the same solvent that was used to dissolve the fullerenes. Steps at 1, 2, 3, and 4 G_0 were observed and ~1000 approach and withdraws were acquired for each tip. The upper conductance threshold was set to ~6 G_0. After these approach and withdraw sequences, EDS spectrum (Fig. 2.4) of the "used tips" were gathered. The "new tips" only showed x-ray peaks corresponding to Ag, Au, and Pt respectively. No oxygen, sulfur, or trace metal peaks were observed. This shows that the tips are pure and free of contamination.

Al peaks are routinely present in this SEM resulting from the Al sample stage. The "used tips" show nearly identical EDS spectrum to the "new tips". Screenshot (Fig. 2.4, right) of the EDS spectrum (red) with built-in peak identification show that Au lines (indicated by blue and yellow placement lines) are not present in the Ag and Pt tips and clearly align with the Au tip spectrum. I also note that sulfur peaks are not present as indicated by a yellow placement line. Kα, Lα, and Mα energies for Pt and Au are close, however, the instrument resolution is more than sufficient to observe, detect, and auto assign elements to these peaks. Au plates onto Pt and Ag by hard-pressing, the pressures here were limited by our threshold conductance (~6 G_0), and did not result in any transfer of Au onto the tips. Finally, no light elements were visible verifying the absence of contamination. For thermopower measurements the approach threshold is 0.1 G_0 making metal-metal contact and cross contamination of metals impossible.

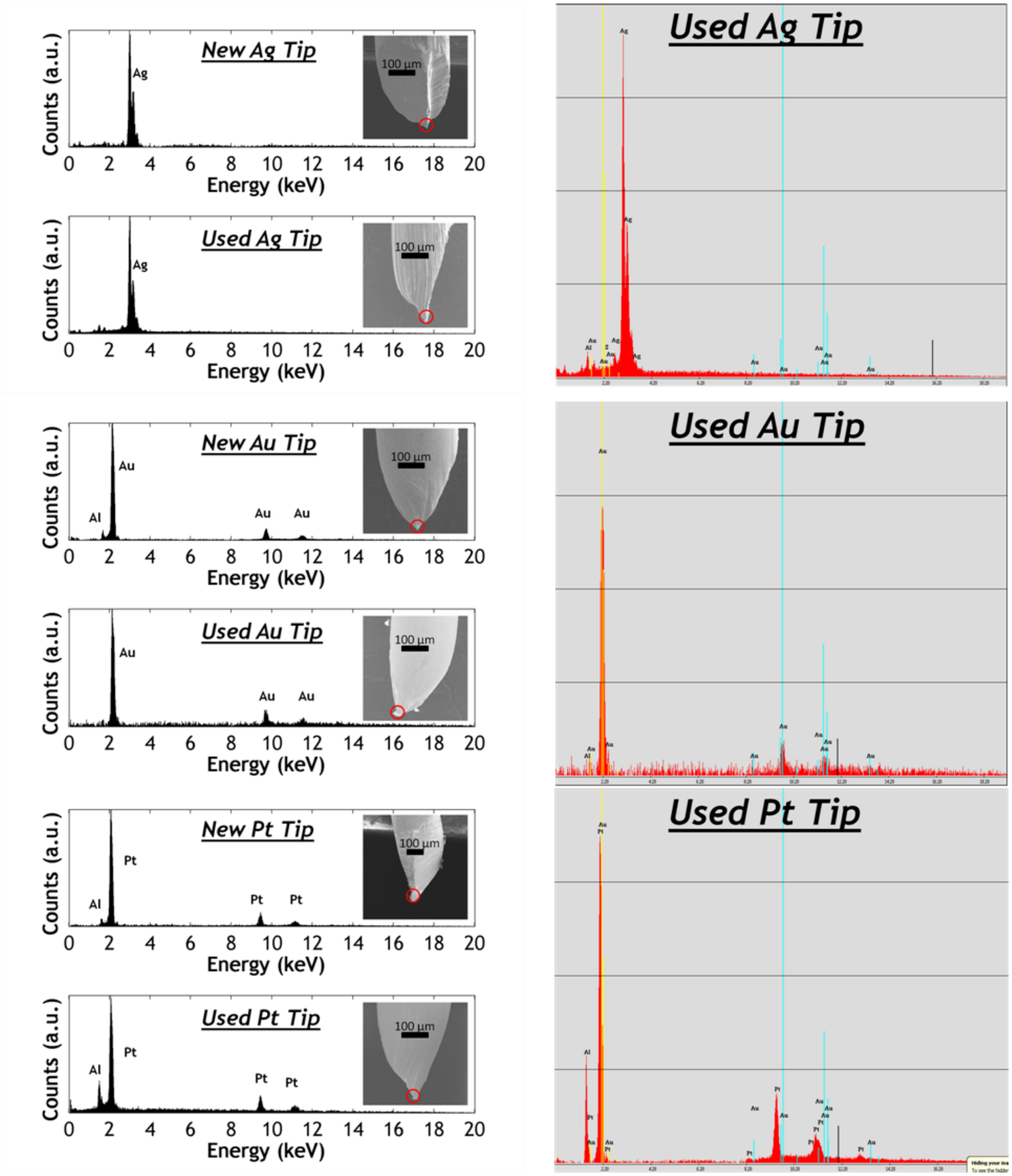

Figure 2.4 EDS Spectrum. (Left) EDS spectrum comparing "new" and "used" tips showing the purity of the tips free of contamination. (Right) Screenshots of "used" tips showing the automated peak identification of the SEM's EDS. There is no evidence that the Au substrate is picked up during measurements.

2.3 Single Fullerene Molecule Results and Discussions

The conductance histograms are found in Fig. 2.5a-l. The first row (Fig. 2.5a,d,g,j), second row (Fig. 2.5b,e,h,j), and third row (Fig. 2.5c,f,i,l) represent the conductance with Pt, Au, and Ag STM tips all with Au substrates, respectively. The first column represents the junction conductance in the absence of any fullerene molecules (Fig. 2.5a,b,c); only a single peak corresponding to the quantum of conductance is visible near 1 G_0. The second column (Fig. 2.5 d,e,f), third column (Fig. 2.5g,h,i), and fourth column (Fig. 2.5j,k,l) represent the conductance of C_{60}, PCBM, and C_{70}, respectively. Note the large variation in the apparent molecular conductance peaks. Prior studies suggest that variation comes from the multiple orientations that fullerenes take on the electrodes. This variation is compounded by the use of different tip and substrate materials (and thus different crystal direction and bonding geometries) in this study. While the spread in the conductance makes reporting a single fullerene conductance value challenging, the peak of the smallest observed conductance and the FWHM of that peak (when present) have been plotted against the average work function of the tip and substrate in Fig 2.6. Using the average work function of dissimilar contacts, Beebe *et al*. identified trends in conductance of alkanethiol junctions.[72,73] In contrast, Fig. 2.6 shows that we observe no clear trend in the conductance.

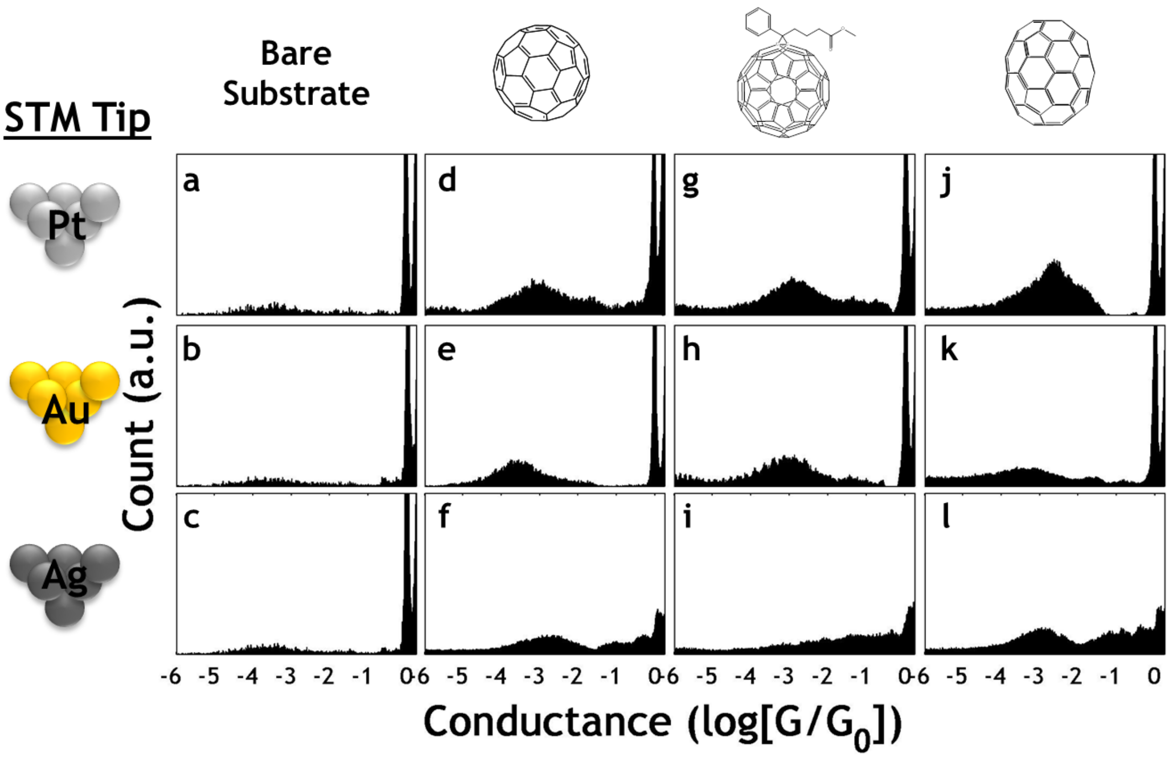

Figure 2.5 Conductance Histograms. A matrix summarizing the normalized conductance data for ~2000 consecutive junctions organized in columns by fullerene derivative and rows by electrode composition. The first column (a-c) represents the conductance of tip and substrate in the absence of molecules showing the recognizable 1 G_0 peak. Log(G/G_0) bin size is -0.006 (*i.e.*, 1000 bins per 6 decades). Vertical scale reduced to emphasize low conductance histograms.

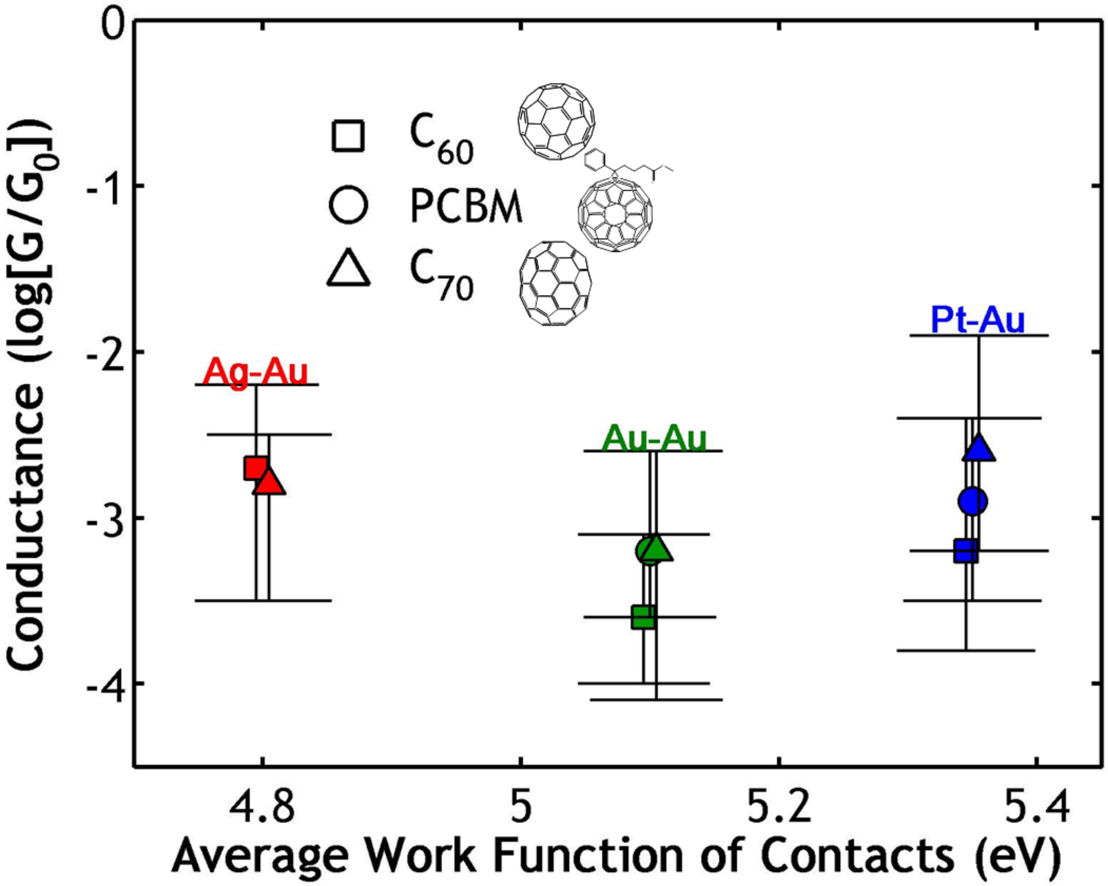

Figure 2.6 Conductance *vs*. Work Function. The observed conductance of C_{60}, PCBM, and C_{70} junctions is plotted vs. the average work function of the electrodes (nominal work functions: Ag≈4.5 eV, Au≈5.1 eV, and Pt≈5.6 eV. A slight x-offset has been applied so individual error bars could be distinguished). Error bars represent the FWHM of the observed lowest conductance peaks in the histograms. The large spread suggests that conductance of fullerene junctions may vary widely, possibly due to molecular orientations in the junction.

Upon inspection of the histograms, the conductance profile using the Ag tip differs from those profiles where Au or Pt tips are used. We attribute this to the breaking of the LUMO's degeneracy (which is 6 fold degenerate for C_{60}) when coupled to the Ag surface in certain orientations, as first recorded by Lu *et al.*[64,65] The high symmetry of some fullerenes creates multi-degenerate LUMO. This degeneracy is broken when the fullerene bonds to Ag, resulting in one orbital being pushed to lower energies and becoming more closely aligned with the Fermi level of Ag. This results in higher observed conductance and provides an explanation for the broadening of the G_0 peak that occurs with the Ag tip. Alternatively, assuming that the degeneracy is not broken, the conductance of a single-orbital would then simply be multiplied by the degeneracy to give the conductance of the molecule. The thermopower, however, will not be affected by the degeneracy as it is the slope of the transmission function normalized to the transmission function as shown in Eqn 1.18. These complications make interpreting trends in conductance more difficult.

Thermopower measurements show a clear trend with respect to the work function of the electrodes. Voltage histograms and the inferred thermopowers are shown in Fig. 2.7a-i, where the rows are for Pt, Au, and Ag tips; the columns are for C_{60}, PCBM, and C_{70} molecules. In the absence of molecules, a small thermoelectric voltage corresponding to the Seebeck effect of the metal STM tip, only occurs when the STM tip crashes into the substrate. Seebeck measurements of Ag, Au, Pt, and Cu STM tips with Au substrates show that my measurement always yields the thermopower of the tip material upon contact. In the presence of fullerene molecules the measured thermopower is far larger in magnitude, indicating that the measured thermopower is a characteristic of the fullerene junction, rather than the metal electrodes alone. When the fullerenes are present, the histogram peak values, V_{peak}, are plotted as a function of ΔT in the insets, where the error bars represent the full-width-half-max of the voltage histograms. The slope of the least squares linear fit is the junction thermopower S and the 95% confidence interval in slope is the error in S (reported in the insets to Fig. 2.7a-i). All of the molecules demonstrated negative S, indicating that the Fermi level of the electrodes are more closely aligned with the LUMO further confirming that these semiconducting molecules behave as electron acceptors (*i.e.*, n-type). The magnitude of S is related to the alignment of the Fermi level and the LUMO. Therefore, if the electrode work function decreases, then the magnitude of S should increase, as the Fermi level aligns more closely with the LUMO as shown in Fig. 2.8c. As expected, as the average work function of the contacts decreases, the Fermi level moves closer to the LUMO of the molecules resulting in higher S.

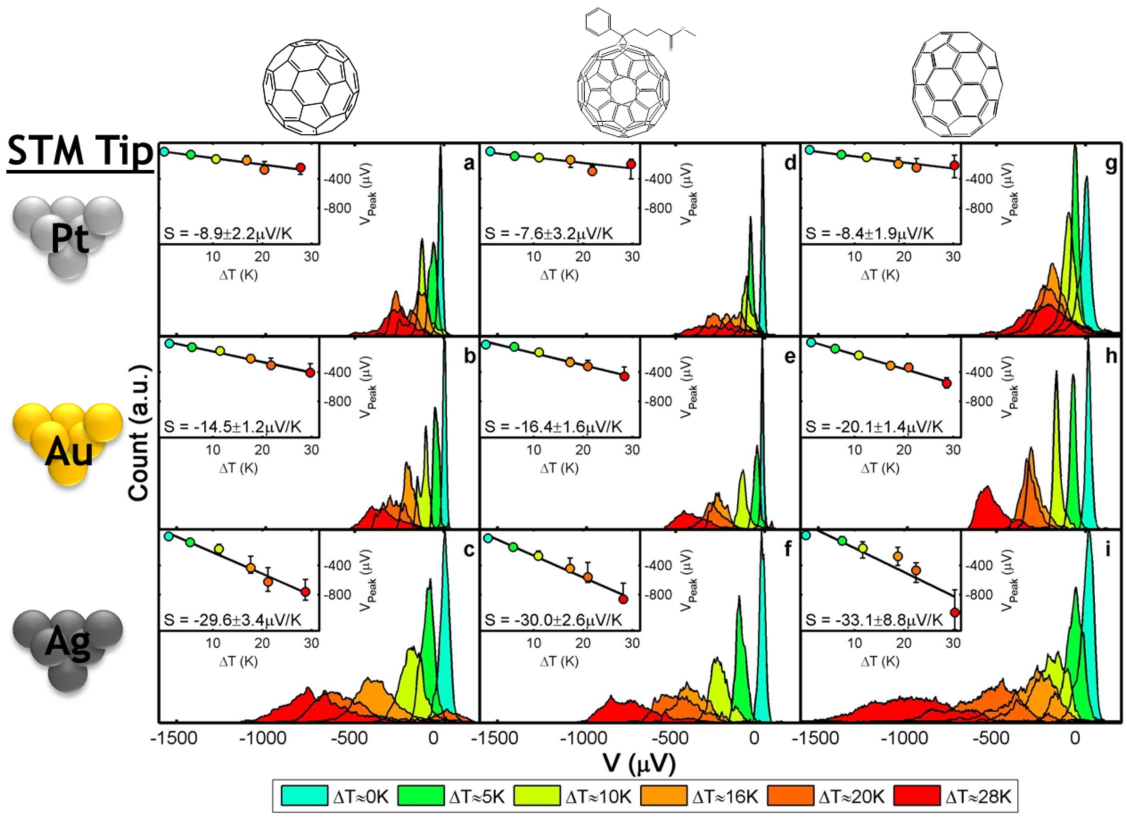

Figure 2.7 Thermopower Histograms and Linear Regressions. A matrix summarizing the thermopower data is organized in columns by fullerene derivative and rows by electrode composition. The normalized voltage histograms compile data for ~500 consecutive junctions at each ΔT, without pre-selection. Insets show the voltage histogram peaks as a function of ΔT, where the error bars represent the full-width-half-max of the associated histogram. The voltage peaks vary linearly with ΔT for all junction combinations. The slope of the linear regression defines the thermopower where the reported error is the 95% confidence interval of the regression.

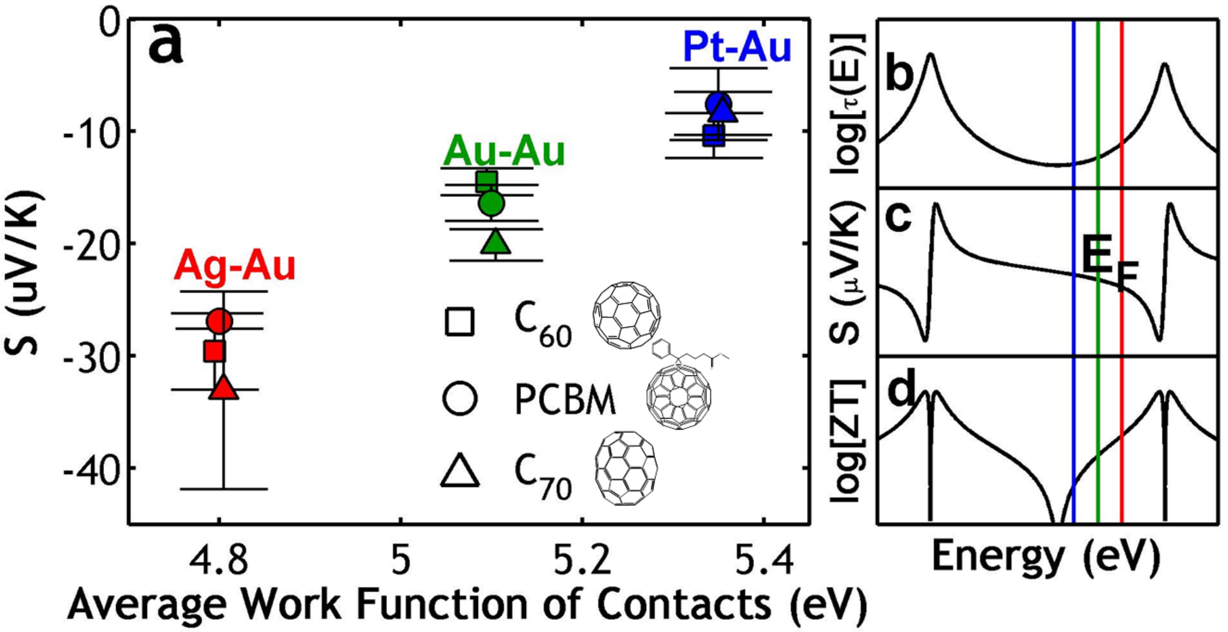

Figure 2.8 Thermopower *vs*. Work Function and its effect on ZT. (a) The observed thermopower of C_{60}, PCBM, and C_{70} junctions is plotted vs. the average work function of the electrodes (nominal work functions: Ag≈4.5 eV, Au≈5.1 eV, and Pt≈5.6 eV. A slight x-offset has been applied so individual error bars could be distinguished). A clear trend indicates that the lower work function electrodes result in higher negative thermopowers. A Lorentzian depiction of the transmission function (b) and the related energy dependent thermopower (c) show that the increasingly negative thermopower results from improved alignment between Fermi level, E_F, and the fullerene LUMO. Blue, green, and red vertical lines approximate the position of the E_F for Pt-Au, Au-Au, and Ag-Au junctions. (d) The *ZT* associated with the transmission function and thermopower in (b) and (c) increases dramatically when E_F is aligned with the LUMO using low work function electrodes.

Landauer formalism can use a Lorentzian transmission function, τ, to describe the thermopower measurements. In this description, the transmission function can be written as

$$\tau = \sum_{i=1}^{N} \frac{4\Gamma_{i,1}\Gamma_{i,2}}{\left(\Gamma_{i,1}+\Gamma_{i,2}\right)^2 + 4\left(E-E_i\right)^2}, \tag{2.1}$$

where, E_i are the MO energies and $\Gamma_{i,1}$ and $\Gamma_{i,2}$ are the broadenings of the i^{th} MOs due to coupling with electrodes 1 and 2. The transmission probability is peaked when the chemical potential aligns well with the energy of the MOs. Figure 2.8b-d shows a cartoon of how the Lorentzian descriptions of τ should effect S and therefore increase ZT. Observations that S grows more negative with reduced work function are consistent with the Fermi level moving towards a position of higher slope on the transmission function (Eqn. 2.1). The vertical blue, green, and red lines in Fig. 2.8b-d represent the position of E_F for Pt-Au, Au-Au, and Ag-Au electrodes. Also from this description one may expect that an increase in conductance should also strictly occur since the conductance is directly proportional to τ. However, this trend need not be true especially if the coupling terms (*i.e.*, $\Gamma_{i,1}$ and $\Gamma_{i,2}$) associated with each MO are not constant between different tip-molecule-substrate permutations. To illustrate this, consider a transmission function which is dominated by one MO, (*e.g.*, the LUMO), in the weak coupling limit $\left(\mu - E_{LUMO}\right)^2 \gg \quad {}_{LUMO\,1} + \Gamma_{LUMO,2}\big)^2$. Hence, the conductance and thermopower can be approximated as

$$G \approx \frac{8e^2}{h} \frac{\Gamma_{LUMO,1}\Gamma_{LUMO,2}}{\left(\Gamma_{LUMO,1}+\Gamma_{LUMO,2}\right)^2 + 4\left(\mu - E_{LUMO}\right)^2} \propto \frac{\Gamma_{LUMO,1}\Gamma_{LUMO,2}}{\left(\mu - E_{LUMO}\right)^2}, \quad (2.2)$$

and, given that Γ varies weakly with energy,

$$S \approx \frac{8\pi^2 k_B^2 T}{3e} \frac{\left(\mu - E_{LUMO}\right)}{\left(\Gamma_{LUMO,1}+\Gamma_{LUMO,2}\right)^2 + 4\left(\mu - E_{LUMO}\right)^2} \propto \frac{1}{\left(\mu - E_{LUMO}\right)}. \quad (2.3)$$

In other words, the conductance depends strongly on these coupling terms while thermopower depends only on the relative alignment of energy levels.[45] Trapping the fullerenes between different metal contacts illustrate this concept as multiple orientations, and thus multiple coupling terms, increase the spread in the data as discussed earlier.[64-67]

2.4 Single Fullerene Molecule Summary

Demonstrated above is the first molecular thermoelectric measurements of fullerene molecules (*i.e.*, C_{60}, PCBM, and C_{70}) trapped between different electrodes (*i.e.*, Pt, Au, Ag). I show that while the electronic conductance is highly varying, which is attributed to the multiple orientations and electrode coupling of molecules between the junctions, the thermopower is a robust measurement and can be predictably controlled by selecting the appropriate electrode material for energy level alignment based upon the work function of the electrodes. Furthermore, this is the first observation of negative (n-type) thermopower for single-molecule heterojunctions and is the highest single-molecule heterojunction thermopower recorded to date of -33 μV/K in comparison to the Au-Au junction thermopower of ~2 μV/K or [1,4]-benezenedithiol thermopower of ~8 μV/K. This alone results in a substantial improvement in molecular ZT and suggests that organic-inorganic interfaces can lead to further enhancements of thermoelectric efficiency.

Chapter 3 Electrical Transport in Single Diode Molecules

Reproduced with permission from the American Chemical Society: Shannon K. Yee[†], Jibin Sun, Pierre Darancet, T. Don Tilley, Arun Majumdar, Jeffrey Neaton, and Rachel A. Segalman, *"Inverse Rectification in Donor – Acceptor Molecular Heterojunctions," ACS Nano* **11**, 9256-9263, 2011.

The thermoelectric transport in p-type (HOMO dominated donor molecules, Chapter 1) and n-type (LUMO dominated acceptor molecules, Chapter 2) molecules was previously discussed. It was found that the energy alignment of the molecular orbitals with the chemical potential (*i.e.*, work function) of the electrodes strongly influences the thermoelectric behavior. It was also shown (Chapter 2) that robust molecular bonds to the electrode are at least of equal importance in describing electrical transport at the interface. Using the simple model (presented in Chapter 1) for interfacial transport, it was shown (Chapter 2) that the Γ-terms, which represent how strongly the molecule binds to the electrodes and how the discrete molecular orbitals hybridize with the continuum of electronic states of the metal electrodes, strongly influence the electrical conductance. The natural extension is to study how Γ can influence electrical transport further in both p- and n- type systems. To compare these systems, it is equally interesting to compare pn-diode (donor-acceptor) molecules. So within this chapter, I describe transport in a junction consisting of a small donor-acceptor molecules bound to Au electrodes. The electrical transport properties can be described in terms of hybrid donor-acceptor-electrode interfaces. A newly-synthesized donor-acceptor molecule consisting of a bithiophene donor and a naphthalenediimide acceptor separated by a conjugated phenylacetylene bridge and a non-conjugated endgroup shows rectification in the reverse polarization, behavior opposite to that observed in mesoscopic p-n junctions. Solution-based spectroscopic measurements demonstrate that the molecule retains many of its original constituent properties, suggesting a weak hybridization between the wavefunctions of the donor and acceptor moieties, even in the presence of a conjugated bridge. Differential conductance measurements for voltage biases as high as 1.5 V are reported. These measurements indicate a large asymmetry in the orbital contributions to transport arising from disproportionate electronic coupling at anode-donor and acceptor-cathode interfaces. A semi-empirical single-Lorentzian coherent transport model, developed from experimental data and density functional theory-based calculations, is found to explain the inverse rectification.

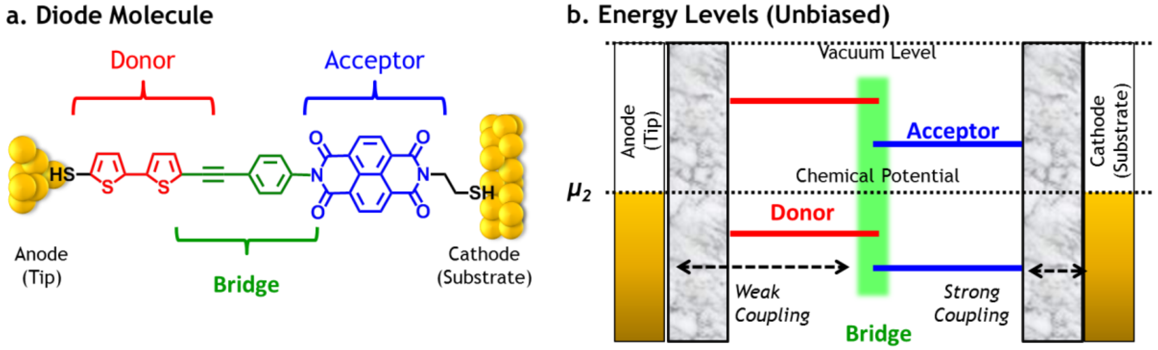

Figure 3.1 Simplified energy level diagram of the diode metal-molecule-metal heterojunction. (a) The structure of the junction: the molecule is connected to the anode (tip) and to the cathode (substrate) through thiol binding groups. The bridge breaks (green) the conjugation of the wavefunctions between the donor and acceptor parts of the molecule therefore localizing the HOMOs and LUMOs. (b) Schematics of the expected MO: the states under the chemical potential are occupied. Due to the bridge and their localization on one side of the molecule, the molecular levels are more strongly coupled to one electrode.

3.1 Single Diode Molecule Investigation Motivation

In a pioneering study more than three decades ago, Aviram and Ratner first proposed that donor-σ-acceptor molecules might behave like diodes.[68] In recent years, measuring transport in single-molecule junctions[25] has become possible with advances in nanoscale manipulation, and the conductance of several molecular junctions[29] have been investigated. Since then, suggestions that light can couple with molecular heterojunctions[33,48] has rekindled interest in molecular diodes, or molecules with rectifying behavior.[74,75] For thermoelectric, which consist of both p-type and n-type semiconductors connected electrically in series, understanding the donor (p-type)/acceptor (n-type) nature of diode molecules is necessary to understand the electrical conductance of the interface.

It is expected that single diode molecules will behave like mesoscopic diodes and display rectification in the forward bias direction. Conductance measurements observing rectification have been performed on self-assembled monolayers (SAMs)[47,76-82] and in single-molecule junctions.[83-86] Furthermore, inverse rectification has also been theoretically predicted[87] where it is argued that asymmetric coupling of the molecule to the electrodes is primarily responsible for the inverse effect. In addition to asymmetric molecules, rectification has been reported in symmetric molecules where the electrode material varied.[83,85] In single-molecule measurements, scanning tunneling microscope (STM) break junctions, conducting atomic force microscopes (CAFMs), mechanically controlled break junctions, cross-wires, and electromigrated breakjunctions are common tools.[88] Of these techniques, CAFM has the benefit of using force as the feedback mechanism, decoupling the electrical measurement from the controls mechanism.

Herein, I report my observations of a newly synthesized molecule consisting of a bithiophene donor and a naphthalenediimide acceptor separated by a phenylacetylene bridge (Bithiophene-Phenylacetylene-Naphthalenediimide-Dithiol) which is referred to as BPNDT (Fig. 3.1a). Due to the localization of the molecular orbitals in the donor-acceptor molecule, it is believed and verified in a similar molecule,[89] that the molecular orbitals are spatially localized (Fig. 3.1b) by the bridging molecule. The resulting energy landscape is (Type II) stair-step heterojunctions. In the forward bias direction, it may be expected that electrons "roll down" the stairs resulting in rectification in the forward bias direction. As will be shown, due to the asymmetry in molecular orbital bonding (represented by Γ), I observe this is not the case and rectification occurs in the reverse bias direction. This further illustrates the interesting transport phenomena that can occur at interfaces that strongly governs electric transport.

3.2 Single Diode Molecule Methodology

Transport measurements are carried out using a modified CAFM technique first developed by Morita *et al*.[36] and samples are fabricated via an elaborate self-assembly. This assembly starts with a near atomically-smooth conducting substrate (with an RMS roughness of 1.68 ± 0.18 Å over a scan area of 50 nm x 50 nm) fabricated using the mechanically stripped silicon template technique.[90-92] The freshly stripped Au substrate is then immersed in a 0.1 mM decanethiol (DeT) anhydrous toluene solution for 5 hours. Next the substrate are rinsed with anhydrous toluene and immersed in a 0.1 mM BPNDT molecule/anhydrous toluene solution for 12 hours. BPNDT molecules directionally insert into the defects of that SAM and protrude above the surface. In this step, the BPNDT molecule has a trimethylsilyl (TMS) group protecting the thiol closest to the donor (see BPNDT Molecular Synthesis). Since only one thiol bonding group (closest to the naphthalenediimide) is exposed, the molecule will preferentially orient itself with the acceptor bound to the substrate. Again the substrate are rinsed with anhydrous toluene and then immersed in an anhydrous ethanol solution of tetra-*n*-butylammonium fluoride (TBAF) for 1 hour. This removes the protection group and exposes a thiol endgroup. Next, the substrate is rinsed in anhydrous ethanol and then immersed in a toluene solution containing 5 nm Au nanoparticles (NPs) for 30 minutes. The Au NPs are synthesized[36,93] in-house and are coated with *n*-tetraoctlyammonium bromide ligands.[23, 27] This allows the unprotected end of BPNDT to covalently bond to a NP. It is believed that the thiol-Au bond is stronger than the ligand-Au bond, and it is expected that BPNDT will displace the ligand[36] allowing the NP to become anchored to the BPNDT. To specify the concentration of the Au NP, the NP solution is added drop wise to toluene until the UVvis absorption optical density (o.d.) in a 1 cm quartz cuvette was ~0.2 at the plasmon resonance peak (approximately 0.1 mL of NP solution in 10 mL of toluene). The substrate was thoroughly rinsed one final time with anhydrous toluene, stored under N_2 for transport, and then measured immediately with an AFM. Using the AFM, contact is made to the NP with a modified conducting AFM cantilever. This entire preparation process is summarized in Fig. 2.

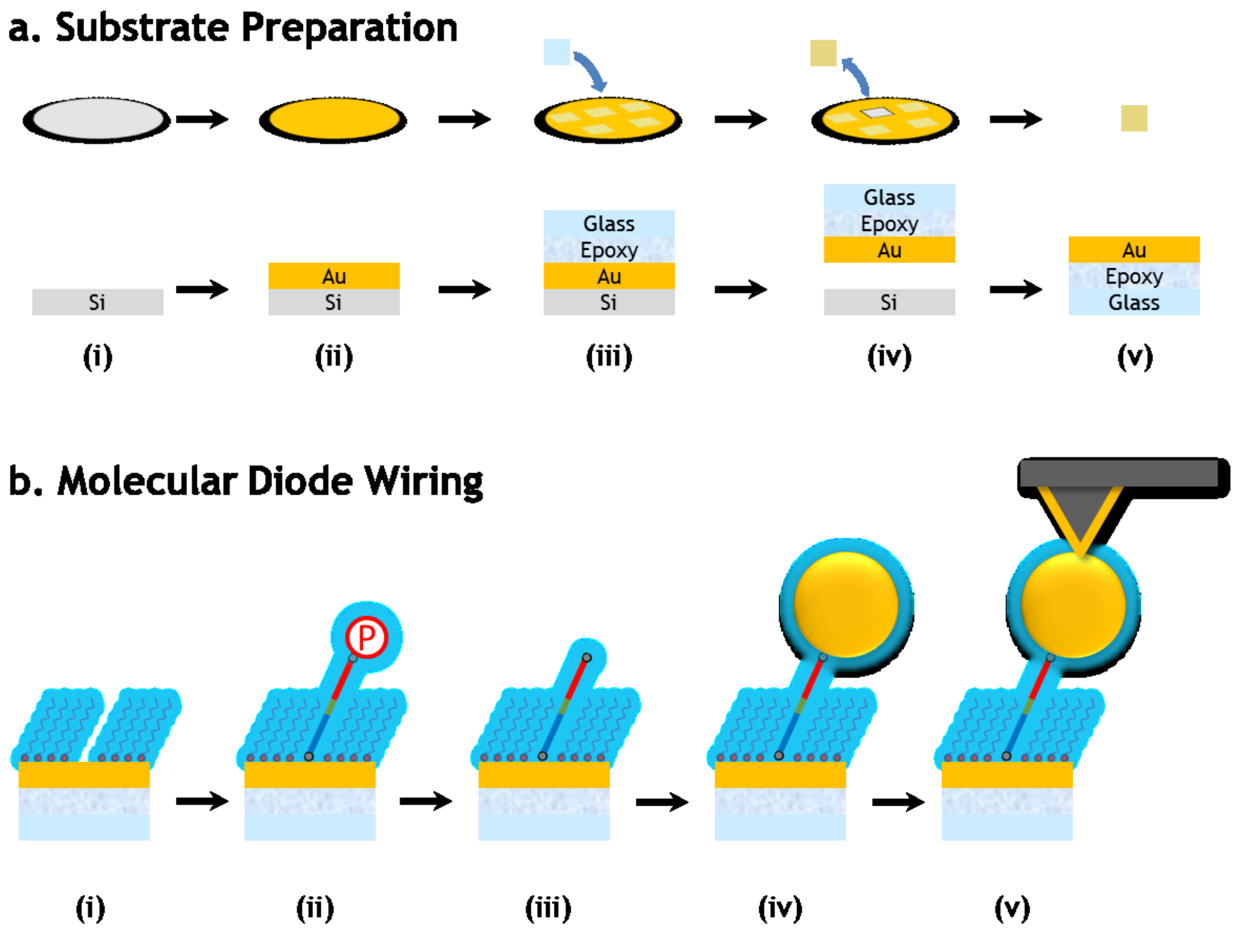

Figure 3.2 Substrate and Molecular Self-Assembly. (a) Substrate preparation: (i) a silicon wafer acts as a template where (ii) 200 nm of Au is sputtered onto the surface. (iii) Next, an epoxy coated glass microscope cover slide is placed directly onto the Au and allowed to cure. (iv) A substrate is mechanically cleaved from the silicon template exposing a (v) fresh, nearly atomically smooth, Au surface. (b) Molecule diode wiring: (i) a SAM of decanethiols form on the Au surface in a toluene solution. (ii) In another toluene solution, the donor-acceptor molecule directionally inserts into the defects of the SAM since only one bonding group is exposed. (iii) The protection group is removed in a separate toluene solution process and then the substrate is immersed in a toluene solution of Au NPs (iv) which then bind to the newly exposed binding group of the donor-acceptor molecule. (v) Finally, a Au coated AFM cantilever contacts the Au NP forming a metal-molecule-metal heterojunction.

Figure 3.3 consists of a sequence of AFM images taken after each phase of assembly described in Fig. 3.2. The SAM survives the assembly, and BPNDT molecules appear to have preferentially attached at the SAM grain boundaries, consistent with the expectation that BPNDT binds strongest to SAM defects. After removing the TMS protection group, the AFM image sharpness is reduced, attributed to free thiols interacting with the AFM tip. When exposed thiol bonding groups are not present, the NPs do not bond to the surface as shown in Fig. 3.3e. A number of 5 nm Au NPs are observed. Lateral AFM tip broadening (tip radius ~30 nm) depicts the NPs as being larger (~60 nm) than 5 nm; however, the size of the NP can be confirmed using the vertical color bar. While this self-assembly contains multiple steps, it can produce repeatable results with areal control using solution processes for longer molecules – such as BPNDT – that protrude above the host SAM and that do not naturally form an ordered monolayer.

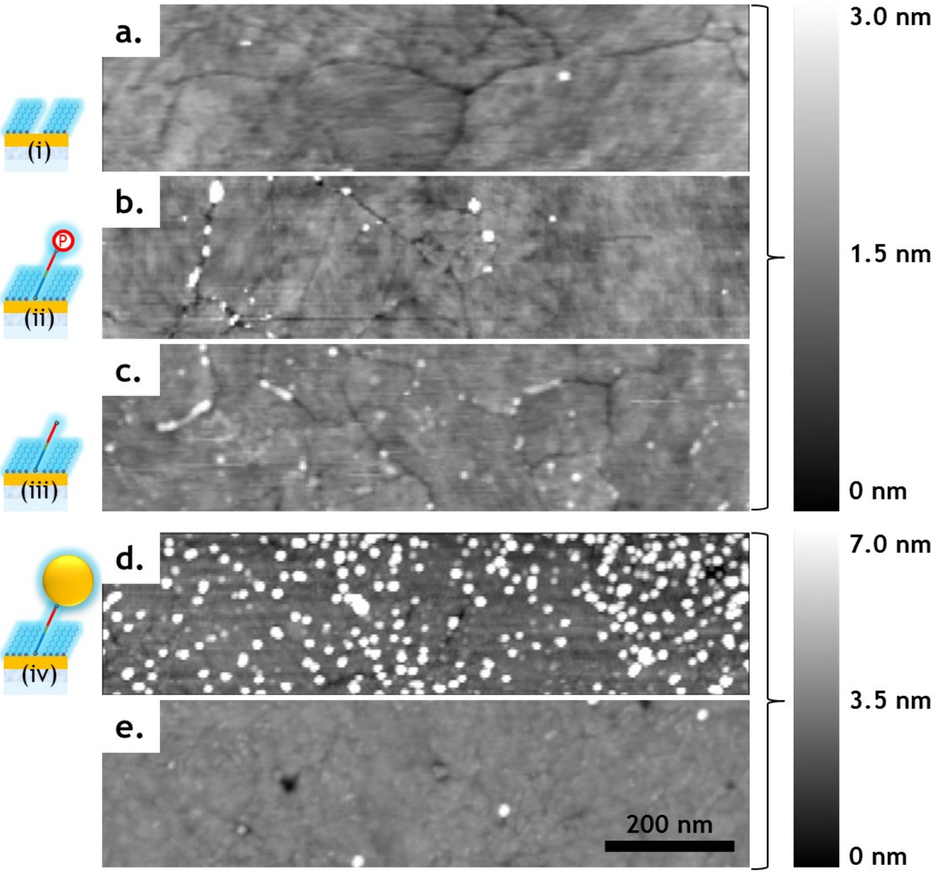

Figure 3.3 AFM images of sample surface at different stages of the molecular assembly process. Images are acquired in tapping mode (i.e., AC mode) interacting with attractive forces between the tip and the sample. The length scale bar is the same for all images but the color bar is only common to a-c and common to d-e. (a) DeT SAM on Au substrate; large grain boundaries are visible. (b) DeT SAM after allowing protected P-N molecules to bind in SAM defects. Large agglomerations appear to concentrate on grain boundaries. (c) DeT SAM and donor-acceptor molecules after protection groups are removed. Large agglomerations still appear at grain boundaries. Images tend to appear slightly less sharp and it is speculated that the exposed thiol endgroups interact more strongly with the AFM tip causing blurring. (d) NPs adhere to the surface via exposed thiol bonds even after a vigorous rinse. The AFM tip broadening artifact is observed but the color bar confirms size of NPs. (d) DeT SAM immersed in NP solution and then rinsed; Au NP do not appear to adhere to the sample because there are no exposed thiols.

When the AFM tip is in contact with the NPs, thermal drift presents a challenge in creating reproducible and controllable measurement. To overcome this, several tapping (AC) images of the NP surface are captured prior to contact. Between sequential images, a built-in image comparison program is used to analyze the images and determine the lateral drift rates. The lateral piezoactutators are then ramped to follow these drift rates. Using this drift compensation routine, NPs on the image remain fixed to within the tip radius (*i.e.*, no perceptible movement) over hour time scales at room temperature operation. Sets of five NP are visually selected for contact from these images. Automated contact to each of the NP is made with a force of 7-13 nN. Upon contact to each NP, ten trianglular current-voltage (IV) sweeps are carried out at a sweep rate of 20 kHz to minimize the capacitive (C~10 pF) hysteresis (of $I=C\ dV/dt$) between the cantilever and the substrate. The average of these ten sweeps is then taken as the IV trace for that molecular heterojunction. After completing the set, additional images of the surface are gathered to guarantee that the sample was not perturbed during contact. Sets that visually showed alternations (*e.g.*, Au flaking from the AFM tip) are excluded from analysis. In this manner, 77 junctions from three separate samples (*i.e.,* 26, 27, and 24 junctions in each sample) are analysed. Approximately 5% of junction acquired (not included in the previous tally) had traces with either (i) zero current or (ii) saturated current attributed to a situation where (i) a metal-molecule-metal junction was not formed or (ii) a short between the tip and substrate occurred due to AFM snap-in; these traces were excluded from analysis. All measured molecular junctions, however, showed the same (reverse) rectification behavior suggesting a high yield on the orientation control.

3.2.1 Mechanically Stripped Atomically Smooth Substrates

Au substrates were prepared using the template stripped gold technique[90-92] and illustrated in Fig. 3.2. First, 200 nm of Au was sputtered onto a pristine silicon wafer using an Edwards Auto 306 DC sputter coater with an Ar flow rate of 20 sccm at a power of 200 W without using an adhesion layer. Next, EPO-TEK 377 (Epoxy Technology, Inc.) is prepared following manufacturer's instructions (equal parts by mass) and a single drop is applied to a glass microscope cover slide. The cover slide is then epoxied to the Au-coated silicon wafer with care taken to prevent the glass from directly bonding to the silicon wafer. The glass-epoxy-Au-wafer sandwich is then baked at 150 ºC curing the epoxy. The sandwiches can then be stored for extended periods of time before use. When substrates are desired, a piece of tape is used to mechanically strip the substrate from the silicon template. Substrate characterization was carried out using a Molecular Imaging scanning tunneling microscope (STM) and an RMS roughness of 1.68 ± 0.18 Å over a scan size of 50 x 50 nm was measured over multiple samples. An Asylum MFP-3D atomic force microscope was also used to image the surface and Au plateaus were observed over large scan sizes (1 x 1 μm).

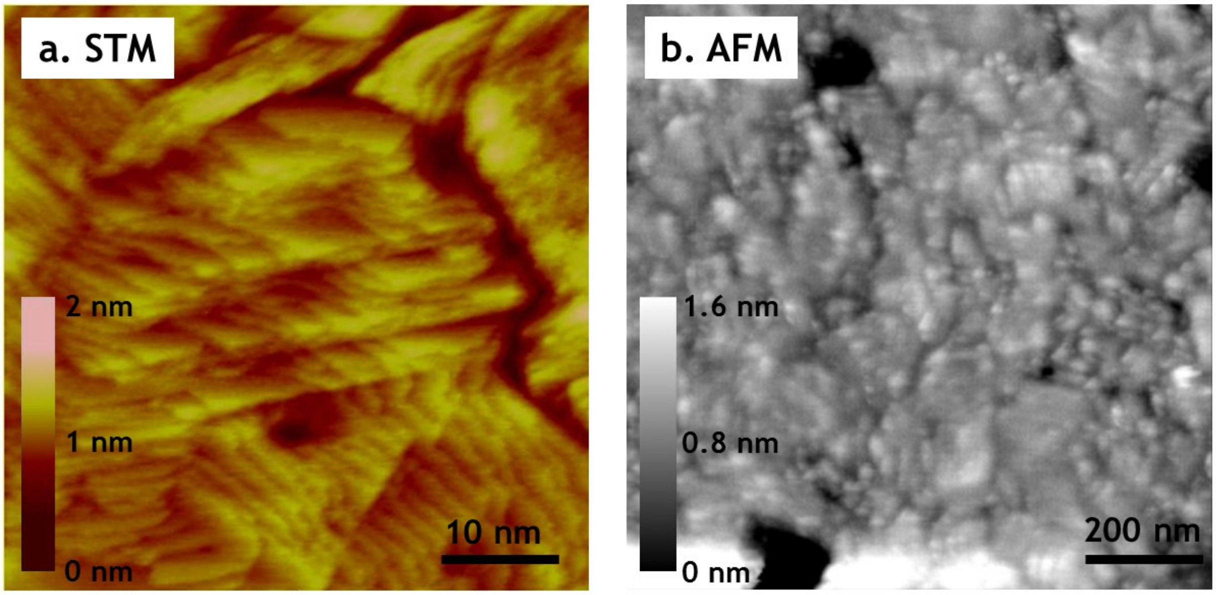

Figure 3.4 Nearly atomically smooth substrate. (a) STM image and (b) AFM image of a Au substrate with RMS roughness of 1.68 ± 0.18 Å showing Au terrace steps over a large area

3.2.2 Conducting AFM Tip Modification

The AFM tips were modified from commercially available Olympus AC240TS silicon AFM cantilevers (spring constant ~2 N/m, tip radius ~9 nm) following the procedure outlined by Morita.[36] Stiffer cantilever can be used to prevent snap-in during electrical measurements. Au and Cr where alternatively evaporated in a Veeco 401 vacuum system and thickness was controlled using a crystal monitor: (bottom, first layer) Cr 25 Å – Au 50 Å – Cr 25 Å – Au 50 Å – Cr 25 Å – Au 100 Å – Cr 25 Å – Au 300 Å (top, final layer). Scanning electron microscope (SEM) images with energy dispersive x-ray spectroscopy (EDS) confirm that Au dominates the final layer of deposition (Fig. 3.5). These cantilevers appear to be robust over hundreds of approach and withdraw sequences and Au flaking is at a minimum.

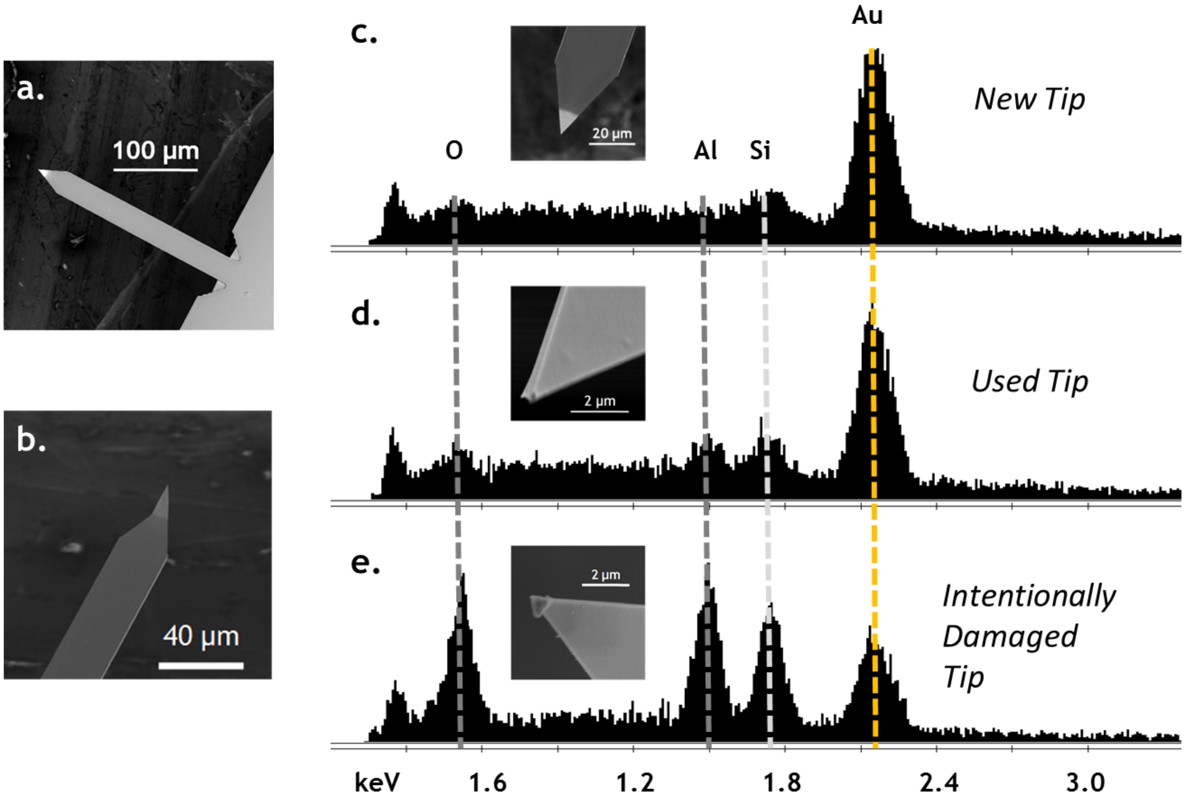

Figure 3.5 Modified AFM cantilevers. SEM images of cantilever (a) before and (b) after Au/Cr coating. SEM and EDS of cantilever tip of (c) a new tip before use, (d) a tip after use, and (e) a tip that has intentionally been damaged. The EDS spectrum of the new tip shows that Au x-rays dominate and Cr is not appreciable. Even after use, Au is still present on the tip however x-rays from the underlying silicon and the aluminum reflective (with native oxide Al_2O_3) top coat are also visible. Some contribution to the Al peak may be from the Al SEM sample holder. A separate tip was intentionally damaged by manually scoring it across the sample several times and the silicon and aluminum x-rays are more visible but some Au still remains.

3.2.3 BPNDT Molecule Synthesis

Synthesis of the BPNTD molecule was performed collaborator Dr. Jibin Sun and his procedures are reproduced in Appendix D. A summary of the synthetic procedures are shown in Fig. 3.6. This robust synthesis produces high yield, stable molecules and affords the option of chemically exchanging the different bridges and endgroups for subsequent study. In particular, three other variations were synthesized where an insulating alkane bridge and conducting phenyl endgroups were used. Herein, I only report results from our conducting-bridge insulating-endroup molecule and focus on the measurement techniques and initial findings. An alternative synthesis for the BPNDT molecule was explored but had a much smaller yield. The most beneficial trait of this synthesis is that the endgroup closest to the acceptor is exposed while the endgroup closest to the donor is protected by the TMS group; only one thiol binding group is exposed and the other binding group is protected. This allows for orientation control of the molecule. BPNDT will always bond with the acceptor closest to the substrate. After bonding to the substrate, the TMS group can then be chemically removed as discussed earlier. In this manner, I know the polarity of the diode molecule when it is bound to the electrodes.

Regarding specific details, all synthesis was performed under a nitrogen atmosphere using standard Schlenk techniques. HPLC-grade solvents were obtained from Fisher Scientific without further purification. ^{1}H and ^{13}C {^{1}H} NMR spectra were recorded at room temperature using Bruker AV-300 MHz or AVB-400 MHz NMR spectrometers. Chemical shifts were measured relative to solvent resonances. Elemental analyses were performed by the Micro-Analytical Laboratory in the College of Chemistry at the University of California, Berkeley. Matrix-Assisted Laser Desorption/Ionization (MALDI) was performed on an Applied Biosystems Voyager MALDI machine with 1,8,9-anthrathenetriol as the matrix. Cyclic voltammetry was performed on a Bioanalytical Systems CV-50W Voltammetric Analyzer with a C-3 Cell Stand. The potentials were measured *vs*. Ag/AgNO$_3$ non-aqueous reference electrodes, with glassy carbon as the working electrode and a Pt wire axial electrode in a 0.1 M tetrabutyl-ammonium-hexafluorophosphate acetonitrile solution. Ferrocene was used as the external standard (HOMO = -4.8 eV) and the potential sweep rate was 100 mV/s unless otherwise stated.

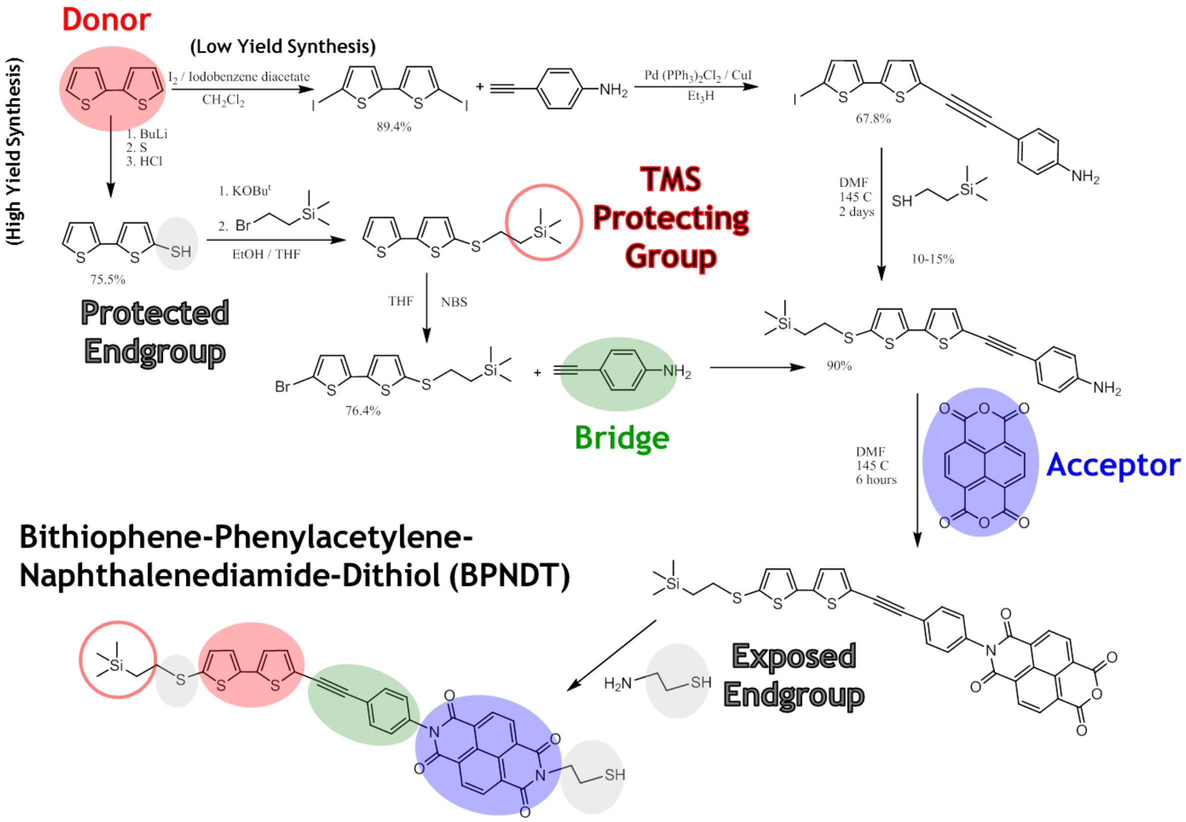

Figure 3.6 Summary of BPNDT synthesis procedures. Two synthetic routes are possible: a high yield synthesis and a low yield synthesis. Detailed description is found in Appendix D. The (p-type) donor endgroup is protected by a TMS which can later be removed after self-assembly. Different bridge, (n-type) acceptor, and endgroups can be interchanged. The resulting BPNDT molecule can only bond to the substrate via one exposed endgroup closest to the acceptor. This allows for orientation control of the diode molecule.

3.2.4 Au Nanoparticle Synthesis

Au nanoparticles were carefully synthesized following similar procedures previously reported in literature.[36,93] First an aqueous solution of $HAuCl_4$ (30 mM, 30 mL) was added to a toluene solution of *n*-tetraoctlyammonium bromide (TOAB, 50 mM, 80 mL) and vigorously stirred at room temperature with a magnetic stirrer for 10 minutes. Using a globe separation funnel, the aqueous solution was discarded and the less dense (reddish-purple) toluene solution was then rinsed three times with 100 mL of de-ionized water. Next, an aqueous solution of sodium borohydride ($NaBH_4$, 400 mM, 25 mL) was added drop-wise to the toluene solution and stirred for one hour using a magnetic stirrer at room temperature. The $NaBH_4$ serves as a reducing agent allowing TOAB ligands to coat Au NPs. After the reaction was complete, the Au-NP-toluene solution was rinsed with 100 mL of de-ionized water (3x), 0.01 M aqueous H_2SO_4 solution (1x), de-ionized water (1x), 0.05 M aqueous Na_2CO_3 solution (1x), and finally with de-ionized water (5x). The NP solution was then dried over Na_2SO_4 for 12 hours before decanting through a filter. The solution was then stored under N_2 shielded from light until use.

The size of the nanoparticles was determined using (i) high-resolution transmission electron microscope (TEM, JEOL 2100) at beam voltage of 200 kV drop cast on a carbon coated TEM grid, (ii) dynamic light scattering (DLS, Viscotek 802), and (iii) UV-vis absorption spectroscopy(Varian/Cary 50 Scan). TEM samples were prepared by depositing one drop of NP solution onto a copper grid using a 0.05 μm filtered syringe and then by allowing the solvent to evaporate. TEM image analysis (Fig. 3.7) of >200 particles suggests a mean diameter of 5.73 ± 0.82 nm. DLS and UV-vis absorption sample were prepared by adding five drops of NP solution to 5 mL of anhydrous toluene and loaded into a 1 cm cuvette for analysis. DLS suggests mean diameters of 5.64 ± 0.21 nm and 5.56 ± 0.25 nm on a number density and mass density basis, respectively. UV-vis absorption finds that the plasmon resonance peak is well defined at 525 nm further confirming the size of the nanoparticles.

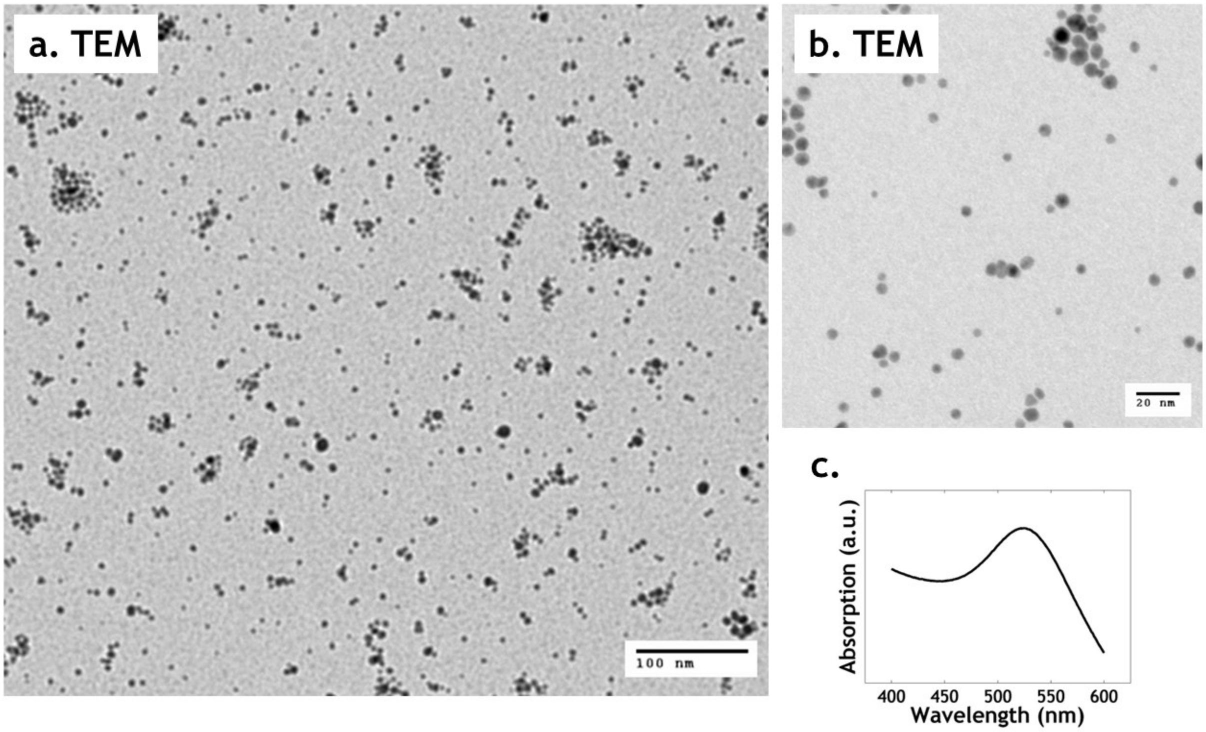

Figure 3.7 Au nanoparticles: (a) TEM image of Au nanoparticles at the 100 nm scale, (b) enlarged TEM image of Au nanoparticles at the 20 nm scale, (c) UV-vis absorption spectra of dilute Au nanoparticle solution in toluene with a plasmon resonance peak at 525 nm.

3.3 Single Diode Molecule Results and Discussion

Current-voltage (IV) characteristics obtained from a sample junction is shown in Fig. 3.8a; larger currents are seen to be present under negative bias. Since the TMS group protects the thiol bonded to the donor, the molecular orientation is controlled so that the acceptor binds to the substrate, and the NP (and tip) makes contact with the donor. This orientation control, built directly into the synthesis of the molecule, allows the unambiguous definition of *forward* bias as *positive* voltages in which the tip is biased relative to the substrate. Under forward bias, the chemical potential of the substrate is greater than that of the tip, and electrons flow from substrate to tip. Interestingly, the molecular junction exhibits higher conductance under a reverse (negative) bias, with electrons flowing opposite to the molecular dipole moment. Evidently, the electrons flow from the tip through the donor, then the acceptor, and into the substrate with a higher conductance. This behavior is opposite to that of a macroscopic p-n junctions, where more current (a larger conductance) is observed when electrons flow from the n-type semicoductor (acceptor) then through the p-type material (donor). Similar to diodes however, asymmetric IV traces with the same polarity are present in every molecular junction.

Taking the IV traces from each heterojunction, the rectifying behavior and the differential conductance (*dI/dV*) of these systems can be explored further. A rectification ratio, *RR*, is defined as the positive ratio of currents of the IV traces at various positive and negative bias voltages, *V*, as

$$RR(V) = \frac{-I(-V)}{I(V)} = \frac{-I_{reverse}}{I_{forward}} \tag{3.1}$$

The *RR* is determined for every sweep for several values of *V*, and then histogrammed which is represented by the color map in Fig. 3.8c. Since each heterojunction may be different (*e.g.*, molecular orientation, contact, *etc*.), we determine the *RR* for each heterojunction. The *RR* obtained from the average IV is nevertheless similar. The *RR* value appears to increase with increasing bias and crosses a *RR*=1 threshold around 0.6 V which is consistent with the shape of the characteristic IV trace in Fig. 3.8a. While the rectification ratio is small which suggests that this is a weak molecular diode, under biases greater than 1 V, all heterojunctions appear to have a *RR*>1. At 1 V, the average *RR* is 1.2 and appears to increase at higher biases. As defined, *RR*>1 suggests that the rectification is opposite that of semiconductor diodes based on p-n junctions, where the *RR* would be defined as the ratio of the forward to reverse bias current (which for p-n-diode would be strictly <1). This suggests that the direct analog to p-n diodes is inappropriate for these single-molecule rectifiers and another description is necessary

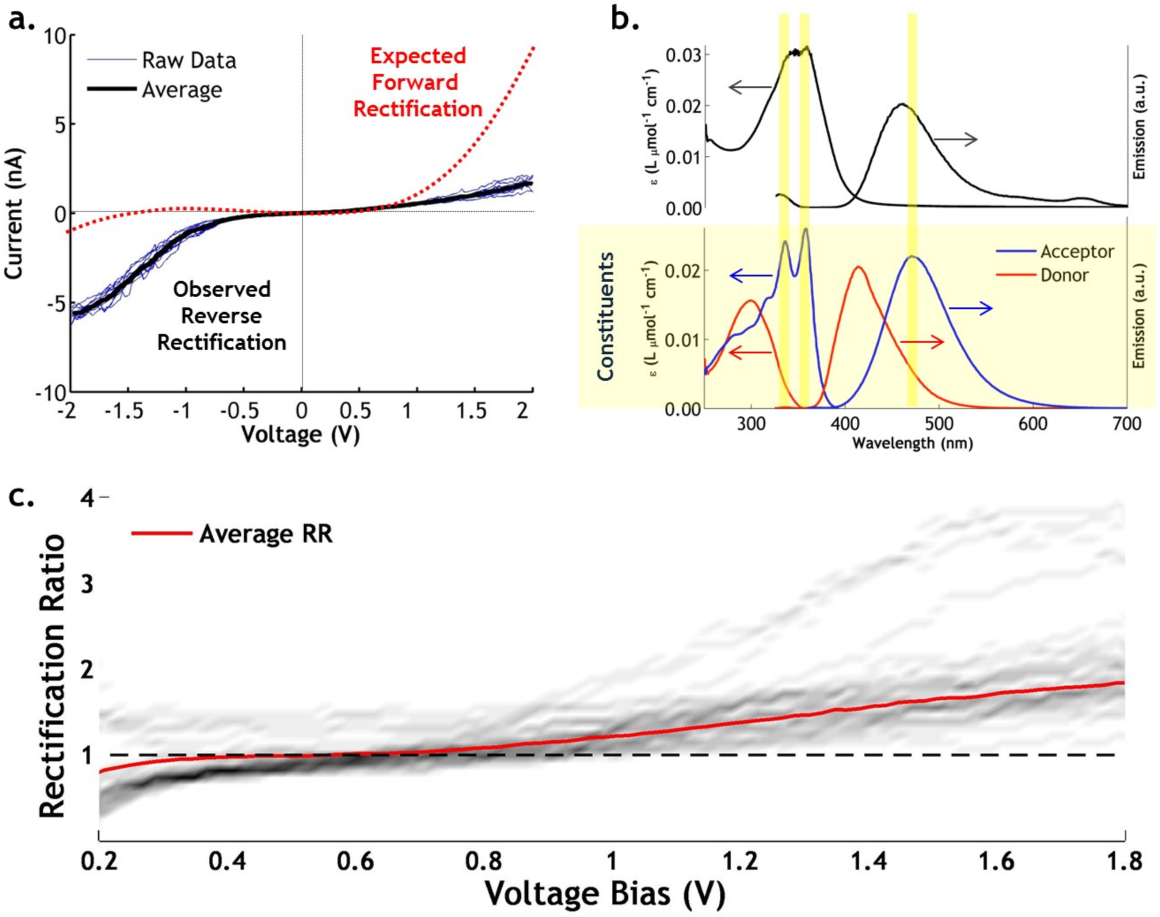

Figure 3.8 Diode molecular measurements. (a) Characteristic IV curve of a metal-molecule-metal junction showing the average IV curve over 10 traces. Asymmetry in the IV curve is visible and has reverse rectification polarity. (b) Absorption (blue) and emission (red) spectra of donor-acceptor molecule (top) and of constituent molecules (bottom) in toluene . The donor-acceptor molecule has spectral characteristics that are most similar to the acceptor constituent spectrum which exhibits two absorption peaks. (c) Average rectification ratio (red) and underlying color map depicting the rectification ratio distribution of individual junctions.

3.3.1 Density Functional Theory of BPNDT

To gain insight into the electronic structure of a junction, we examine the gas- and solution-phase spectroscopy of BPNDT using a combination of theory and experiment. Density functional theory (DFT) calculations using the Δ-self-consistent-field (Δ-SCF) method were performed by collaborators Dr. Pierre Darancet and Dr. Jeff Neaton at Lawrence Berkeley National Laboratory's Molecular Foundry to explore the spatial character of the frontier orbitals of BPNDT molecule with thiol endgroups. The Δ-SCF method expresses the ionization potential and the electronic affinity of the isolated molecule as a difference in total energies of the anion and cation with respect to the neutral species. Namely the ionization potential (IP) is the difference in energy between the neutral species and one containing one fewer electrons while electronic affinity (EA) is the difference in energy between the neutral species and once containing one more electron. Moreover, in the presence of a metallic surface, the charged excitations polarize the metallic surface, resulting in an image correction energy (IC) that scales as the inverse of distance between the orbital and the image plane of the metal. For a Au (111) surface, they calculated that the image plane lies 1 Å into vacuum with respect to the position of the Au atoms. The image correction energy then effectively reduces the HOMO-LUMO gap of a molecule. The calculation of the HOMO-LUMO gap for the isolated molecule is therefore the difference in ionization potential and electron affinity minus the image charge correction energy (*i.e.*, E_{gap}=IP-EA-IC). In this case, considering different configurations of the molecule between two electrodes separated by 30 Å, this reduction of the band gap is always less than 1.2 eV and the Δ-SCF method based on the B3LYP approximation for the exchange and correlation energy for the molecule in the gas phase gives a gap of 4.45 eV.

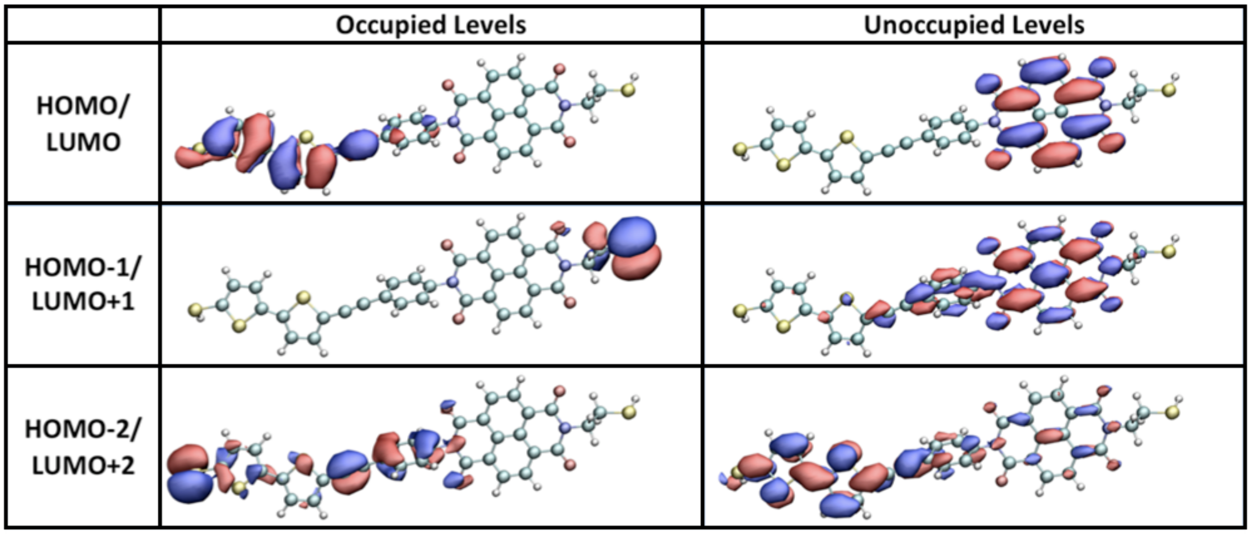

Figure 3.9 Gas phase DFT calculations depicting the localization of molecular orbitals around the bithiophene donor or naphthalene acceptor. This depiction suggests that the wavefunctions weakly overlap and that the molecule should exhibit rectifying behavior. DFT calculations and image courtesy of Dr. Pierre Darancet.

Figure 3.9 shows the last few occupied and first few unoccupied orbitals computed with method discussed above. The hybridization between the donor and acceptor moieties is quite limited. The HOMO lies principally on the donor (*i.e.*, bithiophene), with negligible weight on the acceptor (*i.e.*, naphthalenediimide), and strongly hybridizes with the thiol endgroup. Strong spatial localization on either the donor or acceptor and weak hybridization across the bridge are observed for the other frontier orbitals as well: the LUMO sits on the acceptor, and LUMO+1 sits again on the acceptor. The HOMO-1 orbital is entirely localized on the thiol endgroup on the acceptor side, and thus it in particular would not be expected to affect junction transport properties. Observing that all frontier orbitals are spatially localized to one side of the molecule lends strong support to the simplified level diagram in Fig. 3.1.

Comparisons of UV-vis spectra of BPNDT in solution (Fig. 3.8b) support a picture of weak hybridization between donor and acceptor states in these molecules. A broad peak in BPNDT's absorption spectrum is present at 3.4 ± 0.3 eV, similar to the naphthalenediimide constituent's absorption maxima at 3.3 ± 0.1 eV and 3.5 ± 0.1 eV. Emission spectra are collected upon excitation at 3.80 ± 0.02 eV and increasing the excitation frequency results in negligible change in the spectra. A single peak in the BPNDT's emission spectrum at 2.7 ± 0.3 eV closely resembles that of naphthalenediimide with a small blue shift. (The smaller peaks Fig. 3.8b at 325 nm and 650 nm are harmonics of the excitation.) The absorption peak of the donor constituent at ~4.1 eV is absent in the combined molecule, consistent with the DFT calculations which showed that the HOMO of the donor is strongly affected by the presence of the endgroup. Further, once hybridized with the phenylacetylene bridge and the thiol endgroup, and in the presence of solvent, the donor moiety absorption would be expected to red shift, resulting in an absorption peak on the donor side indistinguishable from the broad acceptor peak. Newly available "charge transfer" states, resulting from the HOMO of the donor and the LUMO of the acceptor, would be expected to appear at low energy in the absorption or emission spectra. The lack of an absorption or emission significantly red shifted suggests that such states have an extremely weak optical cross-section, resulting from a negligible overlap and a corresponding negligible dipole transition matrix. With these measurements and DFT calculations, I conclude that the phenylacetylene bridge moiety effectively decouples the donor and acceptor molecular orbitals.

Table 3.1 Δ-SCF results for the isolated fragments and the complete BPNDT molecule.

	IP (eV)	**EA** (eV)	E_{gap} (eV)
Donor Fragment[*,‡,†]	7.42	0.81	6.61
Acceptor Fragment[*,‖,†]	8.63	2.50	6.13
Complete BPNDT Molecule[†]	7.04	2.55	4.49

[*] The calculations for the fragments are performed by separating the molecule in two parts and passivating the end with hydrogen. [‡] The donor fragment consists of the thiol endgroup coupled to the bithiophene and the phenylacetylene bridge.

[‖] The acceptor fragment consists of the naphthalenediimide and a thiol endgroup.

[†] All calculations were performed using the software Qchem, with the energy of the relaxed structures given by B3LYP approximation on the exchange and correlation.

The energy gap within the molecule will determine much of its transport characteristics. The computed gas-phase energy gap, or difference between ionization potential and electron affinity –which refers to the removal or addition of an electron– is 4.49 eV for BPNDT (see Table 3.1). Computed energy gaps of the thiol-donor-bridge and acceptor-thiol moities are 6.61 eV and 6.10 eV, respectively, and imply a gas-phase level offset between the donor HOMO and acceptor HOMO of ~1.5 eV. Upon junction formation, I expect that the gap will be further reduced by static polarization from the metal electrodes.[94] Using an electrostatic "image charge" estimate and different molecule-electrode geometries, I expect the electrode polarization narrows the gap by about 0.8 eV. Furthermore, cyclic voltammetry measurements of BPNDT in solution with a Pt electrode (similar work function to Au) would place the HOMO's energy at 1.4 eV below the Fermi level. This suggest that, with the ±2 V bias window, at most one resonant level ~2 eV from the Fermi level will be observed, substantiating the hypothesis of a single transmission channel. Furthermore, if this resonant energy level is bias dependent, then the applied bias will force this resonant channel either into or away from the bias window, resulting in a rectifying behavior opposite of the expected mesoscopic behavior of a p-n junction. In this case, direct but highly asymmetric coupling between both electrodes and each the MOs is present, and rectification can be explained by a single bias-dependent frontier orbital energy level.

3.3.2 Single Diode Molecule Transport Model

Given the spectroscopy and DFT calculations above, a hypothesis of the junction electronic structure is posed in Fig. 3.1. With this junction electronic structure, a straightforward single-Lorentzian Landauer expression for the current-voltage characteristic, coupled with the DFT calculations and solution-phase spectroscopy, can explain the measured transport data. In the Landauer formalism, charge carriers tunnel coherently through the junction with an energy dependent probability given by the transmission function, τ, as discussed in Chapter 1. Neglecting inelastic scattering events, and assuming that the tunneling is fast compared with typical vibration frequencies, the current $I_{1\text{-}2}$ induced by an applied bias $V_{1\text{-}2}$ between electrode 1 and electrode 2 is given by

$$I_{1-2} = \frac{2e}{h}\int_{-\infty}^{\infty} \tau\left(E, E_n\right)\left(f_1 - f_2\right) dE, \tag{3.1}$$

where E is the energy of the electron participating in transport through a one-dimensional, single bias-dependent resonance level, E_n, and f_1 and f_2 are the equilibrium occupation probabilities of electrons in electrodes 1 and 2 (for metallic contacts these are Fermi distributions $f_i = \left(1 + e^{(E-\mu)/(k_B T_i)}\right)^{-1}$). The difference in occupation probabilities (f_1-f_2) can be approximated as a top-hat under small symmetric biases at low temperatures, yielding the approximations

$$I_{1-2} \approx \frac{2e}{h}\int_{-eV_{1/2}/2}^{eV_{1/2}/2} \tau\left(E, E_n\right) dE, \tag{3.2}$$

Considering the case of well-separated molecular energy levels, one can write the transmission function as

$$\tau = \frac{4\lambda\Gamma^2}{\left(1+\lambda\right)^2\Gamma^2 + 4\left(E - E_n\right)^2}, \tag{3.3}$$

where the coupling of the level to the closest lead is given by Γ and to the furthest lead by $\lambda\Gamma$ where by convention $\lambda<1$. Assuming that Γ and λ do not vary as a function of the bias (which is associated with the absence of variation of the wavefunctions with the bias) and performing the integration analytically, the current is given by

$$I_{1-2} = \frac{4\lambda\Gamma e}{h(1+\lambda)}\left[\arctan\left(\frac{eV_{1-2}+2E_n}{\Gamma(1+\lambda)}\right)+\arctan\left(\frac{eV_{1-2}-2E_n}{\Gamma(1+\lambda)}\right)\right]. \tag{3.4}$$

To develop a minimal physical model that explains the differential conductance and inverse rectification, first consider a linear dependence of the resonant transmission level with bias,

$$E_n = \frac{\alpha}{2}eV_{1-2} + E_0 \tag{3.5}$$

where E_0 represents the position of the molecular orbital at zero-bias, and α describes how the resonant energy level varies linearly with the bias. Here, $\alpha=\pm 1$corresponds to the level moving rigidly with the chemical potential of an electrode (Tersoff-Hamann limit) while $\alpha=0$ indicates that the energy of the molecular orbital is bias independent. Next, the differential conductance can be expressed, using the simple Lorentzian, as

$$\begin{aligned}\frac{dI_{1-2}}{dV_{1-2}} &= \frac{G_0}{2}\left[\tau\left(\frac{-eV_{1-2}}{2},E_n\right)+\tau\left(\frac{eV_{1-2}}{2},E_n\right)\right]\\ &+\frac{\alpha G_0}{2}\left[\tau\left(\frac{-eV_{1-2}}{2},E_n\right)-\tau\left(\frac{eV_{1-2}}{2},E_n\right)\right].\end{aligned} \tag{3.6}$$

where G_0 is the quantum of conductance. The first part of this equation is symmetric with respect to the sign of the bias, and therefore does not contribute to the rectification. The second part is anti-symmetric with respect to the applied bias and is non-zero only when $\alpha \neq 0$ and $E_n \neq 0$. *This simple model shows that only a bias-dependent position of the molecular orbitals results in rectification.*

Expanding Eqn. 3.6, yields

$$\begin{aligned}\frac{dI_{1-2}}{dV_{1-2}} = 2G_0\lambda\Gamma^2 &\left[\frac{1+\alpha}{\Gamma^2(1+\lambda)^2+\left((1+\alpha)eV_{1-2}+2E_0\right)^2}\right.\\ &\left.+\frac{1-\alpha}{\Gamma^2(1+\lambda)^2+\left((1-\alpha)eV_{1-2}-2E_0\right)^2}\right].\end{aligned} \tag{3.7}$$

This shows, that the height of the peak at resonance in the differential conductance can be approximated as $4\lambda G_0/(1+\lambda)^2$, which is experimentally close to 10^{-5} G_0 demonstrating that $\lambda \ll 1$ in the case of BPNDT. Using that simplification,

$$\begin{aligned}\frac{dI_{1-2}}{dV_{1-2}} \approx 2G_0\lambda\Gamma^2 &\left[\frac{1+\alpha}{\Gamma^2+\left((1+\alpha)eV_{1-2}+2E_0\right)^2}\right.\\ &\left.+\frac{1-\alpha}{\Gamma^2+\left((1-\alpha)eV_{1-2}-2E_0\right)^2}\right].\end{aligned} \tag{3.8}$$

To validate this picture, the numerical derivative of individual experimental IV data is performed to produce differential conductance traces. Histograms of these traces taken at discrete voltages are created and illustrated in a color map in Fig. 3.10. Equation 3.8 provides a good fit to the average differential conductance with the parameters: α=-0.19, λ=3.8x10^{-5}, Γ=1.31 eV and E_0=-1.9 eV. Consistent with expectations, the molecular orbital energy is below the Fermi level, indicating that the transmission is dominated by the HOMO; and the field moves the HOMO with 19% efficiency, in line with the computed dipole matrix element in the gas-phase. The ratio λ between the strongly and weakly coupled lead is $\sim 10^{-5}$, which follows from the strong spatial separation of the HOMO and LUMO computed from DFT. Thus overall, this fit is highly consistent with the DFT calculations, spectroscopy experiments, and electrochemical measurements on BPNDT.

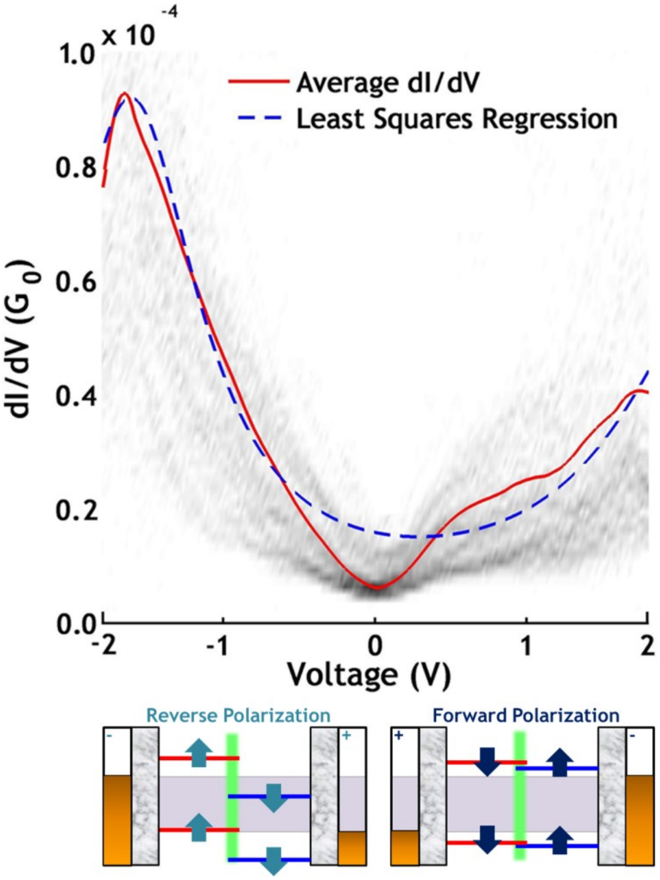

Figure 3.10 Average differential conductance *dI/dV* of the BPNDT molecule (red) and the underlying color map corresponds to histograms fit to the experimental data of the one level model (blue). Below: Schematics of the molecular orbitals under finite bias. Due to the electric field present in the junction at finite bias, the energy of the levels changes as a function of their coupling with the leads. The forward polarization tends to reduce the intramolecular dipole and pulls the levels out of the bias window (yellow dashed line). The reverse polarization increases the intramolecular dipole and pushes the orbitals inside the bias window.

Most importantly, the coherent tunneling model described above provides an explanation for the inverse rectification. From Fig. 3.1, the reverse polarization drives the HOMO of the donor towards the bias window, and the forward polarization pushes it away from the bias window, resulting in a larger current for reverse bias, as experimentally observed. The magnitude of the current is tied to the position of the resonance energy E_0 and coupling Γ; the level energy E_0 must be close enough to the chemical potential of the electrodes –and the coupling Γ must be large enough– to yield observable current. The low peak height ($<<G_0$) at resonance is rigorously connected to the small λ associated with the donor's HOMO being much more strongly coupled to the NP than to the substrate. This picture of transport suggests that rectifying behavior of BPNDT originates, in this case, with the strength and asymmetry of the orbital coupling, and the alignment of orbital energies with the junction chemical potential.

3.4 Single Diode Molecule Summary

In summary, a newly synthesized molecule constructed from a bithiophene donor, naphthalenediimide acceptor, and phenylacetylene bridge is demonstrated to operate as a bipolar molecule. *Via* a robust self-assembling CAFM technique, this molecule exhibits rectification in the reverse direction over a wide range of voltages. A simple single-level coherent tunneling model was able to explain the differential conductance and rectification. This suggests that both are highly sensitive to the position of the levels relative to the electrode chemical potential and the strength of electrode-orbital coupling and asymmetry. This work further suggests that a suite of molecules can be synthesized to further explore connections between junction electronic structure and rectification. For organic-inorganic hybrid thermoelectrics, this further illustrates the need for robust interfaces where both energy level alignment and strong, symmetrical, covalent bonds are required between the organic and inorganic components.

Chapter 4 Towards Polymer-based Thermoelectric Materials

Reproduced with permission from the Royal Society of Chemistry: Shannon K. Yee[†], Nelson E. Coates, Arun Majumdar, Jeffrey J. Urban, and Rachel A. Segalman, "Thermoelectric power factor optimization in PEDOT:PSS tellurium nanowire hybrid composites," *Physical Chemistry Chemical Physics*, **15**, 4024-4032, 2013.

&

Reproduced with permission Wiley-Blackwell: Nelson E. Coates[†], Shannon K. Yee[†], Bryan McCulloch, Kevin C. See, Arun Majumdar, Rachel A. Segalman, and Jeffrey J. Urban, "Effect of Interfacial Properties on Polymer–Nanocrystal Thermoelectric Transport," *Advanced Materials*, **25**, 1629-1633, 2013.

Through the development of single-molecule thermoelectric transport, three principles for the development of bulk polymer-based hybrid thermoelectric materials are identified. First, low thermal conductivity (<1 W/m-K) can be achieved by the use of the polymer and/or the large acoustic (phononic) mismatch between the organic and the inorganic. Second, energy alignment between the discrete molecular orbitals of the organic and the chemical potential of the inorganic manifest the unique interfacial transport phenomena identified in single-molecules heterojunction. Finally, robust covalent bonds between the organic and inorganic moieties with a large fraction of repeating interfaces allow these interfacial phenomena to be realized in bulk materials. One such bulk material was first synthesized by See *et al.*[95] and serves as a representative material for other hybrid polymer-nanoparticle composites which display many of the interfacial transport phenomena that I identified in the previous chapters.

In this chapter, the thermoelectric properties of a unique hybrid polymer-inorganic nanoparticle system consisting of tellurium nanowires (Te NWs) and a conducting polymer, poly(3,4-ethylenedioxythiophene) poly(styrenesulfonate) (PEDOT:PSS) is investigated. The vibrational modes in the Te NW and the PEDOT:PSS are largely mismatched which should facilitate a low thermal conductivity, consistent with the first principle. The work function of the inorganic (*i.e.*, ϕ_{Te}=4.95 eV) and the organic (*i.e.*, $\phi_{\mathrm{PEDOT:PSS}}$=5.10 eV) components align well, consistent with the second principle. And finally, the PEDOT:PSS is covalently bound to the surface of the NW; films consisting of these hybrid NWs allow interfacial phenomena to manifest in bulk, consistent with the third principle.

The thermoelectric properties of this material are investigated. The hybrid material has a highly conducting interface which results from the polymer becoming structurally doped at the surface of the NW (see Fig. 4.1). The thermoelectric properties of this material can then be optimized by both controlling the shape of the NW and the loading and doping of the polymer with polar solvents. This optimization results in considerable improvement in the power factor ($S^2\sigma$) above the first published results of this material.[95] The mechanism for the improvement in power factor is attributed to the unique conducting nature of PEDOT:PSS, which exhibits a transition from a hopping transport-dominated regime to a carrier scattering-dominated regime upon doping with polar solvents. Near this transition, the electrical conductivity can be improved without significantly reducing the thermopower. Relying on this principle, the power factor optimization for this new thermoelectric material is experimentally carried out and found to exceed 100 μW/m-K^2, which is nearly five orders of magnitude greater than pure PEDOT:PSS.

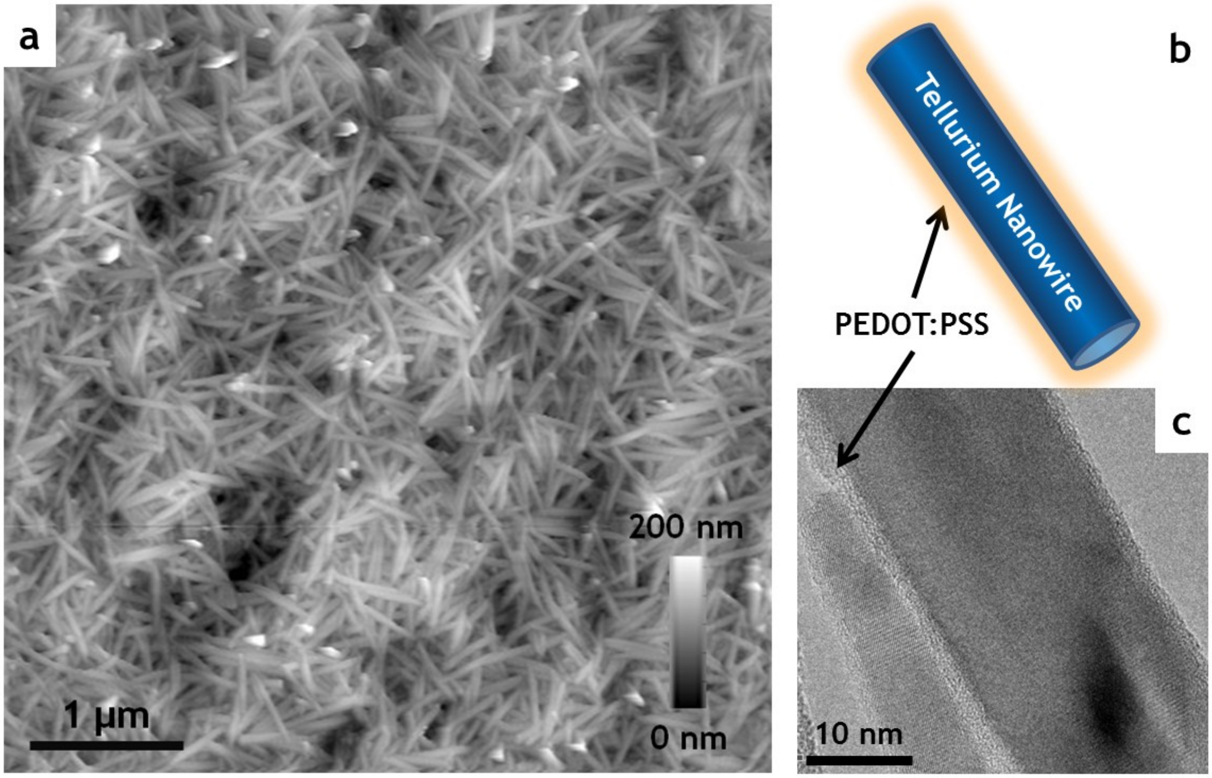

Figure 4.1 Hybrid Te-PEDOT:PSS NW Material. (a) AFM image of a PEDOT:PSS coated Te NW film. (b) Cartoon of a crystalline Te NW coated in the polymer PEDOT:PSS. (c) TEM image of a single Te NW.

4.1 Polymer-based Thermoelectric Motivation

In the last decade and a half, thermoelectric material improvements have largely been realized by diminishing thermal conductivities via nanostructuring without sacrificing electrical performance.[8] An alternative approach would be to start with a material that has an inherently low thermal conductivity, such as a polymer, and find ways of increasing its power factor. However, polymer materials tend to exhibit either hopping-like or band-like transport discussed in Chapter 1. In either of these types of transport S and σ are anti-correlated; ways of increasing σ result in a decrease in S. As a result, even for pure polymer are constrained by the decoupling challenge of thermoelectrics. Table 4.1 illustrates two classes of polymers: (i) common low σ high S polymers and (ii) common high σ low S polymers. From these examples, even though the thermal conductivity is low, it is clear that the power factor is not large enough. As a comparison, the most common commercially available thermoelectric material is doped Bi_2Te_3, which has a power factor of ~4500 µW/m-K^2 and a thermal conductivity of ~1.4 W/m-K yielding. While polymers have a thermal conductivity near ~0.3 W/m-K, their power factors are >2 orders of magnitude smaller than Bi_2Te_3.

Table 4.1 A few illustrative polymer thermoelectric properties.[96]

	σ (S/cm)	S (µV/K)	$S^2\sigma$ (µW/m-K^2)	
Polycarbazolenevinylene	5×10^{-3}	230	0.02	**Low σ, High S**
Doped Polyalkylthiophene	1×10^{-3}	200	0.04	
Doped Polyaniline	92	9	0.75	**High σ, Low S**
Doped Polythiophene	100	21	4.41	

Is there a way to decouple S and σ in polymers and allow for simultaneous improvements? Examples exist where the anti-correlation between S and σ can be broken. One of those examples is a metal-molecule-metal heterojunction[43,44,88] discussed in previous chapters. Another concept to improve the power factor that relies on energy alignment is the use of energy filtering.[20-24] In energy filtering, energy dependent scattering (*i.e.,* $t_s=t_s(E)$) is employed, and charge carriers are selectively scattered at interfaces, modestly reducing the electrical conductivity but greatly improving the thermopower. This increase in thermopower is caused by an increase in asymmetry in the distribution of mobile charge carriers, which in turn results from the asymmetry of the energy dependent scattering time about the chemical potential (*i.e.,* $t_s(E)(E-\mu)$ is not symmetric about μ). Because the power factor scales as S^2, this trade-off results in a net increase in the power factor.

Beyond energy dependent scattering, weakly or non-energy dependent scattering mechanisms (*e.g.*, boundary, void, electron-phonon, and impurity scattering) still reduce the electrical conductivity, but they have little impact on the thermopower. To demonstrate this, the scattering mechanism can be separated into terms that are energy dependent, $t(E)$, and terms that are not energy dependent. These non-energy dependent scattering mechanisms may be functions of some characteristic scattering length, L (such as in boundary, interface, or void scattering), or they may be functions of temperature (such as in phonon-electron scattering), and are written as $t(L,T)$. If the scattering times of the energy dependent mechanisms are much longer than those of the non-energy dependent scattering then, by application of Matthiessen's rule, the following approximation can be made:

$$\frac{1}{t_s}=\frac{1}{t(E)}+\frac{1}{t(L,T)}\approx\frac{1}{t(L,T)} \tag{4.1}$$

Applying this approximation to the electrical conductivity and thermopower for band-like transport yields:

$$\sigma_{\mathrm{B}}=-\frac{e^2}{3}t(L,T)\int v^2\frac{\partial f_0}{\partial E}g\,dE \tag{4.2}$$

$$S_{\mathrm{B}}=\frac{-1}{eT}\frac{\int(E-\mu)v^2\frac{\partial f_0}{\partial E}g\,dE}{\int v^2\frac{\partial f_0}{\partial E}g\,dE} \tag{4.3}$$

where the scattering time only reduces the electrical conductivity and not the thermopower.

For hopping transport, a similar behavior is observed as the scattering effects are only captured in the σ_0 prefactor appearing in Eqn. 1.3 and not in Eqn. 1.4. Therefore, when non-energy dependent scattering dominates in either transport regime, the electrical conductivity is reduced while the thermopower remains largely unaffected. Similarly, if non-energy dependent scattering is reduced, then the conductivity will increase while the thermopower remains largely unaffected, resulting in an increase in the power factor.

One material system that may demonstrate some of these transport phenomena is the Te NWs coated in PEDOT:PSS. It has previously been shown[97] that this material (i) has an electrical conductivity higher than either constituent component, (ii) maintains a high thermopower, and (iii) retains the low thermal conductivity properties of the host polymer. Furthermore, the conductivity of PEDOT:PSS has been shown to increase by nearly four orders of magnitude with the addition of a small volume fraction (5 vol%) of polar solvents, such as ethylene glycol (EG) or dimethylsulfoxide (DMSO). Though the mechanism of this improvement (true electrical doping or a morphological effect) is still under debate,[98-106] the use of polar solvents to enhance conductivity has already been adopted for application.[107,108] Regarding the mechanism, one leading theory suggests that the solvent induces a structural change in the PEDOT and causes an elongation of individual polymer chains (sometimes referred to as extended or linear coils), as demonstrated in both solution[98] and in solid state.[101,103] These extended chains are thought to have higher conductivity because charge carriers travel further along the backbone of the polymer before encountering a scattering site (*e.g.*, a kink in the polymer chain). One alternative theory is that the PEDOT and PSS can phase segregate producing larger, more conducting PEDOT domains absent of the insulating PSS phase.[104,109] Another alternative theory is that the polar solvents behave like chemical dopants and increase the number of charges carried along the backbone of the polymer.[103,106] Regardless of mechanism, the improved conductivity suggests PEDOT:PSS as an attractive thermoelectric material due to its potential low cost and processability with a power factor exceeding 10 μW/m-K^2.[110-115]

Herein, the effects on conductivity and thermopower associated with (i) the Te NW morphology, (ii) the use of EG and DMSO to improve the performance of the PEDOT:PSS, and (iii) the tunability with the amount of polymer in the composite are investigated. The standard synthesis procedures are modified to realize better performance in combination with the addition of EG and DMSO. This variation yields a natural systematic optimization in power factor. Finally, understanding this optimization facilitates an explanation for the unexpected large thermopower and electrical conductivity present in this material and other interfacial hybrid composite materials.

4.2 Hybrid Te-PEDOT:PSS Nanowire Investigation Methodology

Hybrid Te-PEDOT:PSS nanowires were synthesized based on the procedures previously described[97] with a few variations. The two primary variations in the standard synthesis are (i) to control the amount of PEDOT:PSS used during synthesis and (ii) to add additional PEDOT:PSS after synthesis. Since the PEDOT:PSS coats the NWs it acts as a surfactant/ligand or structure directing agent. Similar to colloidal nanoparticle synthesis, having a high concentration of ligand results in smaller nanoparticles. Therefore, starting will with a high concentration of PEDOT:PSS should yield smaller NWs. Also, since it is presumed that the effect is an interfacial effect, dispersing the NWs by backfilling with additional polymer should demonstrate the degree of contribution from the interface. In other words, if the NWs are close together (*i.e.*, high NW volume density) the interfacial effect should be more pronounced than if the NWs are further dispersed (*i.e.*, low NW volume density). In this manner the composition (*i.e.*, polymer or Te NW weight fraction), should be a measure for the interfacial transport contribution.

4.2.1 Synthesis of Hybrid Te-PEDOT:PSS NWs

As summarized in Fig. 4.2, 1 g of L-ascorbic acid (Sigma Aldrich, reagent grade) was dissolved in 45 mL of 20 MΩ Millipore water in a 100 mL round bottom flask. A 1” Teflon coated magnetic stir bar was used to stir the solution until the acid was fully dissolved. Next, a commercially available solution of PEDOT:PSS (Clevios™ PH1000) was filtered through a 0.45 µm pore size PVDF syringe filter. Various amounts of PEDOT:PSS solution were added to the flask to achieve specified NW lengths: (i) for short wires (lengths nominally 300 ± 50 nm), 4 mL of the PEDOT:PSS solution was used, (ii) for medium wires (lengths nominally 450 ± 100 nm), 2 mL of the PEDOT:PSS solution was used, (iii) and for long wires (lengths nominally 900 ± 100 nm), 1 mL of the PEDOT:PSS solution was used. The resulting solution was dark blue. Next, 70 mg of sodium tellurite (Na_2TeO_3, 99%, Sigma Aldrich) was added to the solution. This resulting milky-white bluish solution was then stirred continually as the flask was heated to 90 ºC for 19 hours then allowed to naturally cool while stirring. The sensitivity of the reaction time was investigated by prematurely truncating the reaction at different times (*e.g.*, 1 hour, 3 hours, 6 hours, and 12 hours). After 3 hours, the NWs had reached their terminal length as observed by AFM and SEM; after 6 hours, little batch-to-batch variation in the measured electrical properties was observed. Regardless, a 19 hour reaction time was used for consistency to the previously published synthesis.

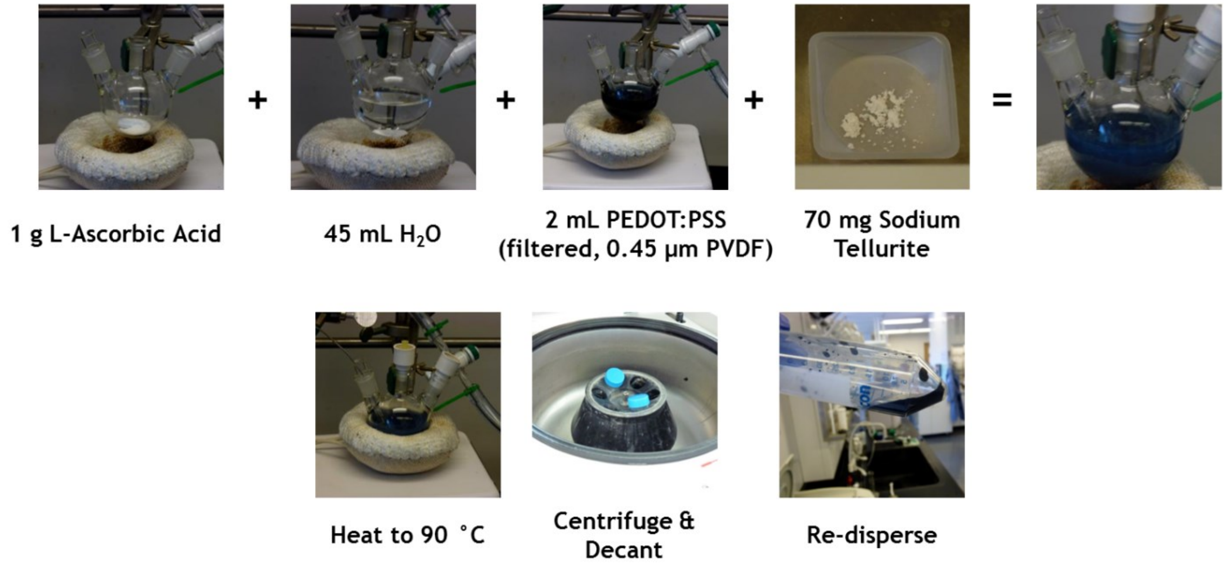

Figure 4.2 Schematic summary of synthesis procedures. Simple one-pot synthesis of the Te NW hybrid material requires modest heating. Centrifuging the resultant mixture separates the Te NWs from excess water and PEDOT:PSS.

After cooling, the terminal solution was transferred to two 1" centrifuge tubes (~25 mL in each) and centrifuged at 9000 rpm for 20 minutes. After centrifuging, the bluish-black supernatant was gently decanted, leaving a dark blue puck. The puck was re-dispersed in ~25 mL of 20 MΩ Millipore water, agitated with a vortexer, and centrifuged again at 9000 rpm for 20 minutes. The light bluish supernatant was then discarded. This puck was then re-dispersed in ~3 mL of 20 MΩ Millipore water and agitated with a vortexer, yielding the final product.

4.2.1.1 Structural Doping with DMSO or EG and Composition Control

To improve the conductivity of the PEDOT:PSS, DMSO (99.9% Sigma Aldrich) or EG (99.9% Sigma Aldrich) was added to the solution either (i) pre-synthesis or (ii) post-synthesis. In this manner, the pre-synthesis addition and the post-synthesis addition could be directly compared to each other and to the larger body of PEDOT:PSS literature. Note the same bottle of PEDOT:PSS solution was used for all samples in this study.

In the pre-synthesis addition, 5 vol% EG or DMSO was added to the PEDOT:PSS solution before the PEDOT:PSS solution was added to the reaction flask. This value was selected based on PEDOT:PSS concentration optimizations previously reported in literature.[107,108] In detail, the PEDOT:PSS (Clevios ™ PH1000) solution contained 0.65 wt% solid post-filtering (or 99.35 wt% water) as determined by thermogravimetric analysis (TGA); see Fig. . This is in agreement with the vendor's claim that the dissolved solids are between 0.45 and 1.5 wt%. So in the pre-synthesis case, 5 mL of DMSO was added to 100 mL of PH1000 solution yielding a 5 vol% DMSO addition. Given that the specific density of the PH1000 solution is nearly 1 g/cm^3, this is 5 mL of DMSO to every 0.65 g of PEDOT:PSS.

In the post-synthesis cases, EG or DMSO was added after the final solution was prepared. Amounts of EG or DMSO were normalized to the amount (mass) of polymer present. In the post-synthesis case, the amount of PEDOT:PSS in the resulting dry hybrid material was also determined again by TGA where the amount of PEDOT:PSS was taken as the amount that decomposes at low temperature (100 $^\circ$C < T < 350 $^\circ$C) and the amount of Te was taken as the amount that decomposes at high temperatures (T > 350 ºC). See sample TGA in Fig. 4.3. So for normalization, an equivalent amount of DMSO was used to match the pre-synthesis cases. For example, if the resulting dry hybrid material contained 0.01 g of PEDOT:PSS in 3 mL of product, then (0.01/0.65)*(5 mL) = 76.9 µL of DMSO would be added to the 3 mL of product yielding the equivalent of 5 vol% DMSO addition of the pre-synthesis case.

Furthermore, the composition of the resulting material can be controlled by backfilling with additional PEDOT:PSS (either un-doped PEDOT:PSS or PEDOT:PSS that has been augmented with DMSO or EG) post-synthesis. The compositional control is achieved by measuring the Te weight fraction in the synthesized hybrid Te-PEDOT:PSS NWs, ϕ_0, the weight fraction of PEDOT:PSS in the PH1000 solution, α_0, and the solid content of the hybrid Te-PEDOT:PSS NW solution, C_0. Using these parameters, a simple algebraic relation can determine the amount of PEDOT:PSS solution, $(\rho V)_{PEDOT:PSS}$, that should be added to the initial amount of the hybrid NW solution, $(\rho V)_{Hybrid}$, to achieve a desired dry polymer weight fraction, ϕ:

$$(\rho V)_{PEDOT:PSS} = \frac{C_0}{\alpha_0}\left(\frac{\phi-\phi_0}{1-\phi}\right)(\rho V)_{Hybrid}. \tag{4.4}$$

After making solutions with various predicted polymer weight fractions, the actual weight fraction was measured with the TGA for verification and found to agree well (<2 wt%) with this algebraic relation.

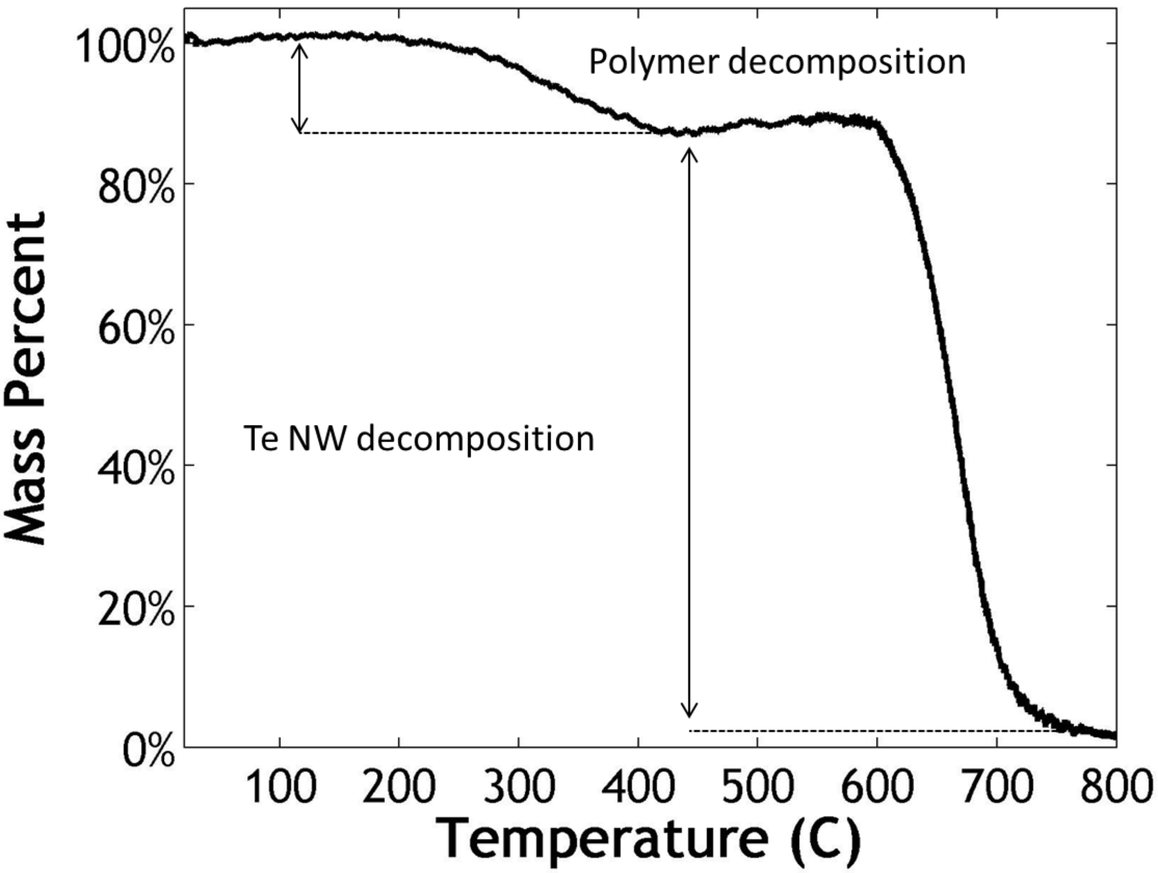

Figure 4.3 Example TGA of the TeNW hybrid material. The material was dried thoroughly before the TGA so there was no appreciable mass loss before 100℃. Boiling point of Te is ~980℃ which exceeds the temperature range of the TGA. A slow temperature ramp rate (~1 degrees C/min) was used to facilitate evaporation of Te.

4.2.1.2 Control Samples

A neat PEDOT:PSS solution was prepared as a control by filtering the PH1000 solution. Highly conducting polymer solutions were prepared by adding 5 vol% EG or DMSO to the filtered polymer solution. Analogously, control Te NWs were prepared following the same hybrid material synthesis above with the omission of PEDOT:PSS. Before heating, this solution was a milky-white color and at ~85 ºC, the solution turned to a dark-grey. SEM images of the dried material revealed NWs that likely have a thin coat of ascorbic acid ligands, as seen in other nanoparticle syntheses.[116] The control Te NWs may oxidize over time; however, it is not of central concern for the basis of the control comparison in this body of work.

4.2.1.3 Thin Films Casting

Thin films of these materials were cast on 1 cm x 1 cm, R-plane sapphire substrates. Substrates were pre-cleaned by sequential sonication in acetone, chloroform, and isopropyl alcohol each for 3 minutes. The substrates were then dried under nitrogen and cleaned with O_2-plasma (Harrick Plasma Cleaner PDC-32G) for 5 minutes to improve wettability. The substrates were then placed on a shiny aluminum block and 50-100 µL of solution were drop cast onto each substrate; the amount of solution was varied in order to obtain a nominal thickness of ~2.5 µm for the various concentrations of solution. A heat lamp was then used to heat the liquid and facilitate slow evaporation. Resultant films were shiny and reflective after drying. The substrates were then transferred to a hot plate where they were annealed at 140 ºC for 5 minutes.

4.2.2 Transport Measurements

The in-plane electrical conductivity (via the Van der Pauw technique), the in-plane thermopower (via the suspended Seebeck technique), and the through-plane thermal conductivity (via the 3-omega technique) were performed on the same sample as illustrated sequentially in in Fig. 4.4 a-c.

4.2.2.1 Thin Film Electrical Conductivity Measurements

Four Au electrical measurement contacts pads (~150 nm thick) were then deposited near the corners using a shadow mask in a thermal evaporator. To eliminate any edge-bead effects, a scribe and template were used to isolate the edges of the film (~1 mm around the entire substrate) from the uniformly flat center. Thickness of each film was then measured using a profilometer (Dektack 150) across the entire breadth of the film where the edge-scribed trenches served as the reference. Several identical samples from the same solution (and several identical solutions) were prepared to capture sample-to-sample (and synthesis-to-synthesis) variations of this material. Therefore, unless otherwise stated, the error bars in the transport measurements represent the sample-to-sample variation (not the measurement uncertainty, which is always much smaller).

Micromanipulators with tungsten tips were used to make electrical contact to the Au contacts pads. Ohmic behavior was always observed, and contact resistance was negligible compared to film resistance. In-plane electrical conductivity was acquired using the four-point van der Pauw technique. The substrates were placed on a temperature-controlled Peltier stage using thermal grease to ensure good thermal contact. The samples were then heated and cooled to reproducibly acquire the temperature dependent electrical conductivity; temperatures always remained well below the annealing temperature, which is also well below the degradation temperature (180 ºC in atmosphere).

4.2.2.2 Thin Film Seebeck Measurements

The thermopower was measured by suspending the substrate between two temperature-controlled Peltier stages (separated ~3 mm) and applying a small temperature difference between the stages ($\Delta T < 10$ºC). These temperature-controlled stages can be independently heated or cooled, thus facilitating temperature dependent thermopower measurements. Again, thermal grease was used to ensure good thermal contact. The thermal conductivity of sapphire is sufficiently low (and the substrates are sufficiently thin) that there was minimal thermal shunting between the stages, permitting a temperature difference across the film. The thermoelectric voltage was measured between two Au contact pads on separate stages using micromanipulators and tungsten probe tips. The temperature of each pad was measured with a (k-type) thermocouple in close proximity to the probe tip. A small amount of thermal grease was applied to the thermocouple tips to insure that good thermal contact was made; there was no evidence that this grease influences the electrical measurements. The thermoelectric voltage versus temperature difference was always linear, yielding a positive thermopower (*e.g.*, $S = -\Delta V/\Delta T$) for all (p-type) samples. An evaporated (99.99% pure) nickel film (100 nm thick) was used to verify this technique, and it had a measured thermopower of -11.2 μV/K, which is in good agreement with the accepted values of -11.5 μV/K at room temperature for nickel films.[117]

4.2.2.3 Thin Film Thermal Conductivity Measurements

Through-plane thermal conductivity was measured using the differential 3-omega technique. For the through-plane 3-omega measurements, a 100 nm insulating layer of electrically insulating Parylene-N was deposited atop the films, followed by fabrication of the 3-omega heater lines via thermal evaporation of Au through a shadow mask. Heater lines were 2 mm long, 80 µm wide, and 60 nm thick. Thermal epoxy (Epoxy Technologies) was used to mount the substrates to a heat sink and Au wires were silver-epoxy-bonded to the contact pads of the heater lines. For the differential 3-omega technique a bare quartz substrate was prepared with Parylene-N alongside each sample. The reference contribution to the thermal signal, which gives the thermal conductivity of the pure Parylene-N film, was subtracted. Heating frequencies ranged between 100 Hz and 5 kHz.

In-plane thermal conductivity measurements of these films were attempted, but have not been successful. The self-heating suspended films technique was not successful because the thin-films are not sufficiently mechanically robust, and the variable heater line width method was not successful as lithographic developing liquids cause the films to swell, which prevents fabrication of the necessary narrow heater lines.

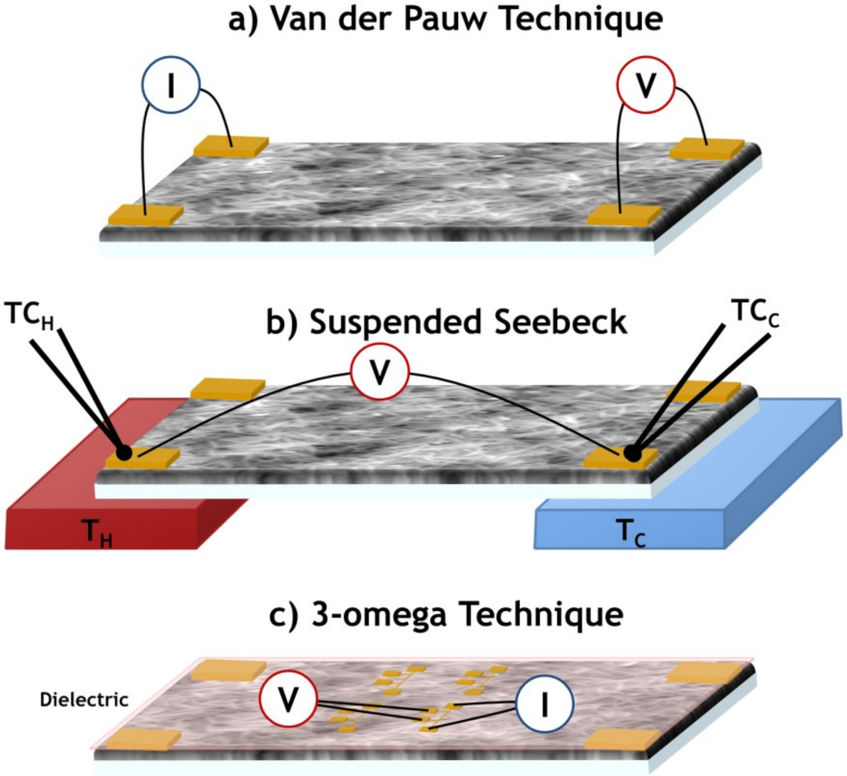

Figure 4.4 Thin Film Measurement Setup. (a) The Van der Pauw Technique is used to measure the in-plane electrical conductivity by sourcing a current and measuring a voltage in adjacent contact pads. All eight permutations are measured, and appropriately averaged, before solving the Van der Pauw equation for the sheet resistance. (b) In-plane thermopower measurements were performed using the suspended Seebeck technique. Two thermalcouples in close proximity to the voltage probes measure the local temperature. Temperature controlled stages apply a small (<7 K) temperature difference. (c) Through-plane thermal conductivity measurements are performed using the 3-omega technique where current is sourced at a frequency ω and the thermal voltage response at 3ω is measured with a lock-in amplifier.

4.2.2.4 Anisotropy and NW Alignment

Measurements of the electrical conductivity and thermopower were performed in-plane and measurements of the thermal conductivity were performed through-plane. Given that these properties are measured in different direction, there may be a degree of anisotropy. However, other work, involving the thermoelectric performance of PEDOT:PSS investigated the difference in in-plane and through plane-thermal conductivity and noted at most an 11% variation.[118] With the numerous interfaces inside the NW film, I expect more phonon scattering than the pure PEDOT:PSS. Regardless, the mean free path is still likely to remain much smaller than the film thickness (*i.e.*, not attributed to 2D confinement), but rather anisotropy can come from NW alignment.

Glancing incidence small angle x-ray scattering (GISAX) can quantify the degree of alignment. However, due to the spread in NW length (*i.e.*, 10%-20%), the scattering form-factor uncertainty is larger than the apparent shift in the scattering pattern due to alignment allowing for only a qualitative measure of the NW alignment. If the NWs were vertically aligned, the scattering pattern would have high intensity along the horizontal (q_{xy}) direction. If the NWs were horizontally aligned, the scattering pattern would have a high intensity along the vertical (q_z) direction. As shown in Fig. 4.5, the NWs appear only slightly aligned parallel with the substrate, but the circular profile indicates that they are mostly randomly oriented, especially for higher weight fractions of Te. It is possible that the film thickness is biasing the NWs to lie parallel to the substrate; if the film thickness is comparable to (or smaller than) the nanowire length, then the nanowires may lie parallel to the substrate. However, no trend in thickness with through-plane thermal conductivity is observed over this range when thickness was comparable to the nanowire length. Measurement of in-plane thermal conductivity by varying the 3-omega heater line width were attempted but the lithographic techniques to pattern various heater line are not chemically compatible with PEDOT:PSS.

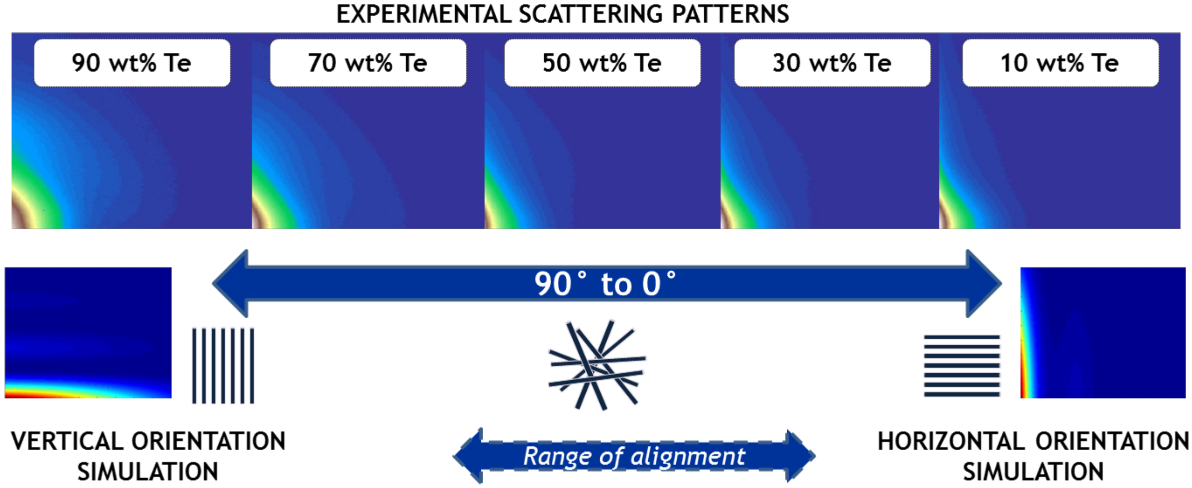

Figure 4.5 NW Alignment. Glancing incident x-ray scattering patterns for various polymer loading qualitatively suggest that NWs are slightly aligned parallel to the substrate.

4.3 Hybrid Te-PEDOT:PSS Nanowire Investigation Results and Discussion

As previously reported,[97] films of Te NWs coated in PEDOT:PSS (i) exhibit an electrical conductivity higher than either constituent component, (ii) maintain a high thermopower, and (iii) retain the low thermal conductivity of the host polymer. This combination of attributes makes this material an excellent thermoelectric candidate. However, until now, an understanding of the mechanism and a demonstration of the tunability and optimization of the transport properties had yet to be realized. In this discussion, I report the results of controlling (i) NW morphology, (ii) polymer structural doping, and (iii) polymer loading of this hybrid composite. Finally, I demonstrate how the transport properties of this material can be uniquely tuned and optimized.

4.3.1 PEDOT:PSS and Te NW Control Sample Results

To understand transport in this hybrid composite, it is first useful to understand the transport characteristics in the individual components. To that end, I investigated both control films of the pure polymer and of (uncoated) Te NWs, as described in the methodology section. The temperature-dependent thermopower and electrical conductivity of the PEDOT:PSS variants and the properties for the control Te NWs can be found in Fig. 4.6. For the control Te NWs, the thermopower was high (~400 μV/K) and relatively constant throughout the temperature range of interest; the electrical conductivity, however, was low: ~0.1 S/cm at room temperature and increases to ~0.2 S/cm at 80 ºC, consistent with the semi-metallic nature of Te having thermally activated conductivity. The morphology of these ascorbic acid coated NWs is very similar to the hybrid NWs, as illustrated in Fig. 4.7a. The conductivity of the pure PEDOT:PSS is low (~1 S/cm) and is insensitive to the addition of ascorbic acid (a reagent in the subsequent synthesis of the Te NWs). The conductivity increases with temperature (see Fig. 4.6), in agreement with hopping transport for polymers and is described well by Eqn. 1.3 with a negative temperature coefficient of resistance, TCR, (*i.e.*, positive slope in σ *vs*. T). With the addition of 5 vol% EG or DMSO, the conductivity increases by nearly four orders of magnitude and then exhibits a positive TCR (*i.e.*, negative slope in σ *vs*. T), as expected. This later, metallic-like behavior in PEDOT:PSS is not solely described by hopping transport but, like in metals, the decrease in electrical conductivity is attributed to increased carrier scattering. While the Debye temperature of PEDOT:PSS has not been measured or assigned to our knowledge, it is likely to be much lower than 0 ºC. (The Debye temperature is proportional to the speed of sound. The speed of sound for polymers is >5x smaller than most metals. The Debye temperature in metals is ~10^2 K, therefore, it is likely that the Debye temperature for PEDOT:PSS is smaller than 0 ºC.) Given that the degradation temperature is ~180 ºC (open to atmosphere), we believe it is justified to assign electron-phonon scattering as the dominant scattering mechanism near room temperature.

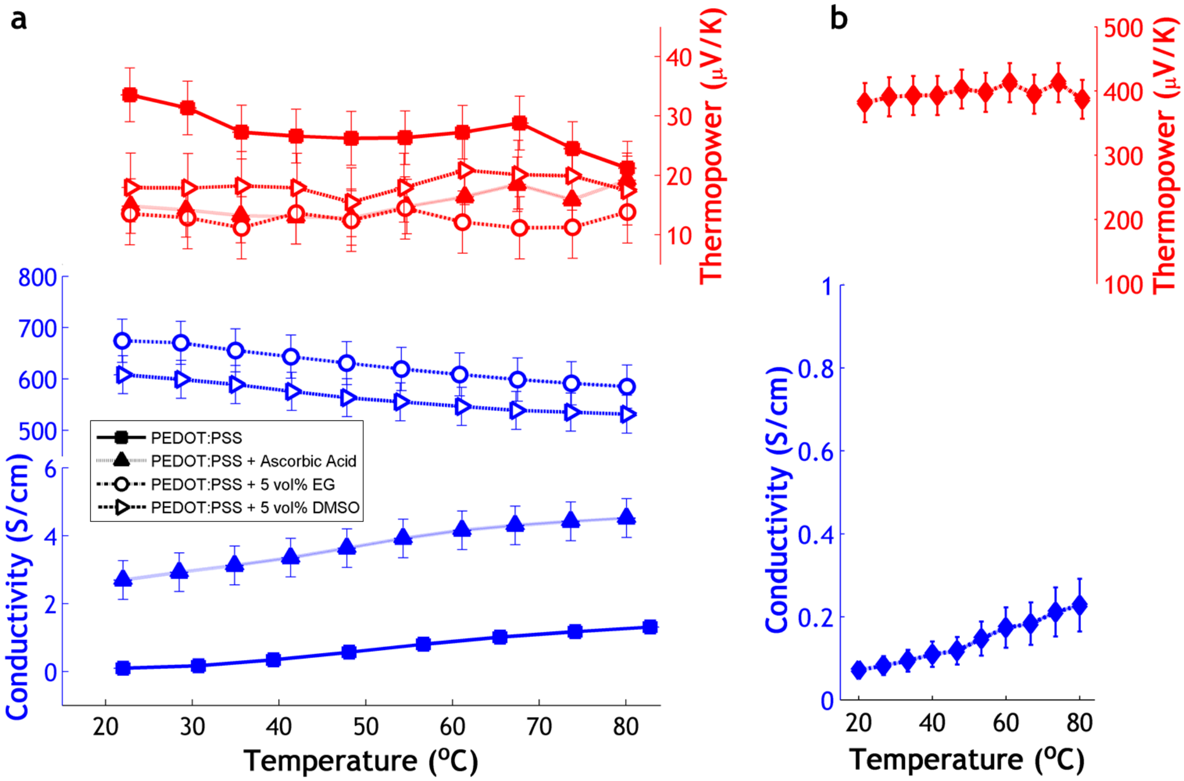

Figure 4.6 Temperature dependent properties of control samples. (a) PEDOT:PSS- The low electrical conductivity PEDOT:PSS (solid markers) are explained well by Mott's variable range hopping.[19,20] The high electrical conductivity PEDOT:PSS with EG and DMSO (open markers) have a metallic characteristic. In all cases, the thermopower remains characteristically low and relatively constant. (b) Ascorbic coated Te NWs- Temperature dependence of thermopower and electrical conductivity for Te NWs coated in ascorbic acid.

Interestingly for PEDOT:PSS, the thermopower does not decrease much upon addition of EG or DMSO while the conductivity increases significantly. The thermopower stabilization mechanism can be attributed to the transition from hopping transport to a band-like transport mechanism. The use of EG or DMSO structurally dopes PEDOT:PSS, allowing charge carriers to travel further by increasing the mean free path and/or mobility. This change induces a transition from hopping transport (where phonons assist in transport with a positive TCR) to a band-like transport (where charge carriers are more delocalized and phonons scatter charge carriers with a negative TCR). Going through this transition, the thermopower should initially decrease as the hopping range increases with the addition of EG or DMSO. Given the weak electron energy dependence on phonon scattering, additional phonon scattering should do little to change the thermopower past the transition. Thus, given that the thermopower of PEDOT:PSS is already nearly as low as some metals, drastically increasing the conductivity may not result in much of a further decrease in thermopower.

4.3.2 Hybrid Te-PEDOT:PSS NW Morphology Results

In addition, the NW morphology plays an important role that needs to be considered for the hybrid material. Nanostructure shape and size influence the electronic and phonon density of states in a way that is different from the bulk and can be advantageous for thermoelectrics.[9] As described in the methodology section, the NW dimensions can be controlled by varying the synthesis conditions. Most noticeably, the NW length can be increased by decreasing the amount of PEDOT:PSS present during synthesis (*i.e.*, pre-synthesis addition). The PEDOT:PSS serves as the structure-directing agent, and therefore a higher concentration of PEDOT:PSS yields shorter NWs. AFM images of various NW lengths are shown in Fig. 4.7 b-g.

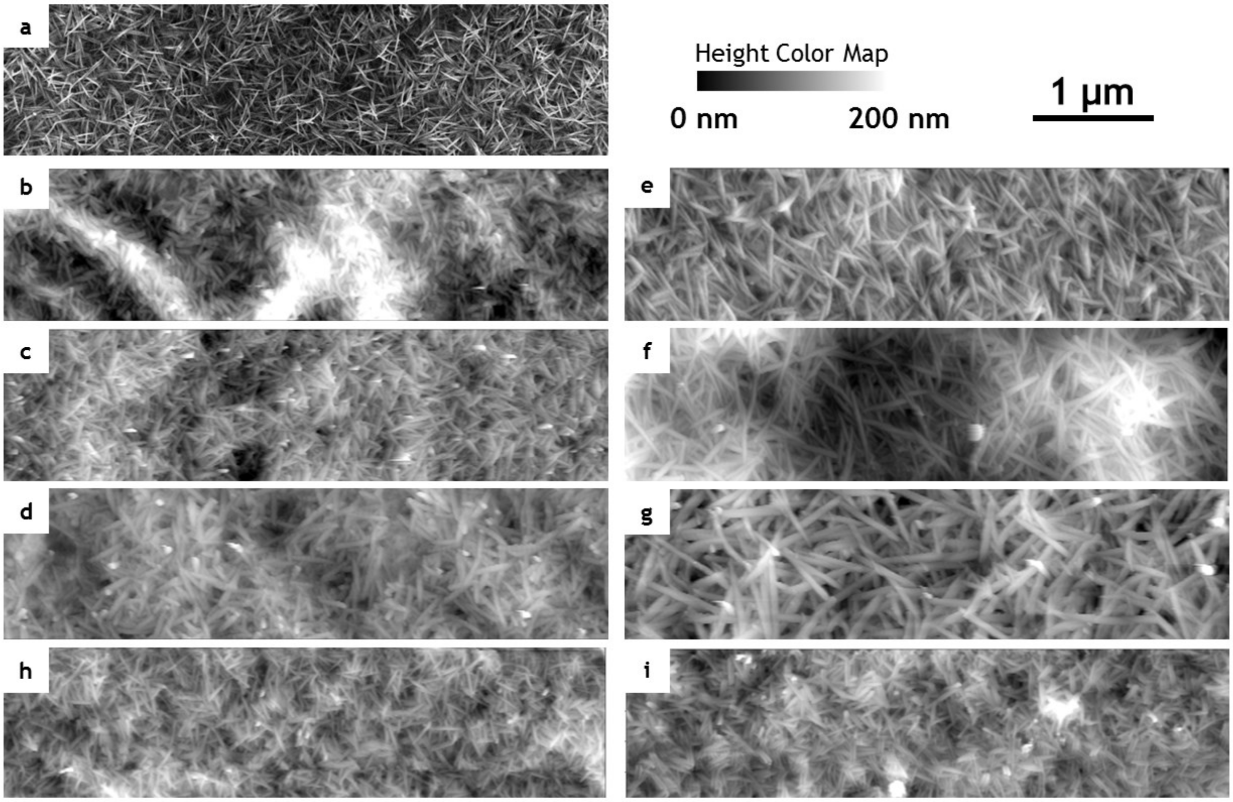

Figure 4.7 AFM images of NW films. (a) NWs formed in the absence of PEDOT:PSS are weakly coated with the ascorbic acid that is present during synthesis. NW lengths can be controlled by the amount of PEDOT:PSS added during synthesis: [4 mL of PEDOT:PSS- (b) L = 284 ± 46 nm, (c) L = 319 ± 35 nm (d) 391 ± 47 nm]; [2 mL of PEDOT:PSS- (d) L = 391 ± 47 nm (e) L = 595 ± 81 nm]; and [1 mL of PEDOT:PSS- (f) L = 867 ± 101 nm, (g) L = 970 ± 134 nm]. Adding DMSO or EG to the polymer prior to synthesis does not appear to alter the morphology for any of the NW lengths [4 mL of PEDOT:PSS- (h) with 5 vol% DMSO, L = 325 ± 51 nm, (i) with 5 vol% EG, L = 299 ± 49 nm]. All images have the same scale bar and height color map.

Lengths and diameters of these NWs were measured by analysis of AFM and SEM images of >30 NWs, and a normal distribution of length and diameter was observed. For the AFM image analysis, three dimensional coordinates (x,y,z) of the ends of NWs (for length measurements) and the edges (for diameter measurements) can be obtained directly. For the SEM images, only the lateral dimensions can be obtained (x,y). Since both ends of the NW must be visible for this measurement, it does bias toward NWs that are laying parallel to the substrate's surface. However, the horizontal NWs should be a good representation of all NWs in the sample based upon the GISAX data. This allows for good agreement between the SEM with only (x,y) and the AFM with (x,y,z) coordinates. Also to verify this approach, a dilute solution of NWs was spun cast, allowing for the NWs to separate and lie parallel to the substrate. Upon analyzing several NWs, it is evident that the variation in length between separate NWs is much greater than any length measurement uncertainty ($\Delta l = \sqrt{2}\Delta x$ where the coordinate uncertainty,

Δx, is primarily due to AFM tip broadening of <10 nm) as shown in Fig. 4.8. The distribution of NW lengths and diameters has a Gaussian profile and therefore the standard deviation in NW lengths is reported as the uncertainty in NW size.

In addition to the NW length varying, the NW diameter also increases with increasing length. The aspect ratio, $\beta=L/D$, of these NWs decreases linearly from 8.0±2.1 in the longest NWs to 4.2±1.1 in the shortest NWs. While centrifuging is likely the best technique to separate the NWs from the solvent, inevitably some small fraction of polymer that is un-bound to NWs remains even after repeated centrifuging. As a result, while the amount of polymer (as determined by TGA) in the hybrid composite is directly related to the amount of PEDOT:PSS used in the synthesis (more PEDOT:PSS is used to produce shorter NWs), there is a small spread (<5%) in the exact amount of polymer present in the resulting hybrid composite.

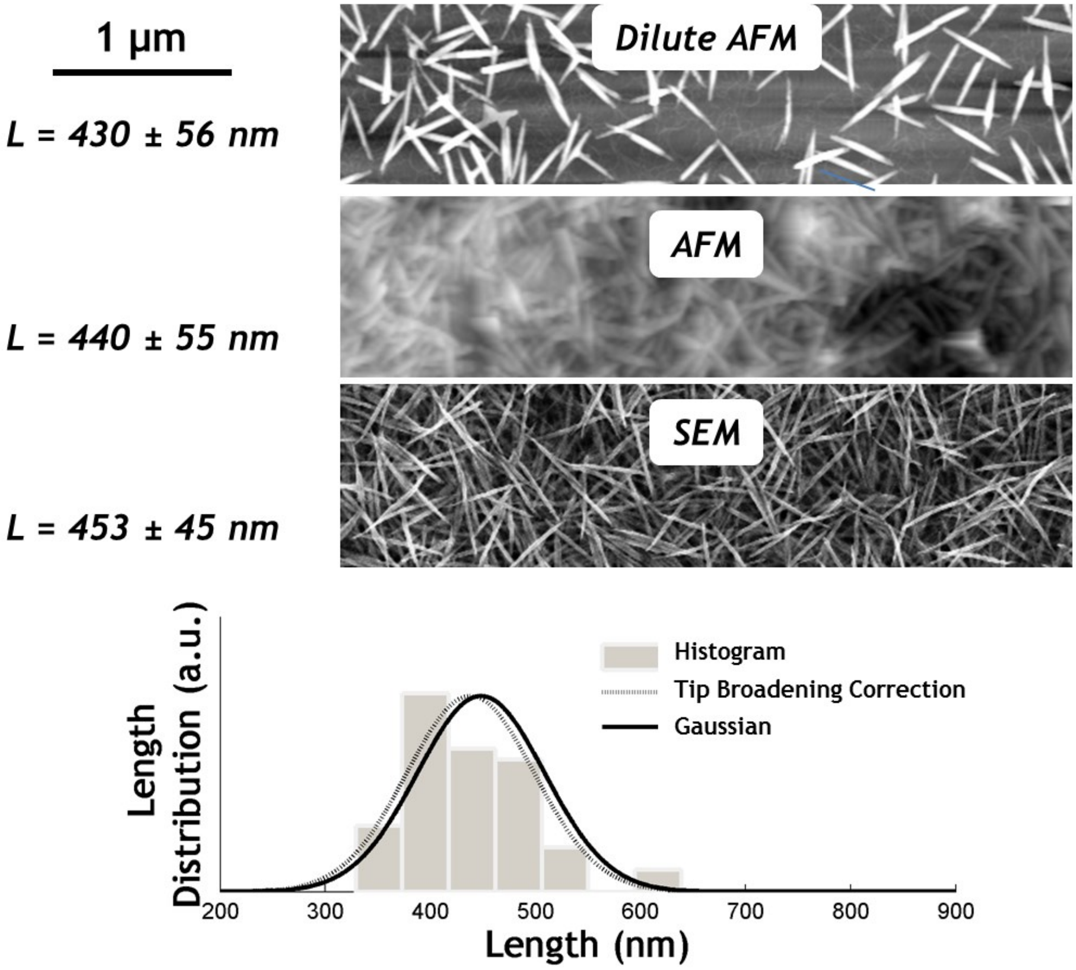

Figure 4.8 Example NW length measurement. Example AFM and SEM images of NW films used to measure the size of the NWs and an example histogram showing a Gaussian fit and the minor shift in distribution when correcting for AFM tip broadening.

Although these three variables (length, diameter, and polymer content) are inextricably linked in this synthesis, there is a clear trend in both thermopower and electrical conductivity, as shown in Fig. 4.9. For simplicity, consider the properties a function of NW length. Linear trends in thermopower and electrical conductivity result with a slope of 153±31 µV/K/µm and -20±2 S/cm/µm, respectively. Extrapolating to a NW length of zero yields a thermopower and electrical conductivity of 31 µV/K and 26.1 S/cm.

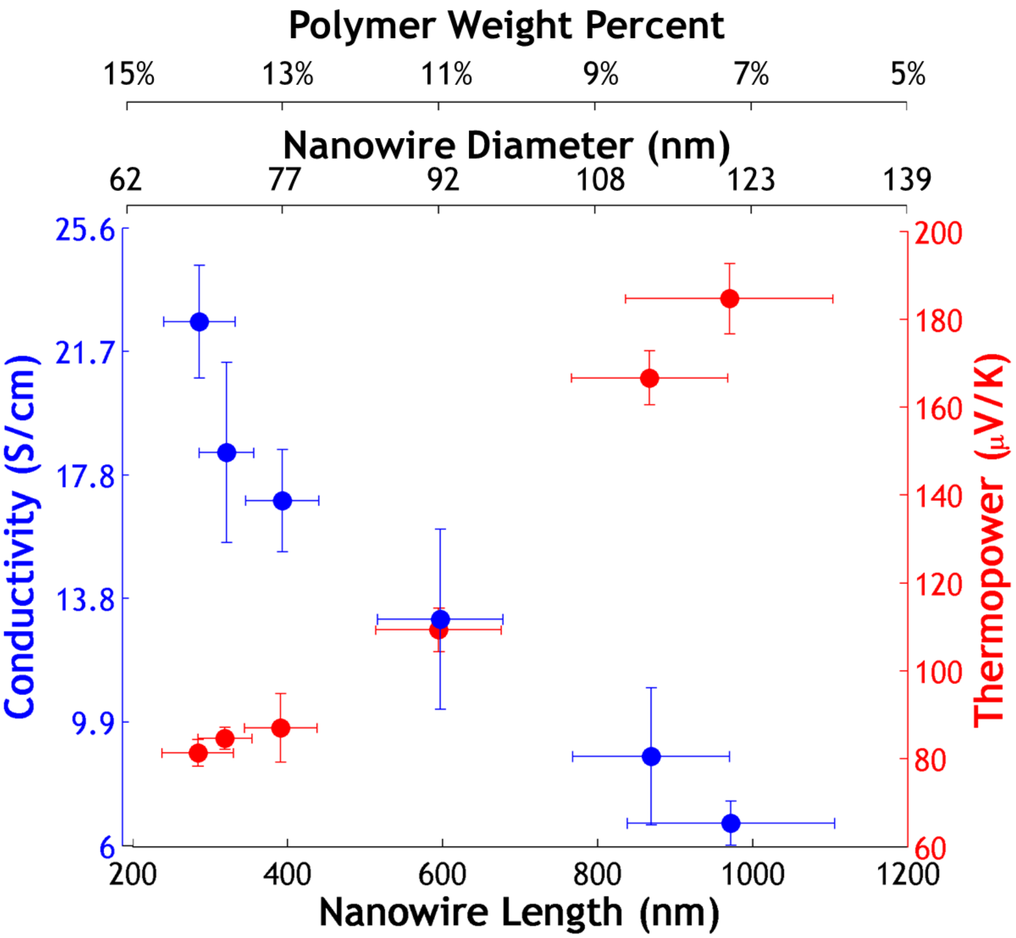

Figure 4.9 NW length dependent properties. Due to the synthesis and separation techniques, non-uniform length and polymer content convolute the data. AFM images of several NWs were used to determine a Gaussian distribution in length and diameter where the standard deviation in length is represented in the horizontal error bars. The post-synthesis polymer content varied linearly from 14.5 wt% polymer in the shortest NWs to 7.5 wt% in the longest NWs as determined by TGA. This is consistent with the short NW synthesis starting with more polymer and the long NW synthesis starting with less polymer. In addition, as the length increases the diameter of the wire also increases. Due to the synthesis procedures, it is impossible to separate these variables independently.

There are several explanations for these trends given the inextricable variables, and we present two plausible hypothetical explanations. The simpler explanation is that the trend follows a composite model as a function of the amount of polymer present. Linearly extrapolating to 0 wt% polymer yields a thermopower of 298 µV/K. This is ~ 25% smaller than the value of the control Te NWs. Linearly extrapolating the electrical conductivity yields a non-physical, negative electrical conductivity and it is more likely that the conductivity approaches the value of intrinsic tellurium (0.1-1 S/cm). While a linear extrapolation is not the most appropriate, it illustrates the plausibility that the data can be explained by a parallel connected composite model with the ascorbic acid-coated Te NWs serving as one end point.

An alternate explanation is that a highly conductive interface is present around the nanowires. This highly conductive interface is caused by the hybridization between the Te and PEDOT:PSS. If a high conducting interface exists, then as the NWs get longer, the interface may get thinner, as evident by the increase in aspect ratio and decrease in the amount of polymer. A thinner conducting interface reduces the conductivity and augments the scattering interactions between the charge carriers in the polymer and NWs.

4.3.3 Hybrid Te-PEDOT:PSS NW Composition Dependence Results

In order to gain a better understanding of the explanation and mechanism, the composition control of the Te NW films is investigated. This is accomplished by the addition of PEDOT:PSS after synthesis (*i.e.*, post-synthesis addition) as described in the methodology section. After synthesis, the interface component is the PEDOT:PSS that coats the Te NWs. By adding PEDOT:PSS post-synthesis, the relative degree of contribution of that interface region compared to the matrix PEDOT:PSS can be determined. For film morphology, the effect of additional matrix PEDOT:PSS causes the NWs to disperse therefore reducing any interface contributions between NWs as shown in Fig. 4.10.

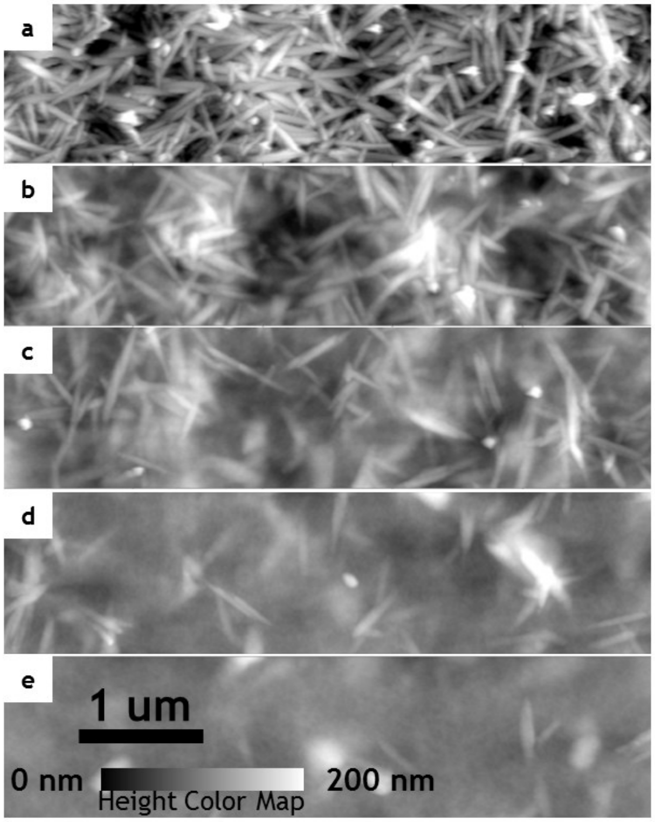

Figure 4.10 AFM image of Te NW films. NW Density can be controled by the Te NW weight fraction. Weight fractions and RMS roughnesses are approximately: (a) 90%, 22.2 nm, (b) 70%, 18.8 nm, (c) 50%, 12.8 nm, (d) 30%, 10.8 nm, and (e) 10%, 7.3 nm, respectively. Backfilling with additional polymer spreads the NWs and decreasing the contribution of the interface.

If the interface region is more highly electrically conducting than the matrix PEDOT:PSS that is added, then a composite conductivity higher than either constituent (pure PEDOT:PSS

$\sigma \approx 1$ S/cm, and pure Te NW $\sigma \approx 0.1$ S/cm) would be observed. This is exactly what is observed as shown in Fig. 4.11, where the higher electrical conductivity cannot be explained by percolation theory or effective medium theory. What does explain the data well is a three component mixture model consisting of (i) a Te NW core, (ii) a conducting PEDOT:PSS interface, and (iii) a matrix PEDOT:PSS component.[119] Furthermore, the decrease in the thermal conductivity around 80 wt% Te, suggests the presence of void (*i.e.*, air) between the NWs resulting in a low thermal conductivity, porous material; this void contribution can further help explain the decrease in electrical conductivity. *Further note, how S and σ are positively correlated; increasing S results in an increase in σ consistent with the single-molecule, hybrid organic-inorganic motivation.*

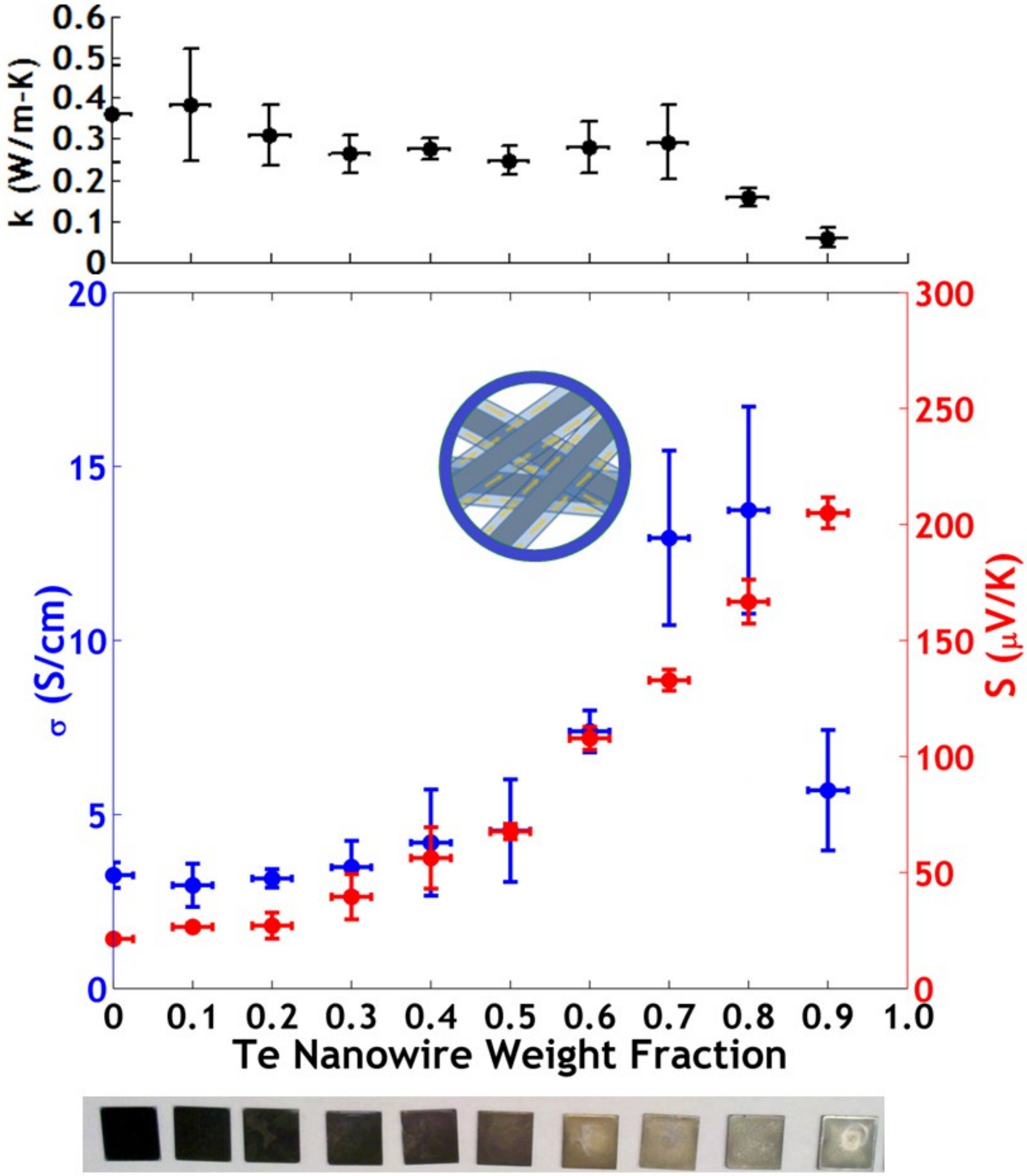

Figure 4.11 Composition dependent properties of Te NW hybrid. The thermal conductivity (black) electrical conductivity (blue) and Seebeck coefficient (red) are functions of the Te NW weight fraction. Vertical error bars represent the standard deviation between 6 identical samples; horizontal error bars represent the uncertainty in the weight fraction measurement (*i.e.*, TGA analysis). The thermal conductivity is small and relatively constant over all compositions.

4.3.4 Hybrid Te-PEDOT:PSS NW Structural Doping

Returning to the morphology dependence (Fig. 4.9), the net result from either explanation is that longer NWs have a larger thermopower. This larger thermopower is attractive from an optimization perspective, and the electrical conductivity could further be improved by the use of structural dopants, such as EG or DMSO. As mentioned in the methodology section, EG and DMSO can be incorporated by either (i) pre-synthesis or (ii) post-synthesis addition. For the pre-synthesis addition, 5 vol% of EG or DMSO was added to the PEDOT:PSS solution before the PEDOT:PSS was added to the reaction vessel. The resulting transport properties as a function of NW length are reported in Fig. 4.12, and AFM images of the resulting NW films are shown in Fig. 4.7 h-i. For comparison, the lines from Fig. 4.12 are reproduced in Fig. 4.9 to represent the neat PEDOT:PSS case. For most lengths, there is a clear increase in electrical conductivity over the neat scenario, as demonstrated by the shaded regions that show the areas of improved conductivity and thermopower (*i.e.,* above the neat line). Also note that for both EG and DMSO, linear trends in both conductivity and thermopower are present as a function of NW length. However, they appear to have different slopes, which suggests that DMSO and EG influence the interface region. The remaining polymer that may be present after centrifuging may also be influenced by the EG and DMSO, as the properties extrapolate to different values than the neat scenario.

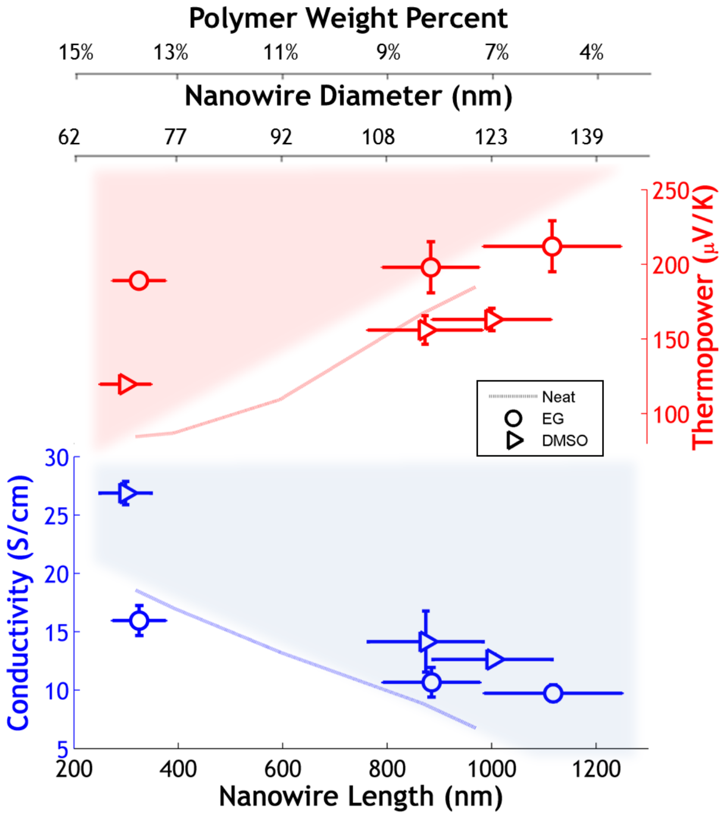

Figure 4.12 Solvent addition pre-synthesis length dependence. In most situations, adding DMSO or EG to the PEDOT:PSS solution prior to synthesis has a modest improvement in the power factor for a variety of NW lengths. The lines (neat) represent the average length dependent performance without the addition of DMSO or EG; therefore, the shaded regions above these lines represent areas of higher power factor.

For the post-synthesis addition, various volume fractions of EG and DMSO were investigated, as shown in Fig. 4.13. In this situation, the volume fraction was normalized to the polymer content as discussed in the methodology section. The use of EG and DMSO have the same trend, but quantitatively, DMSO out performs EG in both thermopower and electrical conductivity. Here, it is observed that ~5 vol% addition yields an improvement in conductivity with only a minor decrease in thermopower. Adding even more EG or DMSO decreases the thermopower drastically and thus reduces the material's performance. This result is expected as it is likely that EG or DMSO is still present even after drying due to the low vapor pressure of these solvents. Also note that regardless of adding the EG or DMSO pre-synthesis or post-synthesis, nearly the same values of electrical conductivity and thermopower are observed. This observation suggests that the polar solvents influence the conducting interface and not just the matrix polymer regardless of when they are added. This further supports the claim[119] that this interface region is primarily responsible for the improvements in this system but the absolute magnitude of the conductivity may vary from 12 to 20 S/cm. While there is an improvement in conductivity (~15 S/cm), it is significantly less than the improvement observed in the PEDOT:PSS control samples (~800 S/cm) indicating that there is further room for optimization by controlling the polymer content in the composite by backfilling with the structurally doped PEDOT:PSS infused with EG or DMSO.

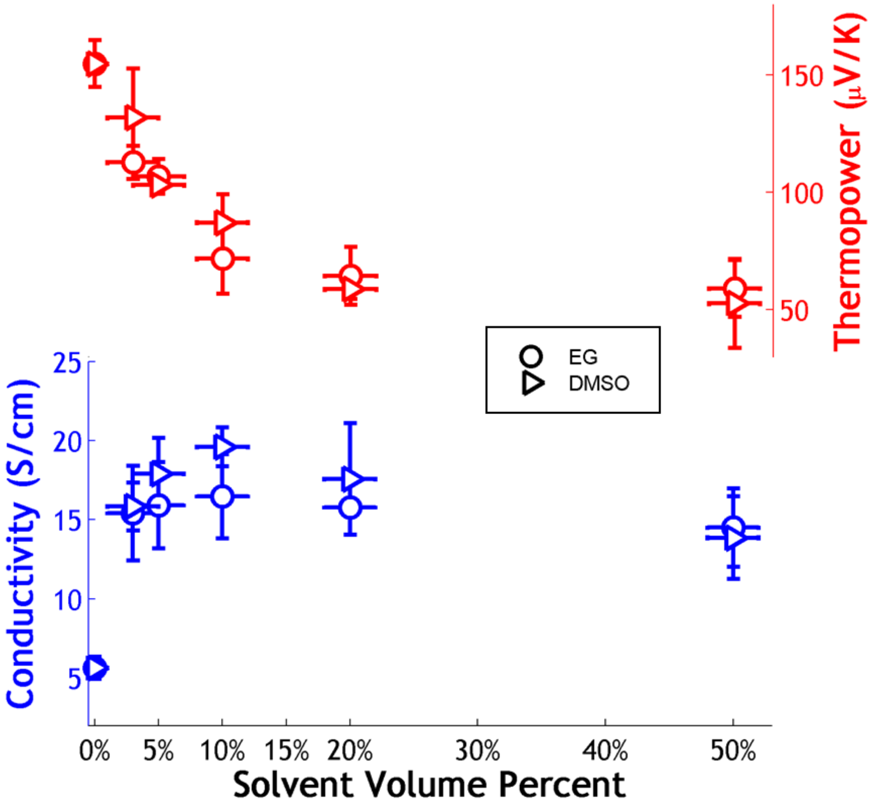

Figure 4.13 Solvent addition post-synthesis dependence. Adding DMSO or EG after synthesis to the NWs has a modest improvement in the electrical conductivity at low volume percent (normalized to the PEDOT:PSS content) but drastically reduces the thermopower for all lengths of NWs; this data is for L = 861 ± 86 nm. The improvement in electrical conductivity is attributed to improving the conductivity of excess PEDOT:PSS that is not bound to the NW but is instead free in the solution.

4.3.5 Hybrid Te-PEDOT:PSS NW Temperature Dependence

Furthermore, it is insightful to consider the temperature dependent properties of the NW films with the addition of EG and DMSO. The subset of data shown is for the longest NWs that have the highest thermoelectric performance, but all NW lengths have similar characteristic trends. The temperature dependence on conductivity for the hybrid NWs shows a negative TCR where the conductivity increases strongly with increasing temperature and then begins to flatten between 40 and 60 ºC. This result suggests that the hybrid NWs initially have an increase in conductivity caused by either (or both) the temperature dependence on hopping or by the thermal activation of carriers within the semiconducting NWs. However, at slightly higher temperatures, there is a flattening in conductivity, which is attributed to an increase in (electron-phonon or electron-boundary) scattering. Throughout this temperature range, there appears to be a slight increase in the thermopower.

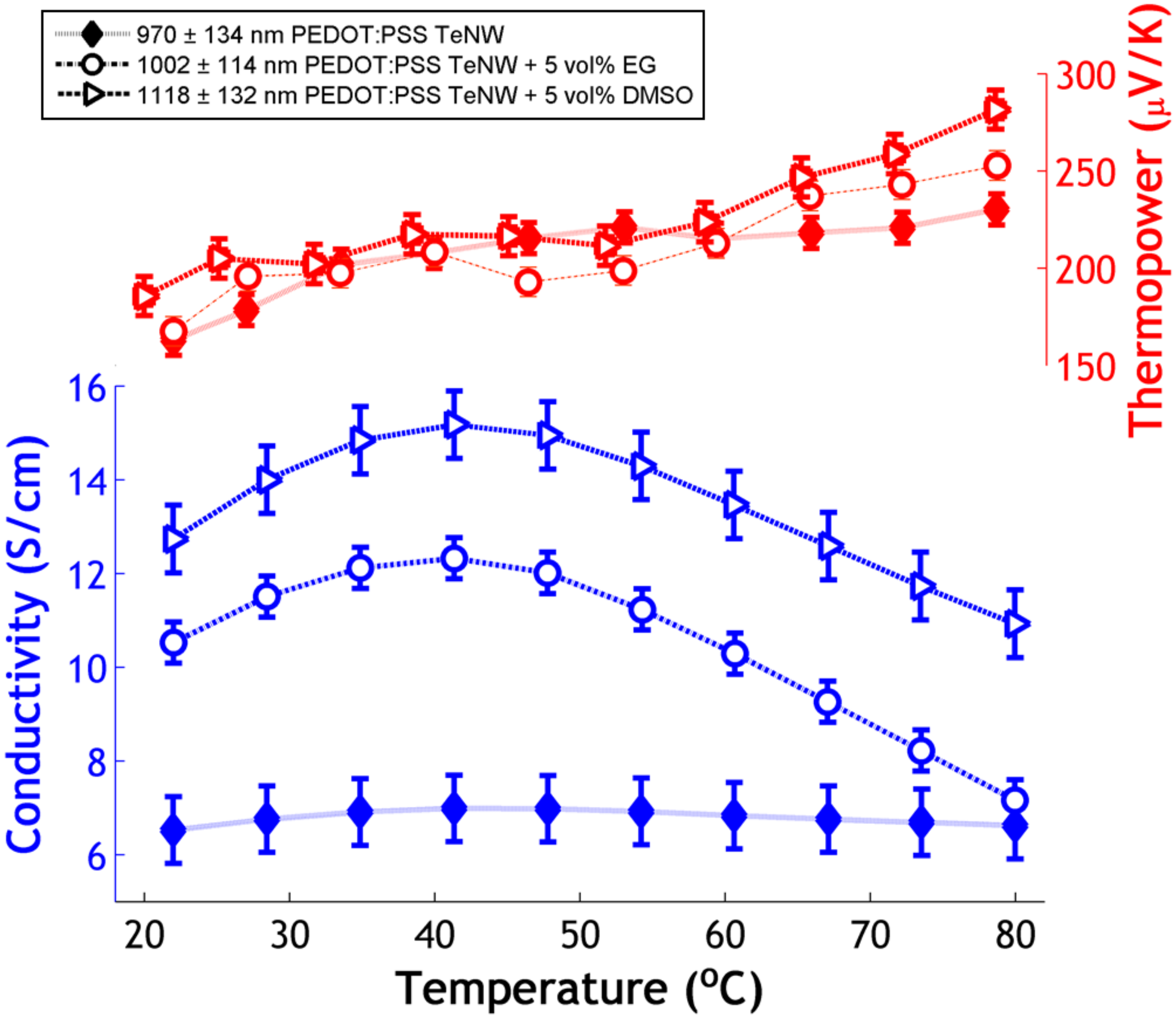

Figure 4.14 Temperature dependence of NW films. All NW films without DMSO or EG (solid markers) have a characteristic increase in conductivity with increasing temperature that is not well described by Mott's variable range hopping[104, 105]. The NW films with DMSO or EG added to the polymer before the synthesis (open markers), initially increase, go through a maximum, and then decrease in conductivity with increasing temperature. NW films with additional polymer enhanced with DMSO or EG (not shown) have a steady decrease in conductivity similar to the high electrical conductivity polymer in Fig. 4.6.

With the addition of EG or DMSO, the resulting NW film reproducibly goes through a maximum in conductivity at slightly elevated temperatures and then decreases below the room temperature values. Going from a negative TCR to a positive TCR suggests that these hybrid NW composites may be near a transition, which could explain the simultaneously high thermopower and high electrical conductivity, consistent with the scattering description previously discussed. I attribute the transition in properties to the structural change of the PEDOT:PSS from the coil-like (benzoidal phase) to the linear (or extended)-like (quinoidal phase) morphology. As discussed in the methodology, EG or DMSO act as structural dopants. After structural doping, charge carries are able to travel along the polymer backbone farther before scattering. Since this scattering is primarily due to interfaces or boundaries, which is weakly dependent on the energy of the charge carrier, the thermopower is not reduced with the increase in electrical conductivity because the thermopower results from the asymmetry in the distribution of high and low energy charge carriers. Intuitively, if the conductivity is reduced by interface or boundary scattering along the length of the polymer backbone, then the conductivity can be increased by simply reducing this scattering. Since reducing the scattering is the same across all charge carrier energies, it does not change the energy distribution of charge carriers and the thermopower remains unaffected. This combination allows for enhanced power factor of the hybrid composite.

By tuning the amount of polymer present with the addition of highly conducting PEDOT:PSS that has been enhanced with either EG or DMSO, even greater improvement can be realized. This compositional tuning is similar to what has previously been done in literature, but now it is conducted with structurally doped polymer. This composition dependence is shown in Fig. 4.15 using the weight fraction of polymer present as determined by TGA. For comparison, the neat PEDOT:PSS data has been reproduced. Note that even with a small addition of the structurally doped PEDOT:PSS, the conductivity increases several orders of magnitude, approaching that of the pure polymer phase. In addition, the thermopower drops off quickly and also approaches that of the pure polymer phase. This trend is indicative of a parallel connected composite.[120] In this model, the pure phases are taken as the structurally doped PEDOT:PSS (denoted by subscript 1) and neat hybrid NWs (denoted by subscript 2). The effective parallel thermopower is expressed as

$$S_{effective,\,parallel} = \frac{S_1\sigma_1 x_1 + S_2\sigma_2\left(1-x_1\right)}{\sigma_1 x_1 + \sigma_2\left(1-x_1\right)}, \tag{4.5}$$

and the effective parallel electrical conductivity can be expressed as

$$\sigma_{effective,\,parallel} = x_1\sigma_1 + \left(1-x_1\right)\sigma_2, \tag{4.6}$$

where S_i is the thermopower, σ_i is the electrical conductivity, and x_i is the volume fraction of component 1 and 2. The volume fraction is related to the weight fraction through the ratios of the film density and component density.

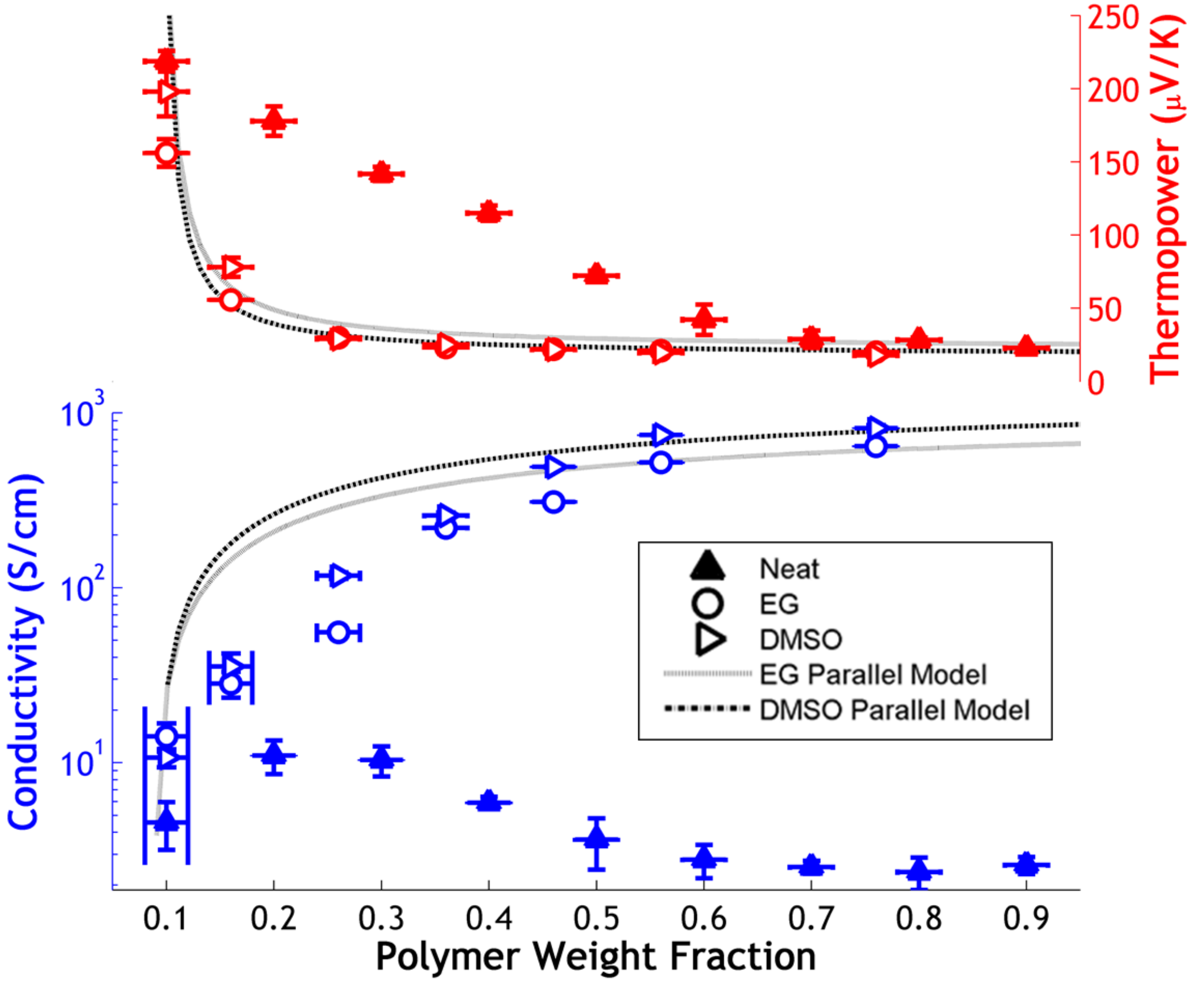

Figure 4.15 Polymer content dependence. The lines represent a two-component parallel connected model where the pure materials are taken at the 0.1 and the 1.0 polymer weight fraction limits. This simple model does not account for carrier scattering between the materials which explains the reduction in electrical conductivity in the experimental data and it has little effect on the thermopower.

There is good agreement between this model and the experimental data, except near low concentrations of polymer where the conductivity is suppressed below that predicted from the parallel connected composite model. I attribute this suppression in conductivity to additional carrier scattering (electron-phonon or boundary scattering) that occurs due to the interactions between the two materials not accounted for by the simple two component parallel connected model or the contribution from void present in these porous films. This enhanced scattering decreases the electrical conductivity and does not appreciably affect the thermopower as discussed in the introduction to this chapter.

4.4 Towards Polymer-based Thermoelectric Materials Summary

Given the tradeoffs between thermopower and electrical conductivity apparent with varying morphology and composition of the hybrid Te-PEDOT:PSS NW composites, an optimum power factor is sought. The use of EG or DMSO can improve the conductivity of

PEDOT:PSS by nearly four orders of magnitude, and adding even a small amount of this highly conducting polymer to the hybrid composite results in a large improvement in the electrical conductivity at the sacrifice of the thermopower. However, when a small amount of EG or DMSO is added to the polymer pre-synthesis of the longest NW composites the conductivity is improved slightly without decreasing the thermopower.

Given these observations, a systematic improvement in power factor is carried out as shown in Fig. 4.16. Only the results of DMSO addition are shown because it out performs EG. Starting first with the pure PEDOT:PSS, the hybrid NW composite shows nearly a four order of magnitude improvement over the pure polymer. Varying the synthesis to produce longer NWs nearly doubles the power factor. The addition of 5 vol% DMSO to the PEDOT:PSS solution pre-synthesis shows another doubling in the power factor by simply doubling the electrical conductivity without much change to the thermopower. Finally, with the addition of a small amount of PEDOT:PSS already infused with 5 vol% DMSO (bringing the total polymer weight fraction to 16% as determined by TGA), the power factor can be increased to greater than 100 μW/m^2-K. These systematic improvements more than double the average power factor previously reported in literature,[97] yielding the highest power factor observed to date in this material system.

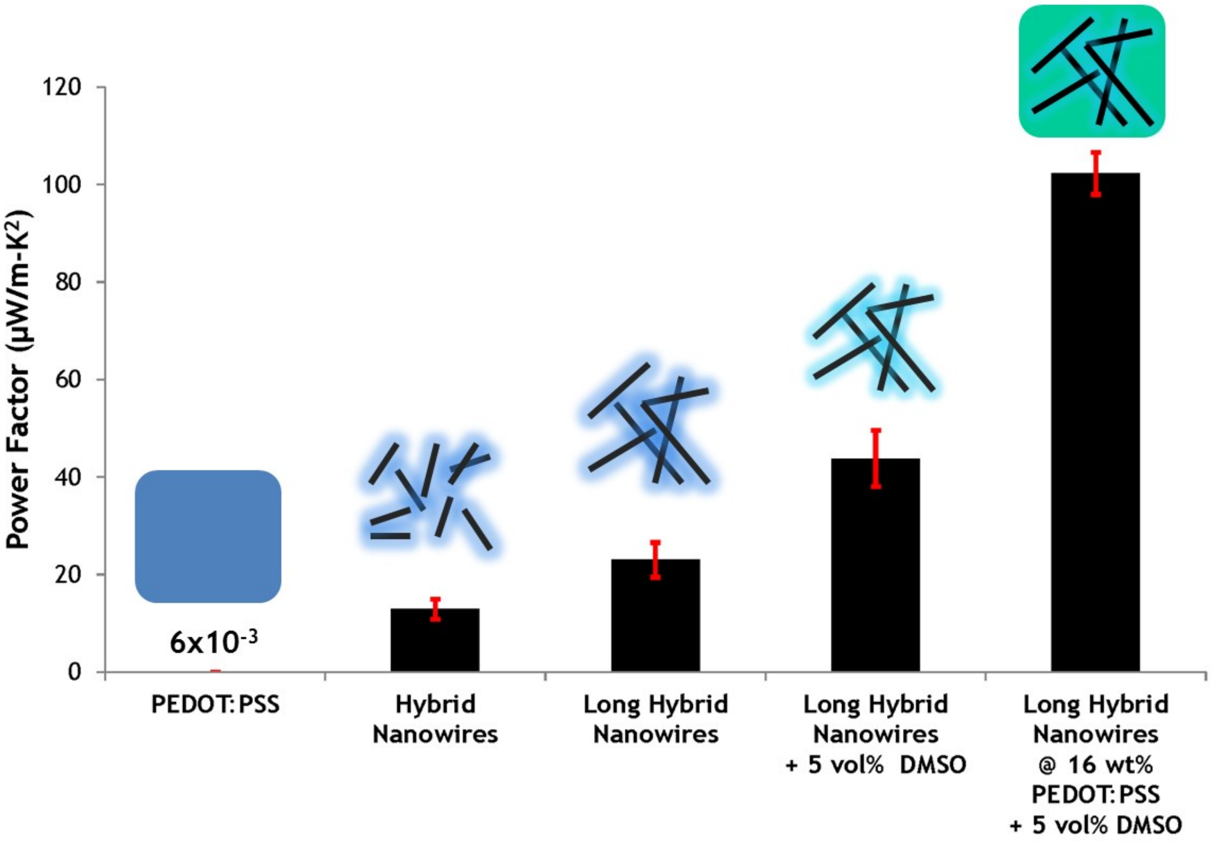

Figure 4.16 Power factor improvements. Nearly a five order of magnitude improvement in the power factor of pure PEDOT:PSS can be obtained by introducing hybrid Te-PEDOT:PSS NW, controlled by the addition of high conductivity PEDOT:PSS infused with DMSO.

To summarize, I have demonstrated the tunability and optimization of a hybrid composite consisting of Te NWs dispersed in PEDOT:PSS. By varying the synthesis, the effect of NW morphology on transport properties was investigated. It was found that longer NWs have a larger thermopower but a lower electrical conductivity. The conductivity of PEDOT:PSS can be improved with the addition of polar solvents and shows a transition from hopping transport with a negative TCR to a transport regime that has a metallic characteristic with a positive TCR. This transition is also apparent in the hybrid material where carrier scattering is integral to the stabilization of a high power factor. By the addition of structurally doped polymer, the conductivity can be tuned to maximize the power factor. This mechanism allows for thermoelectric performance improvements while maintaining the low thermal conductivity of the host polymer, making this material system even more attractive for thermoelectric applications. Ultimately, this material demonstrates the potential that polymer-based materials have to be a low cost thermoelectric alternative to inorganic thermoelectrics.

Chapter 5 Thermoelectric Device Cost Analysis

Reproduced with permission from the Royal Society of Chemistry:: Shannon K. Yee[†], Saniya LeBlanc, Kenneth E. Goodson, and Chris Dames, "\$/W Metrics for Thermoelectric Power Generation: Beyond ZT," *Energy & Environmental Science,* DOI: 10.1039/C3EE41504J, 2013.
&
Submitted for publications: Saniya LeBlanc[†], Shannon K. Yee[†], Matthew L. Scullin, Chris Dames, and Kenneth E. Goodson, "Material and Manufacturing Cost Considerations for Thermoelectrics," 2013.

While there will be continued scientific progress in developing higher efficiency hybrid organic-inorganic thermoelectric materials, practical engineering considerations are equally important when developing thermoelectric devices. The most important practical engineering consideration is undoubtedly cost on a \$/W basis. The overnight capital cost of a thermoelectric generator and the amortized operating cost of a thermoelectric refrigerator will ultimately determine the impact of a thermoelectric device. Thermoelectric materials are typically compared using the dimensionless figure-of-merit ZT because it relates directly to the device efficiency. However, for practical applications, the overnight capital cost – as governed by material, manufacturing, and heat exchanger costs – is a critical factor which is not captured in ZT.

In this chapter, a cost-performance metric for thermoelectric power generation is derived and an analysis of current thermoelectric material systems is presented. The dominant costs considered in this analysis are the material, manufacturing, and balance of system (*i.e.*, heat exchanger) costs. The analysis yields the first expressions for optimizing the thermoelectric leg length, L, and the system fill factor, F, as a function of cost. This optimization yields the minimum \$/W value for thermoelectric power generation and a framework for comparing materials beyond ZT. Even very expensive thermoelectric materials have the potential to be the most cost effective at the system level, if incorporated with sufficiently short legs and small fill factor. Furthermore, an approximate scaling analysis delineates various cost dominant regimes with different priorities for materials development: (i) a heat exchanger cost dominated regime, the best case, where ZT should be increased regardless of material or manufacturing costs; (ii) an areal cost, C'', dominated regime at fixed F, where ZT/C'' should be maximized, and (iii) a volumetric cost, C''', dominated regime at fixed F, where $ZT/(kC''')$ should be maximized, reinforcing the need for low thermal conductivity, k.

The cost-performance framework derived in this work is then applied to a number of practical materials and manufacturing processes. Considered herein is a new thermoelectric power generation cost metric G, in [\$/W], for power generation and the analogous operating cost metric H, in [\$/kWh], for cooling applications. The tradeoff between efficiency and cost through electrical and thermal transport at the system level, raw material prices, system component costs, and estimated manufacturing costs for both bulk and thin film materials are considered. The results indicate that, for typical thermoelectric power generation applications at a hot-side temperature below 250 °C, most thermoelectric material costs are too high whereas above 500 °C many bulk thermoelectrics can achieve materials costs alone below \$1/W. It is shown that the major barrier to economic thermoelectric power generation is due to the upfront systems costs for heat exchangers and ceramic plates. This is encouraging for polymer-based materials since their system costs have the potential to be lower for low temperature (<250 °C) applications.

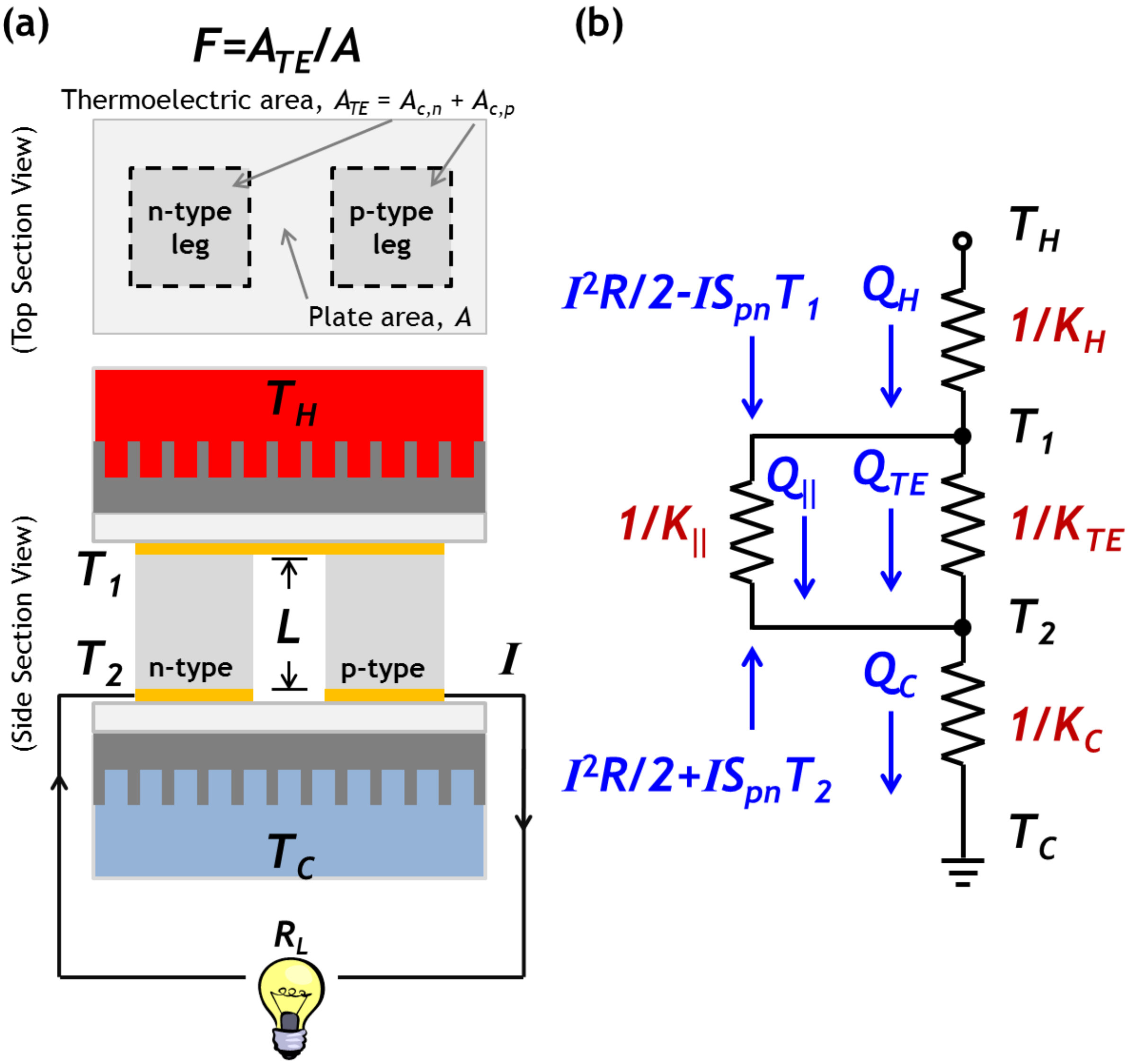

Figure 5.1 Diagram of thermoelectric module and the equivalent thermal circuit. The n- and p-type thermoelectric materials are connected electrically in series with a metal (shown in orange). The thermoelectric legs are thermally in parallel between electrically insulating ceramic plates (shown in light grey). The analysis is conducted for constant hot and cold-side temperatures, T_H and T_C. There are two thermal conductance terms between the junction temperatures T_1 and T_2 representing heat transfer through the thermoelectric material legs and in the gap between the legs. The internal heat generation term, $I^2R/2$, is the Joule heating component. The Peltier term is $IS_{pn}T$.

5.1 Thermoelectric Cost Analysis Motivation

Thermoelectric generators have the potential to be used commercially for electric power generation in a variety of applications, such as distributed solar generation[121] enabled by the development of more efficient solar thermoelectric generators.[122,123] However, the efficiency of most thermoelectric devices is reportedly too low to be competitive with other energy conversion technologies.[124] While efficiency is a useful metric, the cost of generating electricity is more important for the development of commercial devices. This is the case for photovoltaics,[125] where component costs are expressed in the units of [$/W]. More sophisticated photovoltaic materials give higher efficiencies resulting in higher power output, but this must be weighed against the increase in capital cost to determine the net effect on the overall system costs and the merits of implementation. The same can be said about thermoelectric generators, where the overall system costs [\$/W] decrease as ZT increases, if holding all other parameters constant. For this reason, rankings of thermoelectric materials are almost universally given in terms of their ZT values. However, ZT does not capture device architectures, material costs, manufacturing costs, and the cost of the heat exchangers, all of which strongly influence the overall cost of a thermoelectric generator. These additional factors must be included in any cost-performance metric before a conclusion is made regarding the potential competitiveness of thermoelectric energy conversion and to select the best thermoelectric material for an application.

Some cost analyses for thermoelectrics have been reported previously.[125-128] One earlier analysis considered the cost of fuel for generating heat and concluded that, when heat was essentially free, the thermoelectric generator should be designed to produce maximum power.[126] While this finding is useful, a comprehensive assessment must also consider the material, manufacturing, and heat exchanger costs associated with the system. The cost of the raw materials has also been considered, by comparing the ratio of a material's ZT to its molar specific cost.[129] This work provided a limited comparison of the cost-performance of various thermoelectric materials, because it neglected the device architecture, manufacturing costs, and cost of the heat exchangers which as will be shown below dramatically influence the overall cost-performance. A third cost analysis focusing on device architecture found a geometric condition that first maximized the areal power density and then used this optimum geometry to consider the material cost.[127] This analysis suggested a method to assign a \$/W value to a thermoelectric generator, although manufacturing and heat exchanger costs were not considered. Since a material's thermoelectric performance has recently been improved by the use of potentially expensive nanostructuring techniques,[1,130] appropriately accounting for the manufacturing cost is now necessary. Also one cannot neglect the cost and system-level influence of the heat exchangers, especially for applications where the fill factor is low. Finally, a prescription for determining the device dimensions that minimize the \$/W are currently missing from literature, and in general are different from the well-known optimized dimensions for maximizing efficiency or areal power density.

Thermoelectric technologies also face several commercialization challenges. Specifically, the cost of many thermoelectric materials is thought to be prohibitively high, largely due to the use of tellurium and germanium in the most common contemporary thermoelectric applications.[131] Safety concerns preclude toxic materials such as lead.[132] The weight and specific power of thermoelectric devices are particularly important for mobile applications such as vehicle waste-heat recovery,[133] yet few weight minimization solutions have been proposed. While government funding of thermoelectrics research and development has expanded significantly in the past decade, the relative lack of private sector familiarity with the technology made early-stage financing in the private sector comparatively slow to follow.[47]

In spite of the remaining challenges, there has been a rapid development of higher performance materials due in part to nanostructuring and novel crystal structures.[1,4,6] Recent prototypes demonstrate the feasibility of thermoelectric devices for widespread, terrestrial, scalable applications.[134-137] Multiple start-up companies have received recognition and funding while also forming partnerships with established academic and industrial research units.[133,138-141]

The continued development and deployment of scalable thermoelectric devices depends on the device cost and energy conversion performance.[1,127]

Herein, I derive the more comprehensive metric than *ZT* for power generation, namely, the ratio of the thermoelectric system costs to the power generated, denoted by *G* in units of $/W. In addition, I also derive a more comprehensive metric for cooling applications, which is a function of the electricity consumption and amortized capital cost of the system, denoted by *H* in units of $/kWh. Accurately determining the material, manufacturing and heat exchanger costs is difficult and these uncertainties[126,127,129] necessarily propagate into *G* and *H*, but nevertheless these new metrics are more meaningful than *ZT* for realistically comparing thermoelectric options.

For power generation, operating costs, fuel/heat costs, and parasitic heat losses are omitted and beyond the scope of this analysis, although they, in principle, can be incorporated with suitable generalizations. The analysis reveals a natural scale for *G*, given the symbol G_0, which is referred to as the cost-performance metric. G_0 describes a system's $/W value when the material costs dominate. In contrast, *G* describes a system's $/W value when heat exchanger and areal manufacturing costs are also significant. *G* and G_0 addresses many of the challenges currently present in ranking materials based solely on *ZT* or *ZT/$/*mol.[129] Furthermore, *G* can also be used to compare thermoelectric systems against other power generation technologies on an overnight capital cost basis. This cost-minimization, performance-maximization in this chapter provides the first analytical design framework for a $/W optimization of thermoelectric leg length and fill factor.

For refrigeration applications, operating costs and parasitic heat losses are omitted but the cost of electricity, which is purchased to operate the refrigerator, is included. Furthermore, unlike power generation, cooling applications do not consider the cost of heat exchangers but rather, the module is thought to be in intimate contact with the object being cooled. The analysis reveals that the cost of purchasing electricity dominates and as a result, the most efficient thermoelectric material has the lowest cost *H*. So unlike, power generation, there is not a tradeoff between cost-minimization and performance-maximization but rather the highest efficiency should be sought. This is the result of thermoelectric devices having effectively infinite-life since they are solid-state devices with no moving parts.

Finally, herein, this chapter applies the cost metrics *G* and *H* to thirty promising thermoelectric materials reported for seven material classes and four manufacturing classes in Table 5.1. These metrics enable an assessment of which materials may be most promising and sets targets for future thermoelectric development. The analysis is performed for five operating temperatures shown in Table 5.2 to reflect the myriad of potential thermoelectric applications.

5.2 Thermoelectric Cost Analysis Methodology

To derive the cost-performance metrics, I begin with a standard analysis of a thermoelectric power generator,[142] as shown in Fig. 5.1, for a dual leg device. I make several common simplifying assumptions: (i) the n- and p-type legs have identical geometries and thermophysical properties (except the Seebeck coefficients which are equal in magnitude but opposite in sign), (ii) the thermal and electrical contact and metallization resistances are negligible (the heat exchanger thermal resistance is considered separately), and (iii) the cross sectional areas of the thermoelectric legs do not vary along their length. The efficiency, η_{th}, of the device relates the electrical power output, P [W], to the heat entering the thermoelectric generator, Q_H [W]. The electric power can be expressed as a function of the current, I [A], or the voltage, V [V], the electrical resistance of the load, R_L [Ω], and of the module, R [Ω], as

$$P_{gen} = I^2 R_L = \left(\frac{V}{R_L + R} \right)^2 R_L = \left(\frac{S_{pn}\left(T_1 - T_2\right)}{R_L + R} \right)^2 R_L , \tag{5.1}$$

where T_1 [K] and T_2 [K] refer to the hot and cold junction temperatures $S_{pn}=S_p-S_n$ [V/K] is the junction Seebeck coefficient (the difference in Seebeck coefficients of the p-type and n-type semiconducting legs). As an additional assumption, (iv) the temperature dependence of material properties (S, σ, and k which results in Z being independent of T) are neglected over the temperature range between the hot and cold reservoirs. An energy balance at the hot-side junction in Fig. 5.1b (*i.e.*, at T_1) gives

$$Q_H = K_T\left(T_1 - T_2\right) + S_{pn} I T_1 - \tfrac{1}{2} I^2 R = K_H\left(T_H - T_1\right), \tag{5.2}$$

where K_T [W/K] is the thermal conductance of the module and K_H [W/K] is the thermal conductance of the hot-side heat exchanger between T_1 and the hot reservoir at T_H. Likewise, the heat flowing out of the device is determined by an energy balance at the cold-side junction in Fig. 5.1b (*i.e.,* at T_2),

$$Q_C = K_T\left(T_1 - T_2\right) + S_{pn} I T_2 + \tfrac{1}{2} I^2 R = K_C\left(T_2 - T_C\right), \tag{5.3}$$

where K_C [W/K] is the thermal conductance of the cold-side heat exchanger. The efficiency relates the power generated and the heat entering the generator and can be expressed as

$$\eta_{th} = \frac{P_{gen}}{Q_H} = \frac{I^2 R_L}{K_T\left(T_1 - T_2\right) + S_{pn} I T_1 - \tfrac{1}{2} I^2 R}, \tag{5.4}$$

Since P_{gen} depends strongly on the junction temperatures and the heat entering the device, the heat exchangers and the thermal conductance of each component are important. These conductances are lumped parameters that also account for the temperature drops across the insulating ceramic plates and any thermal contact resistance present in thermoelectric devices. The heat transfer coefficient, U [W/m^{2}K], of the heat exchanger describes the series conductances through $K=UA$, where A [m^2] is the area of the ceramic plate that joins the thermoelectric generator to the heat exchanger. Also in many applications the hot- and cold-side heat exchangers have approximately the same heat transfer coefficient, so for simplicity I take $U_H=U_C=U$, $A_H=A_C=A$, and $K_H=K_C=K$ for the remainder of this analysis.

The conductance of the thermoelectric device, $K_T=K_{||}+K_{TE}$, depends on the conductance of the thermoelectric legs, K_{TE}, and the parallel thermal conductance, $K_{||}$, between legs (*i.e.*, convection, conduction, and/or radiation across the gap between the plates). These conductances describe the heat flowing through the device which is divided into the portion that conducts through the legs, $Q_{TE}=K_{TE}(T_1-T_2)$, and the portion that goes around the legs, $Q_{||}=K_{||}(T_1-T_2)$. K_T can be expressed as

$$K_T = \frac{k_{||} A\left(1 - F\right)}{L} + \frac{k_p A F}{2L} + \frac{k_n A F}{2L}, \tag{5.5}$$

where $F=A_{TE}/A$ is the fill factor (see Fig. 1a) and L [m] is the thermoelectric leg length. The cross sectional area of one leg is then $A_{c,n}=A_{c,p}=\frac{1}{2}AF$ and the legs have thermal conductivities k_n, and k_p, respectively. The parallel thermal conductance is represented using an equivalent thermal conductivity $k_{||}$, which could also represent linearized radiation and/or natural convection.

Here for simplicity I make the idealization that the heat flowing around the legs is negligibly small (*i.e.*, $K_{||} << K_{TE}$). In practice, more detailed calculations[14] show this is valid for most applications with $F>0.1$ because the thermal conductance through radiation and the gas is found to be much less than that through the thermoelectric legs. For applications with $F<0.1$ additional measures (*e.g.*, evacuated tubes and radiation management strategies) are used to minimize the thermal leakage conductance. Neglecting $K_{||}$ and taking $k_p = k_n = k$, the module conductance simplifies to

$$K_T \approx \frac{kAF}{L} \quad (5.6)$$

Likewise, the electrical resistance of the device is

$$R \approx \frac{2L}{\sigma_p AF} + \frac{2L}{\sigma_n AF} \approx \frac{4L}{\sigma AF} \quad (5.7)$$

under the approximation that the electrical contact resistance and metallization resistances are negligible and $\sigma_p = \sigma_n = \sigma$.

5.2.1 Derivation of *ZT*

With these simplifications, the efficiency of the device is ultimately determined by the load on the generator. With the algebraic simplification $m = R_L/R$,

$$P_{gen} = \frac{S_{pn}^2 (T_1 - T_2)^2}{R} \left(\frac{m}{(m+1)^2} \right) \quad (5.8)$$

and the efficiency of a generator under a variable load can be expressed as

$$\eta_{th} = \left(\frac{m}{\frac{1}{2}\left(\frac{T_2}{T_1} - 1\right) + K_T R \frac{(m+1)^2}{S_{pn}^2 T_1} + (m+1)} \right) \left(\frac{T_1 - T_2}{T_1} \right), \quad 0 < m < \infty. \quad (5.9)$$

This expression does not include the familiar thermoelectric figure of merit, ZT. To introduce ZT, consider a collection of terms in the denominator where

$$ZT \equiv \frac{S_{pn}^2 T}{K_T R}, \quad (5.10)$$

known as the *module* figure of merit. This derivation can be extended from a dual leg device to a module consisting of N pairs of legs electrically in series with minor modifications to Eqn. 5.1 and carried through to yield

$$ZT = \frac{(NS_p - NS_n)^2 T}{(NK_T)(NR)} = \frac{S_{pn}^2 T}{K_T R} \quad (5.11)$$

Note that Eqn. 5.9 is a function of $K_T R$; therefore, to maximize the efficiency, the minimum value $K_{TE}R$ is sought.

$$K_{TE}R = \frac{k_p}{\sigma_p} + \left(\frac{k_n}{\sigma_p}\right)\left(\frac{A_{c,n}L_p}{A_{c,p}L_n}\right) + \left(\frac{k_p}{\sigma_n}\right)\left(\frac{A_{c,p}L_n}{A_{c,n}L_p}\right) + \frac{k_n}{\sigma_n}, \tag{5.12}$$

where the length, L_i, and cross sectional areas $A_{c,i}$ of each leg (*e.g.*, $i = p$ for p-type leg) may differ from one another. Minimizing Eqn. 5.12 by taking the derivative with respect to $A_n L_p / A_p L_n$ and setting the result equal to zero yields the condition

$$\left(\frac{A_{c,n}L_p}{A_{c,p}L_n}\right) = \left(\frac{\sigma_p k_p}{\sigma_n k_n}\right)^{1/2}. \tag{5.13}$$

This is the condition for an optimum geometry of the device which minimizes Eqn. 5.12

$$\left(K_{TE}R\right)_{min} = \left[\left(\frac{k_n}{\sigma_n}\right)^{1/2} + \left(\frac{k_p}{\sigma_p}\right)^{1/2}\right]^2. \tag{5.14}$$

The minimum of value $K_{TE}R$ can be used to determine the maximum value of ZT which is expressed as

$$Z_{max}T = \frac{\left(S_p - S_n\right)^2 T}{\left[\left(\frac{k_n}{\sigma_n}\right)^{1/2} + \left(\frac{k_p}{\sigma_p}\right)^{1/2}\right]^2}. \tag{5.15}$$

Allowing for the simplification that $k_n = k_p = k$, $\sigma_n = \sigma_p = \sigma$, and $S_p = -S_n = S$, the *material* ZT is expressed as:

$$ZT = \frac{S^2 \sigma T}{k}. \tag{5.16}$$

This shows the number of idealized steps, geometry constraints, and simplifications that are made to obtain this commonly used *material ZT* which serves as the figure of merit for thermoelectrics. For this chapter, the *material ZT* will be used to identify the materials in the figures while the *module ZT* is used in the analysis under the simplification that the n- and p-type legs have the same thermopower magnitude, same electrical conductivity, and same thermal conductivity. Finally, the figure of merit can be included to simplify the efficiency expression of Eqn. 5.4 and 5.9 to

$$\eta_{th} = \left(\frac{mZT_1}{ZT_m + mZT_1 + \left(m+1\right)^2}\right)\left(\frac{T_1 - T_2}{T_1}\right) = \eta_{Module}\eta_{Carnot}, \tag{5.17}$$

where $T_m = (T_1 + T_2)/2$ is the average junction temperature. The thermal efficiency of a thermoelectric generator is the product of the module efficiency, η_{module}, and the Carnot efficiency, η_{Carnot}.

5.2.2 Thermoelectric Efficiency Selection

Thermoelectric generators can be operated at maximum power or maximum efficiency or anywhere in between. In applications where the heat source is essentially free (*e.g.*, solar thermal, nuclear power, or waste heat recovery), the minimum overall \$/W cost is achieved by operating at maximum power, as shall be confirmed below. On the other hand, when heat is costly (*e.g.*, fossil fuel combustion), operating much closer to the maximum efficiency condition may be preferred. In both cases, operating at either maximum power or maximum efficiency is achieved by varying the electrical load resistance on the generator as compared to the internal resistance of the module. The present analysis, however, will be limited to the former case where heat is abundant/free and therefore the maximum power condition is preferred. This condition is determined by the value of m that maximized Eqn. 5.8, which by inspection is m=1. It has recently been suggested that, due to thermal feedback from the load resistance affecting the junction temperatures, m should be somewhat greater than unity even at maximum power.[143,144] Although this higher-order feedback effect could be incorporated here for better accuracy, for algebraic simplicity the analysis below will use the more conventional[142] load matching condition of m=1. In this case the efficiency is given by

$$\eta_{mp} = \left(\frac{ZT_1}{ZT_m + ZT_1 + 4} \right) \left(\frac{T_1 - T_2}{T_1} \right). \tag{5.18}$$

If ZT is small, Eqn. 5.18 simplifies to

$$\eta_{mp} \approx \left(\tfrac{1}{4} ZT_1 \right) \left(\frac{T_1 - T_2}{T_1} \right). \tag{5.19}$$

Equation 5.19 is an upper bound to the efficiency in Eqn. 5.18.

The efficiency at maximum power is different from the maximum possible efficiency. The value of m that maximizes the efficiency in Eqn. 5.17 is $m = \sqrt{1 + ZT_m}$ which give an efficiency of

$$\eta_{max} = \left(\frac{\sqrt{1 + ZT_m} - 1}{\sqrt{1 + ZT_m} + \frac{T_2}{T_1}} \right) \left(\frac{T_1 - T_2}{T_1} \right). \tag{5.20}$$

5.2.3 Thermal Impedance Matching

It is important to consider how the temperature drop is distributed through the device. Clearly, heat exchangers with high U-values are desirable. Having fixed U, if the thermoelectric legs are made too short then the temperature drop across the module, and thus the power output, would be small (Eqns. 5.8). On the other hand, if the thermoelectric legs are too long then the total thermal resistance (Eqn. 5.11) also becomes large, reducing Q_H, and furthermore the electrical resistance would be large (Eqn. 5.12), both tending to reduce the power output. Therefore there is some intermediate leg length that optimizes this tradeoff, referred to as thermal impedance matching.[145] A simplified optimization published previously[144] argued that having half of the temperature drop occur across the thermoelectric is ideal, and a more detailed optimization[145] that also considered the effects of asymmetric heat exchangers arrived at the same conclusion.

A simplified derivation of this result follows, and will be referred to later. For a typical application with $T_1/T_2 \approx 2$ and $ZT_1 \approx 1$, from Eqn. 5.19 the overall efficiency is $\eta < 13\%$. Thus, from elementary thermodynamics, >87% of the heat entering the device exits the device on the cold-side. Therefore, to within accuracy of order η, it can be shown that the heat flows Q_H, Q_{TE}, and Q_C are all approximately equal,

$$K_H\left(T_H - T_1\right) \approx K_T\left(T_1 - T_2\right) \approx K_C\left(T_2 - T_C\right). \tag{5.21}$$

Then the temperature drop across the module can be expressed simply as

$$T_1 - T_2 \approx \frac{K_H K_C}{K_C K_T + K_H K_T + K_H K_C}\left(T_H - T_C\right). \tag{5.22}$$

This major benefit of this approximation is the resulting analytical simplicity, which is necessary to obtain the key closed form results in the remainder of this paper. It should also be noted that Eqn. 5.22 introduces errors typically at the ~10% level, although this is a minor correction as compared to the order-of-magnitude variations in the \$/W metrics that will be seen below. Further analytical refinement might be possible by accounting for the Peltier and Joule heating terms using an effective thermal conductivity.[122] Proceeding, because here the hot and cold heat exchangers are matched (K_C=K_H=K=UA), with the use of Eqns. 5.6, 5.7, 5.8, and 5.22 the power can be expressed as

$$P = \frac{S_{pn}{}^2 \sigma\left(T_H - T_C\right)^2 AF}{4}\left(\frac{m}{\left(m+1\right)^2}\right)\left(\frac{L}{\left(2L_T F + L\right)^2}\right) \tag{5.23}$$

with the leg length that maximizes the power being

$$L = 2FL_T. \tag{5.24}$$

where L_T [m] is a characteristic thermal length defined as

$$L_T \equiv \frac{k}{U}. \tag{5.25}$$

For F≈1, when L_T is much larger than the thermoelectric leg length L, the heat exchangers dominate the thermal resistance and temperature drop in the device. This thermal length parameter is a useful normalization condition and will be used as a characteristic length scale for comparison throughout this chapter. Once a material and an application (including heat exchanger type) are selected, L_T is a known constant. Equation 5.24 is known as the thermal impedance matching condition[144,145] and is referenced as such in this chapter. At this condition Eqn. 5.22 yields

$$T_1 - T_2 \approx \tfrac{1}{2}\left(T_H - T_C\right), \tag{5.26}$$

which shows that the maximum power output is obtained when half the temperature drop occurs across the module.

5.2.4 Series and Parallel Thermal Resistances

The series thermal resistances ($1/K_H$ and $1/K_C$) are critical for the application of thermoelectric generators. For comparison of materials, typical heat exchanger U-values were selected from literature[146] based upon the application temperature and are summarized in Table 5.2. The metallization layers and electrically insulating plates also add series thermal resistances. To approximate the metallization layers, copper with a thermal conductivity of k_1=400 W/m-K and a thickness of t_1=25.4 μm were selected. For the electrical insulating, top and bottom ceramic plates, alumina silicate with a thermal conductivity of k_2=30 W/m-K and a thickness of t_2=0.38 mm, was selected. All these series resistances are summed together as inverses to yield the overall series resistances:

$$\frac{1}{K_H} = \frac{1}{U_C A} + \frac{t_1}{k_1 A} + \frac{t_2}{k_2 A} \tag{5.27}$$

$$\frac{1}{K_C} = \frac{1}{U_C A} + \frac{t_1}{k_1 A} + \frac{t_2}{k_2 A} \tag{5.28}$$

The thermal model does not consider the radial heat spreading/constriction resistance that may be important in some more novel thermoelectric module designs with small F.

The parallel thermal conductance, $K_{||}$, also has a significant effect on the module performance and must be accounted for correctly as it scales with F. In many applications, the volume between the thermoelectric legs is likely to be occupied by a gas (*e.g.*, air). In these situations, conduction, convection, and radiation all contribute to the parallel thermal conductance.

For convection, the inside of the TE module can be treated as an enclosure where the Rayleigh number, Ra_L, which is a measure of the buoyant forces to viscous forces, is appropriate to determine the contribution of natural convection.[147] A thermally unstable condition, where advection within the cavity becomes important, occurs when Ra_L>1708. Otherwise, conduction through the gas dominates. In this application, the length scale used in the Ra number is taken as the thermoelectric leg length. In general this dimension should be the length in the direction of gravity. Since the aspect ratio of the legs for conventional generators is near unity, and the pitch between legs is near this dimension, orientation is not overly important. Therefore, the module thickness dimension is a valid first order approximation for the characteristic length. In most applications, dry air (or possibly even pure nitrogen) will occupy that volume. If the advection condition is met, then convection contribution can be approximated as[147]

$$\frac{\bar{h}L}{k} = 0.069 Ra_L^{1/3} Pr^{0.074} \qquad 3x10^5 \le Ra_L \le 7x10^9 \tag{5.29}$$

,

and

$$K_{||,conv} = \frac{k_{air}\left(1-F\right)A}{L}\left(0.069 Ra_L^{1/3} Pr^{0.074}\right). \tag{5.30}$$

where $\bar{h}$ is the convective heat transfer coefficient. If the advection condition is not met, then conduction through the gas dominates the parallel thermal leakage and can be expressed as

$$K_{||,cond} = \frac{k_{air}\left(1-F\right)A}{L}. \tag{5.31}$$

For most leg lengths, conduction will dominate, but at large leg lengths convection does contribute. Correcting for this convective contribution does not significantly change the results but should be accounted for nonetheless to accurately determine the parallel thermal conductance.

In addition to conduction and convection, radiation exchange may produce a non-negligible contribution to the parallel thermal conductance. The configuration view factor and the surface emissivities parameters dominate the radiation heat transfer between the hot and cold surfaces and are largely unknown across many thermoelectric applications. To a first approximation, the radiative exchange between the thermoelectric legs and the hot and cold surfaces can generally be neglected relative to conduction/convection along/between the legs. However, to include this contribution in a simplified analysis, the configuration view factor for radiation exchange between two parallel plates is approximated as

$$VF = \left(\sqrt{1 + \frac{L^2}{A}} - \frac{L}{\sqrt{A}} \right)^2 , \tag{5.32}$$

which is motivated by the 1D configuration view factor for two infinitely long, parallel plates of identical finite widths.[147] Thus, the radiation component of the parallel leakage can be approximated as

$$K_{||,rad} \approx \frac{\sigma_{sb} T_m^{\,3} \left(1 - F\right) A}{\left(\frac{\left(1-\varepsilon_1\right)}{\varepsilon_1} + \frac{\left(1-\varepsilon_2\right)}{\varepsilon_2} + \frac{1}{VF} \right)} \approx \frac{\sigma_{sb} T_m^{\,3} \left(1 - F\right) A}{\left(1 + \frac{1}{VF} \right)} , \tag{5.33}$$

where $\boldsymbol{\sigma_{sb}}$ is the Stefan-Boltzmann constant, and ε_i is the emissivity of the parallel plates. The emissivity is assumed to be constant for both plates with a value $\varepsilon = 2/3$ which is comparable to the emissivity of alumina. Combining the radiation and convection/conduction contributions, the total parallel thermal leakage conductance can be determined.

5.2.5 Power Generation Cost Metric

The present analysis considers overnight capital costs while neglecting operating, maintenance, and fuel costs (*i.e.*, heat is treated as free). Thus, the total cost of a thermoelectric generator system can be divided into (i) volumetric module costs, (ii) areal module costs, and (iii) heat exchanger costs. The volumetric module costs, *C'''* [\$/m^3], include the cost of the thermoelectric material, volumetric manufacturing costs (*e.g.* ball milling and hot pressing), and any other costs that scale with the amount of thermoelectric material. The areal module costs, *C''* [\$/m^2], include the cost of the metallization, areal manufacturing costs (*e.g.*, dicing and cutting), and any other costs that scale with the area of the module. Although many materials have similar *C'''* and *C''*, a few (*e.g.* microfabricated nanowires, superlattices grown from molecular beam epitaxy) can have much larger costs due to their specialized manufacturing techniques. While numerical values for *C'''* and *C''* are generally difficult to obtain, they are reported for thirty common thermoelectric materials in a concurrent paper.[14]

The costs of heat exchangers, C_{HX}, are typically normalized to their heat transfer coefficient and expressed with units [\$/(W/K)].[148] For a specific class of heat exchangers and ratio of heat load to temperature drop, C_{HX} is constant to a good approximation. Therefore, the areal cost of the heat exchanger can be expressed as $C_{HX}U$ [\$/m^2].

In this manner, the total cost of the device, *C* [\$], can be expressed as

$$C = \left(C''' L + C'' \right) AF + C_{HX} UA , \tag{5.34}$$

which scales with the area and fill factor. Dividing this cost by the power generated yields the cost on a [\$/W] basis, defined above as *G*. Using Eqns. 5.23 and 5.34, I obtain

$$G = \frac{C}{P} = \frac{4}{S_{pn}{}^{2}\sigma\left(T_1 - T_2\right)^2}\left(\frac{\left(m+1\right)^2}{m}\right)\left(C'''L^2 + C''L + \frac{C_{HX}UL}{F}\right) \qquad (5.35)$$
.

Finally, using Eqn. 5.22 and matched heat exchangers, the unknown junction temperatures T_1 and T_2 can be substituted out in favor of the known reservoir temperatures T_H and T_C, leading to

$$G \approx \frac{4}{S_{pn}{}^{2}\sigma\left(T_H - T_C\right)^2}\left(\frac{\left(m+1\right)^2}{m}\right)\left(2\frac{K_T}{K} + 1\right)^2\left(C'''L^2 + C''L + \frac{C_{HX}UL}{F}\right) \quad (5.36)$$
.

Again, the value of m that minimizes G is clearly the load matching condition $m=1$, corresponding to maximum power. Assuming that heat is free, operating at any other load condition results in higher cost. If heat is not free and fuel costs are significant, then a different optimal load condition will balance the capital cost and fuel costs as discussed elsewhere.[126] The exact temperature difference and therefore the exact G, for a load matched ($m=1$) device, can be determined by performing energy balances at the hot and cold junctions. This yields a system of coupled non-linear equations

$$K_H\left(T_H - T_1\right) - K_T\left(T_1 - T_2\right) - \frac{S_{pn}{}^{2}\left(T_1 - T_2\right)T_1}{2R} + \frac{S_{pn}{}^{2}\left(T_1 - T_2\right)^2}{8R} = 0 \quad (5.37a)$$

$$\frac{S_{pn}{}^{2}\left(T_1 - T_2\right)^2}{4R} - K_H\left(T_H - T_1\right) + K_C\left(T_2 - T_C\right) = 0 \qquad (5.37b)$$
,

which can be solved numerically for the temperature difference T_1-T_2.

Equation 5.35 and the approximate form of Eqn. 5.36 are useful for evaluating the overall cost of the thermoelectric system. These expressions allow for direct comparisons between thermoelectric power generation and other electricity generation technologies on the same \$/W basis. The approximations in Eqn. 5.22 and 5.36 will always over-predict the actual temperature difference and power generated. Therefore, the approximate G from Eqn. 5.36 will always be less than the exact value from Eqn. 5.35, making Eqn. 5.36 a lower (*i.e.* optimistic) bound for the \$/W cost of a thermoelectric system.

Using the electric power and the cost of the device, Eqn. 5.35 can be evaluated in units of \$/W as a function of L for a chosen F as shown in Fig. 5.2a for a doped bismuth telluride example (Material ID #2). By selecting a fill factor, an optimum length, L_{opt}, exists which minimizes G. The heat flowing into the hot-side, Q_H, and the thermal efficiency, $\eta=P_{gen}/Q_H$, are determined as a function of leg length as shown in Fig. 5.2b and the electric power density, P_{gen}/A, generated is determined as a function of leg length as shown in Fig. 5.2c. The leg length which minimizes G is different from the leg length that maximizes efficiency or the leg length that maximizes the electric power output. Figure 5.2 shows the difference between designs optimized for efficiency or power and an alternative design that optimizes G.

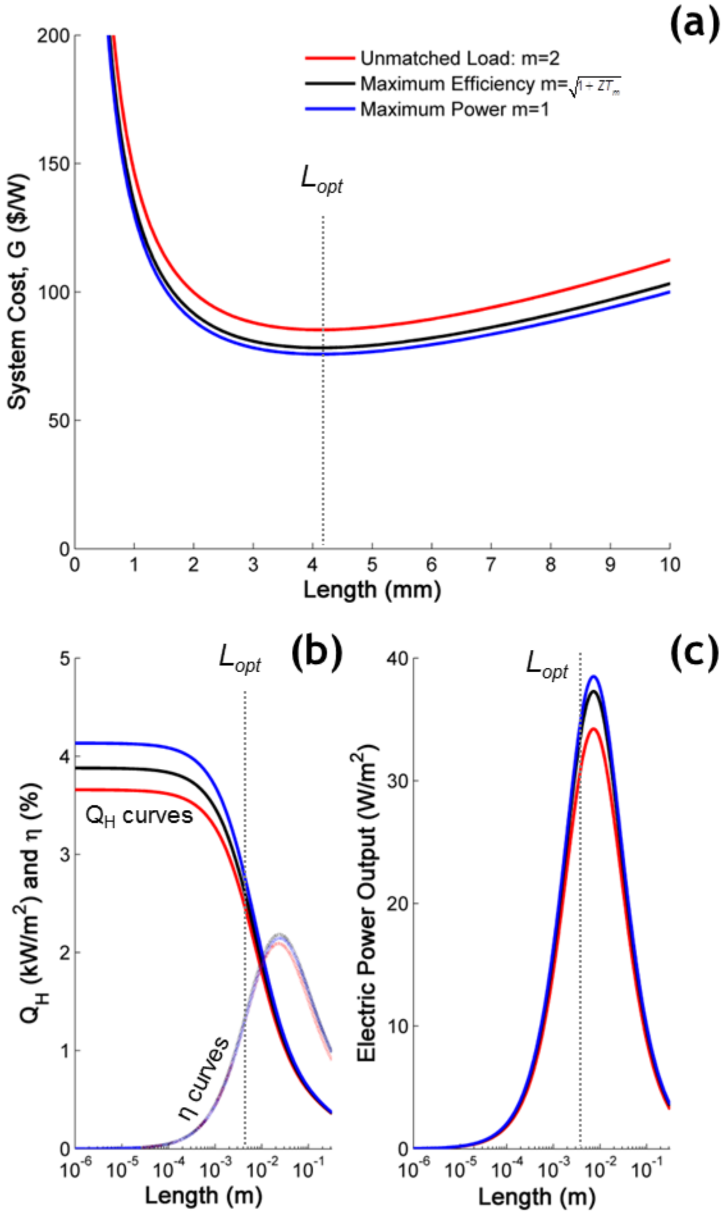

Figure 5.2 System parameters *vs*. thermoelectric leg length. Example of optimum leg length L_{opt} and cost G minimization for power generation using Material ID #2 in Table 5.1 (bulk $Bi_{0.52}Sb_{1.48}Te_3$) with F_{opt}=0.21 and parameters in the Low Temperature Scenario of Table 5.2. The leg length that results in the minimum cost (a: L_{opt}=4.4 mm) is not the same length that maximizes the efficiency (b: $L_{max,\eta}$=24 mm) or output power (c: $L_{max,P}$=7.3 mm). Note (a) is on a linear scale while (b) and (c) are on a log scale. The black and blue η curves in (b) are nearly indistinguishable.

The cost, efficiency, and electric power output are functions of the load condition m as illustrated by the different color lines in Fig. 5.2. In situations where there is excess heat (*i.e.*, fuel/heat is free) the maximum power condition m=1 is most appropriate and yields the lowest cost. In situations where heat is costly, the maximum efficiency condition may be more appropriate. Evaluating fuel costs is beyond the scope of this work but has been investigated elsewhere.[126] The unmatched condition (*i.e.*, m is arbitrary) may also be acceptable depending on the application or cost of power electronic conditioning circuits necessary to load match.

5.2.5.1 Power Generating Electronics

Power electronic conditioning circuits match the resistance of the load to the resistance of the module in order to maintain either the maximum power condition (m=1) or the maximum efficiency condition ($m=\sqrt{1+ZT_m}$). It is useful to consider the additional costs on a \$/W basis for operating at a load condition other than at maximum power, m=1. This cost can be considered the opportunity cost for not properly load matching. Power electronics can be used to load match. If the capital cost of the power electronics system costs more than is recoverable by correcting for the opportunity cost, then it is not cost advantageous to use power electronics. The opportunity cost as a percentage of the capital cost is useful and can be defined as

$$\text{Opportunity Cost} \equiv \frac{G - G|_{m=1}}{G|_{m=1}}. \tag{5.38}$$

Assuming fixed junction temperatures, only terms which are a function of m remain after this normalization. The hot-side heat Q_H from Eqn. 5.2 can be expressed as

$$\frac{Q_H}{K_T\left(T_1-T_2\right)} = 1 + \frac{ZT_1}{m+1} - \frac{Z\left(T_1-T_2\right)}{2\left(m+1\right)^2} \tag{5.39}$$

for generic m with Z representing the *module* figure of merit. Thus, the opportunity cost is

$$\frac{G - G|_{m=1}}{G|_{m=1}} = \frac{G}{G|_{m=1}} - 1 = \frac{\eta|_{m=1}\, Q_H|_{m=1}}{\eta Q_H} - 1. \tag{5.40}$$

By using Eqns. 5.17, and 5.38-5.40, opportunity cost due to operating at a generic m is expressed as

$$\frac{G - G|_{m=1}}{G|_{m=1}} = \frac{\left[\dfrac{ZT_1}{ZT_m + ZT_1 + 4}\right]}{\left[\dfrac{mZT_1}{ZT_m + mZT_1 + \left(m+1\right)^2}\right]} \frac{\left[1 + \frac{1}{2}ZT_1 - \frac{1}{8}Z\left(T_1 - T_2\right)\right]}{\left[1 + \dfrac{ZT_1}{m+1} - \dfrac{Z\left(T_1-T_2\right)}{2\left(m+1\right)^2}\right]} - 1 \tag{5.41}$$

,

where the opportunity cost due to operating at maximum efficiency is

$$\frac{G|_{m=\sqrt{1+ZT_m}} - G|_{m=1}}{G|_{m=1}} = \frac{\left[\dfrac{ZT_1}{ZT_m + ZT_1 + 4}\right]}{\left[\dfrac{\sqrt{1+ZT_m} - 1}{\sqrt{1+ZT_m} + \dfrac{T_2}{T_1}}\right]} \frac{\left[1 + \frac{1}{2}ZT_1 - \frac{1}{8}Z\left(T_1 - T_2\right)\right]}{\left[1 + \dfrac{ZT_1}{\sqrt{1+ZT_m}+1} - \dfrac{Z\left(T_1-T_2\right)}{2\left(\sqrt{1+ZT_m}+1\right)^2}\right]} - 1 \tag{5.42}$$

.

The cost-necessity of these circuits is evaluated in Fig. 5.3. The lack of a proper load condition results in an opportunity cost for power generation which is plotted as a function of ZT_m. The opportunity cost is expressed as a percentage of the capital cost of the device. The m=1 (horizontal blue line) case is the ideal situation where there is no opportunity cost. Other arbitrary load conditions (horizontal red lines) represent different degrees of opportunity costs. The black curve in Fig. 5.3 is the percent difference between G with $m=\sqrt{1+ZT_m}$ and G with m=1; this is the opportunity cost for operating at the maximum efficiency condition rather than the load matched condition. The black circles represent the position of materials considered in this chapter along the maximum efficiency line. For most materials, ZT_m is low enough that operating at the maximum efficiency or maximum power makes little difference. However, at larger ZT_m this difference becomes significant. For a device operating at a condition other than m=1, the opportunity cost is higher, and the added cost of power electronics should be considered. For example, if a material has a ZT_m=1, and throughout normal operation m fluctuates to 1.5 for a large fraction of generating time, then an opportunity cost of 4% of the capital cost is incurred in the absences of conditioning circuits. If the conditioning circuit costs less than 4% of the capital cost of the device, then the additional power delivered warrants the cost of the conditioning circuit. This varies with each material/system as they have different capital costs. For inexpensive systems the additional system cost of conditioning circuits is not justified; whereas, this cost may be justified for expensive systems.

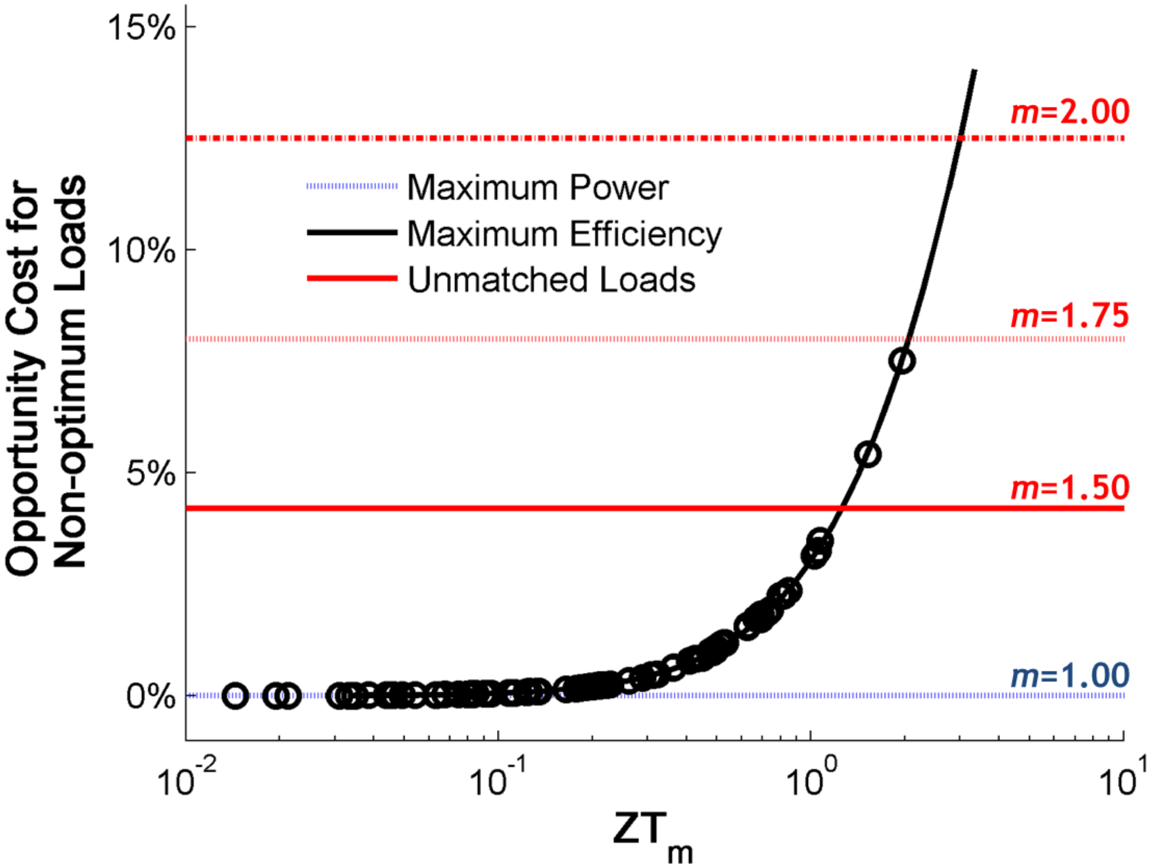

Figure 5.3 Opportunity cost associated with non-optimized load conditions. The opportunity costs are percentages of the total capital cost of the module. Designing the module to operate at the maximum power condition or introducing a power electronics conditioning circuit to load match has appreciable cost benefit. The horizontal lines represent specific load conditions $m=R_L/R$: (blue: m=1) maximum power condition, (black: $m=\sqrt{1+ZT_m}$) maximum efficiency condition, (red: m=1.50, 1.75, 2.00) unmatched load conditions. The circles represent the practical maximum efficiency conditions of the materials investigated in this study. The optimum load is the matched load (m=1), which produced the maximum power and the zero opportunity cost.

5.2.5.2 Levelized Cost of Electricity

The levelized cost of electricity (LCOE) is often used to compare the value of different electricity generating technologies; the lower the LCOE value, the lower the cost to generate electricity.[149] This metric is complex and is typically a function of several variables including the overnight capital cost, the ongoing fuel costs, and the recurring maintenance costs. These costs are spread over the lifetime of the system at a specified capacity factor (uptime) and financial discount rate. The units of LCOE are typically \$/kWh, and determining the LCOE value is application-specific because of the number (and specificity) of input parameters. The analysis in this manuscript only calculates the overnight capital cost of the generator (related to *G*), which is only one input parameter for the LCOE value.

A simplified methodology for calculating the LCOE is presented below which provides a way of converting the \$/W value into a \$/kWh value using more specific parameters which are beyond the scope of this manuscript. First, several input parameters must be selected for a given application and applied to

$$\text{LCOE} = \frac{C + \sum_{t=1}^{n} \frac{\left(F_t + M_t\right)}{\left(1+r\right)^t}}{\sum_{t=1}^{n} \frac{E_t}{\left(1+r\right)^t}} . \qquad (5.43)$$

The terms are as follows: (i) C [\$] = G [\$/W]·P_{gen} [W] is the overnight capital cost, (ii) F_t [\$] is the annual fuel costs, (iii) M_t [\$] is the annual maintenance cost, (iv) r [3%=0.03] is the annual discount rate, (v) α_t [90%=0.90] is the annual capacity factor, (vi) n [yrs] is the system lifetime, and (vii) E_t [kWh] = α_t [%]·P_{gen}[W]·(8.76 [kWh/W]) is the annual energy generated. Here, P_{gen} is the output of the generator in W, and the conversion factor in (vii) is the number of hours in a year divided by 1000 to convert from W to kWh. Systems with low G also tend to have low LCOE. As a simple example, if F_t, M_t, and α are assumed constant, and n is very large, it is easily shown that

$$\text{LCOE} = rG_{eff} , \qquad (5.44)$$

with $G_{eff} = C_{eff} / P_{eff}$, where $P_{eff}=\alpha \cdot P_{gen}$ is the average power output, $C_{eff} = C + \left(F_t + M_t\right)/r$ is an effective capital cost including the present value of all future fuel and maintenance expenses, and r carries units of 1/yr. The limiting form of Eqn. 5.44 illustrates the close relationship between an LCOE analysis and the current G analysis. The simplified expression of Eqn. 5.44 ignores several financial factors, including a corporate tax rate, end-of-life salvage value, and projected system degradation, which other more sophisticated LCOE analyses consider.

5.2.6 Thermoelectric Cooling Cost Metric

The device physics of thermoelectric coolers are similar to those of generators except that electric power is supplied rather than being generated. It is usually desirable to operate thermoelectric coolers at the maximum COP since electricity is continually purchased. For thermoelectric cooling the goal is to maintain a specified temperature difference at the junctions of the module. The hot- and cold-side heat exchangers act as additional thermal resistances. The cold-side junction T_2 needs to be colder than T_C, and the hot-side junction T_1 needs to be hotter than T_H. This over cooling/heating places an extra burden on the thermoelectric module design as the cold-side junction needs to be cooled below the target reservoir temperature. To remove this burden, the thermoelectric junction should be in intimate contact with the object being cooled. Therefore as a simplification, ideal hot-side and cold-side heat exchangers are considered here (*i.e.*, $U=U_H=U_C=\infty$). However, the series thermal resistances of the ceramic plates and metal shunts are still included, so K_H and K_C are finite. This simplification fixes the temperature of the exteriors of the ceramic plates to be the reservoir temperatures. The fill factor F is approximately one because the device should be covered in as much active thermoelectric material as possible in order to pump heat.

Under these simplifications ($U=\infty$, $F=1$), the mean junction temperature is approximated as the mean reservoir temperature, $T_m \approx (T_H+T_C)/2$, enabling an explicit solution for the junction temperatures by performing an energy balance on the cold-side junction. This yields a quadratic equation

$$\begin{aligned}&\left(-\frac{S_{pn}{}^2\sqrt{1+ZT_m}}{R\left(\sqrt{1+ZT_m}-1\right)^2}\right)T_2{}^2+\\ &\left(\frac{S_{pn}{}^2T_m\left(\sqrt{1+ZT_m}+1\right)}{R\left(\sqrt{1+ZT_m}-1\right)^2}+K_T+\frac{K_C}{2}\right)T_2+\\ &\left(\frac{-S_{pn}{}^2T_m{}^2}{R\left(\sqrt{1+ZT_m}-1\right)^2}-K_TT_m-\frac{K_CT_C}{2}\right)=0\end{aligned} \tag{5.45}$$

for which the smallest root is the cold-side junction temperature, and the hot-side junction temperature is determined using $T_1 \approx 2T_m - T_2$. These junction temperatures are used to determine the COP and supplied power $P_{sup.}$

$$\mathrm{COP}=\frac{T_2}{T_1-T_2}\left[\frac{\sqrt{1+ZT_m}-{T_1}/{T_2}}{\sqrt{1+ZT_m}+1}\right] \tag{5.46}$$

$$P_{sup}=\frac{2S_{pn}{}^2\left(T_1-T_2\right)^2}{R\left(\sqrt{1+ZT_m}-1\right)} \tag{5.47}$$

Both of these equations are functions of leg length and can be evaluated numerically.

Just like thermoelectric generators, there is a tradeoff between the capital cost of the module and the efficiency. In order to reduce the capital cost of the module, shorter leg lengths are used. However, this reduces the efficiency of the thermoelectric cooler. Since thermoelectric coolers consume electricity and provide a cooling service, the cost of electricity is important, so a thermoelectric module with a large coefficient of performance, COP, is desirable. The COP is the ratio of the cooling power removed from the cold-side to the electric power consumed. Electricity is purchased on a $/kWh$_e$ basis, so the most appropriate metric is the operating cost expressed in units of $/kWh$_{th}$ where the subscripts represent electric and thermal (cooling) energy, respectively. The capital cost of the thermoelectric cooler is amortized over the lifetime and added to the operating cost. Operating continuously and purchasing electricity hourly over the lifetime allows for a simplification in the amortization where the capital cost is multiplied by the amortization (discount) rate, *r*, on an hourly basis. This allows for both capital cost and operating costs to be considered for cooling applications. The appropriate operating cost metric is

$$H=\frac{C_e}{\mathrm{COP}}+r\frac{C}{\mathrm{COP}\cdot P_{sup}}, \tag{5.48}$$

where C_e represents the price of electricity. The price of electricity varies. In the United States,[37] the average industrial user purchases electricity at a price of \$0.068/kWh$_e$, and residential users purchase electricity at a price of \$0.12/kWh$_e$. The average price of electricity is taken as \$0.098/kWh$_e$ in this analysis and is bounded by the industrial and residential prices (*i.e.* the error bars). The product of the COP and P_{sup} is the thermal cooling power delivered, in kW$_{th}$, and yields the thermal energy delivered in kWh$_{th}$ once divided by *r*. Finally, using the cost expression in Eqn. 5.34 and neglecting the cost of the heat exchanger (*i.e.*, C_{HX}=\$0.00/(W/K)), the cooling cost metric can be expressed as

$$H=\frac{C_e}{\mathrm{COP}}+r\frac{C'''L^2+C''L}{\frac{1}{2}S_{pn}{}^2\sigma\left(T_1-T_2\right)^2}\frac{\sqrt{1+ZT_m}-1}{\mathrm{COP}} \tag{5.49}$$

where the junction temperature difference and COP are determined by solving the quadratic equation in Eqn. 5.45. In power generation and thermoelectric cooling, the thermal conductance of the device, the electrical resistance, and overall cost are complex functions of the leg length *L* and fill factor *F*.

5.2.6.1 Thermoelectric Cooling Coefficient of Performance

The analysis for thermoelectric cooling is similar to the analysis of a thermoelectric generator with the same approximations: (i) thermal and electrical contact/junction resistance are negligible, (ii) the cross-sectional areas are constant along the length of each leg, (iii) the material properties *S*, *k*, σ, and *Z* are evaluated at the mean temperature and are temperature independent near this nominal temperature, and (iv) the electrical resistance of the metallization layer and shunt are negligible.

For the cooling analysis, the resistive load in the dual leg thermoelectric generator in Fig. 5.1 is replaced with a voltage supply, V_{sup}, which drives the current in the reverse direction of the arrows in Fig. 5.1. The thermoelectric cooler coefficient of performance, COP, relates the cooling power removed from the cold-side to the electrical power supplied.

$$\mathrm{COP}=\frac{Q_C}{P_{sup}} \tag{5.50}$$

The electric power supplied can be expressed as a function of current, thermopower, and module resistance

$$P_{sup}=\left(S_{pn}\left(T_1-T_2\right)+IR\right)I=S_{pn}I\left(T_1-T_2\right)+I^2R. \tag{5.51}$$

The cooling power removed from the cold-side can be determined by a net energy balance of the cold-side node T_2 under reverse bias

$$Q_C=S_{pn}T_2I-K_T\left(T_1-T_2\right)-\tfrac{1}{2}I^2R. \tag{5.52}$$

Combining Eqns. 5.50-5.52, the COP can then be expressed as

$$\mathrm{COP} = \frac{S_{pn} T_2 I - K_T \left(T_1 - T_2\right) - \frac{1}{2} I^2 R}{S_{pn} I \left(T_1 - T_2\right) + I^2 R}. \tag{5.53}$$

Simplifying this equation by introducing *f* yields

$$f \equiv \frac{IR}{S_{pn}} = \frac{V_{sup}}{S_{pn}}, \tag{5.54}$$

$$\mathrm{COP} = \frac{f T_2 - \frac{1}{2} f^2 - K_T R \frac{\left(T_1 - T_2\right)}{S_{pn}^{\ 2}}}{f\left(T_1 - T_2\right) + f^2}. \tag{5.55}$$

This is the most general COP equation and the *module* figure of merit defined in Eqn. 5.11 can be re-introduced.

$$\mathrm{COP} = \frac{f T_2 - \frac{1}{2} f^2 - \left(T_1 - T_2\right)/Z}{f\left(T_1 - T_2\right) + f^2} \tag{5.56}$$

It is also useful to determine the maximum COP which is accomplished in an analogous manner to the maximum efficiency given there is no parallel leakage heat loss (*i.e.*, $K_{||} = 0$ and $K_T = K_{TE}$), and the optimized geometry of Eqns. 5.13 are used. The result is

$$f_{max} = \frac{\left(T_1 - T_2\right)}{\sqrt{1 + Z\overline{T_m}} - 1} \Rightarrow \left(\mathrm{COP}\right)_{max} = \frac{T_2}{\left(T_1 - T_2\right)} \left[\frac{\sqrt{1 + Z\overline{T_m}} - T_1 / T_2}{\sqrt{1 + Z\overline{T_m}} + 1} \right]. \tag{5.57}$$

5.2.6.2 Amortized Capital Cost

For most cooling applications, the cost of electricity over the lifetime of the module dominates the overall cost. An example of a typical commercial TE module[†] illustrates this point. The module costs \$16.60 and consumes 45 W_e of electric power. It would cost \$775 to operate this continuously for 20 years at a fixed price of \$0.098/kWh_e. It is appropriate to amortize the cost of the module over the lifetime and add this to the cost of electricity since the module cost is not negligible. The capital cost is normalized by the power consumption, CAP=\$16.60/0.045kW_e=\$368.89/kW_e, and divided into payments, PMT, with the appropriate amortized payment period being hourly since electricity is sold on a kWh_e basis. This is expressed as

$$\mathrm{PMT} = \mathrm{CAP} \frac{r\left(1 + r\right)^n}{\left(1 + r\right)^n - 1}, \tag{5.58}$$

where *r* is the period discount rate taken at 3% annually or 0.00034% hourly (using simple interest) corresponding to an average inflation rate, and *n* is the number of hours in 20 years (*i.e.*, 175,200 hours in 20 years). Since this approaches the limit of large *n* (*i.e.*, amortized continuously), this expression simplifies to PMT ≈ *r*CAP, so 0.00034% of the normalized capital cost is added to the cost of electricity. In the current example of a commercial module, the amortized cost is \$0.0013/kWh_e which is 1.3% of the cost of electricity. Because the uncertainty

---

[†] Custom Thermoelectric, Inc., Part #: **12711-5L31-03CQ** http://www.customthermoelectric.com/tecs_Qcmax.html

in the projected price of electricity over time (especially due to regional and seasonal variations) is much larger than this amortization, accounting for the capital cost of the module becomes more important in modules requiring expensive materials or manufacturing techniques.

5.2.7 Cost Considerations

In addition to the device physics, both material and manufacturing costs influence the overnight system cost. The cost, C in Eqns. 5.35 and 5.48, is a function of the bulk raw material cost C_B [\$/kg], the processing bulk material cost $C_{M,B}$ [\$/kg], the areal manufacturing cost $C_{M,A}$ [\$/m^2], and the cost of both heat exchangers C_{HX} [\$/(W/K)] as summarized in Table 5.2.[‡]

The overall cost C is also dependent on the heat exchanger heat transfer coefficient U, the density of the active material ρ, the leg length, and area of the ceramic plates, A:

$$C = \left(\underbrace{(C_B + C_{M,B})\rho L}_{C'''} + \underbrace{C_{M,A}}_{C''} \right) AF + C_{HX} UA \qquad (5.59)$$

The collection of terms in the first expression is a volumetric cost C''' [\$/m^3], and the second term is an areal cost C'' [\$/m^2] as discussed with Eqn. 5.34. The cost of the extracted raw, bulk material C_B captures the fundamental differences in material costs. The material cost is determined from the 2011 price of each element as reported by the U.S. Geological Survey; it is based on the worldwide production of the element and represents the average price an industrial consumer would pay.[150] Manufacturing costs are divided into two categories based on the method of material processing. Processes enacted on the entire bulk volume of material such as ball milling and spark plasma sintering have costs denoted by $C_{M,B}$. Other processes like dicing and metallization depend on the area of material processed; these costs are indicated by $C_{M,A}$. The cost is calculated by dividing the equipment capital cost by the equipment lifetime and throughput.

The materials in Table 5.1 are separated by common material types: chalcogenides, silicides, clathrates, half heusler alloys, skutterudites, and oxides. The polymer PEDOT:PSS, doped with DMSO, was also included.[151] The areal manufacturing costs associated with the polymer material are unique since a polymer device would likely be made using a process like screen printing. A solution printing process can also be used for the metallization layer in these cases, eliminating the need for dicing. Hence, $C_{M,A}$ for polymer or solution-processed materials could be significantly lower than other materials.

The costs of heat exchangers are typically reported in units of dollars per thermal conductance [\$/(W/K)] which can be expressed in units of [\$/m^2] by multiplying C_{HX} by the heat exchanger's U-value. The resulting areal cost of real heat exchangers[1] is linear with the U-value as shown in Fig 5.4. Approximating each line as passing through the origin, the slope is the C_{HX} value for that class of heat exchangers and for that specific design demand conductance (*i.e*,

---

[‡] Justification for cost estimates can be found in Saniya LeBlanc, Shannon K. Yee, Matthew L. Scullin, Chris Dames, and Kenneth E. Goodson, "Material and Manufacturing Cost Considerations for Thermoelectrics," submitted, 2013.

$Q/(T_H-T_I)$); different heat exchanger types and different design requirements will have different C_{HX} values.

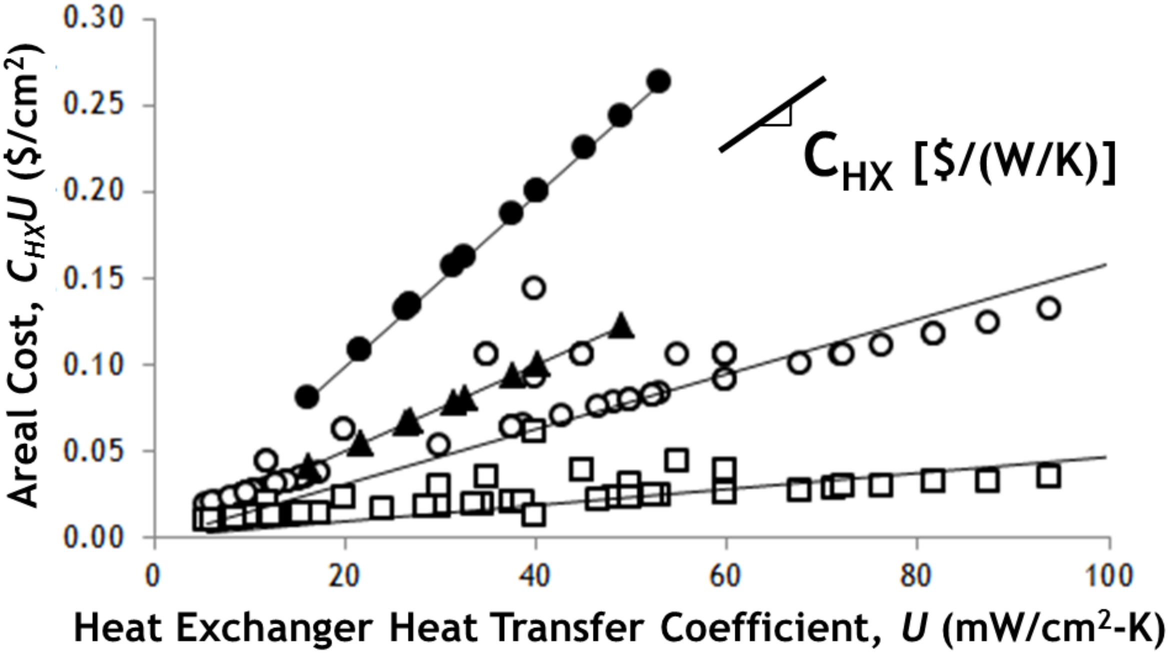

Figure 5.4 Heat exchanger costs. Typical areal cost as a function of heat transfer coefficient for tube and shell (open points) and plate and fin heat exchangers (solid points). The cost depends on the heat flow Q_H and temperature difference (T_H-T_I). For K_H= $Q_H/(T_H-T_I)$= 5 kW/K (circles), 10 kW/K (triangles), and 30 kW/K (squares). Data extracted from Ref. 148.

Table 5.1 Material Identification Table. Color coding identifies material types: red for chalcogenides and SiGe, blue for silicides, purple for clathrates, green for skutterudites, black for oxides, yellow for half heuslers, and grey for others

Material Class	**ID #**	**Material Name**	**Manufacturing Class**	**Density**	**Mat'l. and Manu. Costs**			**Ref.**
				ρ (kg/m^3)	C_B (\$/kg)	$C_{M,B}$ (\$/kg)	$C_{M,A}$ (\$/m^2)	
Chalcogenides & SiGe	1	Bi_2Te_3	Bulk	8098	109.85	0.00	168.23	151,152
	2	$Bi_{0.52}Sb_{1.48}Te_3$	Bulk	6900	125.47	0.00	168.23	153
	3	$Bi_{0.52}Sb_{1.48}Te_3$	Nanobulk	6900	125.47	2.03	168.23	153
	4	$Bi_{0.54}Te_{0.46}$	Nanowire	8582	83.77	1,072.96	168.23	154
	5	$(Na_{0.0283}Pb_{0.945}Te_{0.9733})(Ag_{1.11}Te_{0.555})$	Nanobulk	9214	81.14	0.06	168.23	155
	6	Bi-doped $PbSe_{0.98}Te_{0.02}/PbTe$	Superlattice	8820	55.10	3,9911.10	168.23	156
	7	$AgPb_{18}SbTe_{20}$	Bulk	9273	83.81	0.00	168.23	157
	8	SiGe	Bulk	4486	678.76	0.00	168.23	158
	9	$Si_{80}Ge_{20}$	Nanobulk	3504	371.00	1.10	168.23	158
	10	SiGe	Nanowire	4486	678.76	1,072.96	168.23	159
Silicides	11	$Mg_2Si_{0.85}Bi_{0.15}$	Nanobulk	4309	6.67	1.10	168.23	160
	12	$Mg_2Si_{0.6}Sn_{0.4}$	Bulk	4166	4.04	0.00	168.23	161
	13	Si	Nanobulk	2330	3.09	1.10	168.23	162
	14	Si	Nanowire	2330	3.09	1,072.96	168.23	163
	15	$MnSi_{1.75}$	Bulk	5022	1.46	0.00	168.23	164
	16	$Mn_{15}Si_{28}$	Nanobulk	4210	1.51	1.10	168.23	164
Clathrates	17	$Ba_8Ga_{16}Ge_{28}Zn_2$	Bulk	5068	615.03	1.26	168.23	165
	18	$Ba_8Ga_{16}Ge_{30}$	Bulk	5015	644.02	0.06	168.23	166
	19	$Ba_7Sr_1Al_{16}Si_{30}$	Bulk	3240	1.64	0.01	168.23	167
Skutterudites	20	$CeFe_4Sb_{12}$	Bulk	6776	37.45	1.26	168.23	168
	21	$Yb_{0.2}In_{0.2}Co_4Sb_{12}$	Bulk	7683	23.95	1.26	168.23	169
	22	$Ca_{0.18}Co_{3.97}Ni_{0.03}Sb_{12.40}$	Bulk	6491	13.23	1.10	168.23	170
Oxides	23	$(Zn_{0.98}Al_{0.02})O$	Bulk	5920	2.30	1.10	168.23	171
	24	$Ca_{2.4}Bi_{0.3}Na_{0.3}Co_4O_9$	Bulk	5559	30.01	1.10	168.23	172
	25	InGaZnO	Nanowire	6875	510.59	1,072.96	168.23	155
	26	$Na_{0.7}CoO_{2-\delta}$	Bulk	5387	36.37	0.00	168.23	173
Half-Heuslers	27	$Zr_{0.25}Hf_{0.25}Ti_{0.5}NiSn_{0.994}Sb_{0.006}$	Bulk	8296	9.71	0.01	168.23	174
	28	$Zr_{0.5}Hf_{0.5}Ni_{0.8}Pd_{0.2}Sn_{0.99}Sb_{0.01}$	Bulk	9335	8.51	1.26	168.23	175
	29	$Ti_{0.8}Hf_{0.2}NiSn$	Bulk	8077	10.70	0.00	168.23	176
Polymer	30	PEDOT:PSS	Polymer	1500	0.34	0.00	4.76	177

5.3 Thermoelectric Cost Analysis Results and Discussion

With knowledge of thermoelectric costs and device physics, the coupled thermoelectric cost performance (both power generation and cooling) can be analyzed. The analysis of thermoelectric power generation is particularly interesting as it suggest new design for thermoelectrics that minimize the \$/W cost. Specifically, a non-dimensionalization of the governing cost function, *G*, provides new insight into thermoelectric tradeoffs. This insight can then be applied to promising thermoelectric materials to ultimately compare thermoelectric options for specific applications. In this analysis, one refrigeration application and four power generation applications were considered as summarized in Table 5.2

For hybrid organic-inorganic materials or polymer-based materials, this analysis suggests new geometries and future directions for low cost thermoelectric power generation.

Table 5.2 Scenario parameters, device temperatures, *U*-values, and heat exchanger (HX) costs. Representative applications are provided for each temperature scenario.

Applications	Thermoelectric cooling	Low temperature recovery	Solar thermal generator	Automotive exhaust heat recovery	Industrial furnace heat recovery
Scenario Temperature	(Cooling)	**Scenario #1** Low	**Scenario #2** Medium-Low	**Scenario #3** Medium-High	**Scenario #4** High
Hot-side temperature, T_H (°C)	15	100	250	500	800
Cold-side temperature, T_C (°C)	5	20	20	50	50
Average temperature, T_m (°C)	10	60	135	275	425
Hot-side *U*-value, U_H (W/m^2-K)	∞	102	102	120	120
Cold-side *U*-value, U_C (W/m^2-K)	∞	105	105	105	105
HX & Plate Costs, C_{HX} (\$/(W/K))	-	18.48	18.48	18.48	18.48

5.3.1 Non-dimensionalization

G captures the coupled economic and thermal-electrical nature of the technology. To provide additional insight I simplify the analysis using non-dimensionalization and scaling arguments. First, it is necessary to identify the pertinent dimensionless groups, summarized in Table 5.3. In many applications the heat exchangers (and therefore the *U*-value) and the thermoelectric material (and therefore *k*) are pre-selected and held as design constants. As a result the thermal length L_T (Eqn. 5.25) is often fixed, so I adopt it as the main normalizing factor, indicated with an over-tilde. The first dimensionless group is

$$\tilde{L} \equiv \frac{L}{L_T} = \frac{UL}{k}, \qquad (5.60)$$

which can also be referred to as a device Biot number. This group quantifies the distribution of the temperature drops in the device. At the thermal impedance matching condition, $\tilde{L}=2F$. For $\tilde{L}>2F$, the temperature drop is primarily across the module while, for $\tilde{L}$ less than this, the temperature drop is primarily across the heat exchangers.

Another useful length scale is the module cost length, L_C [m], defined as the ratio of the module's areal and volumetric costs

$$L_C \equiv \frac{C''}{C'''} . \qquad (5.61)$$

Referring to the total cost in Eqn. 5.34, when $L_C >> L$ the module's volumetric costs can be neglected. When $L_C << L$ the module's areal costs can be neglected. L_C can be normalized by L_T to form another helpful group,

$$\tilde{\ } \qquad L_T \qquad \frac{C''}{C'''}\frac{U}{k} . \qquad (5.62)$$

Finally, the last useful length is the ratio of the heat exchanger areal cost to the module volumetric cost, termed the heat exchanger cost length, L_{HX} [m]

$$L_{HX} \equiv \frac{C_{HX}U}{C'''} . \qquad (5.63)$$

Referring to Eqn. 5.33, when $L_{HX} << LF$, the heat exchanger costs can be neglected compared to the module's volumetric costs. When $L_{HX} >> LF$, the heat exchanger cost dominates the module's volumetric costs. Normalizing to L_T gives the dimensionless group

$$\tilde{\ } \qquad L_T \qquad = \frac{C_{HX}U}{C'''}\frac{U}{k} . \qquad (5.64)$$

These three dimensionless groups help simplify Eqns. 5.35 and 5.36. To proceed with an exact solution, the temperature drop across the thermoelectric legs (*i.e.,* T_1-T_2) can be solved numerically from the non-linear system Eqn. 5.37. However, to retain analytical insight with only a modest loss of accuracy, I proceed by invoking the same approximations used in Eqn. 5.22. As discussed earlier, this approximation gives a lower bound on the costs. With the help of Eqns. 5.36, 5.60-5.64, the cost can now be expressed as a product of dimensionless groups

$$\frac{G}{G_0} \approx \frac{1}{4}\left(\frac{(m+1)^2}{m}\right)\bigl(2F + \tilde{\ } \qquad \tilde{\ } \quad \tilde{\ } , \qquad (5.65)$$

where

$$G_0 = \frac{16C'''L_T{}^2}{S_{pn}{}^2\sigma(T_H - T_C)^2} , \qquad (5.66)$$

and $\tilde{L}_C$ and $\tilde{L}_{HX}$ are understood to be constants once a material and heat exchangers have been selected.

The parameter G_0 has units of \$/W and can be used as a new cost-performance metric for comparing thermoelectrics. This metric incorporates the material cost, application temperatures, heat exchanger performance, and thermoelectric material properties. Ultimately, the minimum value of G determines the cost when comparing power generating options. However, since G_0 is a characteristic scale for G, comparing G_0 values can also be useful. Furthermore, when a system is dominated by its material costs, and F is limited while L is arbitrary, the optimization for G yields $G=4G_0F^2$. The values for G and G_0 can differ by orders of magnitude; G_0 represents the material cost while G represents the entire system cost.

While G_0 arose naturally from the mathematics, it can also be recast in a more intuitive form

$$G_0 = \frac{C''' L_T A}{\frac{1}{4} Z T_H \left(\frac{T_H - T_C}{T_H} \right)} \frac{1}{UA\left(T_H - T_C\right)} \qquad (5.67)$$

.

This form is readily seen to be the natural scale for G of a thermally-impedance matched system ($L=2FL_T$) with $F=1$ and dominated by the material's volumetric costs. For such a system, the numerator of the first term is the material cost, while the denominator of the first term is a scale for the system efficiency in the small ZT limit (Eqn. 5.19). Furthermore, the denominator of the second term gives a measure of the heat flow [W] that can be delivered by this application. To achieve small G_0, a low volumetric cost and low thermal conductivity are necessary. The device must also have large ZT and therefore high efficiency. Finally, the heat exchangers should have large U-values in order to allow for large thermal power density.

Table 5.3 Summary of key dimensional and non-dimensional quantities.

	Module Length	**Module Areal Cost**	**Heat Exchanger Cost**
Dimensional [m]	$L \quad , \quad L_T \equiv \frac{k}{U}$	$L_C \equiv \frac{C''}{C'''}$	$L_{HX} \equiv \frac{C_{HX}U}{C'''}$
Non-dimensional	$\tilde{L} \equiv \frac{L}{L_T} = \frac{UL}{k}$	$\tilde{\imath} \quad L_T \quad \frac{C''}{C'''}\frac{U}{k}$	$\tilde{\imath} \quad L_T = \frac{C_{HX}U}{C'''}\frac{U}{k}$

5.3.2 Cost-Performance Optimization

We now consider the minimization of G with respect to the design parameters m, L, and F. The m optimization is trivial and Eqns. 5.36 and 5.65 are minimized for $m=1$. But, what are the optimal values of L and F? To answer this question, Figure 5.5 depicts a G-surface as a function of F and L. Although Fig. 5.5 is generated using realistic properties based on a Bi_2Te_3 application (see caption), the figure can also be cast using universal, material-independent axes (see section 5.3.2.4). This figure shows there is no global minimum in the $G(\tilde{L},F)$ function, excluding the impractical $\tilde{\imath}$ =0 and F=0 point where there is no device. However, there is a trough along the thermal impedance matching line $2F=\tilde{\imath}$. Whereas $\tilde{\imath}$ or F approaches zero, G approaches $8G_0\tilde{L}_{HX}$. This trough results from a competition between cost and thermoelectric performance. As the device is made thinner (smaller L at constant F), or the leg density more sparse (smaller F at constant L), less material is used, thus reducing the cost. However, decreasing $\tilde{L}$ at fixed F also reduces the temperature drop across the device, resulting in less electrical power generated. Similarly, as the device is made sparse (smaller F, fixed L), the internal electrical resistance increases, and less electrical power is generated. This is another example of the trade-off between cost and power output: a lower power device may be preferred if the cost savings are good enough on a \$/W basis.

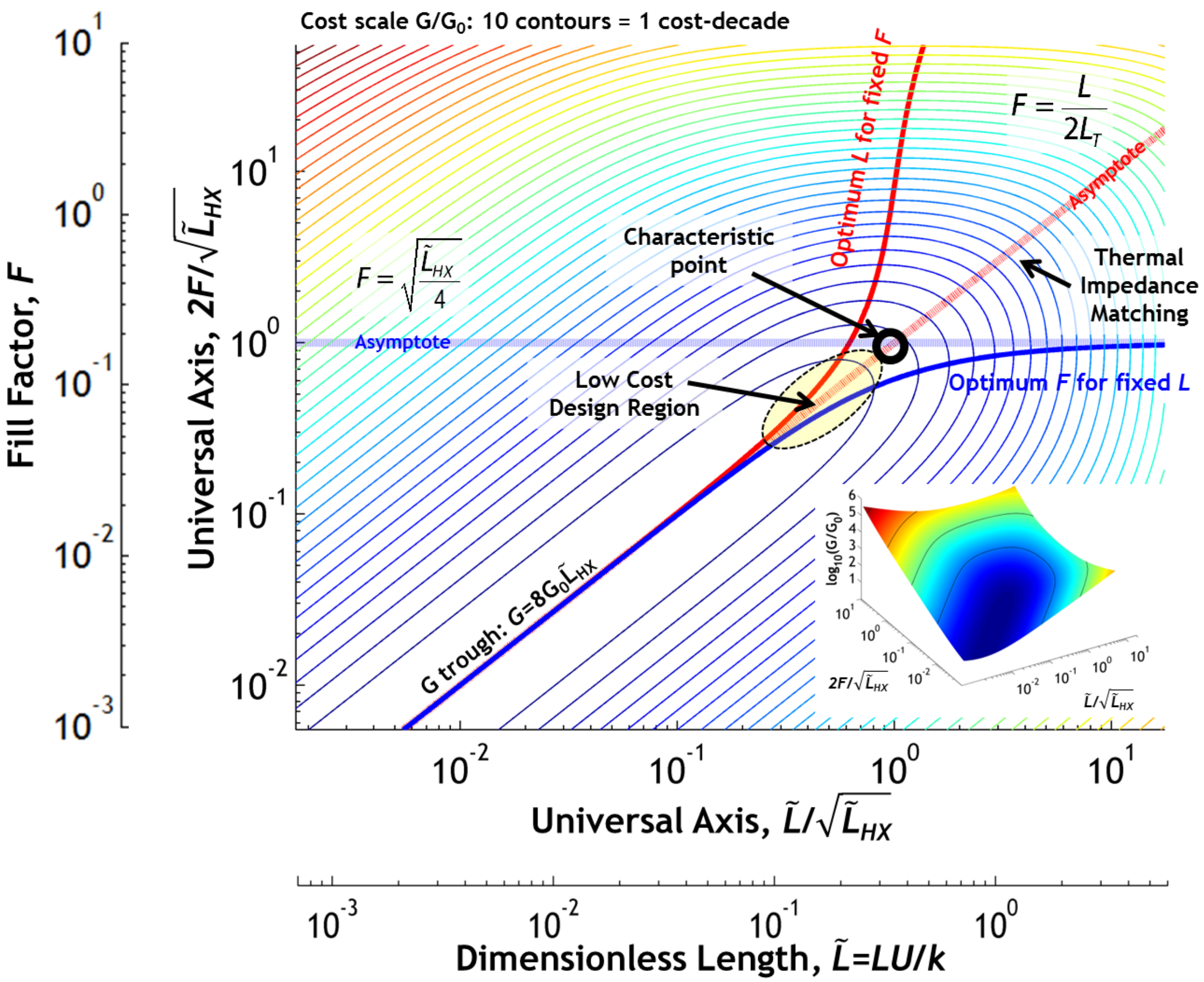

Figure 5.5 Example cost-design field for Bi$_2$Te$_3$.[152, 153] This figure was calculated for a specific application of Bi$_2$Te$_3$ (outer pair of axes). As discussed in the text, this G surface can also be expressed in a material-independent form using scaled universal axes (inner pair). The parameters are: S_{pn}=464 µV/K, σ=682 S/cm, k=1.57 W/m-K, C'''=\$0.89/cm^3, C''=\$0.017/cm^2, C_{HX}=\$18.48/(W/K), U=100 W/m^2-K, T_H=100 °C, T_C=20 °C. The contours represent lines of constant G/G_0 as given by the surface in the inset. For fixed F, optimizing G with respect to L gives the dark red curve; likewise, optimization at fixed L gives the dark blue curve. Both converge at low F and L. The characteristic point is taken as the intersection of the two asymptotes (light lines). The low cost design region is along the thermal impedance matching line $F=L/(2L_T)$ but below the characteristic point; there is little further benefit in G if F and L are decreased further.

While there is no minimum in G, there is a point of diminishing returns. This is a characteristic point below which further decreasing L or F has only marginal benefit, and this point will be discussed more fully in section 5.3.2.3. First, consider minimizing G with respect to F while holding L fixed. After solving $\left.\frac{\partial G}{\partial F}\right|_L = 0$, the resultant condition on F is the solid blue line in Fig. 5.5 given as

$$F_{opt} = \frac{\sqrt{\text{[illegible]}}}{4(\text{[illegible]}} . \qquad (5.68)$$

For small and large L this can be approximated as

$$\begin{aligned} L \to 0: &\quad F_{opt} = \frac{L}{2L_T} \quad \underset{m=1}{\Rightarrow} \quad G\big|_{F=F_{opt}} \approx 8G_0\tilde{L} \\ L \to \infty: &\quad F_{opt} = \sqrt{\frac{\tilde{L}}{4}} \quad \underset{m=1}{\Rightarrow} \quad G\big|_{F=F_{opt}} \approx G_0\left(\frac{L}{L_T}\right)^2 . \end{aligned} \tag{5.69}$$

Similarly, minimizing G with respect to L for fixed F gives the solid red line in Fig. 5.5 and

$$L_{opt} = \frac{4FL_T\sqrt{F\tilde{L}}}{\sqrt{F\tilde{L}}} \quad , \tag{5.70}$$

which can be approximated for small and large F as

$$\begin{aligned} F \to 0: &\quad L_{opt} = 2L_T F \quad \underset{m=1}{\Rightarrow} \quad G\big|_{L=L_{opt}} \approx 8G_0\tilde{L} \\ F \to \infty: &\quad L_{opt} = L_T\sqrt{F\tilde{L}} \quad \underset{m=1}{\Rightarrow} \quad G\big|_{L=L_{opt}} \approx 4G_0F^2 \end{aligned} \tag{5.71}$$

The two optimum conditions (Eqn. 5.68 and 5.70) converge at low values of L and F along the design condition

$$2F = \frac{L}{L_T} = \tilde{L} , \tag{5.72}$$

which is exactly the thermal impedance matching condition in Eqn. 5.25 and the light red line in Fig. 5.5. Under this condition and the load matching condition m=1, Eqn. 5.36 simplifies to

$$\left.\frac{G}{G_0}\right|_{\tilde{L}} \approx 4\left(4F^2 + 2\tilde{L} \quad ,\right. \tag{5.73}$$

or equivalently

$$\left.\frac{G}{G_0}\right|_{F=\frac{\tilde{L}}{2}} \approx 4(\tilde{L} \quad , \tag{5.74}$$

which shows G as a direct function of either F or L (the latter through $\tilde{L}=L/L_T$). These forms are useful because they highlight the benefit of reducing F and L together to minimize G. The three terms in Eqn. 5.73 and 5.74 can be tracked back to Eqn. 5.34. The first term represents the module volumetric cost, the second term represents the module areal cost (*i.e.*, $\tilde{L}$), and the third term represents the heat exchanger cost (*i.e.*, $\tilde{L}$).

5.3.2.1 Example Calculation for Bi_2Te_3

To illustrate this new framework, I present an example calculation for Bi_2Te_3 using the material and application properties given in the caption of Fig. 5.54 and comparing the exact (Eqn. 5.35: numerical) and approximate (Eqn. 5.36: analytical) calculations. This same analysis is applied to 30 materials and 4 different applications shortly. By way of illustration for Bi_2Te_3, I perform the approximate analysis for a fixed fill factor of F_{opt}=0.18, whose origin will be shown later in Eqn. 5.78. At this F, Eqn. 5.70 gives an optimum leg length of L_{opt}=3.5 mm, and Eqn. 5.36 returns a minimum cost of G=\$55.45/W. For this same fill factor of 0.18, the exact analysis

(Eqn. 5.35) can be evaluated using the exact junction temperatures. This numerical solution now gives L_{opt} = 4.5 mm and a minimum cost of G=\$97.64/W. While these \$/W values may appear large, they incorporate the entire system cost including a specified heat exchanger (with U=100 W/m^2-K at a cost of C_{HX}=\$18.48/(W/K)). The scenario of a free heat exchanger will yield much smaller \$/W values and is presented later. Furthermore, this scenario has a very modest reservoir temperature difference of 80 °C, and G scales as $\left(T_H - T_C\right)^{-2}$. The approximate cost always under predicts the exact calculation, providing a lower (*i.e.,* optimistic) bound for what is achievable. This level of agreement between approximate and exact analyses is typical for materials with ZT~1, and I have confirmed that the two analyses converge as $ZT \rightarrow 0$, consistent with the discussion around Eqn. 12. This agreement to within tens of percent confirms that the analytical simplifications made above are reasonable and prove helpful both for physical insight and for rapid screening of candidate materials.

As long as L_{opt} and F_{opt} are practically achievable (*e.g.*, manufacturable, have sufficient mechanical robustness, *etc.*) for the application, the total cost is limited only by the heat exchanger, and this design would approach the best possible \$/W given the input parameters. On the other hand, if these calculated values of L_{opt} and/or F_{opt} are considered impractically small (*e.g.*, due to manufacturability, mechanical robustness, non-negligble contact resistances or thermal parasitics, *etc.*), then the optimization must be repeated with the minimum allowable L and/or F (see heavy blue and/or red lines in Fig. 5.5), and the cost contributions from C'' and/or C''' can no longer be neglected in the final design.

5.3.2.2 Special Case: "Free" Heat Exchanger and Prescribed *F*

In some cases it may be appropriate to exclude the cost of the heat exchangers when performing the overall \$/W optimization. For example, the cost of the heat exchangers may be excluded when incorporating thermoelectric power generation into a solar hot water heater since the heat exchanger hardware already exists. This scenario is instructive because it isolates the cost of only the thermoelectric module. However, even a small heat exchanger cost can have a dramatic effect on the system optimization, including L, F, and G, so proper cost accounting is essential.

In this special case, the third term in the cost equation can be dropped, and Eqn. 5.36 reduces to

$$\frac{G}{G_0} \approx \frac{1}{4}\left(\frac{(m+1)^2}{m}\right)\left(2F + \tilde{L} \right. \qquad (5.75)$$

In contrast to Eqn. 5.36 and Fig. 5.5, Eqn. 5.75 does not exhibit an optimum or even a diminishing returns region in its $G(\tilde{L}, F)$ surface. Therefore, I focus on situations where the value of F is fixed. For example, F can be fixed by some other practical constraint excluded from the above analysis (*e.g.*, mechanical robustness, parasitic heat losses, manufacturability, *etc.*), or it can be fixed to the asymptotic value in Fig. 5.5. Holding F fixed and optimizing for L yields

$$L_{opt} = \frac{4L_T F}{1+\sqrt{1+16F/\tilde{L}}} , \qquad (5.76)$$

which is a simplification of Eqn. 5.70 with $\tilde{L}_{HX}$=0. This optimum leg length produces the best cost-power tradeoff for a fixed *F* and "free" heat exchanger. Making the leg length longer than this increases the cost *C*. Making the legs shorter, while reducing *C*, reduces the temperature drop across the module and therefore decreases the power.

In this fixed-*F* condition the limiting behavior for large and small $\tilde{L}_C$ is

$$\begin{array}{lll} & m=1 & L_{opt} \\ & m=1 & =L_{opt} \approx 4G_0F^2 \end{array} \tag{5.77}$$

In the large $\tilde{L}_C$ limit, the thermal impedance matching condition is recovered: since the total cost is dominated by the *C''* term, there is no additional cost penalty in setting *L* equal to the full thermal-impedance-matched value to maximize power. In the small $\tilde{L}_C$ limit, L_{opt} is the geometric mean of FL_T and L_C, which reflects the compromise between thermal efficiency and cost. In this case, a smaller *G* is achieved by reducing *L* well below the thermal-impedance-match value of $2FL_T$ with the reduction in power more than offset by the reduction in cost. The optimum leg length and cost results of Eqns. 5.75 and 5.76, along with their asymptotic approximations from Eqn. 5.77, are shown in Fig. 5.6 in non-dimensional form. Consistent with the criteria of Eqn. 5.77, the transition between these extremes happens around $L_C \approx FL_T$ (that is, $\tilde{L}_C \approx F$).

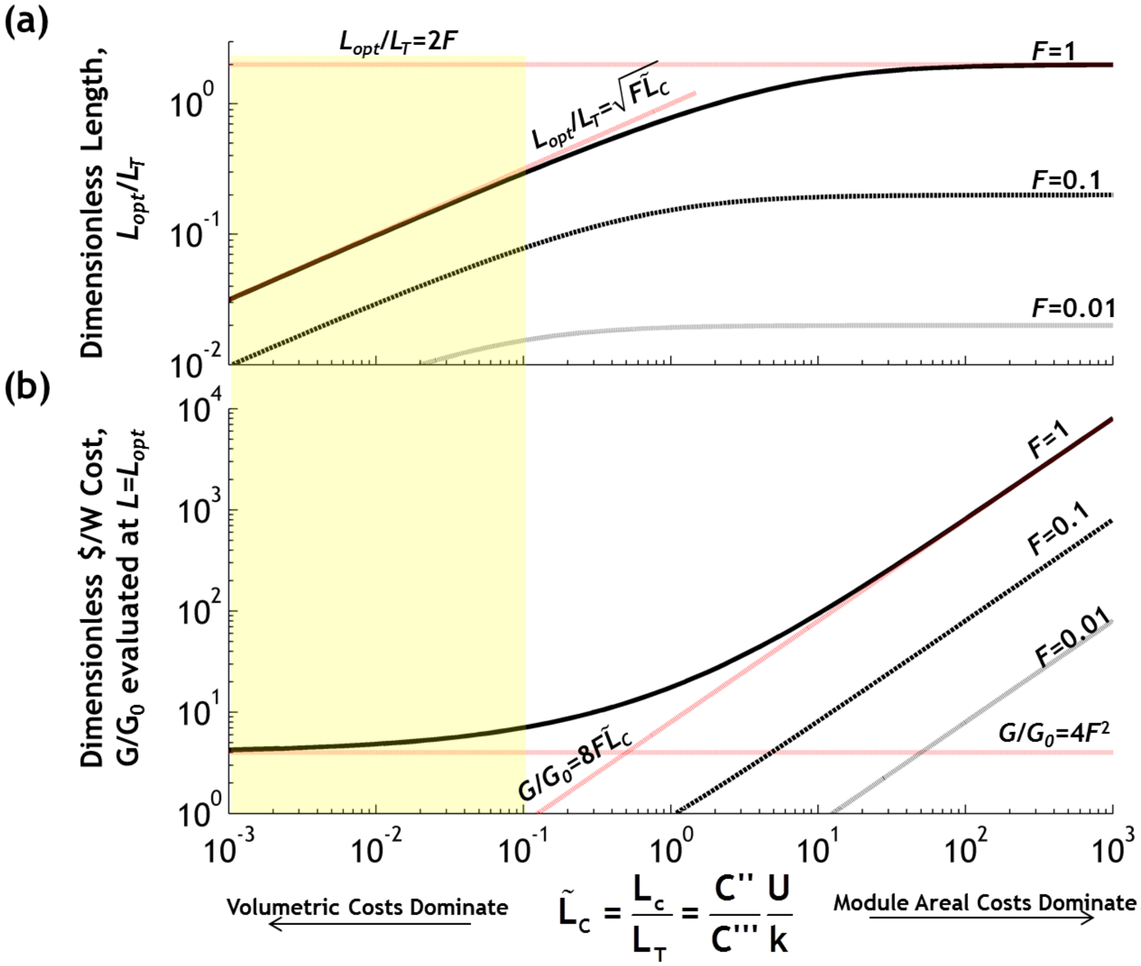

Figure 5.6 Dimensionless cost analysis for the special case of a "free" heat exchanger. (a) The dimensionless optimum length and (b) dimensionless \$/W cost evaluated at the optimum length, both given as functions of F and the dimensionless parameter $\tilde{L}_C$. For most realistic materials and applications, $\tilde{L}_C$ typically ranges between 0.001 and 0.1 (shaded region), in which case the cost considerations force the optimal leg length to be well below the usually assumed thermal impedance matching condition.

For most currently available materials and manufacturing processes, a detailed survey shows that $\tilde{L}_C$ typically ranges between 0.001 and 0.1 (shaded region in Fig. 5.6).[14] Practical values of F also range widely, from close to unity down to ~0.01. Therefore, Eqn. 5.77 shows the small $\tilde{L}_C$ limit is most common. Thus, if the heat exchanger cost is ignored, \$/W minimization in real systems will typically result in an optimal leg length far smaller than the traditional thermal impedance matched condition. For example, a typical case with $\tilde{L}_C = 0.01$ and F=0.1 should use an L_{opt} over 6 times shorter than $2FL_T$.

Finally, the dimensionless results are recast in dimensional form (Fig. 5.7) to help graphically determine the optimum leg length for the case $F\approx 1$ (Eqn. 5.76). The shaded regions are the domains where typical materials, costs, and applications reside.[14] The red line indicates the asymptotic behavior for a system dominated solely by areal costs (*i.e.*, inexpensive thermoelectric material). With the cost length, L_c, and the thermal length, L_T, for a specific material-application combination, the optimum leg length can be determined from this plot. Returning to the example of Bi_2Te_3, in this special case of a "free" heat exchanger with a chosen fill factor of F=0.18, the approximate solution (Eqn. 5.75) gives G=\$7.90/W (with L=0.69 mm). This is also in reasonably good agreement with the exact numerical solution which gives G=\$14.63/W (with L=0.77 mm). These costs are quadratically sensitive to T_H-T_C through G_0 (Eqn. 5.66), and thus can be improved substantially by increasing the reservoir temperature difference beyond the modest value of 80 °C used here. Most importantly, the L and G values obtained here for a free heat exchanger are all at least 5x smaller than those found in section 5.3.2.1 for a realistic heat exchanger cost of \$18.48/(W/K). These large differences again emphasize the major impact that the heat exchanger costs have on both geometry and costs for a thermoelectric power generator.

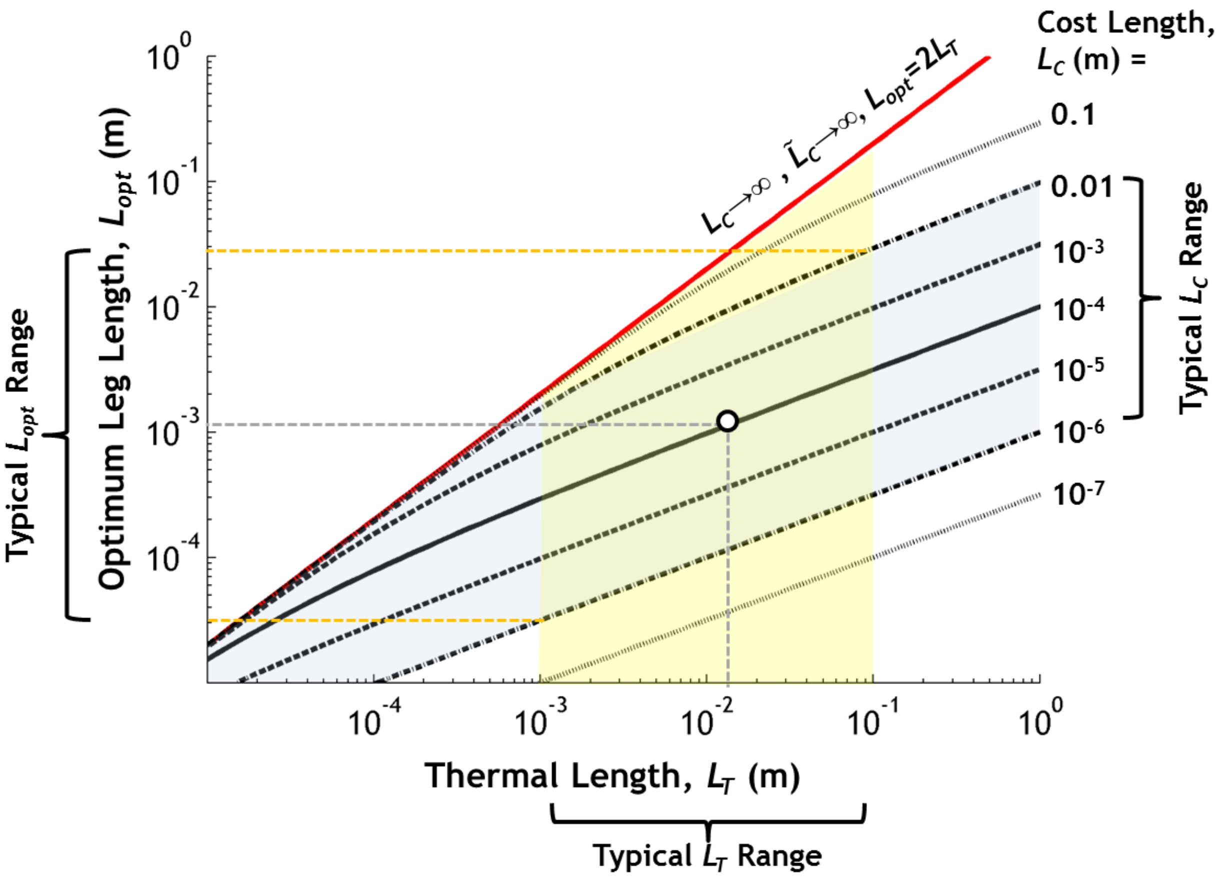

Figure 5.7 Optimum thermoelectric leg length as a function of L_T for various L_C, for the special case of a free heat exchanger and F=1. This is a dimensional representation of Fig. 5.6a. Using these curves, the optimum length of the thermoelectric leg can be determined graphically. The data point corresponds to a Bi_2Te_3 application with the same properties as in Fig. 5.5. The uppermost red line corresponds to the traditional thermal impedance matching condition, but this figure shows that L_{opt} for realistic materials and applications will generally be much smaller.

5.3.2.3 Characteristic Points

As shown in Fig. 5.5, G/G_0 decreases with decreasing F and $\tilde{L}$ along the thermal impedance matching line $\tilde{L}=2F$. As a characteristic point representing the transition to diminishing returns, I take the intersection of the light red and blue lines in Fig. 5.5 which returns the coordinate

$$\frac{L_{opt}}{L_T} = \sqrt{\tilde{L}} \qquad = \sqrt{\frac{\tilde{L}}{4}} \;. \tag{5.78}$$

Although this is not a true optimum, the shorthand “opt” is used for convenience. Alternatively, using the universal axes given in the figure, this is exactly the coordinate (1,1), which is valid for most materials and heat exchangers (see section 5.3.2.4). In the Bi_2Te_3 example of Fig. 5.5, the diminishing returns point is L_{opt}=5.7 mm and F_{opt}=0.18. Importantly, these numerical values are well within the range of practicality. This confirms the appropriateness of this derivation’s key assumptions, including neglecting contact resistances and parallel heat leakage ($K_{||}$). Equation 5.78 shows how the optimal system design depends strongly on the costs of both material and heat exchanger, via $\tilde{L}_{HX}$.

The cost-dominant regime map in Fig. 5.8 is created by considering the additive cost terms in Eqn. 5.34. Comparing the areal cost to the heat exchanger cost produces the conditional statement that

$$\text{if } C''AF \gg \qquad \frac{C''F}{C_{HX}U} \gg \;. \tag{5.79}$$

This is the case when heat exchanger costs dominate areal costs. Similarly, comparing the volumetric costs to the areal costs produces the conditional statement that

$$\text{if } C'''LAF \gg \qquad \frac{L}{L_C} \gg \;. \tag{5.80}$$

Finally comparing the volumetric costs to the heat exchanger costs produces the conditional statement that

$$\text{if } C'''LAF \gg \qquad \frac{C''F}{C_{HX}U} \gg \left(\frac{L}{L_C}\right)^{-1} \tag{5.81}$$

which is a diagonal line on the log-log plot.

The most general case is when the heat exchanger costs dominate. At the coordinates of Eqn.5.78, $G/G_0 \approx 12\tilde{L}_{HX}$, which is 50% greater than the ultimate best-case value of $8\tilde{L}_{HX}$ (Eqns. 5.69 and 5.71). The physical significance of this limit is understood by expanding it as

$$G = 8G_0\tilde{L} \qquad \frac{C_{HX}UA}{\frac{1}{4}ZT_H\left(\frac{T_H - T_C}{T_H}\right)UA\left(T_H - T_C\right)} \;. \tag{5.82}$$

The numerator is within a numerical constant of the heat exchanger cost, which is the dominant cost in this limit. As long as the application and manufacturing constraints are amenable to having sufficiently small F and L, it is possible to design the thermoelectric generator such that the module costs are negligible and only the heat exchanger costs remain. To make the costs as small as reasonably achievable, L and F should be set to values below Eqn. 5.78 subject to the condition $2F=L/L_T$. For example, G can be improved to within 12.5% of the best-case value by reducing F and L both by another factor of two. However, F and L cannot be reduced without bound because manufacturing limitations, mechanical robustness, contact resistance issues, and thermal parasitics will eventually become important.

Next, I consider the special case where the heat exchanger cost is neglected ($\tilde{L}_{HX}\rightarrow 0$), and F is fixed at some minimum value as in Section 5.3.2.2. This leads to two sub-cases (Eqn. 5.77), depending on the tradeoff between volumetric and areal costs. When the minimum allowed value of F is small (compared to $\tilde{L}_C/16$), the areal cost dominates and

$$G = 8G_0\tilde{L} \qquad \frac{C''AF}{\frac{1}{4}ZT_H\left(\frac{T_H - T_C}{T_H}\right)UA\left(T_H - T_C\right)}. \qquad (5.83)$$

Here F should be made as small as practical, followed by setting $L=2FL_T$.

A third regime exists where the module volumetric costs (*i.e.*, material costs) dominate, corresponding to $C_{HX}\rightarrow 0$ and $C''<<C'''L$. In this case, $G \approx G_0\left(2F + \tilde{L}\right.$. If F is practically limited or fixed, then the leg length should be made smaller than $2FL_T$ and specifically set to $L_{opt} = L_T\sqrt{F\tilde{L}}$, which shows that both C'' and C''' are important in determining the leg length. Furthermore, Eqn. 25 simplifies to

$$G = 4G_0F^2 = 2\frac{C'''V}{\frac{1}{4}ZT_H\left(\frac{T_H - T_C}{T_H}\right)UA\left(T_H - T_C\right)} \qquad (5.84)$$

where the numerator is the volumetric cost of the module for an active volume of $V=AF\cdot 2FL_T$. A corresponding expression for constrained L and arbitrary F can be obtained by replacing $F \rightarrow LU/2k$ in Eqn. 5.84.

There are a number of limiting conditions depending on which cost term dominates Eqn. 5.34 and whether there are any practical constraints limiting F and/or L. The three cases considered here are for: (i) when heat exchanger costs dominate (Eqn. 5.82), (ii) free heat exchangers, fixed F, and when areal manufacturing costs dominate (Eqn. 5.83), and (iii) free heat exchangers, fixed F, and when the material costs dominate (Eqn. 5.84). It is noteworthy that Eqns. 5.82-5.84 all take a similar form with the numerator representing each regime's dominant cost. Knowing the dominant costs provides useful feedback to designers regarding what changes could have the greatest reduction in cost. This comparison is summarized in the cost-dominant regime map of Fig. 5.8. The horizontal axis gives the ratio of volumetric to areal costs and is separated at 1. The vertical axis is the ratio of areal and heat exchanger costs and is also separated at 1. The diagonal line represents the comparison between volumetric costs and heat exchanger costs. Finally, at (1,1) all three costs are equal. Figure 5.8 allows for graphical determination of the dominant cost, and it can quickly provide the relative cost break down for a given design.

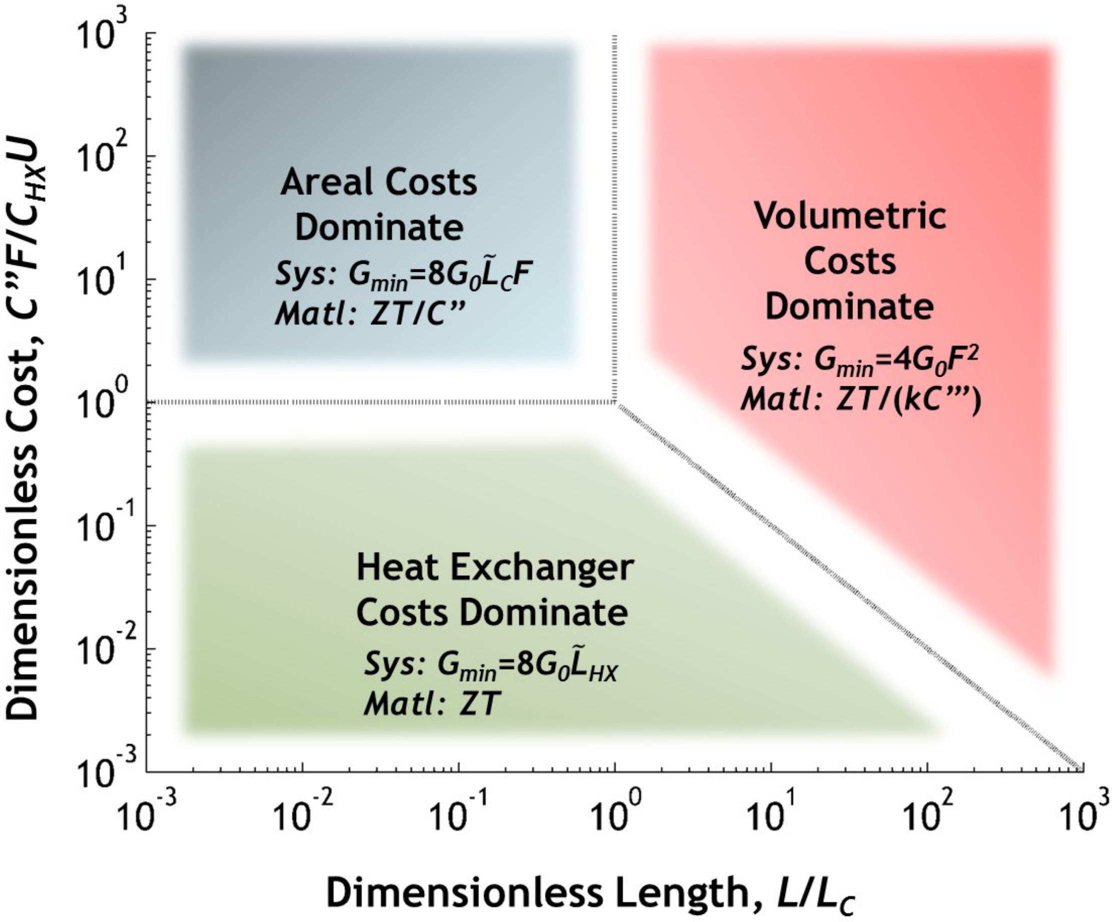

Figure 5.8 Simplified regime map showing which component of Eqn. 5.34 dominates the overall system cost. Also indicated in each sector are algebraic expressions for its minimum G and the corresponding material-specific quantity to maximize. The expressions obtained for the areal and volumetric sectors assumed fixed F and arbitrary L, but different constraints would give different expressions and materials guidelines. If both F and L can be made sufficiently small, the only remaining cost is that of the heat exchanger, consistent with the trough of Fig. 5.5.

5.3.2.4 Universal Axis Justification

The universal axes in Fig. 5.5 are motivated by recognizing that, with *m*=1, Eqn. 5.36 can be recast as:

$$\frac{G}{G_0\tilde{\ }} \qquad x)^2\left(1+\frac{a}{x}+\frac{2}{xy}\right), \tag{5.85}$$

where

$$x\equiv\frac{\tilde{\ }}{\sqrt{\tilde{\ }}} \qquad F \tag{5.86}$$

and

$$a\equiv\frac{\tilde{\ }}{\sqrt{\tilde{\ }}} \qquad \frac{C''}{\ '''C_{HX}}\,. \tag{5.87}$$

For most realistic materials and applications, $a \ll 1$ or is at most on the order of 1.[14] Plotting Eqn. 5.85 for different a shows that the differences in Fig. 5.5 between the cases $a=0$ and $a=1$ are only at the level of tens of percent in the vicinity of the characteristic point of diminishing returns. Such errors may be considered negligible for the present analysis, considering the large overall variations in G by factors of 10 or more. Setting a to 0 in Eqn. 5.85 shows that $\left(\frac{G}{G_0\tilde{L}_{HX}}\right)$ becomes purely a function of the dimensionless quantities x and y defined in Eqn. 5.86, thus justifying the universal axes used in Fig. 5.5 of the main text. In other words, as long as a given material and application correspond to a of around 1 or smaller, the G surface in Fig. 5.5 can be applied directly and quantitatively by using the universal axes. For any such scenario with negligible a, the characteristic point of diminishing returns is $(x,y)=(1,1)$, and Eqn. 5.85 can be simplified to

$$\frac{G}{G_0\tilde{\ }} \qquad \cdot x)^2\left(1+\frac{2}{xy}\right). \tag{5.88}$$

This convenient form can be used to quantify the behavior near the point of diminishing returns. For example, along the line $x=y$ (equivalent to $F=\tilde{L}/2$ and corresponding to the trough of Fig. 5.5), at $x=y=1$, Eqn. 5.88 shows that G will be within 50% of its ultimate best case. Selecting smaller values of x and y will bring G closer to this ultimate limit; for example, at $x=y=½$, G is only 12.5% greater than the best case.

5.3.3 Comparison of Thermoelectric Material Options

The contribution of manufacturing, material, and heat exchanger costs differ by the manufacturing and material classes. Figure 5.9 depicts the cost of power generation for typical bulk, nanobulk, nanowire, and superlattice thermoelectric materials that have approximately the same *ZT*. A similar breakdown can be performed for thermoelectric cooling, but it is less interesting since the cost of electricity dominates. For power generation, the cost of the ceramic plates and heat exchangers are a dominant cost for most manufacturing classes. Although their contribution to the overall cost is substantial, heat exchangers can increase the device performance since they improve heat transfer to and from the hot and cold reservoirs. This analysis suggests that a major reduction in overall system cost can be achieved by making inexpensive heat exchangers (<\$1.00/(W/K)) with high *U*-values (>200 W/m^2-K). Ceramic plates, typically used as substrates in planar thermoelectric modules, provide the necessary electrical insulation and mechanical support for the device and represent a significant cost. A reduction in overall system cost could be achieved by making an inexpensive (<\$0.10/cm^2), thermally conducting (k>40 W/m-K), electrically insulating, and structurally suitable substrate that can operate at the given application temperature.

5.3.3.1 Manufacturing Costs

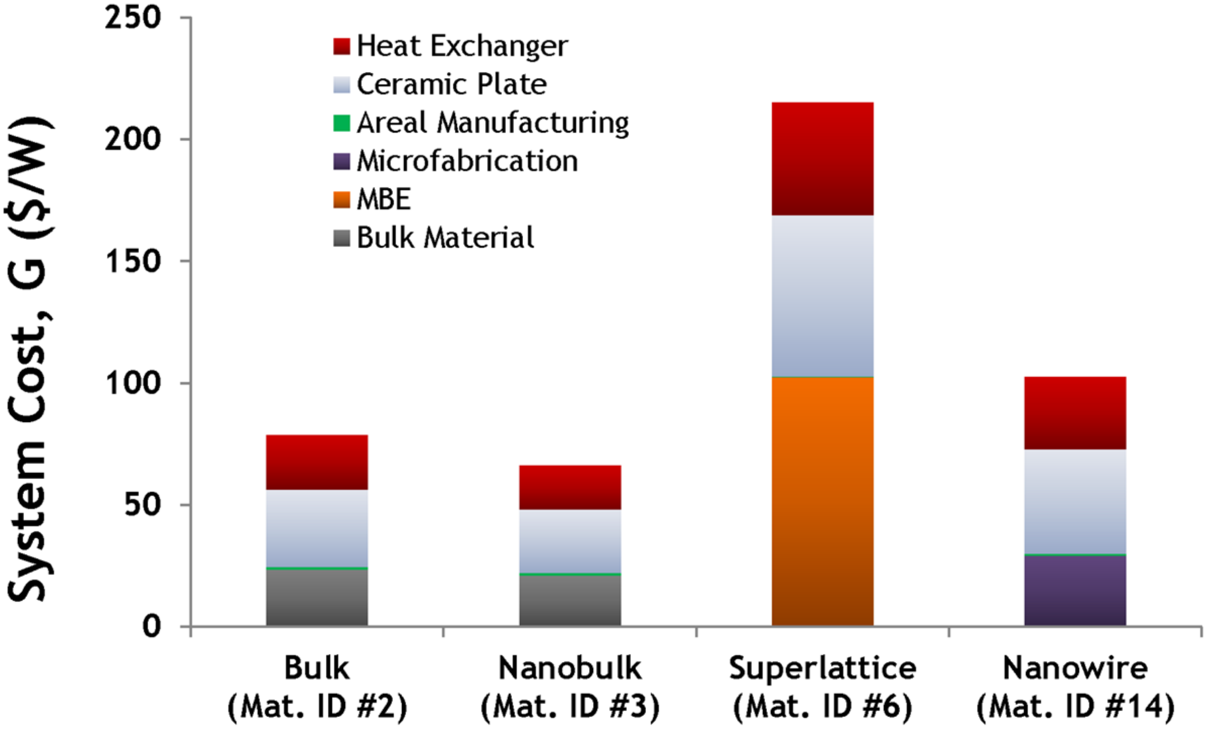

Figure 5.9 Example system cost breakdown for various manufacturing classes on a \$/W basis. These values correspond to the $F = F_{opt}$ case in Fig. 5.10a. The low temperature case (Scenario #1) was used, and the cost was evaluated for the optimum fill factor and leg length ($F = F_{opt}$, $L = L_{opt}$) for each material. For nanowire materials, the value \$2,500/m^2 approximating early production microfabrication cost was used in the analysis and corresponds to about \$1/g for processing silicon. For the superlattice material, \$1,800/m^2 corresponding to \$40/g for processing lead telluride was used. Areal manufacturing cost (in green) represents the cost of dicing and the metallization of thermoelectric material. The electrically insulating ceramic plate and heat exchanger costs are a substantial portion of the overall cost for all thermoelectric devices.

The advantage of nanobulk materials is evident in Fig. 5.9 as illustrated with a nanostructured bismuth telluride material (Material ID #3) compared to the similar bulk material

(Material ID #2). The nanobulk material has a lower thermal conductivity than its bulk counterpart, so it has a lower \$/W value. By nanobulk processing, a hierarchy of length scales relevant for thermal and electrical transport can be engineered to produce a better thermoelectric material.[178] These processing techniques are still affordable and demonstrate the benefit of a slight increase in manufacturing cost that results in an overall reduction in the \$/W value. This example demonstrates a ~17% overall cost reduction on a \$/W basis.

However, the cost of manufacturing both nanowire and supperlattice material are sufficiently high that the improvement in thermoelectric performance does not outweigh the added costs. Nanowire materials may require microfabrication processes like those used in semiconductor manufacturing. In semiconductor device manufacturing, cost typically scales with the number of fabrication steps involving lithographic patterning and etching, so there is a range in microfabrication costs. The minimum of this range corresponds to a high-volume process similar to the current state of silicon photovoltaic fabrication. The maximum of this range corresponds to multi-mask processes used to make complementary metal oxide semiconductor (CMOS) devices. In the middle cost range are fabrication steps that are used to make micro- electro-mechanical systems (MEMS); this is the cost used for nanowire manufacturing in this analysis. Nanowire material may be cost competitive if their manufacturing costs are able to approach the high-volume processing limit with the maturation of the industry. Superlattices are made using molecular beam epitaxy (MBE) which requires many hours to deposit a typical thickness of material, so the cost associated with achieving sufficiently thick thermoelectric legs is high. Since the manufacturing costs associated with thin film materials are significantly higher than those for bulk materials, the increase in power output achieved by these materials must far outweigh the additional cost.

Metallization and dicing costs are areal manufacturing costs; they are applied to all materials considered herein equally since both are required for the traditional approach of assembling individual legs into modules. he metallization category denotes the deposition of diffusion barriers and metallization to improve contact to the electrical shunt. This cost includes both the cost of the equipment and an approximate cost of the metal deposited. An important exception to traditional metallization and dicing processes is the relatively novel polymer thermoelectric material processing. The metallization and formation of individual leg structures would likely be done entirely through screen printing processes or a similar process commensurate with the unique fabrication of polymers. The impact of this exception is evident in the final G values computed for this material where the heat exchanger cost is neglected, and the system parameters used are $L = 100$ mm, $F = 8$, $T_H = 100$ ºC. The screen printing approach would lead to an estimated polymer thermoelectric module cost of \$140/W as opposed to \$550/W if traditional metallization and dicing costs were applied.

Large mismatch in costs can yield interesting new results. Specifically, the inexpensive material and manufacturing costs associated with the polymer and its low thermal conductivity, results in an optimum fill factor greater than one. This occurs because the cost of the heat exchanger is much larger than the cost of the material (*i.e.*, $C_{HX}U^2 >> C'''k$). While a fill factor greater than one does not adhere to traditional thermoelectric architecture, it is not unimaginable. In this analysis, the same heat exchanger was used to compare all materials. This heat exchanger (primarily its cost) is not suitable for polymers. This analysis suggests polymers require different geometries and heat exchangers than traditional thermoelectric materials.

5.3.3.2 Thermoelectric Power Generation

The cost-performance analysis for thermoelectric power generators demonstrates their cost competitiveness when using different thermoelectric materials. Table 5.4 provides an overview of the material/application properties and optimal geometries. In this table, the optimal geometries and ZT are reported for a specific temperature application (identified in Table 5.2 and defined by either "low" or "high") where that material performs best. Other temperatures will have a different optimum leg length and fill factor for each material. In some cases, particularly nanowire and superlattice materials (*e.g.*, Material ID # 6 and 14), only low temperature material property data is available, but the optimal ZT values may be at higher temperatures.

There are complex interplays between the thermal transport properties, electrical transport properties, and costs that influence the thermoelectric leg length. For example, a low thermal conductivity material allows for shorter legs, which results in lower electrical resistances and lower volumetric costs. The consequence of high thermal conductivity is starkly illustrated by nanobulk silicon (Material ID #13) where the high thermal conductivity (>10 W/m-K) results in an optimum thermoelectric leg length of over 90 mm. A high electrical conductivity permits longer legs, which results in larger output power and lower $/W cost. There are also complex interplays between manufacturing areal cost, heat exchanger cost, heat exchanger thermal conductance, and material thermal conductivity that influence the fill factor. For example, expensive materials favor small fill factors to reduce costs while low thermal conductivity materials favor larger fill factors. However, the fill factor is commonly fixed by other system constraints, and an optimal thermoelectric leg length is sought.

This optimum leg length is the length that minimizes the cost for a given fill factor (typically F_{opt}) and is determined for each material and temperature scenario. This optimum leg length is not the diminishing returns point in Eqn. 5.78 but rather the true leg length that minimizes the system cost in Eqn. 5.35 for a fixed fill factor. The optimum leg length is used to calculate the values reported in Figs. 5.9 and 5.10. Three fill factor cases are presented in Fig. 5.10 for each of the temperature scenarios. The first case is for F=1, and the second case is evaluated at the optimum fill factor $F=F_{opt}$ (Eqn. 5.78). The last case is a minimum achievable cost where F is fixed at the same F_{opt} value as the second case (*i.e.*, $G_{min}=4G_0F_{opt}^2$, when $K_{||}$ is negligible). This minimum cost is reached when the system costs of ceramic plates and heat exchangers (C_{HX}) as well as the metal shunts and manufacturing costs (C'') are eliminated, and only the material cost (C''') for the thermoelectric device is considered. The gap between this minimum cost case and the other cases represent the room for improvement in manufacturing and system costs.

Table 5.4 Summary of material properties and results for power generation and cooling

ID #	Material Name	Power Generation								Cooling
		S (μV/K)	**σ** (S/cm)	**k** (W/m-K)	**ZT_m**	**F_{opt}**	**L_{opt}** (mm)	**G_0 Value** ($/W)	**Scenario Temp.***	**L_{opt}** (mm)
1	Bi_2Te_3	-232	682	1.65	0.74	0.18	4.53	38.49	Low	1.65
2	$Bi_{0.52}Sb_{1.48}Te_3$	212	923	1.31	1.05	0.21	4.41	20.96	Low	1.51
3	$Bi_{0.52}Sb_{1.48}Te_3$	235	547	0.66	1.52	0.29	3.47	7.45	Low	0.90
4	$Bi_{0.54}Te_{0.46}$	-32	729	1.18	0.02	0.07	1.10	10,691.77	Low	
5	$(Na_{0.0283}Pb_{0.945}Te_{0.9733})(Ag_{1.11}Te_{0.555})$	300	153	0.66	1.45	0.34	3.01	0.13	High	
6	Bi-doped $PbSe_{0.98}Te_{0.02}$/PbTe	-219	711	0.58	1.96	0.02	0.31	2,028.89	Low	0.13
7	$AgPb_{18}SbTe_{20}$	-295	238	1.10	1.31	0.26	3.59	0.26	High	2.50
8	SiGe	190	518	4.39	0.30	0.07	2.66	17.68	High	
9	$Si_{80}Ge_{20}$	187	558	2.59	0.53	0.13	3.39	2.52	High	2.84
10	SiGe	182	399	2.00	0.22	0.06	1.59	1,390.68	Low	0.80
11	$Mg_2Si_{0.85}Bi_{0.15}$	218	642	3.20	0.67	0.74	29.5	0.06	High	
12	$Mg_2Si_{0.6}Sn_{0.4}$	-197	1072	2.76	1.05	~1	45.5	0.02	High	13.2
13	Si	-147	1646	11.80	0.21	0.71	94.5	0.21	High	
14	Si	317	551	2.55	0.72	0.09	3.38	171.58	Low	0.80
15	$MnSi_{1.75}$	210	76	2.39	0.05	~1	37.5	7.36	Low	
16	$Mn_{15}Si_{28}$	131	291	2.46	0.07	~1	35.7	7.81	Low	
17	$Ba_8Ga_{16}Ge_{28}Zn_2$	-240	139	1.17	0.48	0.13	1.50	3.01	High	
18	$Ba_8Ga_{16}Ge_{30}$	-103	810	1.63	0.36	0.11	1.65	5.65	High	
19	$Ba_7Sr_1Al_{16}Si_{30}$	-53	1129	2.44	0.09	~1	38.6	0.06	High	
20	$CeFe_4Sb_{12}$	145	1520	2.88	0.77	0.28	8.34	0.39	High	4.83
21	$Yb_{0.2}In_{0.2}Co_4Sb_{12}$	-205	976	3.09	0.93	0.31	10.6	0.25	High	5.35
22	$Ca_{0.18}Co_{3.97}Ni_{0.03}Sb_{12.40}$	-187	1279	4.08	0.77	0.39	17.6	0.19	High	11.2
23	$(Zn_{0.98}Al_{0.02})O$	-150	655	12.49	0.08	0.48	58.6	1.21	High	
24	$Ca_{2.4}Bi_{0.3}Na_{0.3}Co_4O_9$	173	118	1.85	0.13	0.43	7.17	0.94	High	
25	InGaZnO	-439	35	3.02	0.07	0.04	1.59	8,574.03	Low	
26	$Na_{0.7}CoO_{2-\delta}$	144	2115	5.90	0.52	0.22	12.7	0.88	High	
27	$Zr_{0.25}Hf_{0.25}Ti_{0.5}NiSn_{0.994}Sb_{0.006}$	-275	786	3.00	1.38	0.49	19.6	0.07	High	
28	$Zr_{0.5}Hf_{0.5}Ni_{0.8}Pd_{0.2}Sn_{0.99}Sb_{0.01}$	-156	1240	3.03	0.69	0.46	15.4	0.16	High	
29	$Ti_{0.8}Hf_{0.2}NiSn$	-173	791	4.04	0.41	0.41	16.5	0.34	High	5.87
30	PEDOT:PSS	15	550	0.35	0.01	~8	101	0.29	Low	10.1

*See Table 5.2 for scenario values

~1: Materials with F_{opt}~1, have high thermal conductivities which suggests that heat exchangers with larger *U*-values should be used.

~8: The cost of polymers and their manufacturing technique are so different from other thermoelectric materials, that a different geometry than conventional TE should be considered.

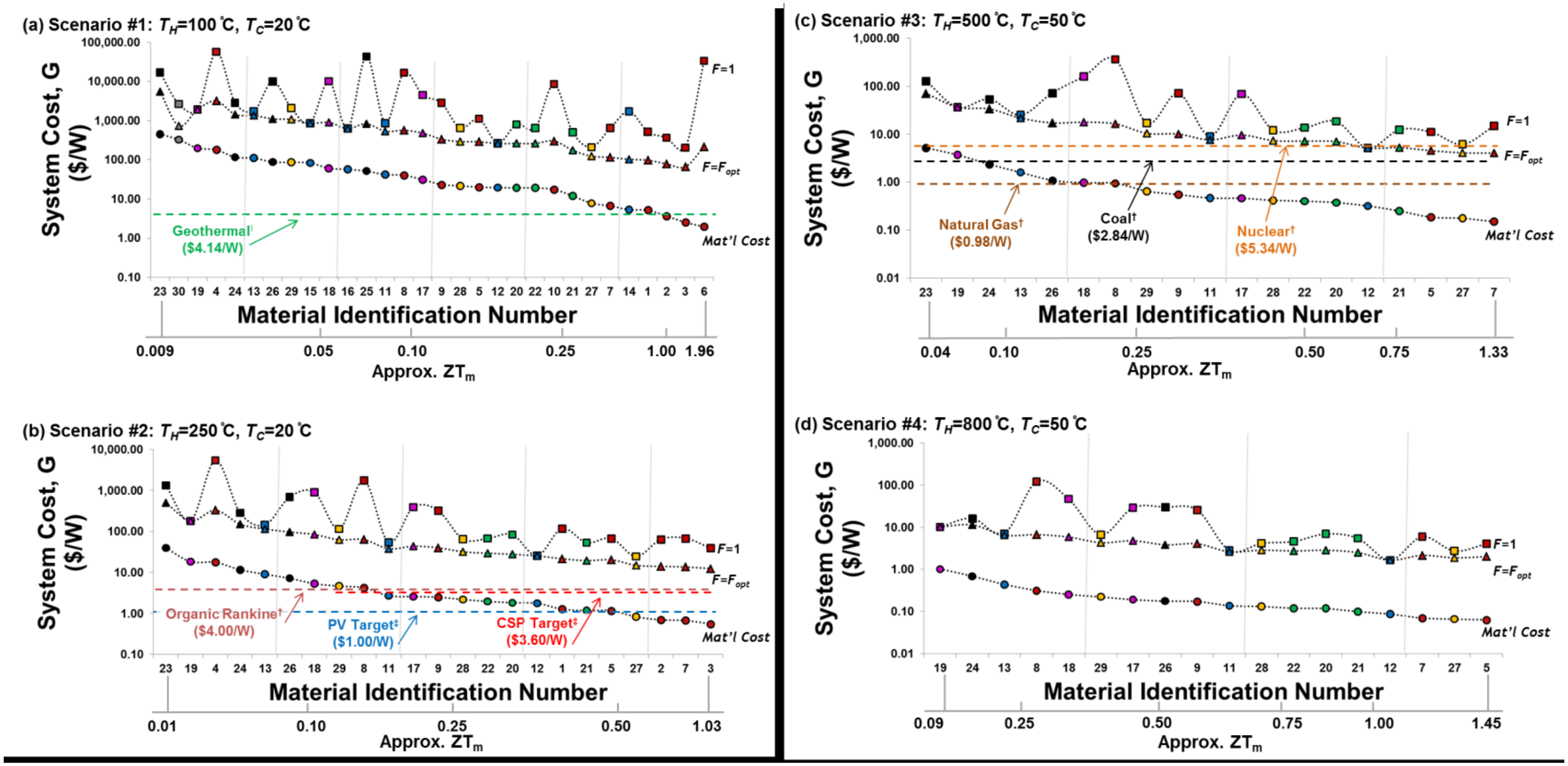

Figure 5.10 Minimum cost of thermoelectric power generation, *G*, in \$/W for materials indicated in Table 5.1. Comparisons are presented for the four scenarios in Table 5.2. Horizontal lines represent costs of competitive electricity generation technologies. The data point colors represent material class and correspond to the color legend in Figs. 5.11 and 5.12. The *F*=1 line represents a fill factor of one; the $F=F_{opt}$ line represents a module design with the optimum fill factors from Table 5.4. At these same $F=F_{opt}$ values, the Mat'l Cost line ($G=4G_0F_{opt}^2$, if $K_{//}$ is negligible) represents the lowest obtainable cost if the heat exchanger costs and areal manufacturing costs are considered negligible. Equivalent material-only costs for other fill factors can be estimated using the Mat'l Cost values presented here. The F_{opt} values tabulated in Table 1 can be divided out to yield $4G_o$ for each material, and another value for F can be inserted ($4G_0F^2$). Hence the material-only costs can be smaller than those plotted by more than an order of magnitude for the smallest practical *F* values (~0.01 to ~0.05). †, ‡, and ǀ correspond to Ref. 180, 181, and 182, respectively.

While there are many materials that can operate at low temperatures for energy scavenging applications, their thermoelectric materials costs alone are above \$1/W (Fig. 5.10a). The materials with the lowest minimum cost for the low temperature scenario, T_m = 60°C, are predominately bismuth telluride-based chalcogenides (Material ID #1-3) although the bismuth telluride nanowire material (Material ID #4) has high costs. The presence of certain nanowire (Material ID #14) and superlattice (Material ID #6) materials at the bottom of the range presented for the minimum cost in Fig. 5.10a highlights the potential of nanostructured materials to also be cost competitive. However, the gap between the minimum cost points and the other cases indicate that the heat exchanger, ceramic plate, and areal manufacturing costs must be reduced (to <\$1.00/(W/K), <\$1.00/cm^2, and <\$0.01/cm^2, respectively, see section 5.3.3.1) for most thermoelectric materials to be competitive. One option to reduce manufacturing costs of nanomaterials may be to use solution-synthesized nanostructures, such as hybrid organic-inorganic materials like the one presented in chapter 4, since they do not require specialized microfabrication equipment and processes. Nanostructured bulk material made with processes like ball milling also have lower manufacturing costs than nanowire and superlattice materials. The combined effects of cost and performance are responsible for this result; the thermoelectric efficiency improvements outweigh the additional costs.

Certain materials are clearly promising for the mid- to high-temperature applications as shown in Fig. 5.10c. The lead telluride-based, half-heusler, skutterudite, and silicide materials designated by Material ID #5, 7, 27, 21, and 12, respectively, have consistently low costs (<\$6/W). In fact, a factor of two reduction in the system costs for these materials would make them highly competitive waste-heat recovery solutions as compared to Rankine or organic Rankine cycles at \$4-5/W, especially when factors such as installation costs, reliability, and maintenance are also considered. A notably high-cost material type is the oxide category (Material ID #23, 24). In spite of the low bulk material cost, the ZT_m is too low, largely due to the high thermal conductivity.

These results should be placed in perspective considering the costs of competing electricity generation technologies, especially with respect to the heat source temperature.[7,124] The horizontal lines on Fig. 5.10 indicate the cost of competing technologies. When the full optimization is performed, Figs. 5.10a-d show that current thermoelectrics are primarily competitive for mid- to high- temperature applications. As shown in Eqn. 5.66, G_0 is related to the inverse of the reservoir temperature difference squared, $(T_H\text{-}T_C)^{-2}$, which makes the cost of thermoelectric power generation sensitive to the reservoir temperature difference.

Thermoelectric power generating systems are more costly than primary power generation sources including coal, natural gas, solar, and geothermal. Primary electricity generating sources such as coal and natural gas power plants cost less than \$3/W,[179] so it is unlikely that thermoelectric power generation would be considered as an alternative to these power sources, especially considering the relatively low efficiencies of thermoelectrics compared to modern Rankine and Brayton cycles. Through cost reductions, renewable energy technologies have recently become more competitive. The current cost target for photovoltaics is ~\$1/W, and the photovoltaic module cost is projected to reach \$0.50/W.[125,180] Although higher at \$3-4/W, the costs of concentrated solar power[180] and geothermal power[179] are still competitive and preferable to the costs associated with thermoelectric power generation. Key exceptions are cases where compactness and portability of the generator are critical, and many alternatives to thermoelectric power generation are not feasible due to resource availability, size, weight, and system complexity.

Thermoelectrics are especially cost competitive compared to other waste-heat recovery technologies. A competitive waste-heat recovery technology is the organic Rankine cycle (ORC) system as shown in Fig. 5.10b. The cost for ORC systems is approximately \$4-5/W.[181] Both ORCs and thermoelectrics can be used to recover unused heat. Thermoelectrics can even be complimentary to ORCs and scavenge additional heat not recovered by the organic Rankine system.[182] The capital costs, system footprint, and maintenance costs for organic Rankine systems are considerable, so thermoelectric devices may be preferable for waste-heat recovery, particularly where reliability is paramount.

5.3.3.3 Thermoelectric Power Generation Module Costs

In Fig. 5.11, the materials can be compared considering two parameters of interest: the total areal costs of the module

$$C''_{module} = C'''L_{opt} + C'' \quad , \qquad (5.89)$$

and the figure of merit ZT_m. The dotted reference lines are drawn for comparison to chalcogenide materials: bismuth telluride and lead telluride for low and high temperature ranges, respectively. These plots provide an image of the current materials landscape and can illustrate targets for future materials research. There is a paucity of materials in the lower right-hand quadrant which indicates new materials are needed that are less expensive (C''_{module}<\$0.05/cm^2) and higher efficiency (ZT>1) than the chalcogenide reference. The clustering of points below the chalcogenide comparison material cost point indicates significant research and development work should consider material cost while improving thermoelectric efficiency. For example, nanowire-based thermoelectric materials requiring microfabrication processes are not currently competitive options as shown of Fig. 5.11b-c. Materials which lie in the upper right-hand quadrant may be desirable in some instances; military applications such as mobile power sources for soldiers or space applications such as space vehicle power generators are two examples.

An important challenge is the selection of materials within a given quadrant. When faced with selecting between materials which lie in relatively close proximity to one another in Fig. 5.11, there are a variety of application-specific factors that govern the selection between, for example, a material having lower cost and performance and another having higher cost and performance. Such decision-making will likely rely on additional parameters related to feasibility such as material stability with respect to time, temperature, and compatibility with the operating environment, material toxicity, mechanical properties, and compatibility with metallization and other module materials, none of which are considered in this analysis.

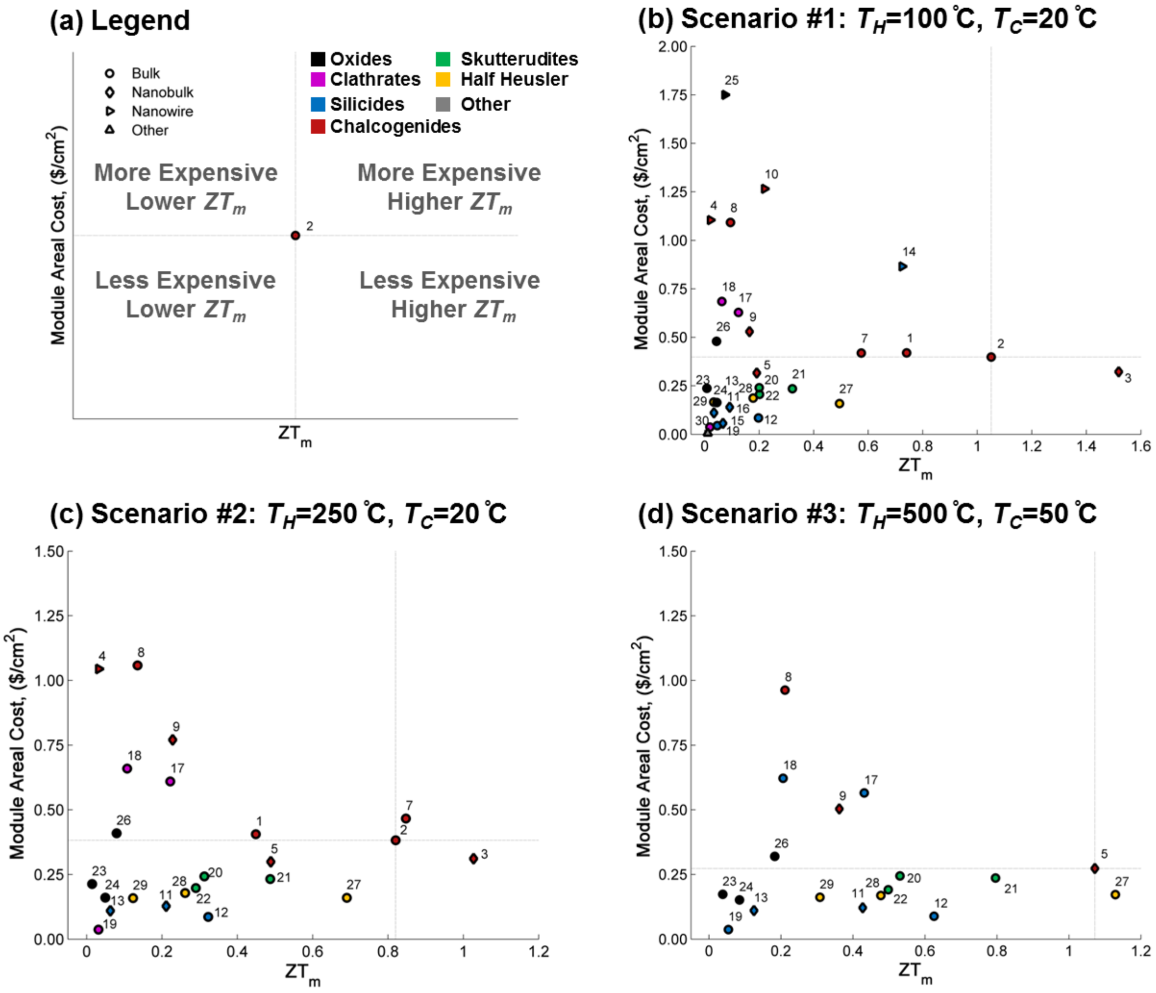

Figure 5.11 Module areal cost vs. ZT_m for select thermoelectric materials with plots showing (a) the legend and (b)-(d) the various scenarios. The horizontal and vertical lines represent comparisons to reference chalcogenide materials. Materials ID# 2 and 5 from Table 5.1 are used for low/medium and high temperature applications, respectively. The shapes represent the manufacturing class of the material (bulk, nanobulk, nanowire, or other), and the color represents the material class.

5.3.3.4 Thermoelectric Cooling

Thermoelectric cooling is an application where thermoelectrics have performed well in the market. Much of this success can be attributed to the room temperature performance of bismuth telluride alloys. However, other thermoelectric materials may also be attractive alternatives. The cost analysis discussed previously, Eqns. 5.48 and 5.49, was performed on the materials listed in Table 5.1 and is presented in Fig. 5.12. Not all materials are able to achieve the targeted $\Delta T=T_1-T_2$ associated with the example application. Eqn.5.46 shows that if a material does not have a sufficiently large ZT for a given ΔT, then the COP is negative indicating that cooling to that ΔT cannot be achieved. The operating cost in Fig. 5.12 is expressed for each material at the optimum leg length that minimizes Eqn. 5.49 (reported in Table 5.4). Materials are listed by their material identification number and are ordered by increasing ZT. There is a clear trend that larger ZTs have lower operating cost. This is because ZT directly influences the COP and the COP is the strongest driving parameter given that the purchased electricity dominates the cost.

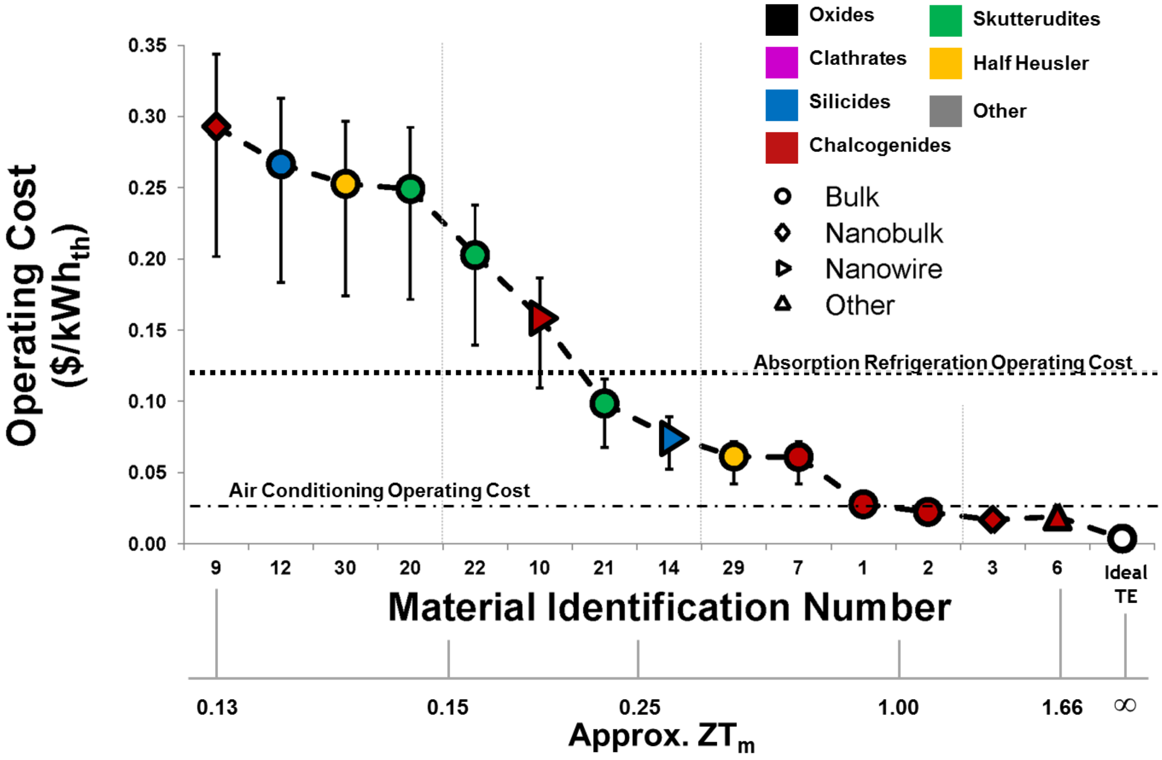

Figure 5.12 Operating costs of a thermoelectric cooler for various materials and the scenario described in Table 5.2. Colors represent material class; shapes represent material structure resulting from different manufacturing techniques. The materials are organized from left to right in order of increasing ZT_m. The error bars represent the variability in electricity price with the average at 9.83 ¢/kWh$_e$. The lower bound is for industrial applications with an electricity cost of 6.77 ¢/kWh$_e$, and the upper bound is for residential applications with an electricity cost of 11.54 ¢/kWh$_e$. In this analysis F=1 and the heat exchanger costs are neglected. In the Ideal TE, the material is completely free and $ZT_m=\infty$; this is equivalent to a Carnot refrigerator operating with only the cost of electricity being significant, giving 0.24 - 0.41 ¢/kWh$_{th}$.

The cost of thermoelectric cooling can be compared against the operating cost of absorption refrigeration and air conditioning,[183,184] and many of the chalcogenides are cost competitive. Material ID #6 has the potential to be the least expensive even considering its costly MBE process. The primary challenge is making high quality superlattices with thickness approaching 130 μm, which is the optimum length as determined by this analysis. Material ID #3 also shows that the improvements in thermoelectric power output and associated cost reduction caused by nanostructuring compensate for the additional manufacturing expenses. Given the straightforward relationship to ZT, an ideal material with $ZT\approx\infty$ can have a cost of \$0.004/kWh$_{th}$ for ΔT=10 °C. This suggests there is still room for material improvements in cooling applications to reduce the cost even further. Cost reduction can be achieved by increasing ZT with a system capital cost that is recovered by the operating cost savings over the lifetime of the device.

5.3.3.5 Thermoelectric Device Targets Summary

The key targets for thermoelectric devices pertain to system parameters and costs. Meeting or exceeding these targets would lead to lower cost values than those determined here. As suggested by G_0 in Eqn. 5.66, both large ZT and small volumetric costs C''' are desirable, but they need not occur simultaneously. Materials with low *ZT* and low volumetric costs can have a lower \$/W value than those having high *ZT* and high costs. Hence, there is no unique target for *ZT* or volumetric cost, but approximate targets can be set for current state-of-the-art system components. The heat exchanger and ceramic plate dominate the overall cost for most devices, and *ZT* becomes much more important than C'''. The \$1/(W/K) target for heat exchanger cost is below the existing minimum cost,[146] and *U*-values above 200 W/m^2K are desirable. Ceramic plates with thermal conductivity above 40 W/m-K and cost below \$0.10/cm^2 would reduce thermoelectric system costs. Since the areal manufacturing costs contribute minimally to the overall cost, these costs should remain at or below the current value of \$0.01/cm^2 for dicing and metallization. Any additional areal processing costs would increase this value, and gains in other parameters would need to mitigate the additional cost.

Polymer-based thermoelectric materials have the potential to be a low cost option for thermoelectrics if their *ZT* can be improved while maintaining their low thermal conductivity and polymer processability. Currently, the thermoelectric performance of polymers is the limiting parameter and much research into their transport properties is necessary if future improvements in *ZT* are to be made.

5.4 Thermoelectric Cost Analysis Summary

This work investigates a new thermoelectrics cost analysis which incorporates material properties, device physics, material costs, manufacturing costs, and system costs. This analysis leads to a new design optimization where the ratio of overnight capital cost to power output/energy expenditure is minimized, as opposed to an optimization of efficiency or power output alone. This work evaluates the status of thermoelectric materials, including the polymer PEDOT:PSS, relative to their cost competitiveness for power generation and refrigeration. The results of this work point to necessary design considerations for polymer-based materials where the low cost, low thermal conductivity and processability of polymers is advantageous. However, to develop polymer-based devices understanding of the cost structure of a device is necessary.

Towards that goal, this work derives a new cost-performance metric, G_0, and a system-level cost metric *G* both with units of \$/W. The new cost-performance metric G_0 is useful in defining the minimum material cost for an application. The system-level metric *G* goes beyond ranking materials by *ZT* (*i.e.*, thermoelectric efficiency) and also accounts for the heat exchanger's thermal conductance and the overnight capital cost of the system. Just as the material *ZT* is useful in describing the module *ZT*, G_0 describes the material cost scale for *G*. The analysis focuses on the case where heat is free, so fuel costs have not been included. Analytical results for the optimum thermoelectric leg length and module fill factor are obtained and reflect an inherent trade-off between cost and thermoelectric performance. Several cost-dominant regimes have been identified, as summarized in Fig. 5.8: (i) a heat exchanger cost dominated regime, where $G_0\tilde{L}_{HX}$ should be minimized; (ii) a module areal manufacturing cost dominated regime, where at fixed F, $G_0\tilde{L}_CF$ should be minimized; and (iii) a volumetric material cost dominated regime, where at fixed F, G_0F^2 should be minimized. Focusing specifically on recommendations for manufacturing and materials development, the relevant material figures-of-merit which should be maximized in each regime are (i) *ZT* regardless of cost; (ii) the ratio ZT / C''; and (iii) the ratio $ZT/(kC'')$. Additional regimes and special-case optimizations can also be identified for other system constraints, such as fixed *L* or non-negligible contact resistances.

Ultimately, this chapter presents the framework for a detailed analysis comparing thirty materials and four different applications. When applied to several traditional and new thermoelectric material classes, the analysis demonstrates the paucity of materials which are both higher performing and lower cost than standard chalcogenides. Novel nanowire and superlattice materials have the potential to have a low $/W value if improvements in *ZT* are made above what is reported, but with the currently reported values they are not competitive in the near-term due to the large costs associated with microfabrication/MBE manufacturing techniques. Polymers also have the potential for low $/W values if improvements in *ZT* are made while maintaining the low thermal conductivity and processability inherent to polymers. However, there are other thermoelectric materials in which could yield systems that are affordable and competitive with other forms of power generation; the key challenges for these materials will be in both engineering devices around them and scaling their production. The utility of the cost metrics presented here will evolve as factors like resource availability and energy costs change over time demonstrating the need to revisit this analysis periodically. The realization of commercial thermoelectric devices depends on the simultaneous improvement and optimization of material properties, system design, system costs, and material and manufacturing costs.

References

1 Zebarjadi, M., Esfarjani, K., Dresselhaus, M. S., Ren, Z. F. & Chen, G. Perspectives on thermoelectrics: from fundamentals to device applications. *Energy & Environmental Science* **5**, 5147-5162, doi:Doi 10.1039/C1ee02497c (2012).

2 Bell, L. E. Cooling, heating, generating power, and recovering waste heat with thermoelectric systems. *Science* **321**, 1457-1461, doi:10.1126/science.1158899 (2008).

3 Tritt, T. M. Thermoelectric Phenomena, Materials, and Applications. *Annual Review of Materials Research* **41**, 433-448, doi:10.1146/annurev-matsci-062910-100453 (2011).

4 Nolas, G. S., Poon, J. & Kanatzidis, M. Recent developments in buk thermoelectric materials. *MRS Bulletin* **31** (2006).

5 Snyder, G. J. & Toberer, E. S. Complex thermoelectric materials. *Nature Materials* **7** (2008).

6 Sootsman, J. R., Chung, D. Y. & Kanatzidis, M. G. New and old concepts in thermoelectric materials. *Angew Chem Int Ed Engl* **48**, 8616-8639, doi:10.1002/anie.200900598 (2009).

7 Shakouri, A. Recent Developments in Semiconductor Thermoelectric Physics and Materials. *Annual Review of Materials Research* **41**, 399-431, doi:10.1146/annurev-matsci-062910-100445 (2011).

8 Vineis, C. J., Shakouri, A., Majumdar, A. & Kanatzidis, M. G. Nanostructured thermoelectrics: big efficiency gains from small features. *Adv Mater* **22**, 3970-3980, doi:10.1002/adma.201000839 (2010).

9 Dresselhaus, M. S. *et al.* New Directions for Low-Dimensional Thermoelectric Materials. *Advanced Materials* **19**, 1043-1053 (2007).

10 Minnich, A. J., Dresselhaus, M. S., Ren, Z. F. & Chen, G. Bulk nanostructured thermoelectric materials: current research and future prospects. *Energy & Environmental Science* **2**, 466-479 (2009).

11 Malen, J. A. *Energy conversion and transport in organic-inorganic heterojunctions* 3383291 thesis, University of California, Berkeley, (2009).

12 Sangi Reddy, P. R. *Transport of charge and energy in metal-molecule-metal junctions* 3306324 thesis, University of California, Berkeley, (2007).

13 Wang, R. Y.-S. *Energy transport and conversion in nanostructured materials* 3353343 thesis, University of California, Berkeley, (2008).

14 LeBlanc, S., Yee, S. K., Scullin, M. L., Dames, C. & Goodson, K. E. Material and Manufacturing Cost Considerations for Thermoelectrics. **Submitted** (2013).

15 Ashcroft, N. W. M., David N. *Solid State Physics*. (1976).

16 Lee, K. *et al.* Metallic transport in polyaniline. *Nature* **441**, 65-68 (2006).

17 Kaiser, A. B. & Skakalova, V. Electronic conduction in polymers, carbon nanotubes and graphene. *Chem Soc Rev* **40**, 3786-3801, doi:10.1039/c0cs00103a (2011).

18 Jaiswal, M. & Menon, R. Polymer electronic materials: a review of charge transport. *Polymer International* **55**, 1371-1384 (2006).

19 Kaiser, A. B. Thermoelectric-Power and Conductivity of Heterogeneous Conducting Polymers. *Physical Review B* **40**, 2806-2813 (1989).

20 Mona, Z. *et al.* Effect of nanoparticle scattering on thermoelectric power factor. *Appl Phys Lett* **94**, 202105 (2009).

21 Faleev, S. V. & Leonard, F. Theory of enhancement of thermoelectric properties of materials with nanoinclusions. *Physical Review B* **77**, 214304 (2008).

22 Mahan, G. D. & Sofo, J. O. The best thermoelectric. *Proceedings of the National Academy of Sciences of the United States of America* **93**, 7436-7439 (1996).

23 Lertsatitthanakorn, C. Electrical performance analysis and economic evaluation of combined biomass cook stove thermoelectric (BITE) generator. *Bioresource Technology* **98**, 1670-1674 (2007).

24 He, M. *et al.* Thermopower enhancement in conducting polymer nanocomposites via carrier energy scattering at the organic-inorganic semiconductor interface. *Energy & Environmental Science* **5**, 8351-8358, doi:Doi 10.1039/C2ee21803h (2012).

25 Aviram, A. & Ratner, M. A. Molecular rectifiers. *Chemical Physics Letters* **29**, 277-283 (1974).

26 Lindsay, S. M. & Ratner, M. A. Molecular transport junctions: Clearing mists. *Advanced Materials* **19**, 23-31 (2007).

27 Service, R. F. Breakthrough of the Year: Molecules Get Wired. *Science* **294**, 2442-2443, doi:10.1126/science.294.5551.2442 (2001).

28 Lortscher, E., Weber, H. B. & Riel, H. Statistical approach to investigating transport through single molecules. *Physical Review Letters* **98**, - (2007).

29 Reed, M. A., Zhou, C., Muller, C. J., Burgin, T. P. & Tour, J. M. Conductance of a molecular junction. *Science* **278**, 252-254 (1997).

30 Park, H. *et al.* Nanomechanical oscillations in a single-C-60 transistor. *Nature* **407**, 57-60 (2000).

31 Park, J. *et al.* Coulomb blockade and the Kondo effect in single-atom transistors. *Nature* **417**, 722-725 (2002).

32 Venkataraman, L., Klare, J. E., Nuckolls, C., Hybertsen, M. S. & Steigerwald, M. L. Dependence of single-molecule junction conductance on molecular conformation. *Nature* **442**, 904-907 (2006).

33 Xu, B. Q. & Tao, N. J. J. Measurement of single-molecule resistance by repeated formation of molecular junctions. *Science* **301**, 1221-1223 (2003).

34 Cui, X. D. *et al.* Reproducible measurement of single-molecule conductivity. *Science* **294**, 571-574 (2001).

35 Lindsay, S. Single-molecule electronic measurements with metal electrodes. *J Chem Educ* **82**, 727-733 (2005).

36 Morita, T. & Lindsay, S. Determination of single molecule conductances of alkanedithiols by conducting-atomic force microscopy with large gold nanoparticles. *J Am Chem Soc* **129**, 7262-+ (2007).

37 Imry, Y. & Landauer, R. Conductance viewed as transmission. *Rev Mod Phys* **71**, S306-S312 (1999).

38 Vanwees, B. J. *et al.* Quantized Conductance of Point Contacts in a Two-Dimensional Electron-Gas. *Physical Review Letters* **60**, 848-850 (1988).

39 Butcher, P. N. Thermal and Electrical Transport Formalism for Electronic Microstructures with Many Terminals. *Journal of Physics-Condensed Matter* **2**, 4869-4878 (1990).

40 Paulsson, M. & Datta, S. Thermoelectric effect in molecular electronics. *Physical Review B* **67**, - (2003).

41 Malen, J. A. *et al.* The Nature of Transport Variations in Molecular Heterojunction Electronics. *Nano Lett* (2009).
42 Malen, J. A. *et al.* Identifying the Length Dependence of Orbital Alignment and Contact Coupling in Molecular Heterojunctions. *Nano Lett* **9**, 1164-1169, doi:doi:10.1021/nl803814f (2009).
43 Reddy, P., Jang, S. Y., Segalman, R. A. & Majumdar, A. Thermoelectricity in molecular junctions. *Science* **315**, 1568-1571 (2007).
44 Baheti, K. *et al.* Probing the chemistry of molecular heterojunctions using thermoelectricity. *Nano Lett* **8**, 715-719 (2008).
45 Malen, J. A. *et al.* The Nature of Transport Variations in Molecular Heterojunction Electronics. *Nano Lett* **9**, 3406-3412 (2009).
46 Pauly, F., Viljas, J. K. & Cuevas, J. C. Length-dependent conductance and thermopower in single-molecule junctions of dithiolated oligophenylene derivatives: A density functional study. *Physical Review B* **78**, - (2008).
47 Wold, D. J., Haag, R., Rampi, M. A. & Frisbie, C. D. Distance dependence of electron tunneling through self-assembled monolayers measured by conducting probe atomic force microscopy: Unsaturated versus saturated molecular junctions. *J Phys Chem B* **106**, 2813-2816 (2002).
48 Venkataraman, L. *et al.* Single-molecule circuits with well-defined molecular conductance. *Nano Lett* **6**, 458-462 (2006).
49 Li, Z. & Kosov, D. S. Nature of well-defined conductance of amine-anchored molecular junctions: Density functional calculations. *Physical Review B* **76**, - (2007).
50 Bergfield, J. P. & Stafford, C. A. Thermoelectric Signatures of Coherent Transport in Single-Molecule Heterojunctions. *Nano Lett* **9**, 3072-3076 (2009).
51 Malen, J. A., Yee, S. K., Majumdar, A. & Segalman, R. A. Fundamentals of energy transport, energy conversion, and thermal properties in organic-inorganic heterojunctions. *Chemical Physics Letters* **491**, 109-122.
52 Song, H., Reed, M. A. & Lee, T. Single Molecule Electronic Devices. *Advanced Materials*, n/a-n/a.
53 Venkataraman, L. *et al.* Electronics and chemistry: Varying single-molecule junction conductance using chemical substituents. *Nano Lett* **7**, 502-506 (2007).
54 Geng, W. T., Jun, N. & Takahisa, O. Impacts of metal electrode and molecule orientation on the conductance of a single molecule. *Appl Phys Lett* **85**, 5992-5994 (2004).
55 Manabu, K. Electrical conductance of single C[sub 60] and benzene molecules bridging between Pt electrode. *Appl Phys Lett* **95**, 073301 (2009).
56 Jang, S. Y., Reddy, P., Majumdar, A. & Segalman, R. A. Interpretation of Stochastic events in single molecule conductance measurements. *Nano Lett* **6**, 2362-2367 (2006).
57 Xiao, X. Y., Xu, B. Q. & Tao, N. J. Measurement of single molecule conductance: Benzenedithiol and benzenedimethanethiol. *Nano Lett* **4**, 267-271 (2004).
58 Kroto, H. W., Allaf, A. W. & Balm, S. P. C60 - Buckminsterfullerene. *Chemical Reviews* **91**, 1213-1235 (1991).
59 Kroto, H. W., Heath, J. R., O'Brien, S. C., Curl, R. F. & Smalley, R. E. C60: Buckminsterfullerene. *Nature* **318**, 162-163 (1985).
60 Yu, G., Gao, J., Hummelen, J. C., Wudl, F. & Heeger, A. J. Polymer Photovoltaic Cells: Enhanced Efficiencies via a Network of Internal Donor-Acceptor Heterojunctions. *Science* **270**, 1789-1791, doi:10.1126/science.270.5243.1789 (1995).

61 Joachim, C., Gimzewski, J. K., Schlittler, R. R. & Chavy, C. Electronic Transparency of a Single C-60 Molecule. *Physical Review Letters* **74**, 2102-2105 (1995).

62 Bohler, T., Edtbauer, A. & Scheer, E. Conductance of individual C[sub 60] molecules measured with controllable gold electrodes. *Physical Review B (Condensed Matter and Materials Physics)* **76**, 125432 (2007).

63 Neel, N. *et al.* Controlled contact to a C-60 molecule. *Physical Review Letters* **98**, - (2007).

64 Lu, X. H., Grobis, M., Khoo, K. H., Louie, S. G. & Crommie, M. F. Spatially mapping the spectral density of a single C-60 molecule. *Physical Review Letters* **90**, - (2003).

65 Lu, X. H., Grobis, M., Khoo, K. H., Louie, S. G. & Crommie, M. F. Charge transfer and screening in individual C-60 molecules on metal substrates: A scanning tunneling spectroscopy and theoretical study. *Physical Review B* **70**, - (2004).

66 NeÌ□el, N., KroÌˆger, J. r., Limot, L. & Berndt, R. Conductance of Oriented C60 Molecules. *Nano Lett* **8**, 1291-1295 (2008).

67 Rogero, C., Pascual, J. I., Gomez-Herrero, J. & Baro, A. M. Resolution of site-specific bonding properties of C[sub 60] adsorbed on Au(111). *The Journal of Chemical Physics* **116**, 832-836 (2002).

68 Quek, S. Y. *et al.* Amine-gold linked single-molecule circuits: Experiment and theory. *Nano Lett* **7**, 3477-3482 (2007).

69 Klitzing, K. v., Dorda, G. & Pepper, M. New Method for High-Accuracy Determination of the Fine-Structure Constant Based on Quantized Hall Resistance. *Physical Review Letters* **45**, 494 (1980).

70 Kittel, C. & McEuen, P. *Introduction to solid state physics*. 8th edn, (J. Wiley, 2005).

71 Smit, R. H. M. *et al.* Measurement of the conductance of a hydrogen molecule. *Nature* **419**, 906-909 (2002).

72 Beebe, J. M., Engelkes, V. B., Miller, L. L. & Frisbie, C. D. Contact resistance in metal-molecule-metal junctions based on aliphatic SAMs: Effects of surface linker and metal work function. *J Am Chem Soc* **124**, 11268-11269 (2002).

73 Engelkes, V. B., Beebe, J. M. & Frisbie, C. D. Length-dependent transport in molecular junctions based on SAMs of alkanethiols and alkanedithiols: Effect of metal work function and applied bias on tunneling efficiency and contact resistance. *J Am Chem Soc* **126**, 14287-14296 (2004).

74 Ward, D. R. *et al.* Simultaneous Measurements of Electronic Conduction and Raman Response in Molecular Junctions. *Nano Lett* **8**, 919-924 (2008).

75 Wu, S. W., Ogawa, N. & Ho, W. Atomic-Scale Coupling of Photons to Single-Molecule Junctions. *Science* **312**, 1362-1365, doi:10.1126/science.1124881 (2006).

76 Wold, D. J. & Frisbie, C. D. Formation of metal-molecule-metal tunnel junctions: Microcontacts to alkanethiol monolayers with a conducting AFM tip. *J Am Chem Soc* **122**, 2970-2971 (2000).

77 Dhirani, A., Lin, P. H., Guyot-Sionnest, P., Zehner, R. W. & Sita, L. R. Self-assembled molecular rectifiers. *The Journal of Chemical Physics* **106**, 5249-5253 (1997).

78 Ashwell, G. J., Tyrrell, W. D. & Whittam, A. J. Molecular Rectification: Self-Assembled Monolayers in Which Donor-Bridge-Acceptor Moieties Are Centrally Located and Symmetrically Coupled to Both Gold Electrodes. *J Am Chem Soc* **126**, 7102-7110 (2004).

79 Nijhuis, C. A., Reus, W. F. & Whitesides, G. M. Molecular Rectification in Metal-SAM-Metal Oxide-Metal Junctions. *J Am Chem Soc* **131**, 17814-17827 (2009).

80 Chabinyc, M. L. *et al.* Molecular Rectification in a Metal-Insulator-Metal Junction Based on Self-Assembled Monolayers. *J Am Chem Soc* **124**, 11730-11736 (2002).

81 Metzger, R. M. Electrical Rectification by a Molecule: The Advent of Unimolecular Electronic Devices. *Accounts of Chemical Research* **32**, 950-957, doi:doi:10.1021/ar9900663 (1999).

82 Metzger, R. M., Xu, T. & Peterson, I. R. Electrical Rectification by a Monolayer of Hexadecylquinolinium Tricyanoquinodimethanide Measured between Macroscopic Gold Electrodes. *The Journal of Physical Chemistry B* **105**, 7280-7290 (2001).

83 Elbing, M. *et al.* A single-molecule diode. *Proceedings of the National Academy of Sciences of the United States of America* **102**, 8815-8820, doi:10.1073/pnas.0408888102 (2005).

84 Metzger, R. M. Unimolecular electronics and rectifiers. *Synthetic Metals* **159**, 2277-2281 (2009).

85 Ng, M. K., Lee, D. C. & Yu, L. P. Molecular diodes based on conjugated diblock co-oligomers. *J Am Chem Soc* **124**, 11862-11863 (2002).

86 Reichert, J. *et al.* Driving Current through Single Organic Molecules. *Physical Review Letters* **88**, 176804 (2002).

87 Pan, J. B., Zhang, Z. H., Deng, X. Q., Qiu, M. & Guo, C. The transport properties of D-sigma -A molecules: A strikingly opposite directional rectification. *Appl Phys Lett* **98**, 013503.

88 Malen, J. A., Yee, S. K., Majumdar, A. & Segalman, R. A. Fundamentals of energy transport, energy conversion, and thermal properties in organic-inorganic heterojunctions. *Chemical Physics Letters* **491**, 109-122 (2010).

89 Tao, C. *et al.* Spatial Resolution of a Type II Heterojunction in a Single Bipolar Molecule. *Nano Lett* **9**, 3963-3967 (2009).

90 Hegner, M., Wagner, P. & Semenza, G. Ultralarge Atomically Flat Template-Stripped Au Surfaces for Scanning Probe Microscopy. *Surf Sci* **291**, 39-46 (1993).

91 Stamou, D. *et al.* Uniformly flat gold surfaces: Imaging the domain structure of organic monolayers using scanning force microscopy. *Langmuir* **13**, 2425-2428 (1997).

92 Wagner, P., Hegner, M., Guntherodt, H. J. & Semenza, G. Formation and in-Situ Modification of Monolayers Chemisorbed on Ultraflat Template-Stripped Gold Surfaces. *Langmuir* **11**, 3867-3875 (1995).

93 Cigang, X. & et al. A combined top-down bottom-up approach for introducing nanoparticle networks into nanoelectrode gaps. *Nanotechnology* **17**, 3333 (2006).

94 Neaton, J. B., Hybertsen, M. S. & Louie, S. G. Renormalization of Molecular Electronic Levels at Metal-Molecule Interfaces. *Physical Review Letters* **97**, 216405 (2006).

95 See, K. C. *et al.* Water-Processable Polymer-Nanocrystal Hybrids for Thermoelectrics. *Nano Lett* **10**, 4664-4667 (2010).

96 Xuan, Y. *et al.* Thermoelectric properties of conducting polymers: The case of poly(3-hexylthiophene). *Physical Review B* **82**, 115454 (2010).

97 See, K. C. *et al.* Water-Processable Polymerâˆ'Nanocrystal Hybrids for Thermoelectrics. *Nano Lett* **10**, 4664-4667 (2010).

98 Choudhury, P. K., Bagchi, D., Sangeeth, C. S. S. & Menon, R. Modified conformation and physical properties in conducting polymers due to varying conjugation and solvent

interactions. *Journal of Materials Chemistry* **21**, 1607-1614, doi:Doi 10.1039/C0jm02304c (2011).

99 Nardes, A. M., Janssen, R. A. J. & Kemerink, M. A Morphological Model for the Solvent-Enhanced Conductivity of PEDOT:PSS Thin Films. *Advanced Functional Materials* **18**, 865-871 (2008).

100 Nardes, A. M. *et al.* Microscopic Understanding of the Anisotropic Conductivity of PEDOT:PSS Thin Films. *Advanced Materials* **19**, 1196-1200 (2007).

101 Ouyang, J. *et al.* On the mechanism of conductivity enhancement in poly(3,4-ethylenedioxythiophene):poly(styrene sulfonate) film through solvent treatment. *Polymer* **45**, 8443-8450 (2004).

102 Xia, Y. J. & Ouyang, J. Y. PEDOT:PSS films with significantly enhanced conductivities induced by preferential solvation with cosolvents and their application in polymer photovoltaic cells. *Journal of Materials Chemistry* **21**, 4927-4936, doi:Doi 10.1039/C0jm04177g (2011).

103 Dimitriev, O. P., Piryatinski, Y. P. & Pud, A. A. Evidence of the controlled interaction between PEDOT and PSS in the PEDOT:PSS complex via concentration changes of the complex solution. *J Phys Chem B* **115**, 1357-1362, doi:10.1021/jp110545t (2011).

104 Crispin, X. *et al.* The Origin of the High Conductivity of Poly(3,4-ethylenedioxythiophene)âˆ'Poly(styrenesulfonate) (PEDOTâˆ'PSS) Plastic Electrodes. *Chemistry of Materials* **18**, 4354-4360 (2006).

105 Kong, F. *et al.* Thermoelectric Performance Enhancement of Poly(3,4-ethylenedioxythiophene):Poly(styrenesulfonate) Composite Films by Addition of Dimethyl Sulfoxide and Urea. *Journal of Electronic Materials* **41**, 2431-2438, doi:10.1007/s11664-012-2162-y (2012).

106 Reyes-Reyes, M., Cruz-Cruz, I. & López-Sandoval, R. n. Enhancement of the Electrical Conductivity in PEDOT:PSS Films by the Addition of Dimethyl Sulfate. *The Journal of Physical Chemistry C* **114**, 20220-20224, doi:10.1021/jp107386x (2010).

107 Kim, Y. H. *et al.* Highly Conductive PEDOT:PSS Electrode with Optimized Solvent and Thermal Post-Treatment for ITO-Free Organic Solar Cells. *Advanced Functional Materials* **21**, 1076-1081, doi:DOI 10.1002/adfm.201002290 (2011).

108 Zhang, B., Sun, J., Katz, H. E., Fang, F. & Opila, R. L. Promising Thermoelectric Properties of Commercial PEDOT:PSS Materials and Their Bi2Te3 Powder Composites. *Acs Applied Materials & Interfaces* **2**, 3170-3178, doi:Doi 10.1021/Am100654p (2010).

109 Kim, J. Y., Jung, J. H., Lee, D. E. & Joo, J. Enhancement of electrical conductivity of poly(3,4-ethylenedioxythiophene)/poly(4-styrenesulfonate) by a change of solvents. *Synthetic Metals* **126**, 311-316 (2002).

110 Du, Y., Shen, S. Z., Cai, K. & Casey, P. S. Research progress on polymer-inorganic thermoelectric nanocomposite materials. *Progress in Polymer Science* **37**, 820-841, doi:10.1016/j.progpolymsci.2011.11.003 (2012).

111 Yue, R. & Xu, J. Poly(3,4-ethylenedioxythiophene) as promising organic thermoelectric materials: A mini-review. *Synthetic Metals* **162**, 912-917, doi:10.1016/j.synthmet.2012.04.005 (2012).

112 Poehler, T. O. & Katz, H. E. Prospects for polymer-based thermoelectrics: state of the art and theoretical analysis. *Energy & Environmental Science* **5**, 8110-8115 (2012).

113 Dubey, N. & Leclerc, M. Conducting Polymers: Efficient Thermoelectric Materials. *J Polym Sci Pol Phys* **49**, 467-475, doi:Doi 10.1002/Polb.22206 (2011).

114 Scholdt, M. *et al.* Organic Semiconductors for Thermoelectric Applications. *Journal of Electronic Materials* **39**, 1589-1592, doi:DOI 10.1007/s11664-010-1271-8 (2010).

115 Bubnova, O., Berggren, M. & Crispin, X. Tuning the Thermoelectric Properties of Conducting Polymers in an Electrochemical Transistor. *J Am Chem Soc*, doi:10.1021/ja305188r (2012).

116 Jana, N. R. Gram-scale synthesis of soluble, near-monodisperse gold nanorods and other anisotropic nanoparticles. *Small* **1**, 875-882 (2005).

117 Thornburg, D. D. & Wayman, C. M. Thermoelectric Power of Vacuum-Evaporated Au[Single Bond]Ni Thin-Film Thermocouples. *Journal of Applied Physics* **40**, 3007-3013 (1969).

118 Bubnova, O. *et al.* Optimization of the thermoelectric figure of merit in the conducting polymer poly(3,4-ethylenedioxythiophene). *Nat Mater* **10**, 429-433 (2011).

119 Coates, N. E. *et al.* Effect of Interfacial Properties on Polymer–Nanocrystal Thermoelectric Transport. *Advanced Materials*, n/a-n/a, doi:10.1002/adma.201203915 (2013).

120 Gelbstein, Y. Thermoelectric power and structural properties in two-phase Sn/SnTe alloys. *Journal of Applied Physics* **105**, 023713, doi:10.1063/1.3068463 (2009).

121 Karni, J. Solar energy: The thermoelectric alternative. *Nat Mater* **10**, 481-482 (2011).

122 Baranowski, L. L., Snyder, G. J. & Toberer, E. S. Concentrated solar thermoelectric generators. *Energy & Environmental Science* **5**, 9055-9067 (2012).

123 Kraemer, D. *et al.* High-performance flat-panel solar thermoelectric generators with high thermal concentration. *Nat Mater* **10**, 532-538 (2011).

124 Vining, C. B. An inconvenient truth about thermoelectrics. *Nat Mater* **8**, 83-85 (2009).

125 Powell, D. M. *et al.* Crystalline silicon photovoltaics: a cost analysis framework for determining technology pathways to reach baseload electricity costs. *Energy & Environmental Science* **5**, 5874-5883 (2012).

126 Rowe, D. M. & Min, G. Design theory of thermoelectric modules for electrical power generation. *Science, Measurement and Technology, IEE Proceedings -* **143**, 351-356 (1996).

127 Yazawa, K. & Shakouri, A. Cost-efficiency trade-off and the design of thermoelectric power generators. *Environmental science & technology* **45**, 7548-7553, doi:10.1021/es2005418 (2011).

128 Kristiansen, N. R., Snyder, G. J., Nielsen, H. K. & Rosendahl, L. Waste Heat Recovery from a Marine Waste Incinerator Using a Thermoelectric Generator. *Journal of Electronic Materials* **41**, 1024-1029, doi:10.1007/s11664-012-2009-6 (2012).

129 Yadav, G. G., Susoreny, J. A., Zhang, G., Yang, H. & Wu, Y. Nanostructure-based thermoelectric conversion: an insight into the feasibility and sustainability for large-scale deployment. *Nanoscale* **3**, 3555-3562 (2012).

130 Vineis, C. J., Shakouri, A., Majumdar, A. & Kanatzidis, M. G. Nanostructured Thermoelectrics: Big Efficiency Gains from Small Features. *Advanced Materials* **22**, 3970-3980 (2010).

131 Miner, A. in *3rd Thermoelectrics Applications Workshop.* (U.S. Department of Energy).

132 Yadav, G. G., Susoreny, J. A., Zhang, G., Yang, H. & Wu, Y. Nanostructure-based thermoelectric conversion: an insight into the feasibility and sustainability for large-scale deployment. *Nanoscale* **3**, 3555-3562, doi:10.1039/C1NR10555H (2011).

133 Fairbanks, J. in *2011 Thermoelectrics Applications Workshop* (ed Department of Energy) (San Diego, CA, 2011).

134 Crane, D. T. in *3rd Thermoelectrics Applications Workshop* (U.S. Department of Energy, Baltimore, MD, 2012).

135 Aixala, L. in *3rd Thermoelectrics Applications Workshop.* (U.S. Department of Energy).

136 Crane, D. T. & Kossakovski, D. in *3rd Thermoelectrics Applications Workshop.* (U.S. Department of Energy).

137 Meisner, G. in *3rd Thermoelectrics Applications Workshop.* (U.S. Department of Energy).

138 Karri, M. A., Thacher, E. F. & Helenbrook, B. T. Exhaust energy conversion by thermoelectric generator: Two case studies. *Energy Conversion and Management* **52**, 1596-1611, doi:10.1016/j.enconman.2010.10.013 (2011).

139 Won, Y. *et al.* Mechanical characterization of aligned multi-walled carbon nanotube films using microfabricated resonators. *Carbon* **50**, 347-355, doi:10.1016/j.carbon.2011.08.009 (2012).

140 Gao, Y. *et al.* Nanostructured Interfaces for Thermoelectrics. *Journal of Electronic Materials* **39**, 1456-1462, doi:10.1007/s11664-010-1256-7 (2010).

141 Gao, Y. *et al.* Impact of nanotube density and alignment on the elastic modulus near the top and base surfaces of aligned multi-walled carbon nanotube films. *Carbon* (2012).

142 Angrist, S. W. *Direct Energy Conversion*. (Allyn and Bacon, Inc, 1965).

143 Rowe, D. M. *Thermoelectrics Handbook*. ??? (CRC Press, 2006).

144 Mayer, P. M. & Ram, R. J. Optimization of heat sink-limited thermoelectric generators. *Nanoscale Microscale Thermophys. Eng.* **10**, 143-155 (2006).

145 Yazawa, K. & Shakouri, A. Optimization of power and efficiency of thermoelectric devices with asymmetric thermal contacts. *Journal of Applied Physics* **111**, 024509 (2012).

146 Shah, R. K., Sekuli & P., D. a. (John Wiley & Sons).

147 Incropera, F. P., Dewitt, D. P., Bergman, T. L. & Lavine, A. S. *Fundamentals of Heat and Mass Transfer*. 6th edn, (John Wiley & Sons, 2007).

148 Shah, R. K. & Sekulic, D. P. *Fundamentals of Heat Exchanger Design*. (John Wiley & Sons, 2003).

149 Branker, K., Pathak, M. J. M. & Pearce, J. M. A review of solar photovoltaic levelized cost of electricity. *Renewable and Sustainable Energy Reviews* **15**, 4470-4482, doi:http://dx.doi.org/10.1016/j.rser.2011.07.104 (2011).

150 Survey, U. S. G. *Commodity Statistics and Information*, <http://minerals.usgs.gov/minerals/pubs/commodity/> (

151 Scholdt, M. *et al.* Organic Semiconductors for Thermoelectric Applications. *Journal of Electronic Materials* **39**, 1589-1592.

152 Parker, W. J. & Jenkins, R. J. Thermal Conductivity Measurements on Bismuth Telluride in the Presence of a 2 MeV Electron Beam. Report No. USNRDL-TR-462, Medium: X; Size: Pages: 38 (1960).

153 Lowhorn, N. D. *et al.* Development of a Seebeck coefficient Standard Reference Material™. *Journal of Materials Research* **26**, 1983-1992, doi:10.1557/jmr.2011.118 (2011).

154 Xie, W., Tang, X., Yan, Y., Zhang, Q. & Tritt, T. M. High thermoelectric performance BiSbTe alloy with unique low-dimensional structure. *Journal of Applied Physics* **105**, 113713, doi:10.1063/1.3143104 (2009).

155 Zhou, J., Jin, C., Seol, J. H., Li, X. & Shi, L. Thermoelectric properties of individual electrodeposited bismuth telluride nanowires. *Applied Physics Letters* **87**, 133109, doi:10.1063/1.2058217 (2005).

156 Andrews, S. C. *et al.* Atomic-level control of the thermoelectric properties in polytypoid nanowires. *Chemical Science* **2**, 706, doi:10.1039/c0sc00537a (2011).

157 Harman, T. C., Taylor, P. J., Walsh, M. P. & LaForge, B. E. Quantum Dot Superlattice Thermoelectric Materials and Devices. *Science* **297**, 2229-2232, doi:10.1126/science.1072886 (2002).

158 Hsu, K. F. *et al.* Cubic AgPbmSbTe2+m: Bulk Thermoelectric Materials with High Figure of Merit. *Science* **303**, 818-821, doi:10.1126/science.1092963 (2004).

159 Joshi, G. *et al.* Enhanced Thermoelectric Figure-of-Merit in Nanostructured p-type Silicon Germanium Bulk Alloys. *NanoLetters* **8**, 4670-4674 (2008).

160 Martinez, J. A., Provencio, P. P., Picraux, S. T., Sullivan, J. P. & Swartzentruber, B. S. Enhanced thermoelectric figure of merit in SiGe alloy nanowires by boundary and hole-phonon scattering. *Journal of Applied Physics* **110**, 074317, doi:10.1063/1.3647575 (2011).

161 Bux, S. K. *et al.* Mechanochemical synthesis and thermoelectric properties of high quality magnesium silicide. *Journal of Materials Chemistry* **21**, 12259, doi:10.1039/c1jm10827a (2011).

162 Zaitsev, V. K. *et al.* Highly effective Mg_{2}Si_{1−x}Sn_{x} thermoelectrics. *Physical Review B* **74**, 045207 (2006).

163 Bux, S. K. *et al.* Nanostructured Bulk Silicon as an Effective Thermoelectric Material. *Advanced Functional Materials* **19**, 2445-2452, doi:10.1002/adfm.200900250 (2009).

164 Hochbaum, A. I. *et al.* Enhanced thermoelectric performance of rough silicon nanowires. *Nature* **451**, 163-167, doi:10.1038/nature06381 (2008).

165 Chen, X., Weathers, A., Moore, A., Zhou, J. & Shi, L. Thermoelectric Properties of Cold-Pressed Higher Manganese Silicides for Waste Heat Recovery. *Journal of Electronic Materials* **41**, 1564-1572, doi:10.1007/s11664-012-1987-8 (2012).

166 Cederkrantz, D., Nygren, M. & Palmqvist, A. E. C. Thermoelectric properties of partly Sb- and Zn-substituted Ba[sub 8]Ga[sub 16]Ge[sub 30] clathrates. *Journal of Applied Physics* **108**, 113711, doi:10.1063/1.3518043 (2010).

167 Toberer, E., Christensen, M., Iversen, B. & Snyder, G. High temperature thermoelectric efficiency in Ba8Ga16Ge30. *Physical Review B* **77**, doi:10.1103/PhysRevB.77.075203 (2008).

168 Roudebush, J. H., Toberer, E. S., Hope, H., Jeffrey Snyder, G. & Kauzlarich, S. M. Crystal structure, characterization and thermoelectric properties of the type-I clathrate Ba8−ySryAl14Si32 (0.6≤y≤1.3) prepared by aluminum flux. *Journal of Solid State Chemistry* **184**, 1176-1185, doi:10.1016/j.jssc.2011.02.027 (2011).

169 Qiu, P. F. *et al.* High-temperature electrical and thermal transport properties of fully filled skutterudites RFe4Sb12 (R = Ca, Sr, Ba, La, Ce, Pr, Nd, Eu, and Yb). *Journal of Applied Physics* **109**, 063713, doi:10.1063/1.3553842 (2011).

170 Peng, J., He, J., Alboni, P. N. & Tritt, T. M. Synthesis and Thermoelectric Properties of the Double-Filled Skutterudite Yb0.2In y Co4Sb12. *Journal of Electronic Materials* **38**, 981-984, doi:10.1007/s11664-008-0624-z (2009).

171 Puyet, M. *et al.* Beneficial effect of Ni substitution on the thermoelectric properties in partially filled Ca[sub y]Co[sub 4 - x]Ni[sub x]Sb[sub 12] skutterudites. *Journal of Applied Physics* **97**, 083712 (2005).

172 Tsubota, T., Ohtaki, M., Eguchi, K. & Arai, H. Thermoelectric properties of Al-doped ZnO as a promising oxide material for high-temperature thermoelectric conversion. *Journal of Materials Chemistry* **7**, 85-90 (1997).

173 Xu, G., Funahashi, R., Shikano, M., Matsubara, I. & Zhou, Y. Thermoelectric properties of the Bi- and Na-substituted Ca[sub 3]Co[sub 4]O[sub 9] system. *Applied Physics Letters* **80**, 3760, doi:10.1063/1.1480115 (2002).

174 Fujita, K., Mochida, T. & Nakamura, K. in *International Conference on Thermoelectrics.* 168-171.

175 Sakurada, S. & Shutoh, N. Effect of Ti substitution on the thermoelectric properties of (Zr,Hf)NiSn half-Heusler compounds. *Applied Physics Letters* **86**, 082105, doi:10.1063/1.1868063 (2005).

176 Shen, Q. *et al.* Effects of partial substitution of Ni by Pd on the thermoelectric properties of ZrNiSn-based half-Heusler compounds. *Applied Physics Letters* **79**, 4165, doi:10.1063/1.1425459 (2001).

177 Katayama, T., Kim, S., Kimura, Y. & Mishima, Y. The effects of quaternary additions on thermoelectric properties of TiNiSn-based half-heusler alloys. *Journal of Electronic Materials* **32**, 1160-1165, doi:10.1007/s11664-003-0006-5 (2003).

178 Biswas, K. *et al.* High-performance bulk thermoelectrics with all-scale hierarchical architectures. *Nature* **489**, 414-418, (2012).

179 Koumoto, K., Wang, Y., Zhang, R., Kosuga, A. & Funahashi, R. Oxide Thermoelectric Materials: A Nanostructuring Approach. *Annual Review of Materials Research* **40**, 363-394, doi:10.1146/annurev-matsci-070909-104521 (2010).

180 *U.S. Department of Energy, Sunshot Vision Study* (2012).

181 Vélez, F. *et al.* A technical, economical and market review of organic Rankine cycles for the conversion of low-grade heat for power generation. *Renewable and Sustainable Energy Reviews* **16**, 4175-4189, doi:10.1016/j.rser.2012.03.022 (2012).

182 Miller, E., Hendricks, T. & Peterson, R. Modeling Energy Recovery Using Thermoelectric Conversion Integrated with an Organic Rankine Bottoming Cycle. *Journal of Electronic Materials* **38**, 1206-1213, doi:10.1007/s11664-009-0743-1 (2009).

183 Esarte, J., Min, G. & Rowe, D. M. Modelling heat exchangers for thermoelectric generators. *Journal of Power Sources* **93** (2001).

184 Goodson, K. E. in *2011 Thermoelectrics Applications Workshop.* (U.S. Department of Energy).

185 Effenberger, F., Wurthner, F. & Steybe, F. Synthesis and Solvatochromic Properties of Donor-Acceptor-Substituted Oligothiophenes. *Journal of Organic Chemistry* **60**, 2082-2091 (1995).

Appendix A Synthesis of the BPNDT Molecule

These synthetic produces were developed by collaborator Dr. Jibin Sun for the synthesis of the BPNDT molecule discussed in Chapter 3.

First, Compound **1** (2,2-bithiophene-5-thiol) was prepared according to literature[185]. Next (as shown in Fig. A1) Compound **3** was synthesizes by combining Compound **1** (35.0 g, 0.18 mol), KOBu^t (20.8 g, 0.19 mol) and 200 mL THF/CH_3OH (v/v = 1:1) in a 500 mL flask with a reflux condenser. This solution was refluxed for 120 minutes and allowed to cool to room temperature. The solvent was then removed under vacuum leaving 41.0 g of Compound **2** as a yellow solid (98% yield) which was used without further purification. Compound **2** (6.5 g, 27.6 mmol) was then dissolved in 150 mL solution of a CH_3OH and THF (10 mL) before TMSCCBr (5.0 g, 27.6 mmol) was added quickly at 0 °C. The resulting yellowing solution was refluxed overnight. The solvent was then removed and the orange solid was extracted by hexanes; the hexanes were removed and the resulting crude product was passed through a silica gel plug (30 cm). 7.6 grams of a light yellow oil (92% yield) was obtained as a pure product. ^{1}HNMR (300 MHz, $CDCl_3$) δ 0.05 (s, 9H), 0.96 (m, 2 H), 2.90 (m, 2H), 7.05 (m, 3H), 7.21 (t, 1H), 7.25 (d, 1H). ^{13}C NMR (75.5 MHz, $CDCl_3$) δ -1.4, 17.9, 35.6, 124.1, 124.87, 128.2, 134.3, 134.5, 137.4, 140.8. Anal. Calcd for $C_{13}H_{18}S_3Si$: C, 52.30; H 6.08. Found: C, 52.47; H 6.13.

Compound **4** was synthesized by mixing Compound **3** (3.15 g, 10.5 mmol) and NBS (1.88 g, 10.6 mmol) in 30 mL of THF at 0 °C. The solution was stirred at room temperature for 4 hours. The solvent was then removed and the product was purified by a silica gel column with hexanes as the eluent to isolate 3.50 g of Compound **4** as a yellow oil (88% yield). ^{1}HNMR (400 MHz, $CDCl_3$) δ 0.02 (s, 9H), 0.93 (m, 2 H), 2.87 (m, 2H), 6.88 (d, 2H), 6.97 (m, 3H). ^{13}C NMR (75.5 MHz, $CDCl_3$) δ -1.5, 17.6, 34.1, 111.5, 124.1, 124.3, 130.9, 134.1, 135.2, 138.8, 139.5. M.S.: 378.01 (M^+).

Compound **5** was synthesized by mixing Compound **4** (3.20 g, 8.5 mmol), 4-ethynylaniline (1.0 g, 8.5 mmol), $Pd(Ph_3)_2Cl_2$ (0.32 g, 0.46 mmol), CuI (0.16 g, 0.84 mmol), and PPh_3 (0.48 g, 0.92 mmol) together in 100 mL of NEt_3. The solution was de-aired by bubbling N_2 for 30 minutes and stirred at 100 °C for 24 hours. The solvent was then removed under vacuum. The resulting brown solid was extracted with diethyl ether. The solvent was then removed and the crude product was purified by a silica gel column with $CHCl_3$ as the eluent to isolate 2.84 g of Compound **5** (81% yield) as an orange oil. ^{1}HNMR (300 MHz, $CDCl_3$) δ 0.04 (s, 9H), 0.96 (m, 2 H), 2.90 (m, 2H), 3.85 (br, 2H), 6.62 (d, 2H), 7.02 (m, 3H), 7.13 (d, 1H), 7.39 (d, 2H). ^{13}CNMR (75.5 MHz, $CDCl_3$) δ -1.4, 17.9, 35.1, 81.0, 95.8, 112.1, 115.1, 123.3, 123.9, 124.4, 132.3, 133.2, 134.1, 135.1, 137.9, 140.1, 147.4. M.S.: 413.25 (M^+).

Compound **7** was synthesized by mixing Compound **5** (1.0 g, 2.4 mmol) and 1,4,5,8-naphthalene-tetracarboxylic dianhydride (4.0 g, 15.3 mmol) together in 50 mL of DMF. The solution was de-aired by bubbling N_2 for 30 minutes and stirred at 145 °C for 12 hours. The solution was then cooled down and excess 1,4,5,8-naphthalene-tetracarboxylic dianhydride was removed by filtering finally yielding a dark brown solution as Compound **6.** The Compound **6** solution was then mixed with 2-aminoethanethiol (2.0 g, 26.0 mmol). This resulting solution was de-aired by bubbling N_2 for 30 minutes and stirred at 145 °C for another 12 hours. The solvent was then removed under vacuum. The resulting brown solid was purified by using a silica gel column with $CHCl_3$ as the eluent to isolate 0.62 g of Compound **7** (33% yield) as a brown solid. ^{1}HNMR (400 MHz, $CDCl_3$) δ 0.02 (s, 9H), 0.92 (m, 2 H), 1.57 (m, 2H), 2.91 (m, 4H), 3.10 (br, 1H), 6.99 (d, 1H), 7.03 (d, 1H), 7.05 (d, 1H), 7.20 (d, 1H), 7.30 (d, 2H), 7.68 (d, 2H), 8.81 (br, 4H). Anal. Calcd for $C_{37}H_{30}N_2O_4S_4Si$: C, 61.67; H 4.18; N 3.87. Found: C, 61.22; H 4.14; N 3.92. Compound **7**, was the final P-N molecule that was used in experiments.

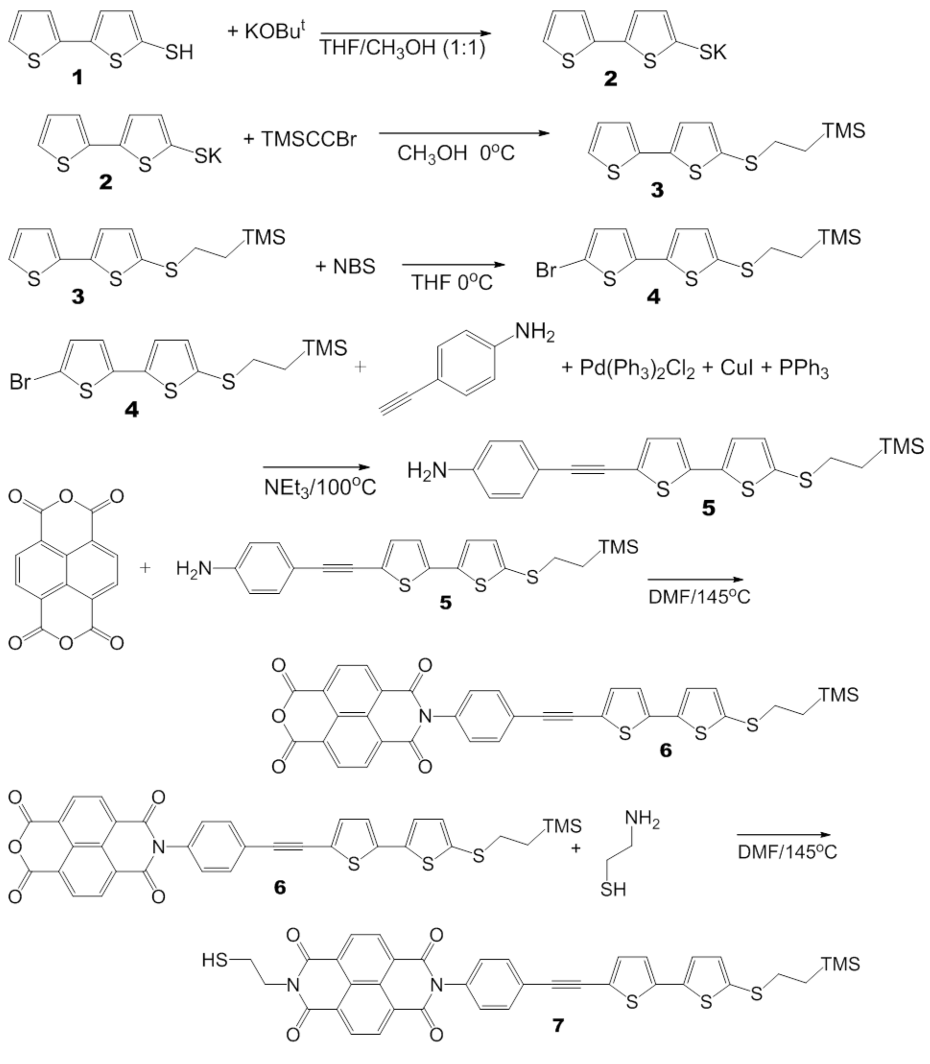

Figure A.1 Synthesis of BPNDT Molecule. Compounds 1 through 7 of the synthesis of the BPNDT.

Appendix B MATLAB Scripts for Cost Analysis

Evaluation of the Power Generation Cost Metric, *G*

```
function [G]=CostG(L,F,m,Th,Tc,S,sigma,k,rho,Cm,CMm,CMA,Chx,Uh,Uc)
%%This function calculates the $/W G value of a thermoelectric system
% L is the thermoelectric leg length, m
% F is the fill factor
% m is the load condition m=RL/R
% Th is the hot reservoir temperature, K
% Tc is the cold reservoir temperature, K
% S is the material Seebeck coefficient, V/K
% sigma is the material electrical conductivity, S/m
% k is the material thermal conductivity, W/m-K
% rho is the density of the material, kg/m^3
% Cm is the specific material cost, $/kg
% CMm is the specific manufacturing cost, $/kg
% CMA is the areal manufacturing cost, $/m^2
% Chx is the heat exchanger cost, $/(W/K)
% Uh is the hot side heat exchanger conductance, W/m^2-K
% Uc is the cold side heat exchanger conductance, W/m^2-K
%%-------------------------------------------------------------------------

%%----------------------------------Inputs---------------------------------
%%GEOMETRY CONDITIONS
A=1; %m^2 %This is arbitrary

%%HOT AND COLD SIDE
t1=25.4E-6; %m
k1=400; %W/m-K copper
t2=0.38E-3; %m
k2=30; %W/m-K alumina silicate
Kh=((Uh*A)^-1+(k1*A/t1)^-1+(k2*A/t2)^-1)^-1; %W/K
Kc=((Uc*A)^-1+(k1*A/t1)^-1+(k2*A/t2)^-1)^-1; %W/K

%%Air Gap
ka=0.03; %W/m-K
eps=2/3; %emissivity
sb=5.67E-8; %W/m^2-K^4
Pr=0.7;
g=9.81; %m/s^2
Beta=2/(Th+Tc); %K^-1
alpha=29.9E-6; %m^2/s
v=20.92E-6; %m^2/s
%%-------------------------------------------------------------------------

%%-------------------------------Analysis----------------------------------
%%MODULE TRANSPORT PROPERTIES
VF=(sqrt(1+L.^2/A)-L/sqrt(A)).^2;
Krad=4*sb*VF*((Th+Tc)/2)^3/(2*(1-eps)/eps+1./VF)*(1-F)*A;
Kcond=ka*A*(1-F)./L;
Ra=g*Beta*(Th-Tc)*L.^3/(v*alpha);
    if Ra>1708
        Kcon=ka*A*(1-F)./L*(0.069*Ra.^(1/3)*Pr^0.074);
    else
```

```
        Kcon=Kcond;
    end
Kp=Kcon+Krad; %W/K
KT=k*A*F./L+Kp; %W/K for both legs
Spn=S-(-S); %V/K Sp=-Sn=S
R=4*L/(sigma*A*F); %Ohms

%%APPROXIMATE TEMPERATURE CALCULATIONS (comment or uncomment for execution)
% T1=Th-(1/Kh)./(1./KT+1/Kc+1/Kh)*(Th-Tc); %K
% T2=Tc+(1/Kc)./(1./KT+1/Kc+1/Kh)*(Th-Tc); %K
% dT=Kh*Kc./(Kc*KT+Kh*KT+Kc*Kh)*(Th-Tc); %K
% Tm=(T1+T2)/2; %K

%%EXACT TEMPERATURE CALCULATIONS (comment or uncomment for execution)
y0=[Th;Tc];
options=optimset('Display','off');
[y,fval]=fsolve(@(y)[Kh*(Th-y(1))-KT*(y(1)-y(2))-...
    Spn^2*(y(1)-y(2))*y(1)/(2*R)+Spn^2*(y(1)-y(2))^2./(8*R);...
    Spn^2*(y(1)-y(2))^2./(4*R)-Kh*(Th-y(1))+Kc*(y(2)-Tc)],y0,options);
T1=y(1); %K
T2=y(2); %K
Tm=(T1+T2)/2; %K
dT=T1-T2; %K

%%PERFORMANCE METRICS
Cost=((Cm+CMm)*rho*L+CMA)*A*F+Chx*mean([Uh,Uc])*A; %$
%Cost=((Cm+CMm)*rho*L+CMA)*A*F; %$ (without heat exchanger costs)
Z_s=S^2*sigma/k; %K^-1
Z=Spn^2./(KT.*R); %K^-1

%%GENERAL THERMAL EFFICIENCY
I=Spn*dT./(R*(m+1)); %Amps
eta=(1-T2./T1).*(m*Z.*T1./(Z.*Tm+m*Z.*T1+(m+1)^2));
qh=KT.*dT+Spn*I.*T1-1/2*I.^2.*R; %W
P=m*I.^2.*R; %W
%Z_s*(T1+T2)/2

%%COST METRIC
G=Cost./P; %$/W
%%-------------------------------------------------------------------------
```

Evaluation of the Cooling Cost Metric, *H*

```
function [H]=CostMin_Cooling_Alt(L,Th,Tc,S,sigma,k,rho,Cm,CMm,CMA)
%%This function calculates the $/kWh H value of a thermoelectric system
% L is the thermoelectric leg length, m
% Th is the hot reservoir temperature, K
% Tc is the cold reservoir temperature, K
% S is the material Seebeck coefficient, V/K
% sigma is the material electrical conductivity, S/m
% k is the material thermal conductivity, W/m-K
% rho is the density of the material, kg/m^3
% Cm is the specific material cost, $/kg
% CMm is the specific manufacturing cost, $/kg
% CMA is the areal manufacturing cost, $/m^2
%%-----------------------------------------------------------------------

%%---------------------------------Inputs---------------------------------
%%GEOMETRY CONDITIONS
F=1; %fill factor
A=1; %m^2
    Ac=A*F/2; %m^2 for one leg

%%HOT AND COLD SIDE
t1=25.4E-6; %m
k1=400; %W/m-K copper
t2=0.38E-3; %m
k2=30; %W/m-K alumina silicate
Uh=inf; %W/m^2-K
Uc=inf; %W/m^2-K
Kh=((Uh*A)^-1+(k1*A/t1)^-1+(k2*A/t2)^-1)^-1; %W/K
Kc=((Uc*A)^-1+(k1*A/t1)^-1+(k2*A/t2)^-1)^-1; %W/K

%%AIR GAP
ka=0.03; %W/m-K
eps=2/3; %emissivity
Pr=0.7;
g=9.81; %m/s^2
Beta=2/(Th+Tc); %K^-1
alpha=29.9E-6; %m^2/s
v=20.92E-6; %m^2/s
%%-----------------------------------------------------------------------

%%------------------------------Analysis----------------------------------
%%MODULE TRANSPORT PROPERTIES
VF=(sqrt(1+L.^2/A)-L/sqrt(A)).^2;
Krad=4*sb*VF*((Th+Tc)/2)^3/(2*(1-eps)/eps+1./VF)*(1-F)*A;
Kcond=ka*A*(1-F)./L;
Ra=g*Beta*(Th-Tc)*L.^3/(v*alpha);
    if Ra>1708
        Kcon=ka*A*(1-F)./L*(0.069*Ra.^(1/3)*Pr^0.074);
    else
        Kcon=Kcond;
    end
Kp=Kcon+Krad; %W/K
KT=k*A*F./L+Kp; %W/K for both legs
Spn=S-(-S); %V/K Sp=-Sn=S
R=2*L/(sigma*Ac); %Ohms
```

```
%%PERFORMANCE METRICS
Cost=(Cm+CMm)*rho*L+CMA; %$/m^2
Z_s=S^2*sigma/k; %K^-1
Z=Spn^2./(KT.*R); %K^-1

%%EXACT TEMPERATURES CALCULATIONS
Tm=(Th+Tc)/2;
m=sqrt(1+Z*Tm);
AA=(-2*Spn^2*m)./(R.*(m-1).^2);
BB=(2*Spn^2*Tm*(m+1))./(R.*(m-1).^2)+2*KT+Kc;
CC=(-2*Spn^2*Tm^2)./(R.*(m-1).^2)-2*KT*Tm-Kc*Tc;
for j=1:length(L)
    X(:,j)=[(-BB(j)+sqrt(BB(j)^2-4*AA(j)*CC(j)))/(2*AA(j));...
        (-BB(j)-sqrt(BB(j)^2-4*AA(j)*CC(j)))/(2*AA(j))];
    T2(j)=min(X(:,j));
end

%%PERFORMANCE METRICS
T1=2*Tm-T2;
dT=T1-T2;
%dT_max=1/2*Z.*T2.^2;

%%MAX EFFICIENCY CONDITION
I_max=2*Spn*(Tm-T2)./(R.*(m-1));
Q_c_max=Spn*T2.*I_max-KT.*dT-1/2*I_max.^2.*R;
P_max=Spn*I_max.*dT+I_max.^2.*R;
COP_max=Q_c_max./P_max;
C_e=0.0983; %$/kWh_e
n=20*365*24; %20 year lifetime
r=0.030/(365*24); %inflation rate 3.0% annually

%%COST METRIC
H=(Cost*A*F*r./(Q_c_max/1000))+C_e./COP_max; %$/kWh
%-----------------------------------------------------------------------
```